DTU Library

Electric Thermal Energy Storage within the Decarbonization of Energy Supply
A challenge-driven study

Knobloch, Kai

Publication date:
2023

Document Version
Publisher's PDF, also known as Version of record

[Link back to DTU Orbit](#)

Modeling and Analysis of Pavements with Asphalt Reinforcement

Development of a new computational model

PhD Thesis
By Julius Nielsen

Modeling and Analysis of Pavements with Asphalt Reinforcement
Development of a new computational model

PhD Thesis
April, 2023

By

Julius Nielsen

Industrial PhD
Mobile: +45 28 35 67 29
E-mail: juliusnielsen93@gmail.com
ORCID: 0000-0002-2225-9799
LinkedIn: https://www.linkedin.com/in/julius-nielsen-93dk/
GoogleScholar: https://scholar.google.com/citations?user=LSx-WG0AAAA
ResearchGate: https://www.researchgate.net/profile/Julius-Nielsen-2

Supervisory Team:

Principal supervisor: Eyal Levenberg, Associate Professor
Section for Geotechnics and Geology, Department of Environmental and Resource Engineering, Technical University of Denmark, 2800 Kgs. Lyngby, Denmark
eylev@dtu.dk

Co-supervisor: Klavs Olsen, Head Engineer European Pavement
S&P Reinforcement Nordic ApS, Hedegårdsvej 11, 8300 Odder, Denmark
klavs.olsen@sp-reinforcement.eu

Co-supervisor: Asmus Skar, Assistant Professor
Section for Geotechnics and Geology, Department of Environmental and Resource Engineering, Technical University of Denmark, 2800 Kgs. Lyngby, Denmark
asska@dtu.dk

Assessment Committee:

Chairman: Thomas Ingeman-Nielsen, Associate Professor
Section for Geotechnics and Geology, Department of Environmental and Resource Engineering, Technical University of Denmark, 2800 Kgs. Lyngby, Denmark

Examiner: Shelley Marie Stoffels, Professor and Associate Dean
College of Engineering, Pennsylvania State University, Pennsylvania 16802, United States

Examiner: Sigurður Erlingsson, Professor
Faculty of Civil and Environmental Engineering, The University of Iceland, 102 Reykjavík, Iceland

"If green is the new black, we should indeed try to change the color of our current and future roads."

Preface

This thesis has been submitted as part of the requirements for the Danish Doctor of Philosophy (PhD) degree. The study followed the Industrial PhD program of the Innovation Fund Denmark (IFD), in a joint collaboration between the Section for Geotechnics and Geology, Department of Environmental and Resource Engineering, Technical University of Denmark (DTU) and the industrial partner S&P Reinforcement Nordic Aps. The project was prepared by the PhD candidate over a three-years-and-three-months period (from February 2020 to April 2023) under the joint supervision of Associate Professor Eyal Levenberg (DTU), Head Engineer Klavs Olsen (S&P), and Assistant Professor Asmus Skar (DTU). The project period constitutes a three months extension that was given due to the COVID-19 pandemic and the resulting university lockdown. The entire research was funded by the IFD [grant number 9065-00107B] and S&P Reinforcement Nordic Aps.

The thesis follows a paper-based format and is divided into two parts: Part I and Part II. Part I commences with an introduction to the subject matter, including the background, research objectives, and study methodology. Next, an extended summary of each involved paper is presented, followed by supplementary unpublished work, final conclusions, and the study's contribution to the pavement engineering field. Part II provides a collection of four scientific papers (three journal papers and one conference paper) that were written during the PhD period. The paper collection constitutes the basis of this work and presents the entire research effort in greater detail.

Julius Nielsen
April, 2023

Modeling and Analysis of Pavements with Asphalt Reinforcement

Acknowledgements

all been critical for me to reach this point. In this context, I take here the opportunity to highlight the most important people in my life, i.e., my parents: Regina Grettisdóttir and Klaus Nielsen, and my sisters: Fenja Nielsen and Emma Nielsen. Thank you for your outstanding love, great inspiration, and unconditional support. I will always appreciate it!

Abstract

Pavement systems are important for ensuring social and economic equality. These systems constantly deteriorate under the pressure of heavy traffic and weather effects, making regular maintenance or rehabilitation necessary. However, these activities challenge societies as they are economically expensive, disruptive to traffic, and require the use of natural resources. With the marked growth in global shipping, the evolution of new types of vehicles, and rapid climate change effects, these societal challenges are expected to aggravate. Accordingly, there is a need to improve the traditional pavement design and rehabilitation methods to maintain an acceptable service level of the overall road network. To meet these challenges, asphalt grid reinforcement (AGR) products have emerged as a possible solution. Previous studies have shown that AGR products can potentially improve pavement performance and prolong service life. Nonetheless, no mechanistic-empirical design method currently applies to asphalt pavements with AGR, which is needed to promote an AGR alternative.

Motivated by this need, the current PhD study focused on developing a mechanistic component (which is concerned with response evaluation) that engineers can use to subsequently quantify pavement performance. Two study objectives were outlined in the dissertation: (i) to develop a versatile, useful, and validated computational model capable of incorporating AGR effects in asphalt pavement systems and (ii) to gain valuable insights into the effects of AGR.

To achieve this, a model formulation was developed by extending the standard linear elastic theory framework to include: fragmented layers, imperfect interface bonding, viscoelasticity, moving loads, and AGR. The AGR model-component was formulated as a combination of three contributions: (i) including AGR as a thin high-modulus elastic layer, (ii) accounting for the AGR's influence on interface bonding between adjacent layers, and (iii) capturing the AGR's impact on the surrounding asphalt concrete properties. In total, seven modeling inputs were required to represent an AGR, and the formulation was implemented into the computational code GRIDPAVE-MM. Several experimental campaigns were carried out for subsequent model validation of GRIDPAVE. These campaigns involved full-scale testing at a newly built test facility called DTU Smart Road. Here embedded sensors were used to collect pavement responses triggered by vehicle loadings. The collected field responses were compared against model simulations to showcase GRIDPAVE's ability to match embedded sensor readings.

The main study findings highlighted that the developed model GRIDPAVE was able to capture the effects of installing AGR products inside an asphalt pavement. Furthermore, general model simulations indicated that adding reinforcement can potentially delay the development of cracks and ruts in road systems, hence improving the overall service life.

In conclusion, the PhD study provides a versatile, useful, and valid tool that can enable engineers, consultants, and contractors (etc.) to include AGR in asphalt pavement design. Specifically, the model can produce traffic-induced stresses, strains, and displacements in various asphalt pavement systems with AGR, which can subsequently be used to evaluate the AGR effects on pavement performance. Ultimately, the study opens up new opportunities for using AGR as a sustainable and robust solution for maintaining an acceptable pavement service level for future road systems.

Resumé

Vejbelægningssystemer er vigtige for at sikre social og økonomisk lighed. Disse systemer forringes konstant under pres fra tung trafik samt vejrforhold, hvilket gør det nødvendigt at reparere og vedligeholde veje på regelmæssig basis. Disse aktiviteter er økonomisk dyre, forstyrrende for trafikken og øger forbruget af naturens ressourcer. Med en markant global vækst i fragtkørsel, udviklingen af nye typer køretøjer samt drastiske klimaforandringer, forventes disse samfundsmæssige udfordringer at blive forværret. Der er derfor behov for at forbedre traditionelle dimensionerings- og vedligeholdelsesmetoder for at opretholde et acceptabelt serviceniveau af vejnettet. En mulig løsning for at imødekomme disse udfordringer er at bruge asfaltforstærkningsnet. Tidligere undersøgelser har vist, at disse forstærkningsprodukter potentielt kan forbedre belægningers ydeevne og forlænge deres levetid. Ikke desto mindre eksisterer der i øjeblikket ingen mekanistisk-empirisk dimensioneringsmetoder, der gør sig gældende for asfaltbelægninger med asfaltforstærkningsnet, hvilket er nødvendigt for at promovere sådanne løsninger.

Motiveret af denne nødvendighed har dette ph.d.-studie fokuseret på at udvikle en mekanistisk model (der omfatter responsevaluering), som ingeniører kan bruge til efterfølgende at vurdere belægningens ydeevne. To projektformål blev skitseret i afhandlingen: (i) at udvikle en alsidig, anvendelig, samt valideret beregningsmodel, der er i stand til at inkorporere effekten ved at installere asfaltforstærkningsnet og (ii) at forbedre forståelsen af, hvordan asfaltforstærkningsnet påvirker vejbelægninger.

I den forbindelse blev en ny model formuleret ved at udvide et alment modelleringskoncept, baseret på lineære elastiske teori, til at inkludere: fragmenterede lag, reduceret vedhæftning mellem lag, viskoelasticitet, flytbare laster samt selve bidraget fra asfaltforstærkningsnet. Forstærkningsbidraget blev formuleret som en kombination af tre komponenter, der: (i) inkluderer nettet som et tyndt, elastisk lag med et høj E-modul, (ii) tager højde for nettets indflydelse på vedhæftningsevnen mellem de tilstødende lag og (iii) betragter nettets påvirkning på de omkringliggende asfaltlags egenskaber. I alt var syv modelleringsinput påkrævet for at repræsentere et asfaltforstærkningsnet, hvortil modelformuleringen blev implementeret i beregningskoden GRIDPAVE-MM. Adskillige eksperimentelle undersøgelser blev udført for efterfølgende at validere koden. Disse undersøgelser involverede fuldskalatest på den nybygget teststrækning DTU Smart Road. Her blev sensorer integreret i vejen og efterfølgende brugt til at måle vejens responser udløst af forbipasserende køretøjer. Herefter blev de indsamlede målinger sammenlignet med modelsimuleringer for at demonstrerer GRIDPAVEs evne til at matche de indbyggede sensormålinger.

Resultaterne fremhævede, at den udviklede model GRIDPAVE var i stand til at producere effekterne ved at installere asfaltforstærkningsnet i en asfaltbelægning. Desuden indikerede modelsimuleringer, at brugen af asfaltforstærkningsnet potentielt kan forsinke udviklingen af revner og sporkøring i vejsystemer og dermed forbedre den samlede levetid.

Overordnet set har dette ph.d.-studie leveret et alsidigt, anvendelig og valideret værktøj, der kan bruges af både ingeniører, konsulenter samt entreprenører (mm.) til at inkludere asfaltarmeringsnet i dimensionering af veje. Helt konkret kan modellen producere trafikudløste spændinger, tøjninger og flytninger i forskellige asfaltbelægningssystemer med asfaltforstærkningsnet, hvilket efterfølgende kan bruges til at evaluere forstærkningsbidraget på belægningernes ydeevne. I sidste ende åbner dette studie op for nye muligheder

med asfaltforstærkningsnet som en bæredygtig og robust løsning til at opretholde et acceptabelt serviceniveau for fremtidige vejsystemer.

List of Scientific Publications

This thesis is based on the following conference proceeding, journal publication, and submitted manuscripts:

i Nielsen, J., Olsen, K., Skar, A., and Levenberg, E. (2022). "Analytic analysis of a grid-reinforced asphalt concrete overlay". In: *Eleventh International Conference on the Bearing Capacity of Roads, Railways and Airfields*, Vol. 1, pp. 346-354), DOI: https://doi.org/10.1201/9781003222880-32.

ii Nielsen, J., Levenberg, E., and Skar, A. (2022). "Mechanistic modelling of grid-reinforced milled-and-overlaid asphalt pavements". *International Journal of Pavement Engineering* May. DOI: https://doi.org/10.1080/10298436.2022.2072502.

iii Nielsen, J. and Levenberg, E. (2022). "Full-scale validation of a mechanistic model for asphalt grid reinforcement". *(submitted to the International Journal of Pavement Engineering and is currently under review).*

iv Nielsen, J., Levenberg, E., Leischner, S., and Falla, G. C. (2022). "Mechanistic investigation of grid-reinforced asphalt pavements with measured interface properties". *(submitted to the Road Materials and Pavement Design and is currently under review).*

To comply with the general guidelines for avoiding plagiarism and self-plagiarism in PhD thesis writing, it should be stated that the dissertation includes the reuse of text and figures from the above-listed publications/manuscripts.

Additional works were published during the PhD study, but are not included in the thesis:

v Nielsen, J., Olsen, K., Levenberg, E., and Skar, A. (2020). "Fleksible belægninger med asfaltarmering - Mekanisk beregningsmodel" (in Danish). *Trafik & Veje* April.

vi Nielsen, J., Levenberg, E., and Skar, A. (2020). "Inference of Pavement Properties with Roadside Accelerometers". In: *Proceedings of the 9th International Conference on Maintenance and Rehabilitation of Pavements – Mairepav9.* Vol. 76, pp. 719-728. DOI: https://doi.org/10.1007/978-3-030-48679-2_67

vii Skar, A., Nielsen, J., and Levenberg, E. (2020). "Pavement instrumentation with near surface LVDTs". In: *Advances in Materials and Pavement Performance Prediction II*, pp. 232-235. DOI: https://doi.org/10.1201/9781003027362-55

viii Levenberg, E., Jensen, P. K., and Nielsen, J. (2022). "The dynamic cone penetrometer as a seismic source for geophysical exploration in urban environments". In: *Proceedings of 11th International Symposium on Field Monitoring in Geomechanics.* URL: https://www.issmge.org/uploads/publications/80/112/7.$_Levenberg_e t.al.pdf$

Table of Contents

Part I

Introduction and Summary

Modeling and Analysis of Pavements with Asphalt Reinforcement

Introduction

1.1 Background and motivation

Pavement systems serve as the economic and social backbone of every country and are important for ensuring societal equality bridging between rural and urban areas. These systems continually deteriorate under traffic loadings, in combination with weather effects, and therefore require regular maintenance or rehabilitation to retain a sufficient service level. In recent years, there has been a marked increase in the dependency on the pavement service level and overall durability (i.e., the ability to withstand damage). One reason for this is due to the increase in heavy traffic, e.g. from the growth in global shipping (Steyn et al. 2012; OECD 2023) or heavier loaded electric vehicles (Znidaric 2015), which is a contributing factor to the deterioration of road conditions. At the same time, the evolution of autonomous vehicles puts additional pressure on pavement structures since platooning and more regular driving patterns are expected to accelerate pavement distresses (Noorvand et al. 2017; Minguela and Muñoz 2019; Chen et al. 2019). These traffic-related trends also go along with rapid climate change effects, e.g. due to more extreme weather situations, sea rise, prolonged rain periods, and higher moisture contents in the unbound layers, which can have a negative impact on roads (Neumann et al. 2021; Qiao et al. 2022). Overall, these new-coming challenges generally affect the structural behavior of pavement systems, which impose an instant need for maintenance services or improved durability.

While one common strategy for maintaining the pavement service level is to rely on more frequent rehabilitation and repair activities, these activities are also economically expensive, interruptive for traffic, and require supplementary utilization of natural resources. Accordingly, they have a direct impact on socioeconomics, traffic congestion, fuel consumption, road safety, and pavement life-cycle costs. Due to the current affairs, there is a demand for more sustainable and robust solutions to maintain an acceptable pavement service level for road systems in the nearest future.

Given that asphalt pavements are the most common pavement type worldwide (EAPA and NAPA 2011), one emerging approach to meeting the new challenges involves the installation of asphalt grid reinforcement (AGR) products. The term AGR refers to products of thin high-modulus materials arranged in a mesh-like geometry, commonly made of polyester, steel, glass-fibers, and/or carbon-fibers (Cleveland et al. 2001; Sanders 2001; Nithin et al. 2015; Zofka et al. 2017; J. H. Lee et al. 2019; Solatiyan et al. 2020; Asphalt Academy 2022). They are (different from geosynthetic products) specifically designed for being installed within asphalt concrete (AC), either between two new AC lifts, between an existing (aged/damaged) AC and a new AC overlay, or on top of an unbound granular base (at the AC bottom). Limited-scale studies, isolated laboratory investigations, and full-scale experiments have demonstrated that AGR products can be beneficial in combating several distress types such as fatigue cracking (Nguyen et al. 2013; Arsenie et al.

2017; Vinay Kumar and Saride 2017; Correia and Zornberg 2018), rutting (Ong et al. 2004; J. Lee et al. 2015; Correia and Zornberg 2016), and reflective cracking (Austin 1996; Bondt 1999; Khodaii et al. 2009a; Saride and Kumar 2017). In general terms, these studies suggest that AGR products can potentially improve pavement performance and prolong service life.

Despite these potential benefits, there is currently no mechanistic-empirical (ME) design method (e.g. AASHTO 2008) that applies to asphalt pavements with AGR. One reason for this shortcoming is the lack of an accepted mechanistic response model that can correctly capture and emulate AGR effects. Consequently, the usage of AGR in pavement systems is currently limited.

This PhD study was motivated by the need for a ME design method applicable to asphalt pavements reinforced with AGR. Specifically, the scope herein was on the mechanistic component, which is concerned with response evaluation. This component can subsequently be used for quantifying pavement performance. Accordingly, the development of a validated and verified modeling and analysis tool was sought, capable of providing traffic-induced stresses, strains, and displacements in various pavement systems, including AGR.

1.2 Study objective and scope

The objective of this PhD project was twofold, i.e.:

(O1) to develop a versatile, useful, and validated computational model that can capture the effects of installing AGR in asphalt pavement systems, and

(O2) use the model to provide valuable insights into the effects of AGR.

Successful completion of these objectives should enable engineers, consultants, and contractors to prescribe an AGR alternative within asphalt pavements in a unified and rational manner. In addition, it should equip manufacturers with a tool to improve existing or develop new AGR products for future applications.

In the context of (O1), a versatile model refers to a generic tool that is relevant to a wide range of different scenarios (and not restricted to a few specific pavement situations). Furthermore, model usefulness is associated with its computational efficiency and few model inputs that can be assessed through e.g. laboratory or field tests. Finally, a validated model concerns the model's ability to capture and reproduce reality correctly.

Accordingly, the following three focus points were outlined to frame the research approach:

- to utilize a mechanistic framework to forecast the mechanical behavior of stresses, strains, and displacements in asphalt pavement systems with AGR. Such a framework allows for modeling a variety of different pavement structures, loading applications, and environmental conditions – addressing model versatility;

- to rely on Layered Elastic Theory (LET) as a modeling kernel (Burmister 1943; Burmister 1945c; Burmister 1945a; Burmister 1945b; Peutz et al. 1968). The main reason for this choice is that LET already serves the majority of current pavement design and analysis codes (e.g., Shell 1978; Shook et al. 1982; AASHTO 2008; ARRB Transport Research 2004; Huang 2004) due to its computational efficiency and relative few set of inputs; and

- to involve model verification and validation efforts that confirm the model's correctness.

1.3 Study methodology

To achieve the stated objectives, the project followed the general model development process of Thacker et al. 2004, illustrated in Figure 1.1. The starting point was to develop/-formulate a modeling approach (mathematical formulation) that captures the mechanistic responses of both new and rehabilitated pavement systems with AGR (the reality of interest). This was done by first extending the LET framework to include: (i) fragmented layers (FLs) for capturing old and damaged AC behavior; (ii) imperfect bonding conditions for capturing relative slippage between layers; and (iii) linear viscoelastic (VE) properties and moving loads for capturing realistic pavement responses and traffic loads. Second, an AGR model-component was formulated and added to the framework, serving as the main modeling contribution of this study.
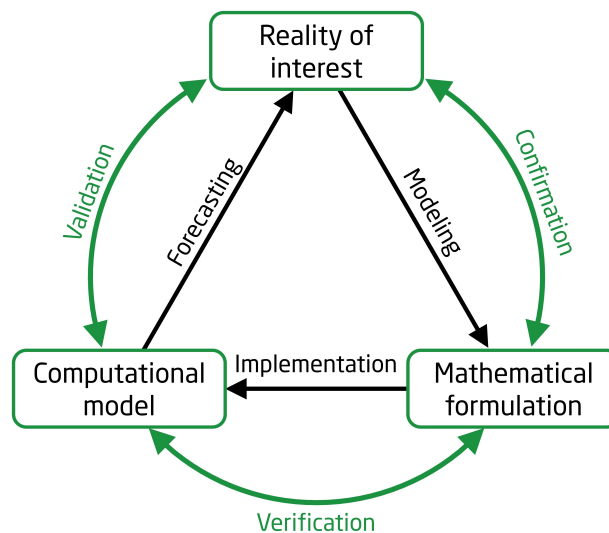
Figure 1.1: Simplified version of the model development process.

Next, the modeling approach was implemented into a computer code (computational model), entitled GRIDPAVE-MM – a Mechanistic Model for Pavements with Asphalt Grid Reinforcement. The code was implemented in a MATLAB-based environment, founded on the existing code Adaptive Layered Viscoelastic Analysis (ALVA) (Skar and Andersen 2020; Skar et al. 2020a; Skar 2021). Herein, ALVA was extended to include FLs, VE, and multiple moving loads, and numerical considerations were implemented to minimize the computational effort. GRIDPAVE was then verified against other accepted computational models and analytic solutions relevant to the problem at hand. This was to confirm its correctness with respect to the applicable theory.

Hereafter, a validation effort was launched to confirm model simulations with experimental data. An experimental full-scale test facility, entitled DTU Smart Road, was designed and constructed, involving the installation of AGRs and embedded sensors. In order to highlight AGR effects (and thus support model validation), GRIDPAVE was used as a tool for guiding the experimental design. An experimental campaign was carried out to collect sensor measurements under vehicular loading for subsequent model validation. Moreover, pavement layering and properties were assessed from additional field and laboratory tests and were utilized as independent model inputs. The overall campaign serves as the main experimental contribution of this study. Model validation of GRIDPAVE was assessed through the ability to match embedded sensor readings – in both unreinforced and reinforced test sections. In particular, the AGR model-component was calibrated and

then validated by proving that it must be activated to reproduce field measurements of a reinforced section correctly. Additional full-scale tests were also carried out in USA and Switzerland. The collected data were not utilized for model validation in this current study but can serve in future studies to reinforce the model validation of GRIDPAVE.

Finally, the overall developed modeling approach was utilized to forecast the effects of including AGR in several specific case studies. Here, attention was placed on synthetic investigations, i.e., purely based on simulations, utilizing GRIDPAVE and model-calibrated properties to demonstrate and quantify the AGR effect. The overall forecasting/demonstration efforts contributed to improving the intuition of AGR effects and providing relevance to the general usage of AGR.

1.4 Thesis outline

The thesis follows a paper-based format and is divided into two parts: Part I and Part II. In Part I, a summary of each scientific paper written during the PhD project is provided. This is then followed by elaborating on noteworthy research activities that were not prepared for publication during the project period. Part I ends with a conclusive summary of findings, limitations, study implications, recommendations for future work, and overall study contribution. In Part II, a collection of four scientific papers (three journal papers and one conference paper) that were written during the PhD period are appended.

Research Output

This section presents a summary of each scientific paper that was written during the course of this PhD project. To provide context, the section begins with a brief overview of how the papers are interconnected and how they are addressed in the general model development process. Presented hereafter is an extended summary of each paper included in Part II. These summaries provide a general explanation of the research objective, methodology, main conclusions, and how each paper contributes to the overall PhD thesis.

2.1 Overview

As a whole, the scientific papers written during the PhD project constitute the major contributions to the overall study objectives. They provide context to the different subjects that were part of the main study activities, which concerned: (a) model formulation, (b) model implementation and verification, (c) model validation, and (d) forecasting AGR effects. These study activities are all chronologically linked to the model development activities lined out in Figure 1.1. The papers were prepared continuously throughout the study activities, and a schematic chart illustrating the undertaken project workflow is presented in Figure 2.1.
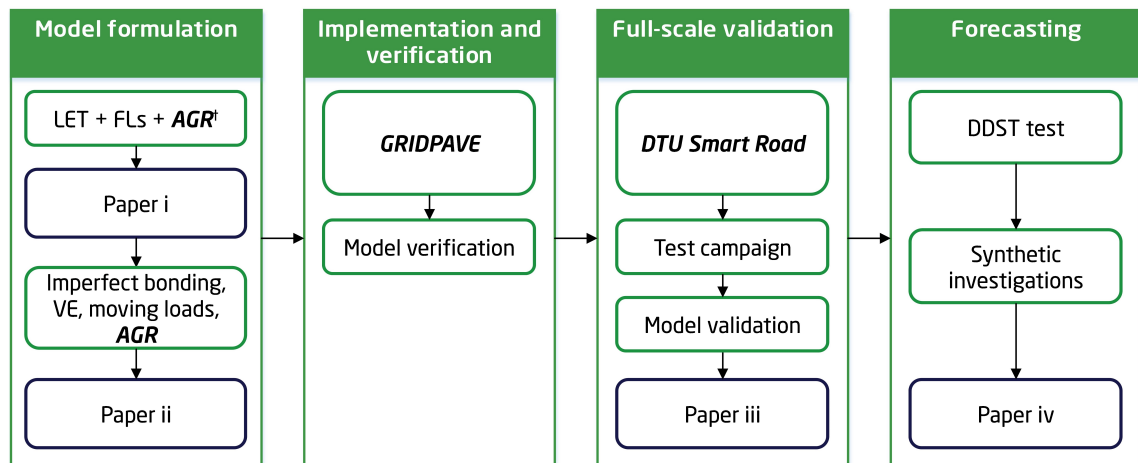
†Thin high-modulus layer

Figure 2.1: Workflow of the PhD project.

Accordingly, Paper i deals with preliminary work on including modeling elements in a simple LET-framework to prescribe the AGR effect in pavement systems. Specifically, it features the inclusion of FLs for emulating the presence of an existing cracked AC layer, and a thin high-modulus layer to represent the AGR contribution. Paper ii elaborates on the modeling concept from Paper i; it further features imperfect bonding conditions between

layers, VE layer properties under moving loading, and two additional AGR contributions that finalize the AGR model-component.

The overall model formulation was implemented to form GRIDPAVE. The code was subsequently verified against existing codes and benchmark solutions. An extensive description of the code implementation and verification will be given later in this thesis but was not included in the papers. This was to avoid excessive details and keep the focus on each paper's objective.

Hereafter, DTU Smart Road was designed and constructed at DTU campus in Kgs. Lyngby, Denmark. DTU Smart Road consists of four instrumented pavement sections, where three of them contain a carbon-fiber AGR product installed at different depths, and the fourth is an unreinforced reference section. A test campaign was carried out on two of four test sections, and collected data were used to validate the model in Paper iii. Since only two test sections were presented in the paper, an extended description of the entire DTU Smart Road will be provided later in this thesis, together with other (unpublished) experimental efforts that are relevant for model validation.

Finally, Paper iv deals with interface bonding between AGR and adjacent AC. It features laboratory testing using the Dresden Dynamic Shear Tester (DDST) (Leischner et al. 2019) to estimate interface bonding properties due to the presence of AGR. Throughout a synthetic investigation, the paper then provides insight into how imperfect bonding conditions influence the overall AGR effect on pavement key responses.

2.2 Summary of Paper i

The first publication in this dissertation was conducted as a first attempt to prescribe a modeling approach for capturing the effect of AGR in flexible pavement systems. The aim was to analyze and gain insight into the potential effect of incorporating AGR in a mill-and-overlay maintenance treatment with a mechanistic model.

2.2.1 Methodology

The study was purely based on simulations considering a layered elastic system that mimics a traditional asphalt pavement system subjected to three mill-and-overlay cases. In all cases, pavement systems consisted (from top to bottom) of a new AC overlay, an existing (damaged and aged) AC layer, an unbound granular base layer, and a soil subgrade. The systems varied in overlay thickness/milling depth, with a fixed combined AC thickness of 150 mm (overlay + existing AC). An AGR was introduced between the overlay and the existing AC, and all layers were assumed fully bonded to each other.

The existing AC layer was taken as an aged layer with fragments that do not interact; it was modeled as a FL P-type layer, according to Levenberg and Skar 2022, with the modeling inputs: $k_v = E_{fl}/h_{fl}$, $k_h = \infty$, and $G = 0\,\text{N/mm}$ (no shear resistance between fragments); here E_{fl} and h_{fl} denotes the modulus and thickness of the FL. The AGR was modeled as a thin high-modulus layer considering the carbon fiber grid product S&P Carbophalt® G 200/200 (S&P Clever Reinforcement Company AG 2023a). The grid properties were: (i) Young's modulus, taken as the carbon fiber modulus, (ii) Poisson's ratio, provided by the manufacturer, and (iii) an effective thickness, based on smearing the volume of fibers per unit area into a homogeneous layer.

Various scenarios were simulated, differing between the overlay thickness/milling depth and the inclusion or exclusion of the AGR. Contour plots of key responses, triggered by a dual-tire assembly loading, were presented for each case, with identified response peaks

compared across the different scenarios. Key responses were those commonly linked to pavement performance in ME design methods.

2.2.2 Conclusions

It was found that for thick overlays, adding AGR under the thick overlay reduced the critical (i.e., largest) horizontal tensile strain and critical von Mises stress in the overlay, indicating a potential reduction in cracking and rutting within the overlay. For a thin overlay case, adding AGR marginally affected the critical tensile strain and critical von Mises stress in the overlay, suggesting that the reinforcement was ineffective. In both thick and thin overlay cases, adding AGR had a marginal effect on the critical vertical stress on top of the unbound base layer and no effect on the vertical stresses in the subgrade. Overall, the findings implied that AGR had an effect on horizontal strains in the AC overlay. The effect was influenced by the overlay thickness and the AGR location within the AC. Results suggested that the AGR effect improves as the grid is placed closer to the AC overlay bottom.

For future research, it was recommended to include the influence of AGR on the material in its vicinity – within a so-called zone of influence (ZoI). Due to the VE nature of AC, this effect was deemed time- and temperature-dependent. It was further recommended to characterize the AGR effects based on full-scale experimental investigations.

2.2.3 Contribution

The paper contributes to the overall dissertation by providing a preliminary modeling concept for AGR in milled-and-overlaid pavement systems. From a model formulation perspective, the grid contribution was introduced to the LET framework as a thin high modulus layer with elastic layer properties. Specifically, the work proposes a simple way of smearing the grid geometry into a homogeneous layer with an effective thickness. Furthermore, the paper proposes to utilize FLs as a modeling feature to emulate cracked layers in a mill-and-overlay situation. Finally, the work elaborates on future research activities that serve as a foundation for the following content of this thesis.

2.3 Summary of Paper ii

This paper was established based on extending and elaborating some of the modeling interpretations and future recommendations from Paper i. Specifically, the main objective was to outline a mechanistic modeling approach for analyzing the situation of milled-and-overlaid asphalt pavements that includes AGR. A secondary objective was to generate some initial intuition on the AGR effects on mechanistic pavement responses.

2.3.1 Methodology

A modeling formulation was proposed for simulating the stresses, strains, and displacements in a milled-and-overlaid asphalt pavement system including AGR. This was done based on further extending the semi-analytic LET framework to include the following: (i) FLs according to Levenberg and Skar 2022 (to emulate old and damaged AC); (ii) imperfect bonding characterized by a horizontal spring k_b according to Goodman and Popov 1968. This was to capture relative slippage between layers; (iii) linear viscoelasticity and moving loads under isothermal conditions based on Schapery's quasi-elastic approximation (Schapery 1962) and the load-unload superposition principle of Levenberg 2013. This was to capture realistic AC behavior and traffic loading conditions; and (iv) AGR effects modeled as a combination of three contributions that accounts for the grid's material properties and geometry together with its effect on the material in its vicinity. A graphical representation of the main model features is offered in Figure 2.2.
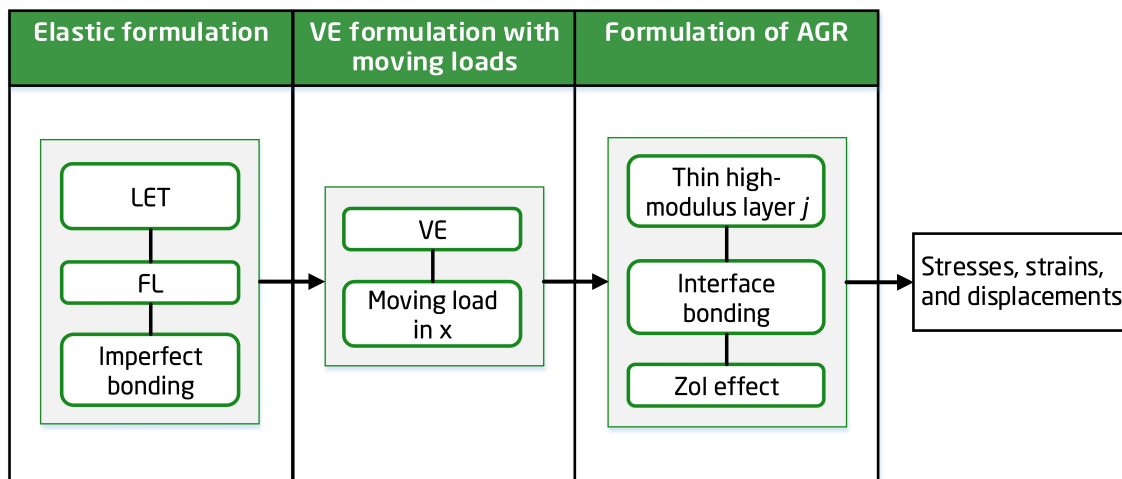
Figure 2.2: Flow chart of the proposed model inputs and features.

The first AGR contribution involved adding a thin elastic layer to the VE system, similar to Paper i. The thin layer approximation was further elaborated by representing the grid's material composition by a set of "effective" elastic properties. In cases where the grid ribs were made of different materials, an averaging process was proposed to determine an effective Young's modulus and effective Poisson's Ratio. Furthermore, the theory assumed that the effective grid modulus must be greater than the short-term AC modulus (E_0) to ensure a reinforcement effect at all times.

The second contribution involved imperfect bonding between the AGR and adjacent layers. This was captured by assigning two horizontal springs to the grid layer j – one between the grid layer and the layer above it ($k_{b,j-1}$), and one between the grid layer and the layer below it ($k_{b,j}$). The two horizontal spring values were deemed related to the so-called EAS-NMAS ratio, i.e., the ratio between the grid's effective aperture size (EAS) and the AC's nominal maximum aggregate size (NMAS). This ratio should be less than (about) five to comply with representative volume element considerations.

The third contribution concerns the ZoI effect, which arises from local interlocking between AC aggregates and grid apertures. When subjected to loading, this interlocking is assumed to partially restrain the movement of aggregates, resulting in additional confinement within an influence zone near the grid. To emulate this effect, the grid's neighboring AC layers are subdivided, and the adjacent sub-layers are assigned a modified relaxation modulus $E^{ZoI}(t)$ and a thickness δ^{ZoI} (refer to Figure 2.3(a)). The added confinement within the defined ZoI is captured by increasing the AC equilibrium modulus from E_∞ to $E_\infty^{ZoI} = \kappa E_\infty$ (refer to Figure 2.3(b)), where κ is a unitless multiplication factor. The κ-factor is restricted to ensure that the grid cannot provide negative confinement within the ZoI (i.e., $\kappa \geq 1$) and to comply with fading memory (i.e., $\kappa E_\infty \leq E_0$). Accordingly, the ZoI effect is fully operational under high temperatures and/or slow-moving loads (when the AC approaches granular-like material behavior), whereas the ZoI effect diminishes under low temperatures and/or fast-moving loads (when the AC approaches a solid-like material behavior). The value of κ was also deemed related to the EAS-NMAS ratio.

The overall modeling approach was demonstrated in a synthetic investigation covering three milled-and-overlaid pavement cases: a reference system without reinforcement, a grid-reinforced system without the ZoI effect, and a reinforced system with the ZoI effect ($\kappa = 3$). The formulation was implemented in a computational model (currently GRID-
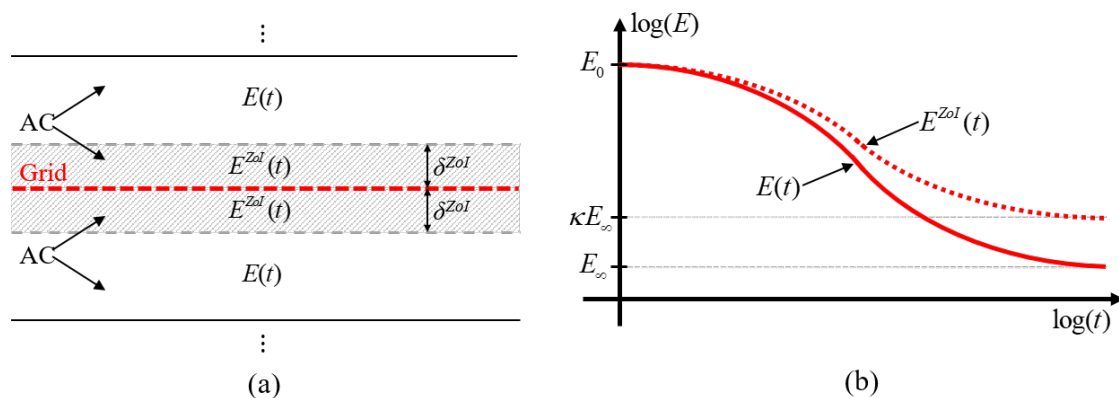
Figure 2.3: Conceptual sketches from Nielsen et al. 2022: (a) sub-division of the AC layer adjacent to an AGR layer and (b) relaxation modulus of the AC inside and outside the ZoI.

PAVE), which was based on extending the LET-code ALVA to handle FLs, VE layers, moving loads, and AGR effects. All pavement cases considered a VE AC overlay placed on top of a (time-temperature independent) FL. Below the two layers was an elastic layer, representing an unbound granular base layer, which was founded on an elastic semi-infinite medium. Key responses commonly related to pavement performance, triggered by a single moving load, were simulated for a wide range of AC temperatures and load travel speeds. In addition, deflection responses were also calculated. The demonstration was carried out for two choices of effective AGR moduli, and it was assumed that the AGR was fully bonded to its adjacent layers.

2.3.2   Conclusions

The synthetic investigation revealed that the presence of AGR positively affected horizontal strains at the AC overlay bottom and, to a lesser degree, vertical strains at the top of the unbound granular base layer. Greater effects were observed when including the ZoI effect with $\kappa = 3$. The AGR effects were more significant under high-temperature/slow-speed conditions and less so under low-temperature/high-speed conditions. The effect was marginal on deflection responses. Finally, a larger effective AGR modulus also provided a larger AGR effect. Overall, these findings supported existing literature and suggested that installing AGR on top of existing cracked AC (before overlay) can potentially extend the overlay service life. However, evaluating AGR effects in the field using surface measurement techniques, such as the falling weight deflectometer (FWD) test, may be difficult in practice.

For future research, it was proposed to carry out a combination of laboratory and field tests to calibrate model inputs and validate the modeling formulation. Here, it was recommended to use instrumented pavement sections with strain gauges or pressure cells near the AC bottom for model validation. Moreover, it was suggested to characterize effective AGR properties and interface bonding properties in the laboratory. Characterization of κ was recommended through inverse analysis of strain measurements in a full-scale test setup.

2.3.3   Contribution

The paper contributes to the overall dissertation by proposing a novel model formulation that combines all relevant effects of AGR, which can be applied to a wide range of pavement systems and load/temperature conditions. Furthermore, it can serve as a useful tool

for optimizing AGR installation locations and improving AGR products, as well as show-casing their existing capabilities. By building upon LET, numerical stability and high computational efficiency are assured. Overall, the paper contributes to the versatility and usefulness addressed in the first study objective (O1). In addition, the synthetic investigation effort provides some valuable insights into the AGR effects addressed in the second study objective (O2). Finally, the work provides future recommendations for designing an experimental setup for validation and for characterizing AGR-related model inputs. These recommendations were followed in the forthcoming content.

2.4 Summary of Paper iii

While Papers i and ii focused on developing a modeling approach for asphalt pavements including AGR, this paper aims to confirm the model's ability to capture realistic pavement responses that accurately reflect real-world conditions. Specifically, the main objective was to provide experimental validation for the mechanistic pavement response model proposed in Paper ii. In particular, attention was placed on validating the AGR model-component. A secondary objective was to evaluate the AGR effects in a synthetic analysis (purely based on simulations). This was done to further improve the intuition on the AGR effects with respect to mechanistic pavement responses.

2.4.1 Methodology

To achieve the main objective, a full-scale validation campaign was initiated. For this purpose, two of the DTU Smart Road sections were utilized, i.e. one including AGR at the AC bottom (section S-1) and the other excluding AGR (S-0 serving as a reference section). The choice to focus on a test section with AGR placed at the AC bottom was due to the model's prediction of the largest AGR effect on strain responses.

Both considered pavement sections included asphalt strain gauges (ASGs) and temperature sensors (PT100s) embedded at the AC bottom. After construction, dynamic cone penetrometer (DCP), FWD, and laboratory tests were carried out to characterize the pavement material properties and layer composition. The test results were also used to confirm that the two sections were nominal identical, except for the presence of AGR. Hereafter, a measurement campaign was carried out on a relatively hot day (in June), where a heavy slow moving forklift of known weight, dimensions, and travel speed was utilized to generate ASG readings in several passes. During each pass, the forklift position was carefully measured with video footage to allocate its transverse position relative to the embedded sensors (Y_0).

The ASG readings were subsequently utilized in a validation effort to demonstrate that GRIDPAVE (developed in Paper ii) was able to simultaneously fit all ASG measurements with model-predicted strain responses. A graphical representation of the overall validation approach is shown in Figure 2.4. Here, VE AC properties from laboratory testing, sub-grade modulus from FWD tests, and layer information from the DCP tests were utilized as model inputs, along with effective AGR layer properties assessed through the AGR's geometric and material composition. All layers were assumed fully bonded (including the AGR). The PT100 readings were utilized in the VE model component to account for the prevailing temperature conditions. The model's ability to simultaneously fit all ASG measurements was assessed through inverse analysis; this was achieved by solving a multi-criterion optimization problem following the so-called min-max approach (Osyczka 1978). First, the model (without the AGR-component) was utilized to fit the ASG measurements from S-0 (unreinforced) for calibrating a Young's modulus E_{ugs} of the unbound granular structure (UGS) (that supported both test sections). Hereafter, the model (including the
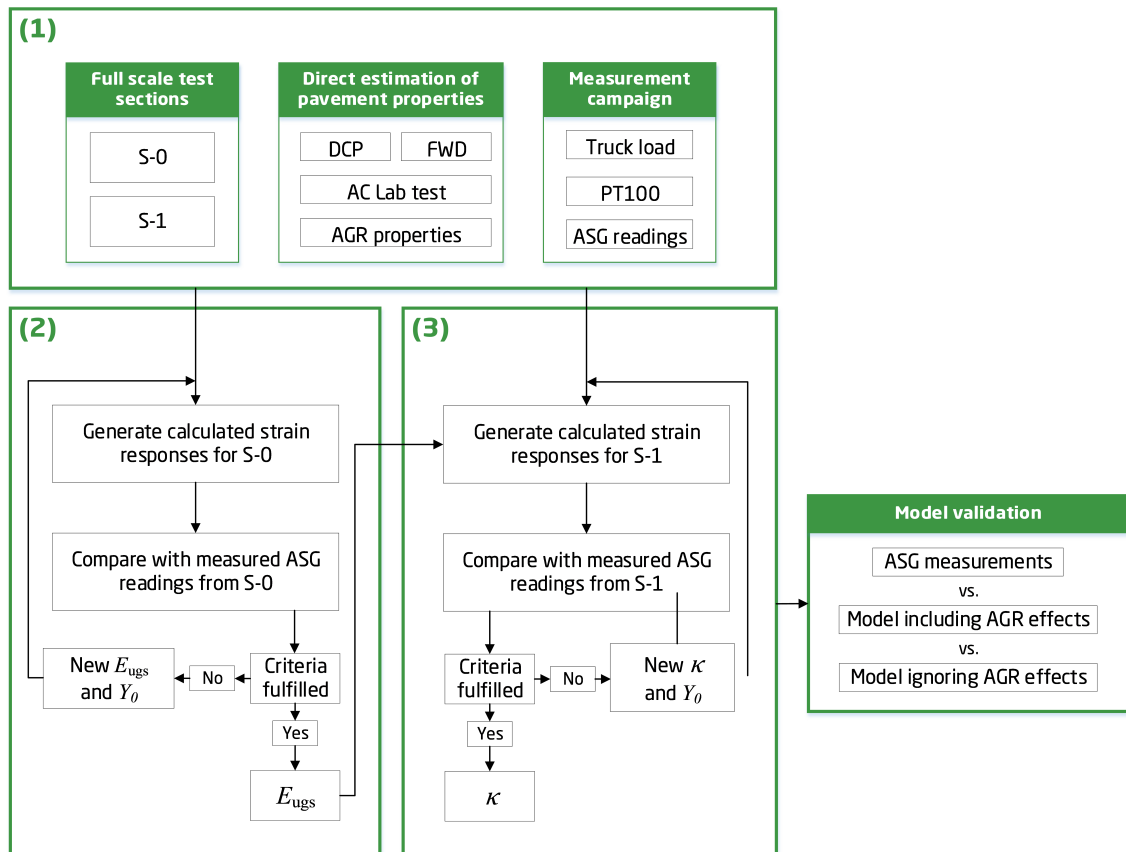
Figure 2.4: Flowchart showing the model validation approach: (1) physical reality, (2) modeling and analysis of the unreinforced (reference) S-0 section, and (3) modeling and analysis of reinforced S-1 section.

AGR-component and the calibrated UGS modulus) was utilized on data from S-1 (reinforced) to calibrate the κ-factor (refer to Paper ii), assuming a ZoI thickness of three times the NMAS of the AC. Finally, model validation was demonstrated by providing evidence that a model with the AGR-component is superior in its ability to reproduce reality compared to a model without the AGR-component.

To address the secondary objective, a synthetic investigation was carried out to further quantify the reinforcement effect. Here the validated GRIDPAVE model, with calibrated model inputs, was applied in cases that emulated the two DTU Smart Road test sections (with and without AGR) subjected to the rear axle loading of the forklift. Key responses commonly related to pavement performance, along with surface displacements, were simulated for two combinations of AC temperatures and load travel speeds.

2.4.2 Conclusions

Based on the model validation effort, an acceptable fit between all measured and model-predicted strain responses was achieved. This achievement suggested that the developed GRIDPAVE model was capable of reproducing field-measure pavement responses with and without AGR. Moreover, it was possible to estimate a fairly consistent κ-factor across all considered passes. In all cases, the value was larger than unity, indicating that a ZoI model-component was active (and valid). In general, the modeled responses were more in tune with field measurements when the AGR model-component was active. These results suggest that the proposed modeling framework for including AGR in pavement systems is valid for ME design.

Based on the synthetic investigation, it was observed that the presence of AGR significantly reduces the AC bottom horizontal strains and, to a lesser degree, the vertical strain on top of the UGS. These findings apply to a situation with a slow loading speed and high AC temperature, and were considerably smaller to a situation with a fast loading speed and low AC temperature. The simulations also suggested that the presence of AGR hardly influences surface displacement. These findings match those observed in Paper ii, and similar implications were derived. Thus, for the particular case where AGR is placed on top of the UGS (before paving with new AC), the AGR can potentially contribute to prolonging the pavement service life with respect to bottom-up fatigue cracking and rutting. However, it is practically difficult to quantify in field experiments based on surface measurement techniques.

For future research, it was proposed to investigate bonding conditions between AGRs and adjacent layers, e.g. via laboratory shear testing of AC cores. It was also recommended to compare strain responses under low AC temperatures and fast loading speeds, as well as surface displacement via deflection techniques, to confirm a marginal AGR effect on associated key responses. Finally, it was suggested to develop a laboratory method for estimating κ and the ZoI thickness.

2.4.3 Contribution

The paper contributes to the overall dissertation by presenting a model validation effort that confirms the model's capability of reproducing measurements from a full-scale test setup. Hence, the paper directly contributes to the model validation addressed in the first study objective (O1). The paper also provides a value for κ, which was used in the following paper (Paper iv). While some insight on κ was provided, the obtained value is only representative of the specific case and is not generic for all pavement situations. In addition, the synthetic investigation effort provides some valuable insights into the AGR effects, addressed in the second study objective (O2). Finally, the work provides future recommendations for testing the bonding conditions between the AGR and adjacent layers (which was the aim of Paper iv). Information about the bonding conditions due to the presence of the grid was (at this point) considered one of the missing pieces with respect to the AGR model-component inputs.

2.5 Summary of Paper iv

While Papers i, ii, and iii have already provided insights into the AGR effect, particularly with respect to the first and third contributions of the AGR model-component (i.e., the thin high-modulus layer and ZoI formulation summarized in Subsection 2.3.1), this paper was motivated by a desire to investigate the second AGR contribution (which addresses interface bonding). The primary objective of this investigation was to understand how interface properties affect key responses in pavements with AGR. Key responses refer to those commonly used in ME design and non-destructive testing, whereas interface properties refer to the ones that dictate the bond conditions between two adjacent AC lifts or between an AGR and its adjoining AC.

2.5.1 Methodology

The investigation involved combining results from the full-scale test in Paper iii, laboratory tests on AC cores, and synthetic (in silico) simulations. The study was initiated by conducting laboratory tests on AC cores to characterize their interface bonding properties. Two AC cores were obtained from two nominally identical full-scale pavement test sections at DTU Smart Road, one including AGR and the other without. The reinforced core was taken from a test section where the AGR was installed between two AC layers

(different section from the one utilized in Paper iii), whereas the unreinforced core was taken from the reference section. Accordingly, one core included an interface with AGR, and the other included an interface without AGR. Sinusoidal shear loading was applied to the interface of both cores using the DDST under small levels of displacement. The test was repeated for several combinations of temperatures, frequencies, normal stress levels, and displacement amplitudes.

The DDST measurements were analyzed to produce several relaxation interface stiffness functions $K(t)$ for both tested cores. Each $K(t)$ was associated with a normal stress and displacement amplitude. Here, $K(t)$ refers to a time-temperature-dependent parameter that captures the relative slippage at the interface between two model layers. The analysis involved three steps: (i) fitting analytic sinusoidal functions to the measured load and displacement histories, (ii) using the obtained sinusoidal function parameters to estimate complex norm values of the interface stiffness $|K^*|$ and associated phase angles φ, and (iii) applying interconversion and inverse analysis to produce the relaxation interface stiffness $K(t)$.

Finally, a synthetic investigation was carried out using GRIDPAVE. The investigation was based on the two DTU Smart Road test sections utilized for coring. Several key responses were simulated for two different AC temperature levels under a moving load, traveling at two different speeds. Also, the displacement level and vertical stresses at the interfaces were calculated. The AC VE properties from laboratory testing and layer information from the DCP were utilized as model inputs along with effective AGR layer properties and the calibrated ZoI properties from Paper iii. The interface bond was characterized using the relaxation interface stiffness $K(t)$ for a displacement level of $10\,\mu m$, and zero normal stress. While the DDST test results were used to provide a single $K(t)$ for each (reinforced or unreinforced) interface, two interface properties were required for the AGR model-component statet in Paper ii. Therefore, two optional bonding models (BMs) were explored: (BM1) where the top AGR interface was assumed perfectly bonded and the DDST-derived $K(t)$ was ascribed to the bottom AGR interface, and (BM2) where the DDST-derived $K(t)$ was equally split between the top and bottom AGR interfaces.

2.5.2 Conclusions

Based on the experimental investigation (using the DDST), it was found that $K(t)$ without AGR was larger than $K(t)$ with AGR at all times – implying a reduced bond level due to the presence of AGR. In general, the $K(t)$ was highly sensitive to the applied displacement level and to the normal stress level, indicating non-linear behavior. Based on the synthetic investigation, it was found that differential displacements across all AC interfaces (in the order of micrometers) were largest when including AGR. However, including all AGR model-components lessened the horizontal tensile strains at the reinforced interface and at the AC bottom compared to simulations without the AGR-components. This effect was more pronounced for low-speed/high-temperature conditions. The choice of BM had a notable influence on responses near the AGR, but not at the AC bottom. The investigation also revealed that the presence of AGR had a marginal influence on surface deflections and vertical strains on top of the layer underneath the AC (i.e., the UGS). The overall implications based on these findings were that adding AGR between two AC lifts can potentially prolong the pavement service life in terms of bottom-up fatigue cracking, even though the presence of AGR seems to reduce the bond level.

For future research, it was recommended to investigate interface bonding conditions in full-scale, e.g. by installing LVDTs inside core-drilled holes and monitoring diameter changes just above and below interfaces with and without AGR. Additionally, more cores

should be tested in the laboratory to gain a statistical basis for $K(t)$. Further aspects were mentioned, involving more AGR products, different AC types, interfaces with milled surfaces, and AGRs placed on top of unbound granular material. These aspects could provide insight into the influence of the EAS-NMAS ratio on interface bonding levels.

2.5.3 Contribution

The paper contributes to the dissertation by completing the model formulation with focus on the second contribution of the AGR model-component (dealing with interface bonding). Overall, the paper improves the usefulness addressed in the first study objective (O1) by proposing and demonstrating a practical approach for estimating model inputs regarding interface bonding. Specifically, the paper handles an AC interface with AGR by one input parameter that was assessed through a laboratory test. It should be noted that the choice of BM needs to be further investigated. Furthermore, the paper provides important insights into the AGR effects, addressed in the second study objective (O2). Specifically, a reduced interface bond level due to the presence of AGR, may not necessarily annul any beneficial AGR effects.

Unpublished Efforts

This chapter presents a selection of unpublished efforts that were carried out during the PhD project. It begins with a brief overview of the unpublished efforts followed by an examination of each subject matter.

3.1 Overview

The unpublished efforts carried out during the PhD project are divided into two categories, i.e.: (i) modeling efforts and (ii) experimental efforts. Figure 3.1 provides a schematic overview of the unpublished topics that were addressed in this PhD study. Some efforts included herein were directly involved in the main study activities (refer to Figure 2.1); specifically, they comprehend the entire modeling effort related to GRIDPAVE and the experimental efforts related to the DTU Smart Road. However, some details were not disclosed in the published papers. Other efforts involve additional experimental activities carried out at DTU Smart Road, as well as in Texas (USA) and Switzerland. Limited by the PhD period, these experimental activities were not prepared for publication during this project. However, they provide data from embedded sensors in full-scale pavement facilities, which can supplement model validation and be utilized by others. Furthermore, they include other sensing techniques that could be useful for future model validation efforts (in general). Thus, they are included in the thesis as they also serve as contributors to the overall field of study and could be relevant for future research.
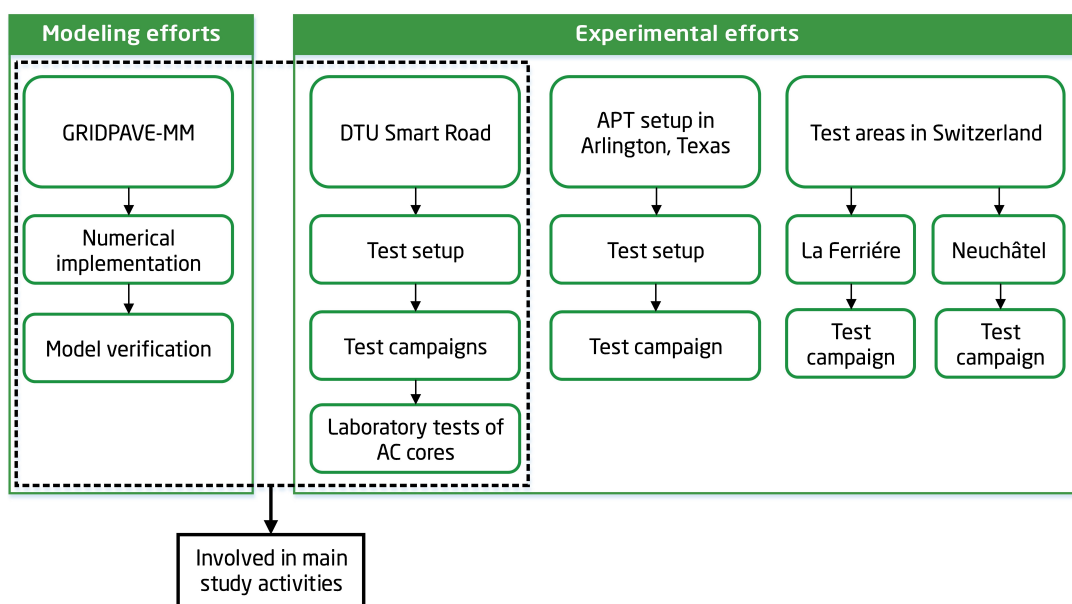
Figure 3.1: Overview of unpublished efforts in the PhD project.

3.2 Modeling efforts

This section describes the numerical considerations and model verification involved in the implementation of GRIDPAVE. GRIDPAVE is a mechanistic analysis tool suited for calculating responses of pavement systems with AGR. It was developed as part of the current industrial PhD study, with the intellectual property rights assigned to S&P Reinforcement Nordic Aps.

With respect to this dissertation, GRIDPAVE was utilized in Paper ii, iii, and iv, as an integral part of each research topic. GRIDPAVE's implementation and verification were not the subjects of a dedicated research publication, as it was considered unsuitable for a standalone research topic. Nonetheless, this section provides a comprehensive description of the implementation and verification efforts related to GRIDPAVE.

The entire model approach stated in Paper ii was programmed into a MATLAB script environment – forming GRIDPAVE. GRIDPAVE utilizes the existing verified LET code ALVA as the elastic engine, which was numerically extended to include: (i) FLs to represent damaged and cracked AC; (ii) VE layer and interface properties; (iii) moving and multiple loads; and (iv) AGR effects. An overview of GRIDPAVE is given in Figure 3.2. Accordingly, the formulation of FLs was first implemented into ALVA, then moving (multiple) loads were added and then extended to a VE solution. As a final point, the AGR model-component was added to represent AGR in the pavement system. Except for ALVA, each of these components (i.e., FL, moving loads, VE, and AGR) can be turned on and off in GRIDPAVE depending on the user's need. This means that the code can emulate all combinations of new or milled-and-overlaid systems (without or with an existing cracked layer), static or moving loads, and systems with or without AGR.
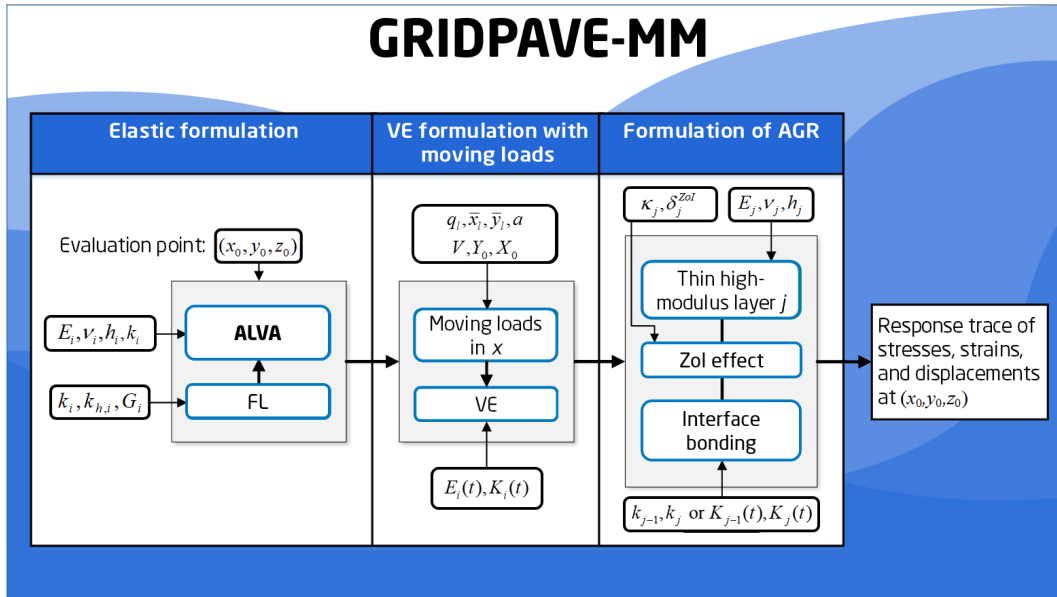
Figure 3.2: Overview of GRIDPAVE-MM.

3.2.1 Main model inputs and outputs

The main model inputs and output are all visualized in Figure 3.2: Accordingly, GRID-PAVE calculates the pavement responses (triggered by a given load application) in a selected evaluation point (x_0, y_0, z_0). The evaluation point is navigated in a right-hand Cartesian coordinate system, with its origin located at the pavement surface and z pointing downwards – see Figure 3.3.
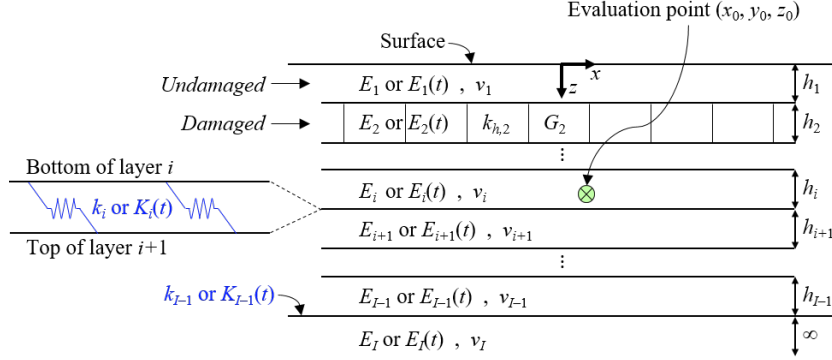
Figure 3.3: Cross-sectional view of a I-layered system in GRIDPAVE-MM.

The code can handle any desired number of layers (identified by the subscript i with $i = 1, 2, ..., I$). A layer can be considered one of four types: (i) undamaged elastic layers, (ii) damaged elastic layers, (iii) undamaged VE layers, or (iv) damaged layers VE. Undamaged elastic layers are characterized by the model inputs: Young's modulus E_i (in MPa), Poisson's Ratio ν_i (unitless), and a thickness h_i (in mm). Damaged elastic layers are characterized by the model inputs: E_i, h_i, a horizontal spring constant $k_{h,i}$ (in MPa/mm), and a shear deformation resistance G_i (in N/mm). Undamaged and damaged VE layers are characterized by replacing E_i with a relaxation modulus $E_i(t)$ (in MPa). The relaxation modulus of layer i is taken as:

$$E_i(t) = \frac{E_{\infty,i}(1 + (t/\tau_{D,i})^{n_{D,i}})}{(t/\tau_{D,i})^{n_{D,i}} + (E_{\infty,i}/E_{0,i})} \tag{3.1}$$

where $E_{0,i}$ and $E_{\infty,i}$ are the instantaneous (short-term) and equilibrium (long-term) modulus (in MPa), respectively, while $\tau_{D,i} = \tau_{D,i}^0 a_{T,i}$ and $n_{D,i}$ (unitless) are shape parameters. Here, $\tau_{D,i}^0$ (in seconds) is a constant that is linked to the reference temperature $T_{0,i}$ (in °C), and a time-temperature shift factor $a_{T,i}$ (unitless), taken as (Williams et al. 1955):

$$\log_{10}(a_{T,i}) = \frac{-C_{1,i}(T_i - T_{0,i})}{C_{2,i} + (T_i - T_{0,i})} \tag{3.2}$$

where T_i (in °C) denotes the temperature of layer i (uniformly distributed across the thickness), and $C_{1,i}$ (unitless) and $C_{2,i}$ (in °C) are temperature constants associated with the material of layer i. The first model layer is always taken as an undamaged layer (elastic or VE); the final layer I is also taken as undamaged, with an infinite layer thickness. Between two undamaged layers i and $i + 1$, imperfect bonding can be captured (either) by a time-independent horizontal spring constant k_i (in MPa/mm) ranging from $k_i = 0$ (full slip) to $k_i \to \infty$ (full bond), or by a relaxation interface stiffness $K_i(t)$ (in MPa/mm), taken as:

$$K(t) = \frac{K_{\infty,i}(1 + (t/\tau_{K,i})^{n_{K,i}})}{(t/\tau_{K,i})^{n_{K,i}} + (K_{\infty,i}/K_{0,i})} \tag{3.3}$$

where $K_{0,i}$ and $K_{\infty,i}$ are the instantaneous (short-term) and equilibrium (long-term) interface stiffness (in MPa/mm), respectively, while $\tau_{K,i} = \tau_{K,i}^0 a_{T,i}^K$ and $n_{K,i}$ (unitless) are shape parameters. Here, $\tau_{K,i}^0$ (in seconds) is a constant that is linked to the reference temperature $T_{0,i}^K$ (in °C), and a time-temperature shift factor $a_{T,i}^K$ (unitless) (similar to Equation (3.2)):

$$\log_{10}(a_{T,i}^K) = \frac{-C_{1,i}^K(T_i^K - T_{0,i}^K)}{C_{2,i}^K + (T_i^K - T_{0,i}^K)} \tag{3.4}$$

where T_i^K (in °C) denotes the temperature and $C_{1,i}^K$ (unitless) and $C_{2,i}^K$ (in °C) are temperature constants associated with the interface between layers i and $i+1$. Hence, the model can handle different time-temperature shifting parameters for the relaxation modulus and the relaxation interface stiffness, which might not be identical.

In terms of load application, the code can handle any desired number of circular loads (identified by the subscript l with $l = 1, 2, ..., L$) – see Figure 3.4. Each load is characterized by a set of local load coordinates $(\bar{x}_l, \bar{y}_l)$ (in mm), a load intensity q_l (in MPa), and a contact area radius a (in mm); the latter must be similar for all loads (therefore without a subscript). In the case of moving loads, the entire load configuration moves from $x = -X_0$ to $x = X_0$ with a constant speed denoted by V (km/h) and transverse load position (offset) denoted by Y_0 (in mm); the latter is defined as the distance (in the y-direction) from the local load coordinates system to the origin of the global coordinate system.
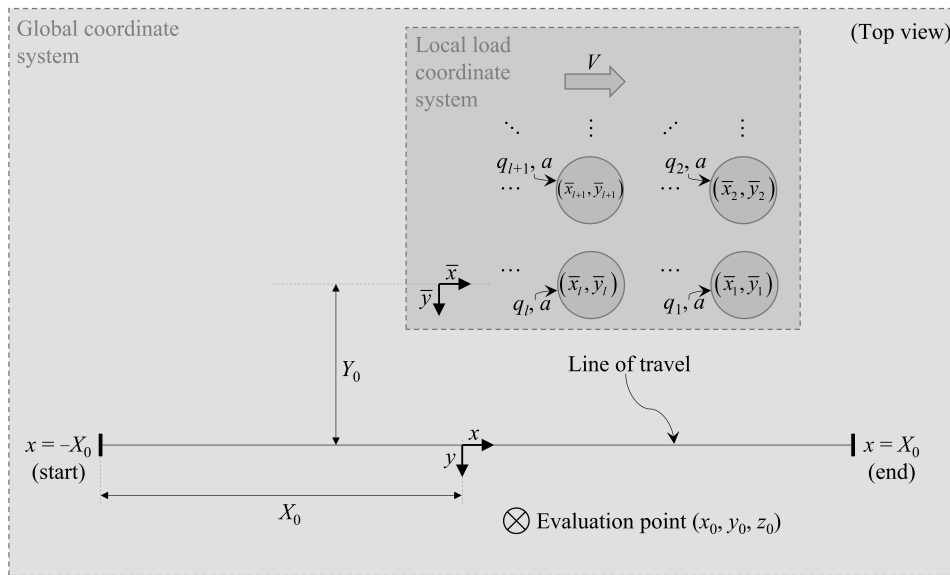
Figure 3.4: Top view of the moving load configuration in GRIDPAVE-MM.

Finally, the code can handle one or multiple AGR layers (identified by the subscript j with $j = 1, 2, ..., J$) given the following inputs: an effective Young's modulus E_j (in MPa), an effective Poisson's Ratio ν_j (unitless), an effective thickness h_j (in mm), a ZoI thickness δ_j^{ZoI} (in mm), a parameter κ_j (unitless), and an upper and a lower interface bond stiffness. The latter can be captured (either) by two time-independent horizontal spring constants k_{j-1} and k_j (in MPa/mm) or by two relaxation interface stiffness $K_{j-1}(t)$ and $K_j(t)$ (in MPa/mm). Figure 3.5 shows a schematic representation of two pavement layers without AGR (left-hand side) versus with AGR (right-hand side). In cases where the grid is placed between two elastic layers, the κ_j input becomes a multiplication factor on the modulus within the ZoI sub-layer (i.e., replacing $E_i^{ZoI}(t)$ by $\kappa_j E_i$). This interpretation can essentially be used to model reinforcement products designed for deeper granular layers (e.g., geogrids). It should be noted that if the AGR resides between two elastically-assumed AC layers, κ must be chosen to reflect on the prevailing load speed and AC temperature conditions.

The final model output involves the stresses $\sigma_x, \sigma_y, \sigma_z, \tau_{xy}, \tau_{yz}, \tau_{xz}$, strains $\varepsilon_x, \varepsilon_y, \varepsilon_z, \varepsilon_{xy}$, $\varepsilon_{yz}, \varepsilon_{xz}$, and displacements U_x, U_y, U_z in the evaluation point (x_0, y_0, z_0). Under moving loads, these responses come out as traces as a function of the load configuration's location in the traveling direction (x).
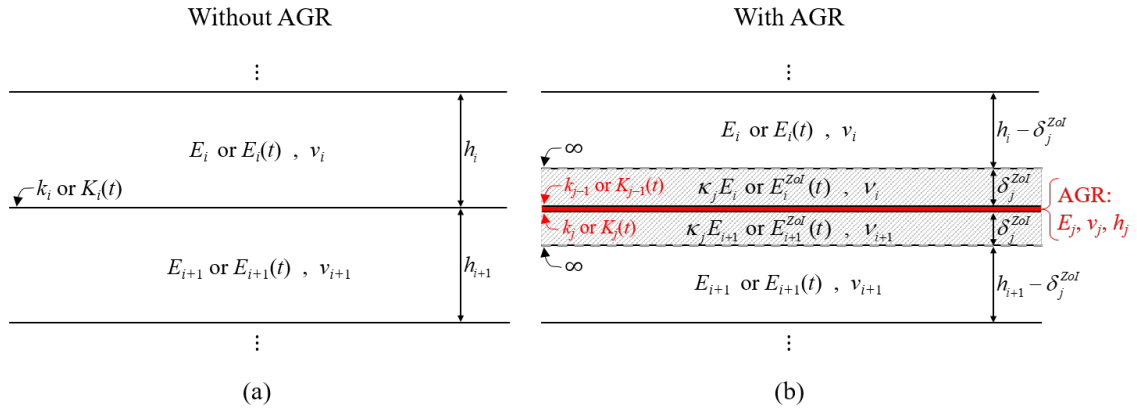
Figure 3.5: Schematic representation of two pavement layers i and $i+1$ in GRIDPAVE-MM, where: (a) exclude AGR and (b) include an AGR.

3.2.2 Numerical implementation

Layered elastic solution

GRIDPAVE was implemented based on the open-source MATLAB code ALVA (Skar and Andersen 2020; Skar et al. 2020a; Skar 2021). The ALVA code solves the standard axisymmetric LET formulation (for undamaged elastic layers) in a normalized format (Levenberg 2020), and includes imperfect bonding conditions between model layers. Herein, undamaged layers are taken as linear elastic, isotropic, homogeneous, and weightless. ALVA also includes a VE component for layered VE analysis with moving loads, which was not utilized in GRIDPAVE. Thus, GRIDPAVE only utilizes ALVA for calculating the elastic responses in a layered system exposed to a single circular load with a uniform stress intensity.

The entire solution involves the integration of several Bessel function products with respect to a (unitless) variable m. In ALVA, this is solved numerically by considering the first $N = 200$ Bessel zeros points, and dividing the overall integral into 200 sub-integrals, each over an interval between two Bessel zeros points. For this purpose, the Gauss integration scheme was used where the first interval (from zero to first Bessel zero) and second interval (from first Bessel zero to second Bessel zero, etc.) were integrated using a 30-point ($n = 30$) Gaussian formula, the third interval was integrated using a ten-point Gaussian formula, and the remaining intervals were integrated using a five-point Gaussian formula. This procedure reduces the expense of numerical integration, wherein most of the relevant information is contained in the initial intervals. In total, 1055 values of the integration variable m were used for integration. To further expedite the process, 96 predetermined values of m in the range of 10^{-10} to 100,000 were used to solve the underlying boundary and continuity conditions – hence reducing the number of matrix inversions from 1055 to 96. Hereafter, a cubic spline interpolation scheme, based on the modified Akima cubic Hermite interpolation tool in MATLAB `makima`, was used to generate results for the 1055 intermediate m values. Finally, to provide integration convergence (especially for evaluation points residing close to the pavement surface), the one-step Richardson extrapolation was employed according to Sugihara 1987.

As an addition to the numerical LET solution, damaged layers were implemented in GRID-PAVE by extending the ALVA code to include the FL formulation provided by (Levenberg and Skar 2022). Specifically, the boundary and continuity conditions defined in the ALVA-function `arb_func` were reformulated to include the set of equations for P-type

FLs. Accordingly, damaged layers were not treated as a mechanical layer, but as a new interface type with the properties $k_{v,i}$, $k_{h,i}$, and G_i. Consequently, undamaged layers must always be present before and after a FL. In terms of assigning a layer modulus E_i and layer thickness h_i to a FL (for practicality), the following relation $k_{v,i} = E_i/h_i$ was assumed. In cases where damaged layers are included, the FL-version of `arb_func` was utilized, and regular interfaces (where damaged layers were not present) between two undamaged layers i and $i+1$ were defined by $k_{v,i} = 10^6$ (MPa/mm), $k_{h,i} = k_i$ (depending on the bonding conditions), and $G = 0$ (N/mm).

Multiple and moving loads

Applications of multiple moving loads were implemented in GRIDPAVE for emulating realistic vehicular loading scenarios. Multiple loads were emulated using the principle of superposition within the linear elastic system. Moving loads were emulated using a quasi-static approximation, simulating multiple elastic solutions for a set of stationary loads by sequentially changing the load's locations along a desired travel direction. The approximation disregards inertia effects, i.e., dynamic variations in the pavement generated by the momentum of a moving load. From a practical point of view, doing so is reasonable since vehicles move significantly slower in comparison to the seismic wave speeds associated with common pavement materials (Levenberg 2015).

It is anticipated herein that the loads move (on the surface) along the x-axis in a global Cartesian coordinate system (x, y), with a constant speed V and a lateral offset Y_0 to the origin; this is illustrated in the upper part of Figure 3.6. The load coordinates are defined in a different "load coordinate system" denoted by $(\bar{x}, \bar{y})$. The origin of the local
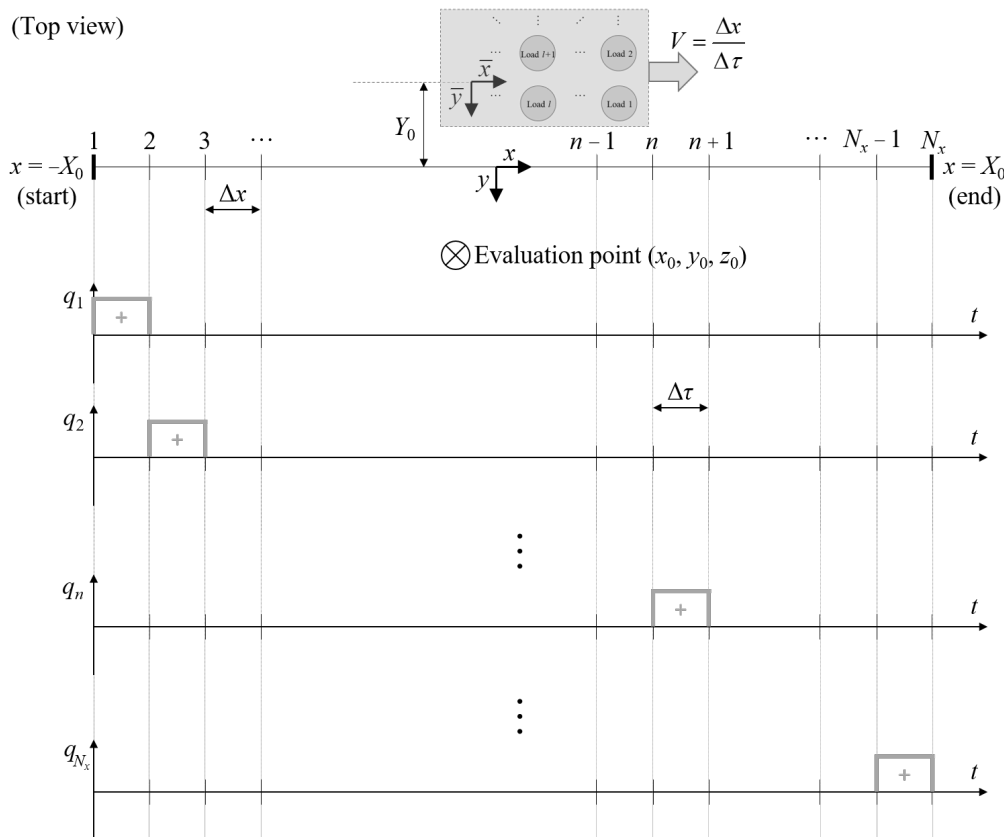
Figure 3.6: Schematic representation of the quasi-static approximation of multiple moving loads.

load coordinates is first applied at $x = -X_0$ mm, allowed to travel along the x-direction to $x = X_0$ mm, and then removed from the system. To generate the transient effect of a moving load configuration, $N_x = 2000$ load locations x_n (with $n = 1, 2, ..., N_x$) were sequentially defined along the x-axis, ranging from $x_1 = -X_0$ to $x_{N_x} = X_0$ with equal spacing of Δx. A unit-step load q_n is applied in each load location with a duration of $\Delta \tau = \Delta x / V$ – as indicated in the lower part of Figure 3.6. Ultimately, one elastic response history $R^e(t_n)$ (where t_n is the time when the load is located in point n) emanates from the described load sequence.

The overall procedure was implemented by first activating the axisymmetric ALVA solution for a single stationary load, with the intensity $q_0 = 1\,\mathrm{MPa}$ and radius a. $N_x^0 = 50$ discretization points were selectively spaced along the radial direction r, from $r = 0$ up to $r = X_0$, and ALVA was used to simulate the corresponding responses $\mathbf{R}_0^{\mathrm{ALVA}}$. Hence, N_x^0 denotes the number of times ALVA is activated. A final discretization point is added, taken as $r = 15X_0$; the response value at this point is set to zero as a guiding point for subsequent interpolation. Hence, an array of discretization points $\mathbf{r}_0$ is defined as:

$$\mathbf{r}_0 = \begin{bmatrix} 0 & \dots & X_0 & 15X_0 \end{bmatrix} \tag{3.5}$$

with the corresponding set of elastic responses $\mathbf{R}_0^e$:

$$\mathbf{R}_0^e = \begin{bmatrix} \mathbf{R}_0^{\mathrm{ALVA}} & 0 \end{bmatrix} \tag{3.6}$$

Next, the local load coordinates $(\bar{x}_l, \bar{y}_l)$ are used to define a set of global coordinate matrices $(\Delta\mathbf{X}, \Delta\mathbf{Y})$, given as:

$$\Delta\mathbf{X} = \begin{bmatrix} x_1 & x_2 & \dots & x_n & \dots & x_{N_x} \end{bmatrix} \cdot \begin{bmatrix} \bar{x}_1 & \bar{x}_2 & \dots & \bar{x}_l & \dots & \bar{x}_L \end{bmatrix}^T - x_0 \tag{3.7}$$

$$\Delta\mathbf{Y} = \begin{bmatrix} y_1 & y_2 & \dots & y_n & \dots & y_{N_x} \end{bmatrix} \cdot \begin{bmatrix} \bar{y}_1 & \bar{y}_2 & \dots & \bar{y}_l & \dots & \bar{y}_L \end{bmatrix}^T - y_0 + Y_0 \tag{3.8}$$

A set of global radial distances $\mathbf{r}$ were then obtained based on Equation (3.7) and (3.8), hence:

$$\mathbf{r} = \sqrt{(\Delta\mathbf{X})^2 + (\Delta\mathbf{Y})^2} \tag{3.9}$$

The resulting axisymmetric responses $\mathbf{R}_l^e$ corresponding to $\mathbf{r}$ were obtained by interpolation over $\mathbf{r}_0$ and the associated $\mathbf{R}_0^e$ solutions. The interpolation was carried out using the built-in MATLAB function `interp1`, with the `'cubic'` method.

Finally, $\mathbf{R}_l^e$ was transformed into symmetric responses, and the principle of superposition was used to generate a final response trace $\mathbf{R}^e$ under moving loads. This procedure was carried out in one step, that for stress/strain responses is mathematically expressed as:

$$\mathbf{R}^e = \sum_l^L \frac{q_l}{q_0} \mathbf{S}^T \mathbf{R}_l^e \mathbf{S} \tag{3.10}$$

whereas for displacement responses is expressed as:

$$\mathbf{R}^e = \sum_l^L \frac{q_l}{q_0} \mathbf{S}^T \mathbf{R}_l^e \tag{3.11}$$

where

$$\mathbf{S} = \begin{bmatrix} \cos\boldsymbol{\theta} & \sin\boldsymbol{\theta} & 0 \\ \sin\boldsymbol{\theta} & \cos\boldsymbol{\theta} & 0 \\ 0 & 0 & 1 \end{bmatrix} \quad , \quad \boldsymbol{\theta} = \tan^{-1}\left(\frac{\Delta\mathbf{Y}}{\Delta\mathbf{X}}\right) \tag{3.12}$$

and the multiplication factor q_l/q_0 (facilitated by the linear elasticity assumption) is used to account for different stress intensities across the considered loads.

Overall, this numerical approach is computationally efficient compared to activating ALVA in each of the N_x location points. This is because the computational effort of spline interpolation is negligible compared to running ALVA. Hence, the computational effort with respect to ALVA executions was reduced from $2000 \times L$ to $N_x^0 = 50$ (by a factor of $40 \times L$). While the numerical interpolation step could provide intermediate solutions (for every r-coordinate within the axisymmetric system) at almost no cost, the computational effort becomes relatively large for transporting axisymmetric responses into symmetric responses. Thus, $N_x = 2000$ was appropriately selected to limit the computational effort with respect to response transformation.

Viscoelastic solution

VE was added to GRIDPAVE by extending the LET solution to include a set of time- and temperature-dependent layer and interface properties (i.e., $E_i(t)$ and/or $K_i(t)$), symbolically represented by $c(t)$. This was done following the numerical implementation procedure in Levenberg 2016, decomposing the load step histories q_n (see Figure 3.6) into load-unload histories, followed by a superposition scheme that successively adds up all the elastic solutions into one VE response $R^{ve}(t)$. The superposition scheme implies N_x number of elastic moving load histories $\mathbf{R}^e$, one for each corresponding set of time- and temperature-dependent properties $c(t_n)$. Accordingly, $N_x \times N_x$ elastic solutions were used to generate the overall VE response $\mathbf{R}^{ve}(c(t_n), x_n)$.

To expedite the computational effort, the numerical VE solution was limited to $N_t = 15$ $\mathbf{R}^e$-solutions for a set of $c(t_m)$ values (with $m = 1, 2, ..., N_t$), logarithmically distributed from $t_m = 10^{-15}$ s to $t_m = 10^5\, s$. The MATLAB function `interp1` with the `'cubic'` method was subsequently utilized to generate N_x intermediate solution to complete the load superposition scheme of Levenberg 2016. Accordingly, a total of $N_x^0 \times N_t = 750$ ALVA evaluations was needed to generate the VE response history $\mathbf{R}^{ve}(t_n)$. Overall, this numerical approach reduced the computational effort with respect to ALVA executions from $4{,}000{,}000 \times L$ ($= 2000 \times 2000 \times L$) to 750 (by a factor of $5333 \times L$).

3.2.3 Model verification

The following model verification aims to ensure that the code behind GRIDPAVE was implemented correctly and to confirm numerical accuracy with respect to the governing model formulation. The work in Skar 2021 already provides a verification effort of the LET-kernel ALVA. Hence, the following content focus on verifying the numerical implementation and accuracy of the added features, i.e. FLs, the AGR component, and VE with moving loads. It is presented in the form of several verification cases (VCs) that cover a variety of model verification efforts done with respect to GRIDPAVE.

VC1

The first verification case (VC1) is focused on the numerical accuracy of the elastic part of GRIDPAVE, i.e., ALVA with the implementation of FLs. Specifically, the numerical accuracy is investigated with respect to the selection of integration points in the Gauss integration scheme.

VC1 considers a three-layered system of (undamaged) elastic layers subjected to a single stationary load. The model inputs are presented in Figure 3.7, where the load is placed in the coordinates $(x = 0, y = 0)$. Three cases of interface conditions, i.e., I1, I2, and I3, are considered with the interface properties given in Table 3.1. Here, I1 represents full bonding between all layers, I2 represents full slip between layers 1 and 2, and I3 represents a FL with no shear transfer between fragments. The following three key responses at $(x_0 = 0, y_0 = 0)$ (i.e., under the load) are investigated: (i) the vertical stress (σ_z), (ii) the horizontal strain in x (ε_x), and (iii) the vertical displacement (U_z). The calculations are repeated for three depths, i.e.: $z = 0\,\text{mm}$, $z = 10\,\text{mm}$, and $z = 100\,\text{mm}$.
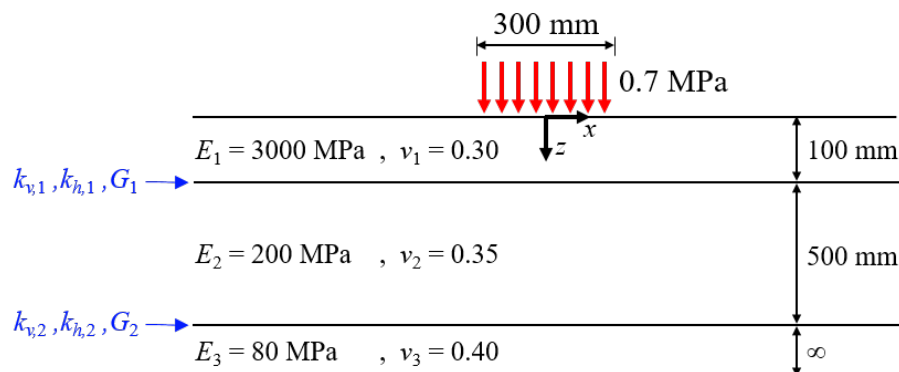
Figure 3.7: VC1: Basic three-layered elastic system.

Table 3.1: VC1: Interface condition properties.

Interface property	I1	I2	I3
$k_{v,1}$ [MPa/mm]	10^6	10^6	5
$k_{h,1}$ [MPa/mm]	10^6	0.01	10^6
G_1 [N/mm]	0	0	0
$k_{v,2}$ [MPa/mm]	10^6	10^6	10^6
$k_{h,2}$ [MPa/mm]	10^6	10^6	10^6
G_2 [N/mm]	0	0	0

Figure 3.8 shows three charts that all represent simulations of key responses for VC1. In each chart, the numerical integration parameter N (i.e., number of Bessel zero points) is plotted along the abscissa (ranging from $N = 1$ to $N = 1000$), whereas the ordinate represents the normalized key response, i.e., σ_z, ε_x, or U_zc, divided by its value for $N = 1000$. The black curves represent σ_z, the red curves represent ε_x, and the blue curves represent U_z; all three interface conditions (I1, I2, and I3) are represented by the same curve since the simulated values came out similar. Each chart is associated with a different key response depth z. As can be seen in the top chart (where the key responses are located at $z = 0\,\text{mm}$), the normalized value of σ_z and ε_x deviates from unity for low values of N. As N increases, this value approaches unity, which means that the code is able to reproduce the same key response value as for $N = 1000$. At approximately $N = 200$, unity is reached for all three key responses. Similar trends are shown in the middle chart (where the key responses are located at $z = 10\,\text{mm}$), where all key responses reach unity at approximately $N = 30$. In the bottom chart (where the key responses are located at $z = 100\,\text{mm}$), all values of N seem to generate similar key response values. According to these results, numerical accuracy across all key responses and location depths is gained for $N \geq 200$.
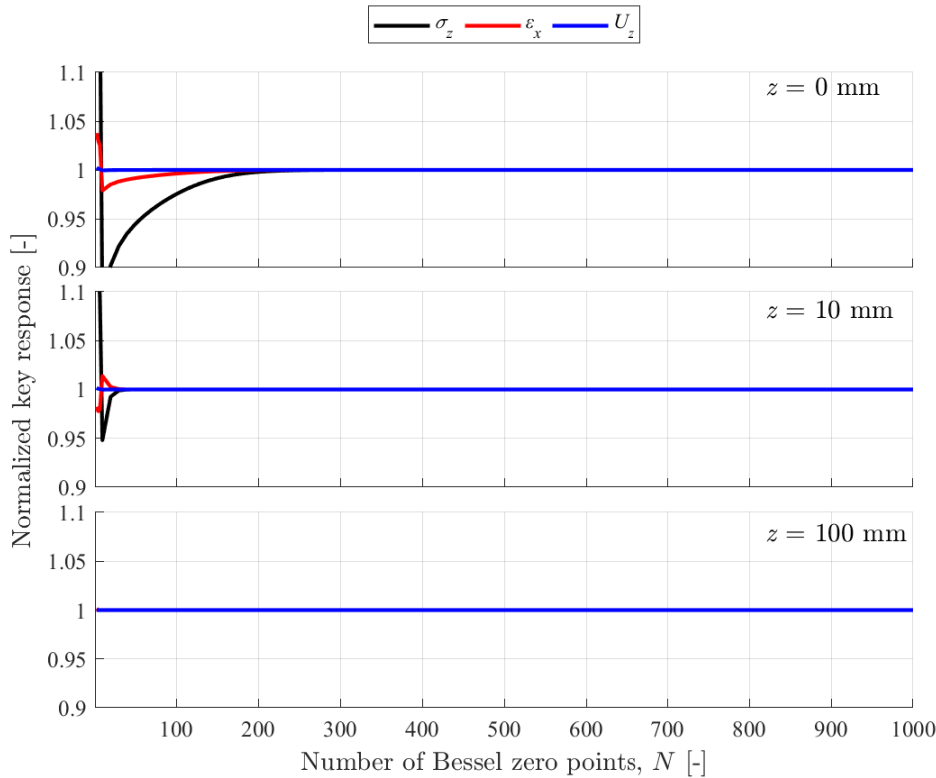
Figure 3.8: VC1 results: Normalized key responses as a function of the numerical integration parameter N for three depths.

Additionally (however not shown herein), the sequence of Gaussian points (i.e., 30 for the first and second intervals, ten for the third interval, and five for the remaining intervals) was compared to solutions generated with 30 Gaussian points between all intervals. Plots, similar to Figure 3.8, were generated with 30 Gaussian points between all intervals. As a result, the computational time increased by 15%, but key response simulations were identical across the two Gaussian point sequences. Hence, the implemented sequence of Gaussian integration points can reproduce similar results to a sequence with 30 Gaussian points between all Bessel zero intervals. Overall, these findings from VC1 imply that the numerical implementation (with respect to $N = 200$ and the chosen sequence of Gaussian integrations points) in GRIDPAVE is numerically accurate.

VC2

The second verification case (VC2) focuses on examining the correctness of the elastic part of GRIDPAVE (again ALVA with FLs). Specifically, it is checked that GRIDPAVE can reproduce similar responses generated in Skar 2021 using the software tools ALVA, BISAR, KENLAYER, and GAMES.

VC2 considers a three-layered system of (undamaged) elastic layers subjected to a single stationary load (taken from Skar 2021). The layer properties are presented in Table 3.2, and the load inputs are $q = 0.7\,\mathrm{MPa}$ and $a = 150.8\,\mathrm{mm}$. In GRIDPAVE, all interfaces are characterized by $k_v = 10^6\,\mathrm{MPa/mm}$, $k_h = 10^6\,\mathrm{MPa/mm}$, $G = 0\,\mathrm{N/mm}$, corresponding to full continuity (both vertically and horizontally) between layers. The considered key responses are: (R1) the vertical stress (σ_z) at the surface; (R2) the horizontal strain (ε_x) at the bottom of layer 1; (R3) the vertical strain (ε_z) at the top of layer 2; and (R4) the vertical strain at the top of layer 3.

Table 3.2: VC2: Pavement layer properties.

Layer	Thickness (mm)	Young's moduli (MPa)	Poisson's ratio
1	260	5000	0.35
2	500	200	0.40
3	∞	50	0.45

The resulting calculations generated by GRIDPAVE, ALVA, BISAR, KENLAYER, and GAMES are presented in Tables 3.3 and 3.4. In Table 3.3, all key responses are located under the load center, whereas in Table 3.4, the key responses are located under the load edge. As can be seen in both tables, the simulations from GRIDPAVE and the other codes are close to identical. This observation indicates that GRIDPAVE is able to reproduce similar responses to already accepted/verified response models like ALVA, BISAR, KENLAYER, and GAMES.

Table 3.3: VC2 results: Key responses under the load center.

Code	R1 [MPa]	R2 [μm/mm]	R3 [μm/mm]	R4 [μm/mm]
BISAR	0.7	-100.5	251.7	185.0
KENLAYER	0.8	-100.5	251.6	185.3
GAMES	0.7	-100.5	251.6	185.1
ALVA	0.7	-100.4	251.6	185.1
GRIDPAVE (elastic)	0.70	-100.5	251.7	185.2

Table 3.4: VC2 results: Key responses under the load edge.

Code	R1 [MPa]	R2 [μm/mm]	R3 [μm/mm]	R4 [μm/mm]
BISAR	0.4	-61.9	192.2	177.5
KENLAYER	0.3	-62.0	192.2	177.0
GAMES	0.3	-61.9	192.2	177.5
ALVA	0.3	-61.8	192.3	177.5
GRIDPAVE (elastic)	0.35	-62.0	192.3	177.6

VC3

The third verification case (VC3) focuses on investigating GRIDPAVE's ability to correctly produce responses in systems that include a damaged layer (FL). Specifically, this was done by comparing GRIDPAVE simulations with calculations presented in Levenberg and Skar 2022.

VC3 considers two axisymmetric systems with four layers – three undamaged layers, and one (damaged) FL. The model inputs are presented in Figure 3.9, showing two systems that are only different by the thickness of layer 1. Specifically, System 1 has a layer 1 thickness of 50 mm, whereas System 2 has a layer 1 thickness of 0.1 mm. Both systems include a FL between layers 1 and 2, which is characterized by a variable set of k_v and G, whereas $k_h = 10^6$ MPa/mm is fixed; full continuity applies between layers 2 and 3. Each system is exposed to a stationary load with its center located at $(r, z) = (0, 0)$.

Figure 3.10 shows four charts that depict the resulting vertical displacements at the pavement surface as a function of radial distance from the load center. The two top charts are associated with System 1, whereas the two bottom charts are associated with System 2. To the left-hand side, $G = 0$ N/mm is assumed, whereas $G = 10000$ N/mm or $G = 1000$ N/mm
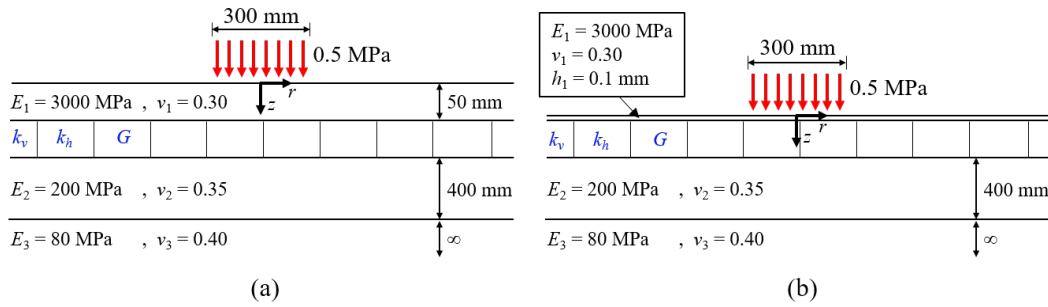
Figure 3.9: VC3: Two four-layered elastic systems with a FL – (a) System 1 and (b) System 2.

is considered to the right-hand side. Each chart presents four black curves, which represent GRIDPAVE simulations with four different values of k_v; four similar red-dotted curves are also included, representing simulations from Levenberg and Skar 2022. As can be seen across all charts, all black and red-dotted curves are indistinguishable, indicating that GRIDPAVE is able to reproduce simulations from Levenberg and Skar 2022.
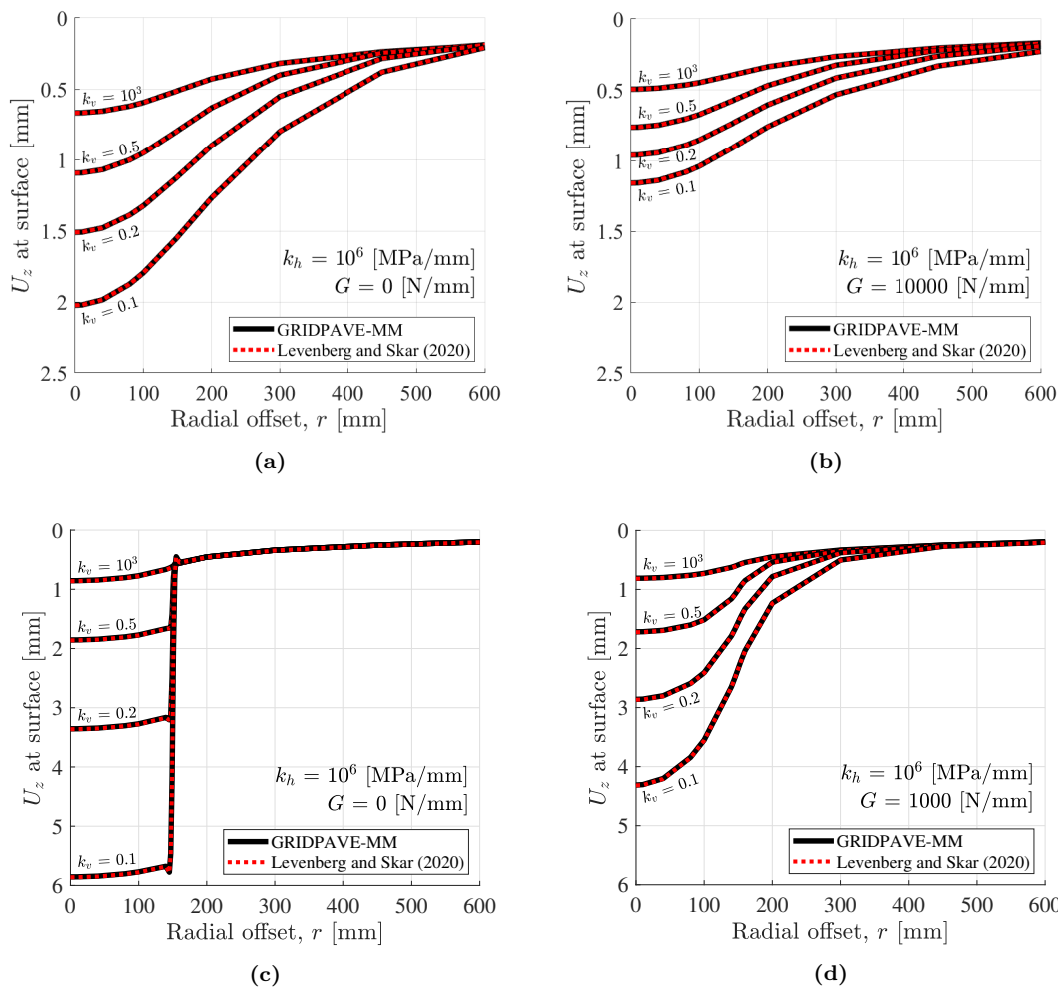
Figure 3.10: VC3 results: Calculated vertical displacement at the surface from GRIDPAVE and Levenberg and Skar (2020) for (a) System 1 with $G = 0\,\text{N/mm}$, (b) System 1 with $G = 10000\,\text{N/mm}$, (c) System 2 with $G = 0\,\text{N/mm}$, and (d) System 2 with $G = 1000\,\text{N/mm}$.

VC4

The fourth verification case (VC4) focuses on numerical stability with respect to adding a thin layer with a high modulus. Specifically, the numerical stability is investigated for the elastic part of GRIDPAVE (i.e., ALVA with the implementation of FLs).

VC4 considers a three-layered system of elastic layers subjected to a single stationary load – presented in Figure 3.11. The second layer represents a layer with a variable Young's modulus, ranging from $500\,\text{MPa}$ to $5\cdot10^{10}\,\text{MPa}$, and a small thickness; the following three thicknesses are examined: $h_2 = 0.0001\,\text{mm}$, $h_2 = 0.01\,\text{mm}$, and $h_2 = 1\,\text{mm}$. Three cases of interface conditions, i.e., I1, I2, and I3, are considered with the interface properties given in Table 3.5. I1 represents full continuity between all layers, I2 represents full (horizontal) slip between layers 1 and 2, and I3 represents a FL (with no shear transfer between fragments) between layers 2 and 3. The following three key responses under the load center are investigated: (i) the vertical stress (σ_z) at $z = 100.1 + h_2$ in mm (i.e., at the top of layer 3), (ii) the horizontal strain in x (ε_x) at $z = 100\,\text{mm}$ (i.e., at the bottom of layer 1), and (iii) the vertical displacement (U_z) at $z = 0\,\text{mm}$ (i.e., at the surface).
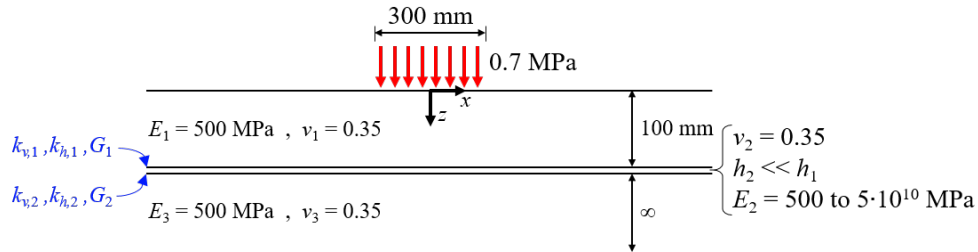
Figure 3.11: VC4: Three-layered elastic system with a thin layer.

Table 3.5: VC4: Interface condition properties.

Interface property	I1	I2	I3
$k_{v,1}$ [MPa/mm]	10^6	10^6	10^6
$k_{h,1}$ [MPa/mm]	10^6	0.01	10^6
G_1 [N/mm]	0	0	0
$k_{v,2}$ [MPa/mm]	10^6	10^6	5
$k_{h,2}$ [MPa/mm]	10^6	10^6	10^6
G_2 [N/mm]	0	0	0

Figure 3.12 shows three charts that all represent simulations of key responses for VC4. In each chart, E_2/E_1 (i.e., the modulus-ratio between layers 1 and 2) is plotted along the abscissa (ranging from $E_2/E_1 = 1$ to $E_2/E_1 = 10^8$), whereas the ordinate represents the normalized key response, i.e., σ_z, ε_x, or U_z divided by its value for $E_2 = E_1(= E_3)$ (corresponding to a half-space solution). Each black curve represents σ_z, the red curves represent ε_x, and the blue curves represent U_z; the three interface conditions, i.e., I1, I2, and I3, are respectively represented by a solid, dotted, and dashed line. Each chart is associated with a different thickness of layer 2 (h_2). As can be seen across all charts, normalized responses associated with I1 and I3 reduce as E_2 increases; the reduction occurs for lower E_2/E_1-ratios as h_2 increases. This effect is largest for ε_x. The effect is hardly realized in the two upper charts for responses associated with I2. While these effects are mechanical, none of the three charts displays irregularities or fluctuations across the presented curves. Hence, the results indicate that introducing a thin layer to the elastic part of GRIDPAVE is numerical stable.
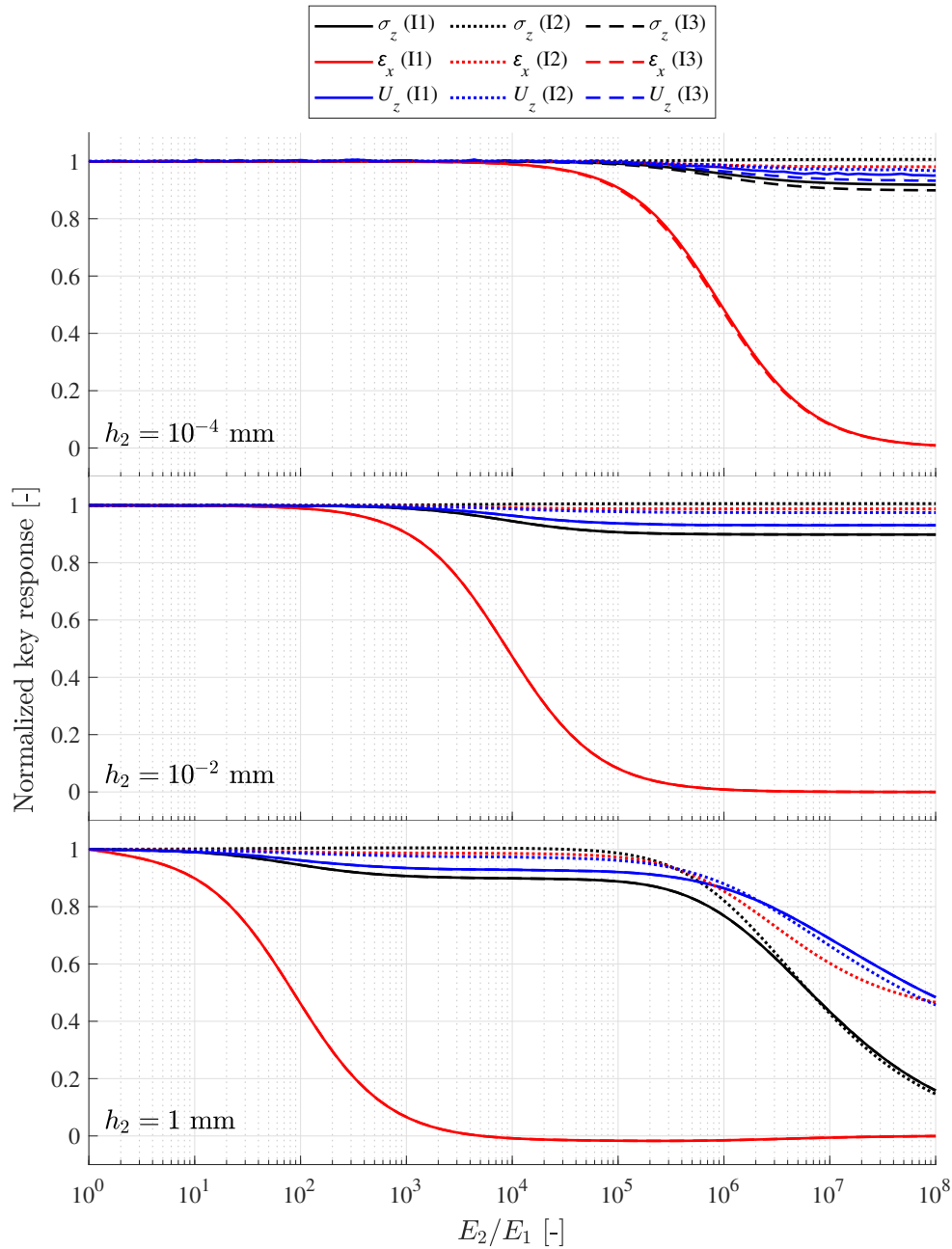
Figure 3.12: VC4 results: Normalized key responses as a function of the modulus-ratio between layers 1 and 2 E_2/E_1 for three thicknesses of layer 2.

VC5

The fifth verification case (VC5) focuses on examining the correctness of the VE part of GRIDPAVE (i.e., ALVA with FL, VE and moving loads). Specifically, it is checked that GRIDPAVE can reproduce similar responses to a benchmark solution for a traveling point load on a homogeneous isotropic VE half-space.

VC5 considers a VE half-space subjected to a moving point load with a force magnitude of $50.2\,\mathrm{kN}$. The load moves in the x direction, from $x = -10,000\,\mathrm{mm}$ to $x = 10,000\,\mathrm{mm}$, in a Cartesian coordinate system with two considered (constant) speeds, e.i., $V = 5\,\mathrm{km/h}$ and

$V = 80\,\text{km/h}$. The half-space is assigned a Possion's Ratio $\nu = 0.35$ and a relaxation modulus $E(t)$ according to Equation (3.1) with the following model inputs: $E_0 = 30,000\,\text{MPa}$, $E_\infty = 100\,\text{MPa}$, $\tau_D = 1000\,\text{s}$, $n_D = 0.35$. The following three key responses at $x_0 = 0\,\text{mm}$ $y_0 = 300\,\text{mm}$ (i.e., the transverse distance to the load center) and $z_0 = 0\,\text{mm}$ (on the surface) are investigated: (i) the horizontal displacements in x (U_x), (ii) the horizontal displacements in y (U_y), and (iii) the vertical displacement (U_z).
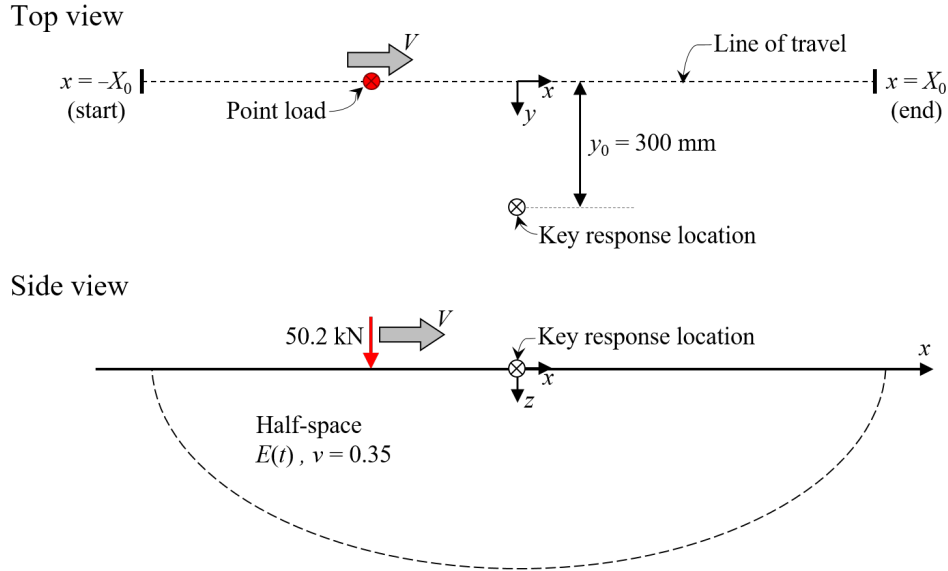
Figure 3.13: VC5: VE half-space with a moving point load.

In GRIDPAVE, the above system is modeled as a three-layered system given in Table 3.6, with full continuity at both layer interfaces (similar to I1 in Tables 3.1 and 3.5). The point load is approximated by a circular load with $a = 1\,\text{mm}$ and $q = 16,000\,\text{MPa}$. Numerically, the GRIDPAVE calculations are composed of $N_x^0 \times N_t = 50 \times 15 = 750$ elastic solutions (refer to Subsection 3.2.2). The benchmark solution for a traveling point load on a homogenous isotropic VE half-space is based on the classical Boussinesq solution for a stationary point load on a homogenous isotropic VE half-space. The Boussinesq solution is extended to VE according to the load-unload procedure in Levenberg 2016. Numerically, the benchmark solution was computed with a high degree of accuracy, composed of $N_x \times N_x = 20,000 \times 20,000 = 400 \cdot 10^6$ (elastic) Boussinesq solutions.

Table 3.6: VC5: GRIDPAVE layer properties.

Layer	Thickness (mm)	Young's moduli (MPa)	Poisson's ratio
1	100	$E(t)$	0.35
2	500	$E(t)$	0.35
3	∞	$E(t)$	0.35

Figure 3.14 presents three charts, each associated with one of the three key responses as a function of the load location in x. Each chart includes two black curves that represent GRIDPAVE simulations for two different speeds and two red-dotted curves representing the benchmark solutions for similar speeds. As can be seen across all charts, all black and red-dotted curves are close to identical, indicating that GRIDPAVE is able to reproduce the benchmark solutions.
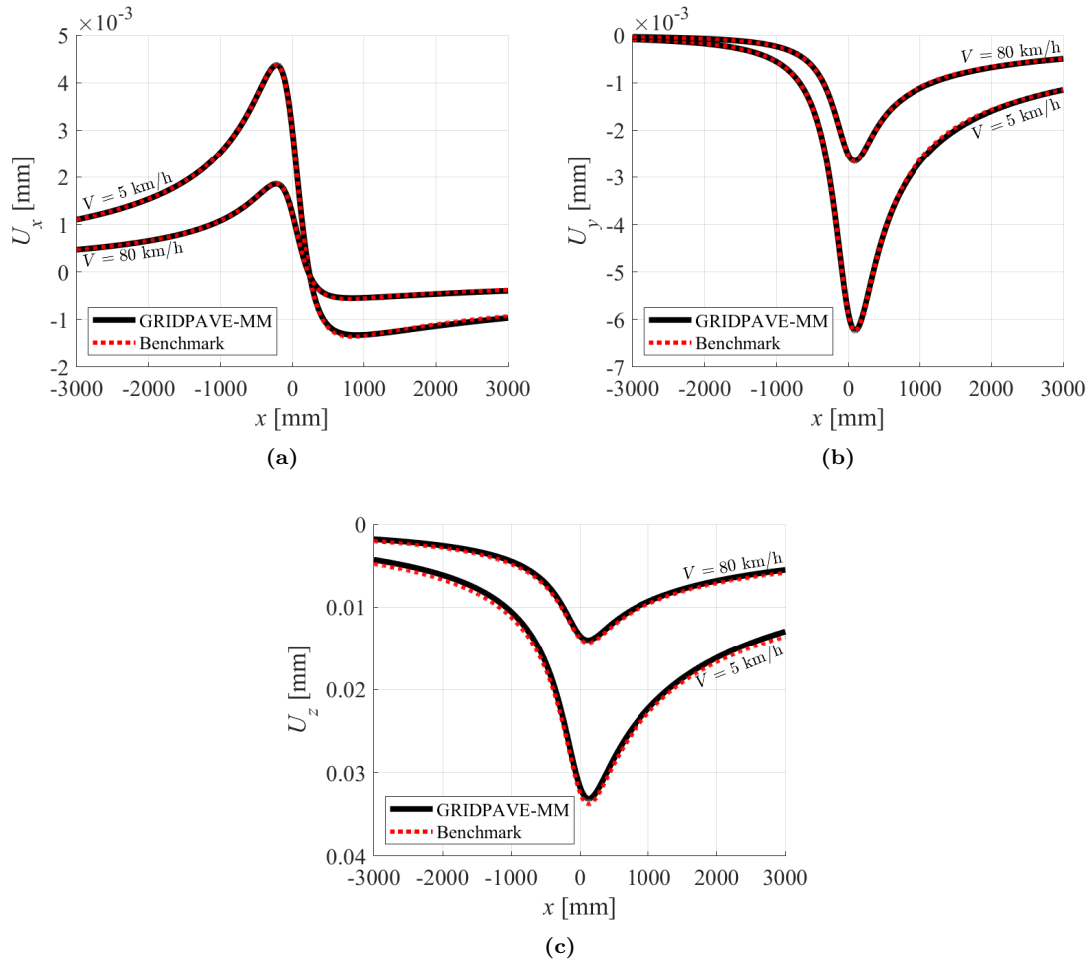
Figure 3.14: VC5 results: Calculated key responses from GRIDPAVE and benchmark solution, where (a) represents the horizontal displacements in x, (b) represents the horizontal displacements in y, and (c) represents the vertical displacements in z.

3.2.4 Contribution

The modeling efforts related to the implementation of GRIDPAVE contribute to the over-all dissertation by providing a computational tool that can produce pavement responses for systems with AGR – addressed in the first study objective (O1). In this context, the implementation and model verification of GRIDPAVE targeted all three aspects considered in (O1), i.e., the versatility, usefulness, and validity of the computational model. Specifically, the implementation of GRIDPAVE ensures that it is a versatile tool in the sense that its modeling components (i.e., FL, moving loads, VE, and AGR) can be turned on/off depending on the user's need. Moreover, model usefulness has been addressed during the implementation by numerical considerations that significantly improve computational efficiency. Lastly, the provided model verification cases demonstrate that the model is numerically stable and accurate, which supports GRIDPAVE's validity.

3.3 Experimental efforts

Several experimental activities were carried out during this PhD project, with a common aim of providing experimental data for model validation. Specifically, they involve full-scale testing at four different pavement facilities with embedded sensing equipment. Three of the facilities were constructed during the PhD period, namely the DTU Smart Road,

an accelerated pavement test (APT) setup in Texas (USA), and a city road in Neuchâtel (Switzerland). The fourth facility was a district road near the city of La Ferriére (Switzerland), which was constructed before the PhD period. The following content provides a summary of the experimental activities that were carried out during the PhD study. For more in-depth details about the experimental setup and test campaigns associated with the DTU Smart Road, the APT setup in Texas, and the test facilities in Switzerland, the reader can refer to Appendix A.

3.3.1   DTU Smart Road

DTU Smart Road is a full-scale pavement facility located at DTU campus in Kongens Lyngby (Denmark). It was built in October 2021 as a reconstruction of an existing two-lane road serving live campus traffic. The whole construction effort was entirely funded by S&P, and the experimental design was carried out by the PhD team. The overall purpose was to create an accessible full-scale test setup that can provide experimental evidence for subsequent model validation. Specifically, the setup was aimed at validating the AGR model-component developed in Paper ii; hence the experimental setup was carefully designed hereafter to expose the AGR effects within the pavement system. As an integral part of reaching this aim, the computational model GRIDPAVE was utilized to guide the design of such an experimental setup.

Prelimenary considerations

The preliminary considerations involve the thoughts and ideas made during the experimental design of DTU Smart Road. The ideas behind were to design a pavement system with AGR that utilizes embedded sensors to capture the reinforcement effects. As the focus was on validating the AGR model-component (and not on the FL model-component), a full-depth reconstruction of an existing road at DTU campus was considered – milling the entire existing AC and replacing it with new AC. Doing so eliminates any potential effects from cracks or aged AC within the pavement system.

To guide the design, GRIDPAVE was utilized to generate a variety of synthetic cases with and without AGR that, by comparison, would clarify the reinforcement effect. In general, it was found that the most dominant AGR effect was associated with a reduction in horizontal strains nearby the AGR (similar to what was found in Papers i and ii). More specifically, placing the AGR at the bottom of the AC structure generally provided the largest reduction in tensile strains within the AC. Based on these findings, it was decided to build a test section with AGR placed at the AC bottom and to place ASGs at the same level (to capture the nearby horizontal strains). Moreover, it was decided to build a nominal identical reference section (excluding reinforcement) with ASGs in similar depth for comparison.

With respect to the arrangement of ASGs at the AC bottom, it was considered to install multiple ASGs in each of the test sections with different lateral positions and orientations to capture horizontal strains at the AC bottom in two perpendicular directions. In theory, the model should be able to simultaneously reproduce all ASG responses, which would be relevant to showcase in a model validation effort. Furthermore, readings from such a sensor arrangement could be used to calibrate the accurate lateral position of a passing vehicle through inverse analysis. Past experience, as well as model simulations, have indicated that the lateral vehicle position is a sensible key parameter for reproducing pavement responses (see e.g. Levenberg 2015; Nielsen et al. 2020).

In order to address model versatility, it was further decided to build two additional and nominal identical test sections with the same AGR product located at different depths

(away from the bottom) within the AC. To accommodate this decision, it was considered to pave the entire DTU Smart Road (i.e., all four sections) in three lifts and install AGRs in-between lifts at different depths among test sections. In order to make the two additional test sections nominal identical to the two previous sections, similar AGS arrangements were also placed at the AC bottom (away from the AGR). This was done for comparison reasons, even though the reinforcement effect was deemed the largest near the grid. Regarding the choice of AC mix, it was considered to pave all three AC lifts with the same mix. While such a design is not common practice, a similar AC mix type was used to simplify model simulations and material characterization activities for subsequent validation efforts.

Finally, it was decided to place a set of PT100 temperature sensors in all test sections to measure any variation in temperature between sections and across the AC layer thickness. Accordingly, three PT100s were placed on top of each other in each section – one on the AC bottom, and the remaining two between the AC lifts.

Test setup

Based on the preliminary consideration, an experimental setup was designed and built in October 2021. Figure 3.15 provides a Google maps snapshot of the entire test area. It is composed of four sections – three of which include AGR at different depths, and a fourth serving as a reference section without AGR. The reinforced sections are referred to as sections S-1, S-2, and S-3, and the reference section is referred to as section S-0. A cross-sectional view of the four DTU Smart Road sections is given in Figure 3.16. All sections consist of a 150 mm thick AC structure placed on an existing UGS. Below the UGS is the local subgrade soil, extending to a large depth. DCP tests were performed in each test section (according to ASTM D6951/D6951M 2018) to identify the layer configuration of deeper layers (i.e., layers below the AC). In sections S-1, S-2, and S-3, AGR were installed at different depths below the surface, i.e.: 150 mm (at the AC bottom), 110 mm (between the bottom and middle lifts), and 40 mm (between the middle and top lifts), respectively. The same AGR type was utilized i all three sections, which was a Carbophalt®G 200/200 (S&P Clever Reinforcement Company AG 2023a).

Figure 3.15: DTU Smart Road: Overview of the four test sections.

Figure 3.16: DTU Smart Road: Cross-sectional view of the four test sections.

As an integral part of the DTU Smart Road, AGSs and PT100s were embedded inside the pavement system. In each section, six ASGs were located at the top of the UGS, or on top of the AGR in S-1, prior to paving of the bottom AC lift; in S-3, a seventh spare ASG was installed on top of the AGR (40 mm below the surface). Moreover, three PT100s were placed (in each section) on top of each other, each installed before an AC lift, i.e., at the depths: 150 mm, 110 mm, and 40 mm. All sensor installation depths are also indicated in Figure 3.16, whereas Figure 3.17 illustrates a top view of the sensor arrangement at the AC bottom of a single test section (identical for all test sections).

Figure 3.17: DTU Smart Road: Top view layout of the ASGs and PT100 in a single test section (taken from Nielsen and Levenberg 2022).

Measurement campaigns

Several measurement campaigns were carried out at DTU Smart Road during the PhD period. One involved FWD testing (according to ASTM D4694 2009), while three others involved testing with different moving vehicle types. The four campaigns are listed in Table 3.7. Two of the campaigns, i.e., the test campaign using the HYSTER forklift, together with the FWD campaign, are already described in Paper iii and therefore not repeated herein.

Table 3.7: List of measurement campaigns carried out at DTU Smart Road.

Date	Load source	Total weight [ton]	Number of axels
Marts 2022	FWD	6-10 (pulse load)	Plate
June 2022	HYSTER forklift	23.0	2
September 2022	Raptor	21.1	3
October 2022	Military tank	29.6	Tracks with 7 rollers
	Dumper truck	16.6	3
	VIAFRIK	17.8	2

One of the remaining measurement campaigns involved using Ramboll's Raptor (see Figure 3.18(a)). The Raptor is a moving measurement platform that provides information about surface displacements generated by its own self-weight (see e.g. Skar et al. 2020b). The measurement campaign only involved testing of sections S-0 and S-1, where AGS readings were recorded during several Raptor passes. Two (aimed) vehicle speeds were considered, i.e., 5 km/h and 40 km/h, and a constant temperature of 14 °C (uniformly distributed across the AC thickness) was measured during all passes. An example of ASG measurements taken during a single Raptor pass is provided in Appendix A (Figure A.7). Additionally, Raptor measurements were also recorded during each pass, providing information about the surface displacements. This information, together with the ASG readings, can be utilized in future model validation efforts with focus on deflection responses or strain responses at lower temperatures and faster load speeds.
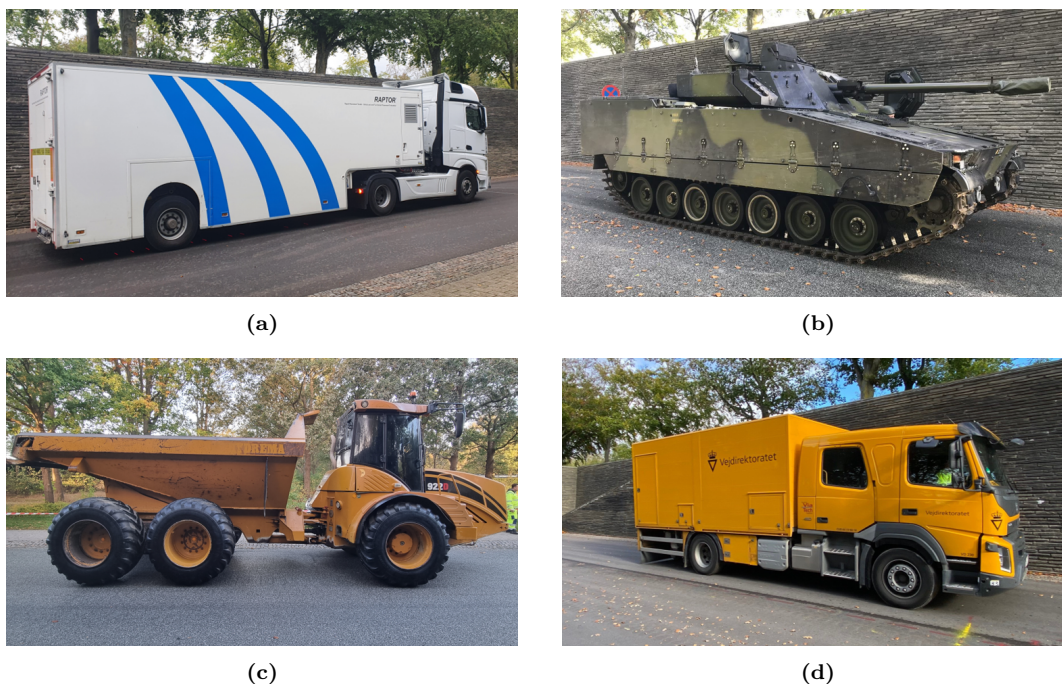
Figure 3.18: Test vehicles at DTU Smart Road: (a) Raptor, (b) Military tank, (c) Dumper truck, and (d) VIAFRIK.

Moreover, a measurement campaign was carried out using three different types of vehicle load configurations. The measurement campaign was part of a MSc's project (Hansen et al. 2023), aimed at investigating the mechanistic responses in asphalt pavements under heavy off-road vehicles. The three utilized vehicles were: a military tank equipped with contin-

uous tracks; a dumper truck equipped with ribbed tires; and Danish Road Directorate's VIAFRIK (friction tester) serving as a reference truckload. The three vehicle types are depicted in Figures 3.18(b)-(d), respectively. The measurement campaign involved testing all four test sections, where several passes with each vehicle were generated, targeted at two different speeds, i.e., 10 km/h and 40 km/h. ASG responses and PT100 readings were recorded during each pass. PT100 measurements indicated an AC temperature varying from 18 °C to 22 °C during the campaign. An example of ASG measurements taken during a single pass with each vehicle type is provided in Appendix A (Figure A.10).

Laboratory tests

In April 2022 (about six months after the DTU Smart Road was constructed), a total of eight AC cores were taken from the DTU Smart Road – two from each section. The layer thicknesses of all cores were measured to confirm the AC lift thicknesses after construction. The results indicated fairly consistent AC thickness, varying within ± 10 mm from the original design.

The cores were subsequently utilized for laboratory testing. A single core from each S-0, S-1, and S-2 was utilized for VE characterization of the AC properties. This procedure followed the experimental approach in Levenberg and Michaeli 2013, where the cores were tested in an indirect tensile test configuration (EN 12697-26C 2022) under several temperature levels. The tests were carried out in the laboratory facility at the Danish Technological Institute, and the derived AC properties were subsequently utilized in Paper iii and iv. Furthermore, one core from both S-0 and S-2 was utilized to characterize the interface stiffness properties between two AC layers – one including AGR and another excluding AGR. The test was carried out in the laboratory facility at the Technical University Dresden using the DDST, and the derived interface properties were subsequently utilized in Paper iv.

3.3.2 APT setup in Arlington, Texas

The APT setup in Arlington (Texas) is a full-scale pavement test area held by the University of Texas Arlington (UTA). In November 2021, eight new pavement sections were constructed with the purpose of testing several pavement systems with and without AGR until failure. This involved applications of cyclic loading with a so-called pavement testing machine (PTM). The research activities were mainly funded by Simpson Strong-Tie A/S (the mother company of S&P), and the experimental setup was designed by the pavement research group at UTA and the engineering team of Simpson Strong-Tie A/S. The PhD project team was not part of the design, but was involved in supervising the construction phase and subsequently in collecting data from embedded sensors during the initial loading phase (before damaging the pavement structure).

Test setup

Figure 3.19 provides drone footage of the entire test facility at UTA, composed of several new and existing (failed) test sections. Sections S1, S2, S3, and S4 (indicated in the figure) are the primary sections considered in this project, as they were the only ones instrumented with sensing equipment. The construction involved both a new UGS and AC structure. S1, S3, and S4 were all reinforced with AGR, whereas S2 served as an unreinforced reference section.

A cross-sectional view of the four instrumented sections is given in Figure 3.20. S1 and S2 consisted of a 100 mm thick AC structure, paved in two similar lifts; the AC was placed on top of a 250 mm UGS. S3 and S4 consisted of a 70 mm thick AC structure, also paved in
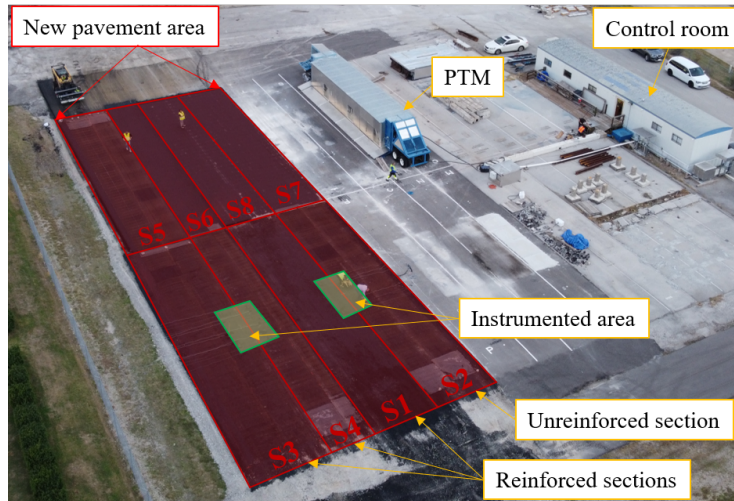
Figure 3.19: Overview of the ATP facility at UTA.

two similar lifts; the AC was placed on top of a 280 mm UGS. Below the UGS is the local subgrade soil, extending to a large depth. In sections S1, S3, and S4, AGRs were placed on top of the UGS before paving; sections S1 and S4 utilized a Carbophalt®G 200/200 (similar to Subsection 3.3.1), whereas a Glassphalt®G (S&P Clever Reinforcement Company AG 2023b) was utilized in S3.
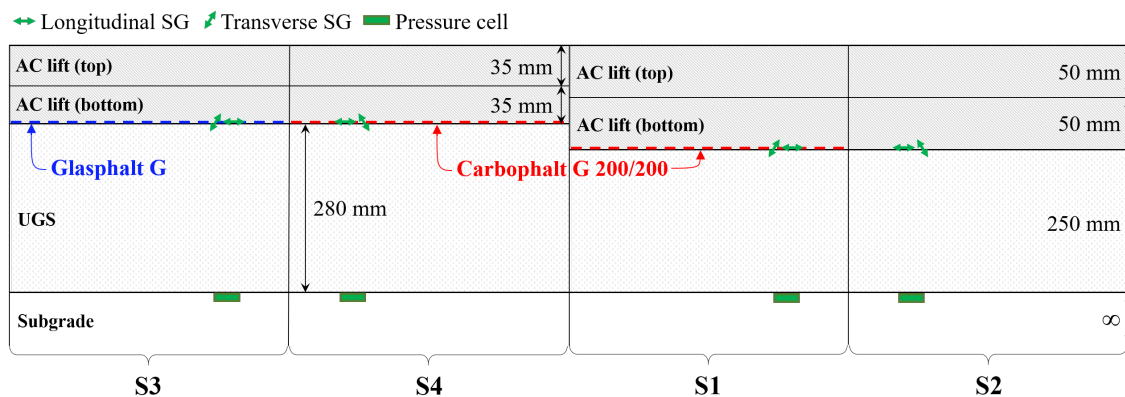
Figure 3.20: Cross-sectional view of the four instrumented test sections at UTA.

As an integral part of the four test sections, three types of sensors were embedded inside the pavement system, i.e., ASGs, pressure cells, and grid gauges. The ASGs were installed to capture horizontal strains at the AC bottom in two perpendicular directions, the pressure cells were installed to capture the vertical stresses at the UGS bottom, and the grid gauges were glued onto the AGR ribs to capture its horizontal strains. In each section, four ASGs (two transverse and two longitudinal) and two pressure cells were installed. The ASGs were all located on the top of the AGR, or on top of the UGS in S2, prior to paving of the bottom AC lift. The Pressure cells were placed on top of the subgrade soil before the UGS was constructed. In each reinforced section, three grid gauges were glued to the grid with a transverse orientation. All sensor installation depths are indicated in Figure 3.20, whereas Figure 3.21 illustrates a top view of the sensor arrangement in two neighboring sections, paired as S1+S2, or S3+S4.
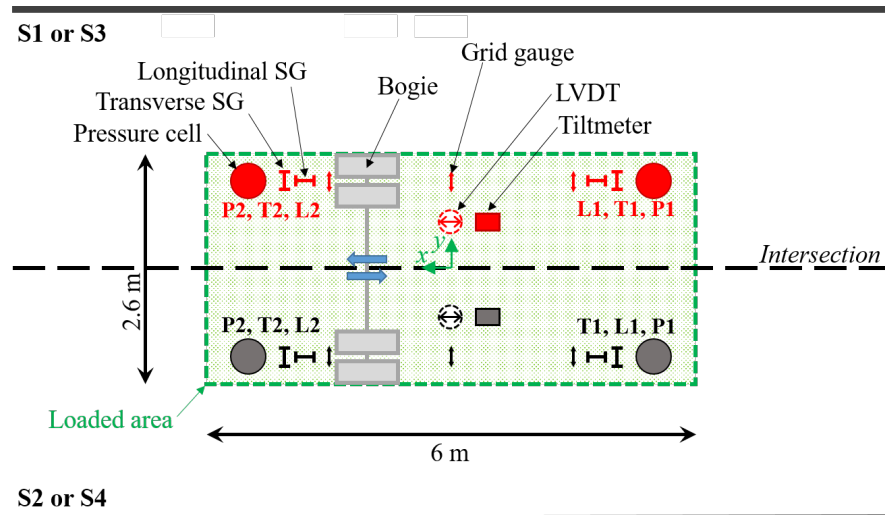
Figure 3.21: Top view layout of instrumented and loaded area at UTA.

Measurement campaigns

A measurement campaign was carried out at the UTA test facility in October 2022, as part of an APT on sections S3 and S4. The campaign itself took place in the initial part of the APT (during the first few load cycles) before the pavement systems were exposed to any damage. The APT setup involved using the PTM (see Figure 3.22) to induce cycling loading to both test sections at the same time. The PTM is a mobile system that simulates vehicle loading in an accelerated manner. The entire machine can be moved from section to section, which is efficient for testing multiple pavement systems within a relatively short period of time. In addition, the PTM is an isolated system that can maintain a fixed temperature within the encapsulated AC area. A heating-and-cooling system controls the temperature condition inside the machine. The PTM is equipped with a bogie, carrying two sets of dual tires that moves back and forth while applying a vertical axle load of 80 kN to the pavement. The PTM was installed such that one set of dual tires applied loading to S3, whereas the other set of dual tires applied loading to S4. The bogie is included in Figure 3.21, where it can be seen that the two-wheel paths are placed directly on top of the embedded sensors (i.e., ASGs, pressure cells, and grid gauges).

(a)   (b)

Figure 3.22: PTM: (a) from outside and (b) from inside.

In the measurement campaign, several load cycles were applied at three different speeds, i.e., 1 km/h, 2.4 km/h, and 4.8 km/h. Two uniform AC temperature levels were considered, i.e. $T = 16\,°C$ and $T = 27\,°C$. As part of the campaign, two types of deployable surface sensors were added to the test setup to provide supplementary response information for subsequent analysis. The two sensor types were linear variable displacement transducers (LVDTs) and dual-axis tiltmeters. A total of two LVDTs and two tiltmeters were placed on the pavement surface (outside the wheel paths) – one LVDT and one tiltmeter in each section (see Figure 3.21). The LVDTs were installed according to Skar et al. 2020c and measured the differential displacement in the traveling direction (in x) at the pavement surface. The tiltmeters were installed according to Nielsen 2019, on top of the AC surface, and measured the surface rotations around the longitudinal and transverse directions. With respect to test sections S1 and S2, a similar measurement campaign is planned but was not carried out during this PhD period. An example of all sensor measurements from taken during on load cycle is provided in Appendix A (Figure A.13).

In addition, an FWD test campaign was carried out on sections S1, S2, S3, and S4 to provide supplementary data for future analysis. Furthermore, AC cores were taken from S6, and a single core was tested in the laboratory at the Danish Technological Institute (in Denmark) to characterize the VE properties of the AC. This data can also serve as input for subsequent model analysis, as a similar AC was used in S1, S2, S3, and S4.

3.3.3 Test areas in Switzerland

Two instrumented pavement systems in Switzerland were also involved in this PhD project. One system was part of a district road connecting the two cities La Ferrière and La Cibourg, and the other was located in the city of Neuchâtel as part of the inner city road network. Both systems were entirely funded by S&P Switzerland as part of the Innosuisse project, entitled: Development of asphalt pavement structures reinforced with embedded composite grids. The two pavement systems were designed by a pavement research group at Bern University of Applied Sciences and the engineering team of S&P Switzerland. As part of the research activities, the PhD project team was invited to collect data from embedded sensors installed in both test areas.

Test setup in La Ferrière

The entire test area near La Ferrière considers a district road of two lanes (one in each direction). Figure 3.23 provides a google earth snapshot of the test area. It consists of three sections – one section (C) including Carbophalt®G 200/200, one section (G) including Glasphalt®G, and one reference section (R) without AGR. Both AGR products were provided by S&P (similar to those used in Subsection 3.3.1 and 3.3.2), and were installed in one of the two lanes, i.e., in the direction from north to south.

All sections were built in September 2019 (prior to this PhD project) as part of a reconstruction of the existing district road between La Ferrière and La Cibourg. The reason for maintenance was due to the presence of structural distresses such as cracks and layer debonding. Specifically, 120 mm of the existing 210 mm thick AC structure was milled and repaved with a new support lift of 80 mm and a new wearing course of 40 mm as depicted in Figure 3.24. In both reinforced sections, the AGR was placed at the interface between the existing AC and the new support lift. To identify the deeper layer composition, a DCP test was carried out in each test section. Results revealed that the entire AC structure was supported by an unbound granular base layer with an approximate thickness of 400 mm. An additional soil layer was identified, sandwiched between the granular base layer and the local bedrock.
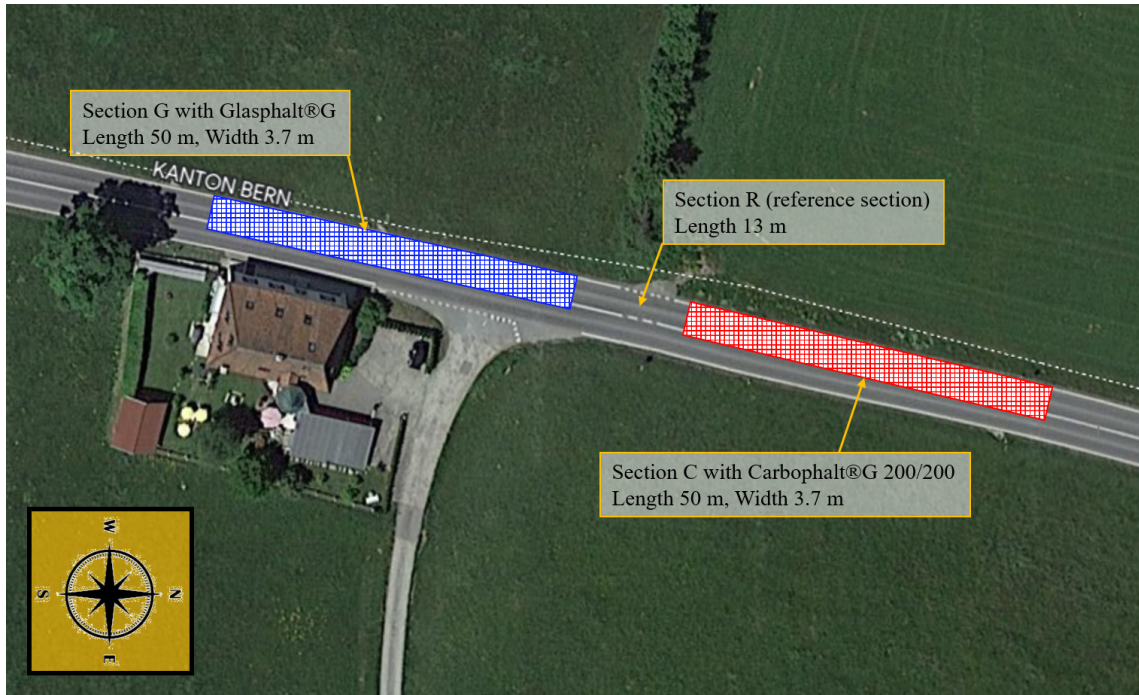
Figure 3.23: Overview of the test sections in La Ferrière.
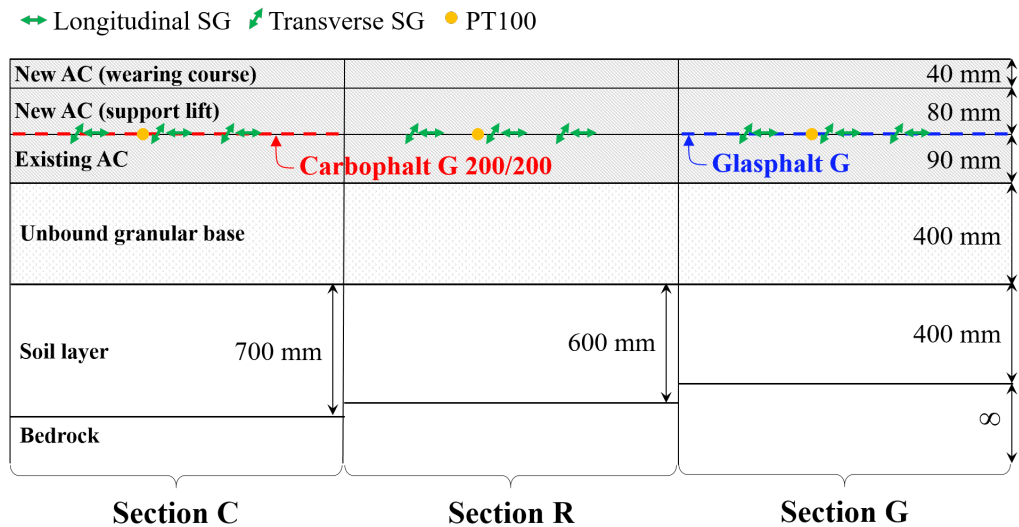
Figure 3.24: Cross-sectional view of the three instrumented sections in La Ferrière.

In each test section, two types of sensors were embedded inside the pavement system, i.e., ASGs and PT100s (identical to those utilized in DTU Smart Road). The sensors were placed on top of the AGR in reinforced sections, whereas the sensors were placed at the interface between the existing AC and the new support lift in the unreinforced section. All sensor installation depths are indicated in Figure 3.24. Specifically, three longitudinal ASGs, three transverse ASGs, and one PT100 were placed in each test section with the sensor arrangement presented in Figure 3.25. They were arranged in a line along the traveling direction to capture the strain response directly under the traffic left-side wheel paths.
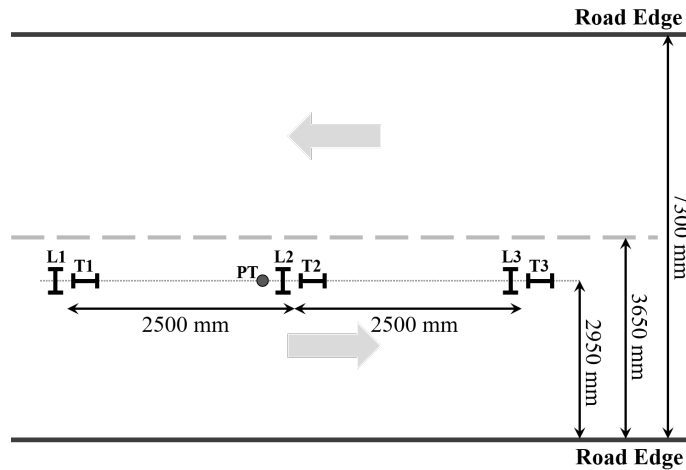
Figure 3.25: Top view layout of embedded sensor arrangement in a single test section in La Ferrière, where L: longitudinal ASG, T: transverse ASG, and PT: PT100.

Test setup in Neuchâtel

The test area in Neuchâtel was part of an inner city road of four lanes (two in each direction). In each direction, the road is divided into a bus lane and a normal lane. Figure 3.26 provides a top view (taken from google maps) of the test area. The tested area consists of three sections – one section (C) including Carbophalt®G 200/200 grids, one section (G) installed with Glasphalt®G grids, and one section (R) without AGR serving as a reference section. AGRs were installed in one of the bus lanes, i.e., in the direction of west to east.
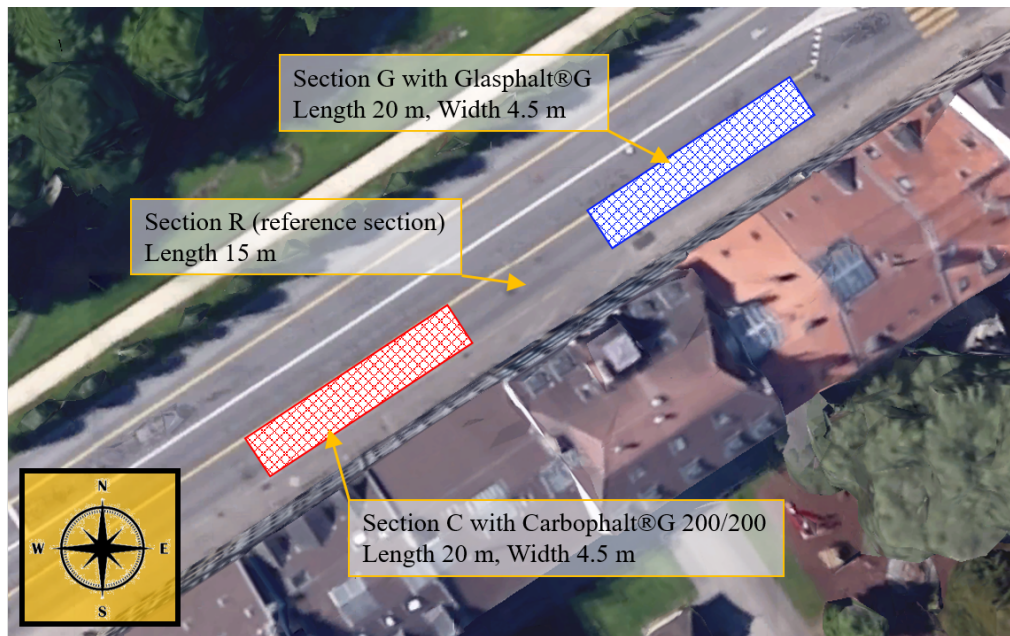
Figure 3.26: Overview of the test sections in Neuchâtel.

All sections were built in August 2020 as part of a full-depth reconstruction of the existing city road. A cross-sectional view of the considered pavement structures is depicted in Figure 3.27. Accordingly, all existing AC was milled and replaced by five AC lifts with a total thickness of 260 mm, illustrated in Figure 3.27. In both reinforced sections, the

AGR was placed at the interface between two AC lifts located 140 mm from the pavement surface. Due to restrictions, the entire research group was not allowed to perform DCP tests on the current test sections. Thus, the configuration of deeper granular/soil layers was unknown.
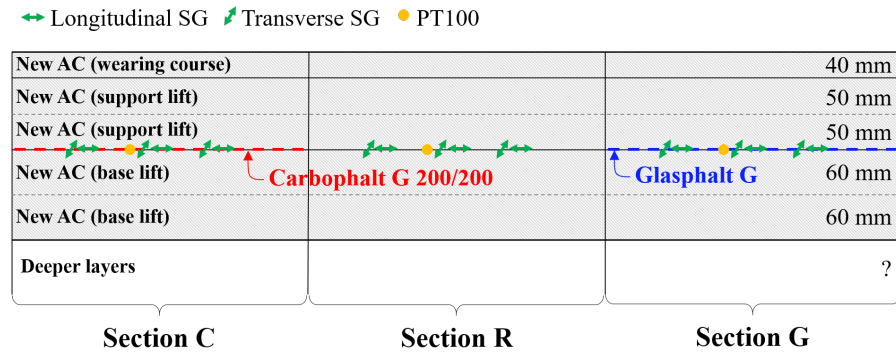
Figure 3.27: Cross-sectional view of the three instrumented sections in Neuchâtel.

In each test section, two types of sensors were embedded inside the pavement system, i.e., ASGs and PT100s (identical to those utilized in DTU Smart Road and La Ferriere). The sensor installation depths are shown in Figure 3.27, indicating that sensors were also located 140 mm from the pavement surface (between two AC lifts). In this context, the sensors were installed on top of the AGR8 in reinforced sections. Specifically, three longitudinal ASGs, three transverse ASGs, and one PT100 were placed in each test section according to the top view representation in Figure 3.28. The ASGs were arranged in a line along the traveling direction to capture the strain response directly under the traffic right-side wheel paths.
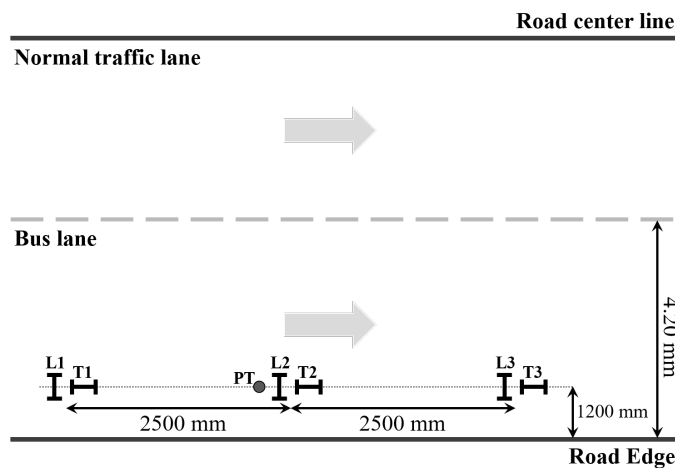
Figure 3.28: Top view layout of embedded sensor arrangement in a single test section at Neuchâtel, where L: longitudinal ASG, T: transverse ASG, and PT: PT100.

Measurement campaigns

A total of two measurement campaigns based on moving vehicles were performed in Switzerland. The first campaign was carried out in August 2020 at the test area near La Ferrière. The campaign involved collecting data from the embedded sensors, as well as from deployable roadside sensors, in all three test sections G, C, and R. Sensor readings were triggered by several passages from a heavy two-axle truckload depicted in Figure

3.29(a). The truck was equipped with a water tank that was filled at three different levels, i.e., empty, half full, and full; this was to test for different variations in load levels. During the measurement campaign, all three sections were tested simultaneously by recording sensor responses as the truck passed by. Several vehicle speeds, ranging from 10 km/h to 70 km/h, and three different lateral vehicle positions were targeted. In-pavement temperatures and surface temperatures were recorded, indicating AC temperatures varying from 15℃ to 30℃ during the campaign (from start to end). As part of the campaign, two types of deployable surface sensors were added to the test setup to provide supplementary response information. The two sensor types were uniaxial accelerometers and dual-axis tiltmeters. A total of four accelerometers and two tiltmeters were fixed to the pavement according to Nielsen et al. 2020 and Nielsen 2019. The accelerometers measured the vertical surface accelerations, whereas the tiltmeters measured the surface rotations around the longitudinal and transverse load-traveling directions. An example of all sensor measurements taken during a single pass in the La Ferrière campaign is provided in Appendix A (Figure A.18).

(a)   (b)

Figure 3.29: Trucks utilized in test campaigns in: (a) La Ferrière and (b) Neuchâtel.

A second measurement campaign was carried out later in August 2020 at the test area in Neuchâtel (short after construction). In this campaign, a four-axle truck was utilized (see Figure 3.29(b)); it was also equipped with a water tank that was filled at two load levels, i.e., empty and full. During the measurement campaign, all three sections were tested simultaneously by recording ASG responses as the truck passed by. Several vehicle speeds, ranging from 10 km/h to 40 km/h, and one lateral vehicle position were targeted. In-pavement temperatures and surface temperatures were recorded, indicating a constant AC temperature of about 23℃ during the entire campaign. No surface sensors were allowed to be installed during the test campaign. An example of ASG measurements from a single pass in the Neuchâtel campaign is provided in Appendix A (Figure A.21).

Moreover, some additional tests were carried out at the test area near La Ferrière. This involved FWD tests and AC coring in all three test sections. With respect to the latter, a total of six AC cores were taken from the La Ferrière test area (two in each section) and used for subsequent laboratory testing. Specifically, one core from section R was used to characterize the VE properties of all AC lifts, i.e., the existing AC, the support layer, and the wearing course. These properties should serve as model input for any future model validation efforts. The final five cores were utilized for testing interface bonding conditions (between AC lifts) using the Leutner test setup (Collop et al. 2003). However, as the core interfaces are sheared under monotonic loading until failure in the Leutner setup, load-

displacement histories are not deemed suitable for estimating an interface bonding stiffness (discussed in Paper iv). Similar FWD tests and AC coring procedures were not conducted in the Neuchâtel test section due to limited accessibility.

3.3.4 Contribution

The experimental investigations related to the four covered test facilities contribute to the overall dissertation by providing experimental data for subsequent model validation addressed in the first study objective (O1). Specifically, the data from the HYSTER forklift campaign, together with the FWD measurements, carried out on S-0 and S-1 at DTU Smart Road are utilized in Paper iii for model validation. The remaining test facilities and test campaigns are not part of the appended papers but have also provided essential data that can later be used to support the overall model validation of GRIDPAVE. Alternatively, the test facilities and the collected data can also be utilized to provide experimental evidence for other model validation purposes.

Conclusion

4.1   Summary

Motivated by the necessity for a ME design method that can be applied to grid-reinforced asphalt pavements including AGR, two study objectives were outlined in this PhD dissertation: (O1) to develop a versatile, useful, and validated computational model that can produce mechanistic responses in asphalt pavement with AGR, and (O2) to gain valuable insights into the effects of AGR.

In light of this, a model formulation was first developed by extending the standard LET framework to include the following model-components: (i) FLs; (ii) imperfect bonding conditions; (iii) viscoelasticity, (iv) moving loads, and (v) AGR. The AGR model-component was formulated as a combination of three contributions: (a) including the AGR as a thin high-modulus elastic layer within the pavement system – characterized by an effective thickness, Young's modulus, and Poisson's ratio; (b) accounting for the AGRs influence on interface bonding between its neighboring layers – characterized by two horizontal spring stiffness parameters; and (c) the AGR's impact on the surrounding AC properties – characterized by a ZoI thickness and a κ-factor. With respect to (b) and (c), the horizontal spring stiffness parameters and the κ-factor were deemed related to the AGR geometry and the asphalt mix properties, defined by the so-called EAS-NMAS ratio. In total, seven modeling inputs were required to represent an AGR.

Hereafter, the formulation was implemented into the computational code GRIDPAVE-MM. The implementation was based on the elastic part of ALVA, which was extended to include FLs, VE, and multiple moving loads. The numerical considerations in GRIDPAVE were focused on minimizing the computational effort, and the overall code implementation was subsequently confirmed in a model verification effort.

Next, several experimental campaigns were carried out for subsequent model validation of GRIDPAVE. These campaigns involved full-scale testing at several test facilities, where embedded sensors were used to collect pavement responses triggered by moving load applications. The testing facilities included DTU Smart Road at DTU campus in Kgs. Lyngby (Denmark), an APT facility located at UTA in Arlington (Texas), and two public roads near La Ferrière and Neuchâtel in Switzerland. Collected field responses from DTU Smart Road were subsequently compared against model simulations to showcase GRIDPAVE's ability to match embedded sensor readings. This was done for two nominal identical pavement systems – one including AGR and one excluding AGR. As part of the validation effort, model inputs were either assessed via supplementary field and laboratory testing or calibrated through embedded sensor data.

Finally, GRIDPAVE was utilized to forecast the AGR effects on critical key responses throughout several synthetic investigations (i.e., purely based on model simulations).

These investigations considered different pavement structural compositions that simulated both new and milled-and-overlaid systems, as well as different AGR locations within the AC. Also, a specific study was dedicated to investigating the AGR effect on interface properties.

4.2 Findings and implications

First sturdy objective (O1)

Concerning the first study objective (O1), the developed computational model GRIDPAVE was capable of simulating mechanistic pavement responses that arise from the inclusion of AGR. The developed model is versatile in the sense that it can emulate a variety of different pavement scenarios. Specifically, the model can: (i) emulate responses within new or rehabilitated asphalt pavement systems (including undamaged and damaged layers), (ii) handle any desirable number of layers with either elastic or time-temperature-dependent properties, (iii) account for imperfect bonding conditions between layers (which can also be time-temperature dependent), (iv) simulate realistic traffic loading with any desired load configuration, and (v) include AGRs of any desired geometry, material composition, and location within the AC. With respect to the latter, the model should not be limited to AGR but could potentially include reinforcement types that are designed for deeper granular layers (e.g. geosynthetics). In case the reinforcement is placed in an "elastic" layer (usually assumed for unbound granular materials), the κ-factor becomes a multiplication factor on the adjacent ZoI layer moduli, which must be corrected for load speed and temperature conditions. However, further model validation is essentially needed to approve this feature. As a final point regarding model versatility, GRIDPAVE can also be used for general design purposes without AGR. In this context, GRIDPAVE includes the model components FL, imperfect bonding, VE, and multiple moving loads, which have not been combined in one single LET-based tool up until this point.

Moreover, GRIDPAVE has been proven to be a numerically stable and computationally efficient modeling tool based on model inputs that all can be assessed through experimental work. Numerical stability and accuracy were showcased in a model verification effort, whereas the assessment of model inputs was demonstrated through laboratory testing and full-scale calibration. Specifically for AGR-related inputs, the effective thickness, Young's modulus, and Poisson's ratio were all provided by the manufacturer; the two horizontal interface stiffness were characterized in the laboratory using the DDST; and the ZoI thickness (taken as three times the NMAS) and the κ-factor were assessed through inverse analysis using field measurements from the DTU Smart Road. Overall, numerical stability and accuracy, high computational efficiency, and accessible model inputs ensure model usefulness.

Finally, GRIDPAVE's ability to accurately simulate pavement responses was demonstrated through model verification and model validation. The verification process involved comparing GRIDPAVE simulations with those of existing modeling tools and benchmark solutions. Model validation was achieved through experiments conducted on a full-scale level, where GRIDPAVE simulations were compared against embedded sensor readings from the DTU Smart Road test facility. In all cases, the model's ability to reproduce benchmark simulations and field measurements was deemed successful.

Second study objective (O2)

With respect to the second study objective (O2), the verified and validated GRIDPAVE model was utilized to increase the understanding of the AGR effect throughout several synthetic investigations. In general, the synthetic investigations indicated that the pres-

ence of AGR could reduce horizontal tensile strains near the grid and, to a lesser degree, vertical strains at the top of the supporting UGS. The AGR effects were particularly noticeable under high-temperature/slow-speed conditions and were less pronounced under low-temperature/high-speed conditions, thereby indicating that the AGR effect is time-temperature dependent. However, the effect on subgrade strains and surface deflections was generally marginal. It was also demonstrated that the above effects were larger for a higher effective AGR modulus or for deeper AGR locations within the AC structure – optimal at the AC bottom. Lastly, results indicated that the presence of AGR could negatively affect the interface bonding conditions between two AC layers but still provide beneficial reinforcement effects overall.

Overall, the above findings implied that adding AGR to asphalt pavement systems can be beneficial for combating fatigue cracking and rutting. These implications supported existing literature (Ong et al. 2004; Khodaii et al. 2009b; Nguyen et al. 2013; J. Lee et al. 2015; Correia and Zornberg 2016; Arsenie et al. 2017; Vinay Kumar and Saride 2017; Correia and Zornberg 2018), and suggests that the utilization of AGR products can potentially extend the overall pavement service life. At the same time, findings also implied that it could be practically difficult to monitor any AGR effects with surface measurement techniques, such as the FWD test, moving measurement platforms (Baltzer et al. 2010; Skar et al. 2020b), or deployable surface sensors (Nielsen et al. 2020; Skar et al. 2020c; Levenberg et al. 2022).

4.3 Limitations

While this study has provided a versatile, useful, and validated modeling framework and highlighted many benefits and practical applications of AGR in asphalt pavement, it is important to acknowledge some study limitations associated with the overall work.

Regarding the modeling framework, one limitation is that the developed model cannot handle non-linear behavior associated with unbound materials, interface bonding conditions between AC layers, and the ZoI effect. Furthermore, the model cannot handle viscoplastic behavior associated with AC, as well as pavement edge effects (given that layers are assumed horizontally uniform and infinite in the LET). Ultimately, these missing features may limit the model's versatility and correctness. While these features could be emulated using finite element analysis, it would require significant computational resources and increase the number of model inputs in order to improve model accuracy. With the current computer technology, such an approach would (in most cases) be impractical for engineering purposes.

Concerning the model validation effort, it was challenging to estimate the precise distance (within centimeters) between embedded sensors and passing vehicles during measurement campaigns, thus making it difficult to reproduce the exact loading event. Furthermore, some embedded ASG readings included signal drift, which the model can not (and should not) reproduce. Overall, these limiting aspects may introduce some uncertainties to the provided model validation effort. However, since the model was able to consistently obtain a satisfactory fit across multiple measured and model-predicted responses (with different locations and orientations), the current model validation effort is deemed acceptable and strong in confirming the model formulation and implementation.

Another limitation regarding model validation is related to the FL model-component, which has not been experimentally investigated in this study (nor in the existing literature). Consequently, using the FL model-component to emulate crack AC layers might not be valid (until proven otherwise).

Lastly, with respect to the characterization of the κ-factor and the ZoI thickness, the proposed model calibration technique (based on inverse analysis and field measurements) is rather expensive and impractical on a full-scale level. In order to improve model usefulness, new methods on a laboratory scale are therefore needed to assess these model inputs for different AGR products or pavement materials. Nonetheless, from an engineering perspective, it is always possible to make a conservative estimate by excluding the ZoI-effect (i.e., selecting $\kappa = 1$).

4.4 Future work

To further improve the computational code GRIDPAVE, several aspects could be investigated, starting with the model formulation. Specifically, it could be beneficial to include horizontal loads in the modeling framework and study the associated AGR effects, e.g., under a load-breaking event. A suitable mathematical formulation for horizontal loads (within the LET framework) can be found in Maina and Matsui 2004 or Kimura 2014.

With respect to model validation, data from various sources, such as the unpublished experimental efforts carried out at DTU Smart Road, the APT facility at UTA, and the test areas in Switzerland, could be used to reinforce the validation of GRIDPAVE. In this context, Ramboll's Raptor surface measurements and deployable surface sensor readings (e.g., from accelerometers, tiltmeters, and LVDTs) could be used to confirm that the AGR effect is marginal on pavement deflections while simultaneously showing that the AGR reduces horizontal strains inside the AC. Investigating the reinforcement effect under lower AC temperatures and faster loading speeds could also provide valuable insights into the AGR model-component. Given that data has already been collected under various load configurations, grid locations, load speeds, temperature conditions, and pavement structural compositions (see Subsection 3.3), this can be leveraged for future model validation efforts.

Another research aspect should be to validate the FL model-component for modeling cracked/damaged layers. This requires building a new full-scale pavement system that includes either cracked AC layers or paving blocks. Here, the model could serve as a guideline for designing such experimental setups. Moreover, full-scale tests involving reinforcing geosynthetic products buried in deeper soil layers (such as geogrids) could also be designed and analyzed using GRIDPAVE, and the measurements could be used to validate GRIDPAVE's applicability to such cases.

Other aspects for future investigations concern the assessment of model inputs associated with the AGR model-component. A practical laboratory setup to characterize the ZoI thickness and the κ-factor is necessary to improve the model's usefulness. This setup could also be used to examine the influence of the EAS-NMAS ratio on κ. Moreover, interface bonding conditions could be examined at full-scale by installing LVDTs inside core-drilled holes and monitoring diameter changes just above and below interfaces (inspired by the LVDT setup at UTA or in Skar et al. 2020c). This information could help examine any interconnection between the two horizontal stiffness inputs associated with the AGR (i.e., in relation to the BMs discussed in Paper iv). Additionally, testing more cores in the laboratory for statistical significance or for different EAS-NMAS ratios could provide more comprehensive insight into the AGR's influence on interface bonding conditions. Overall, these contributions should enhance the model's potential for practical applications as they (most likely) will improve the understanding of model inputs associated with AGR.

4.5   Study contributions

The present dissertation successfully addresses the two study objectives (O1) and (O2). (O1) was met by providing an analytic tool (in the form of GRIDPAVE), which can enable engineers, consultants, and contractors to prescribe an AGR alternative within asphalt pavements. In addition, manufacturers can use the tool to improve existing AGR products, as well as develop new/future products. GRIDPAVE integrates all pertinent effects of AGR in one single mechanistic framework, representing the first model of its kind to comprehensively address this issue.

Furthermore, this PhD study addressed (O2) by providing considerable insight into the research field dealing with AGR, highlighting the reinforcement effects from a modeling perspective. The findings have confirmed some beneficial aspects of AGR on pavement performance related to fatigue cracking and rutting distresses. Moreover, the study has revealed that the presence of AGR can have a marginal effect on surface deflections, which is crucial knowledge with respect to surface testing. These findings warn that AGR effects might not always be detectable using surface testing techniques while still being beneficial.

Finally, the study has collected experimental data that can be used to validate not only GRIDPAVE but also other pavement modeling tools. In this context, the data provides a valuable resource for future model development. Ultimately, this dissertation significantly advances the knowledge and mechanistic impression of AGR in asphalt pavements, contributing to the sustainability and longevity of infrastructure systems.

Bibliography

AASHTO (2008). *Mechanistic-Empirical Pavement Design Guide: A Manual of Practice.* Interim. American Association of State Highway and Transportation Officials. URL: https://fenix.tecnico.ulisboa.pt/downloadFile/563568428712666/AASHTO08.pdf.

ARRB Transport Research (2004). *Pavement Design: A Guide to the Structural Design of Road Pavements.* Tech. rep. URL: https://subdirektoratgpd.files.wordpress.com/2019/08/austroads-pavement-design-a-guide-to-the-structural-design-of-road-pavements-2004.pdf.

Arsenie, I. M., Chazallon, C., Duchez, J. L., and Hornych, P. (2017). "Laboratory characterisation of the fatigue behaviour of a glass fibre grid-reinforced asphalt concrete using 4PB tests". *Road Materials and Pavement Design* 18.1, 168–180. DOI: 10.1080/14680629.2016.1163280.

Asphalt Academy (2022). *Technical Guideline - Asphalt Reinforcement for Road Construction.* Tech. rep. January. URL: https://www.sabita.co.za/wp-content/uploads/2022/02/tg3-february-2022.pdf.

ASTM D2487 (2017). *Standard Practice for Classification of Soils for Engineering Purposes (Unified Soil Classification System).*

ASTM D4694 (2009). *Standard test method for deflections with a falling-weight-type impulse load device.* DOI: 10.1520/D4694-09R20.

ASTM D6951/D6951M (2018). *Standard Test Method for Use of the Dynamic Cone Penetrometer in Shallow Pavement Applications.* DOI: 10.1520/D6951{_}D6951M-18.

Athanasiadis, N. and Zoulis, P. (2019). *Viscoelastic pavement modeling for use with the Dynatest Raptor.* URL: https://findit.dtu.dk/en/catalog/5d3d83d0d9001d32f558c270.

Austin, R. (Mar. 1996). "Enhanced performance of asphalt pavements using geocomposites". *Geotextiles and Geomembranes* 14.3-4, 175–186. DOI: 10.1016/0266-1144(96)00007-6.

Baltzer, S., Pratt, D., Weligamage, J., Adamsen, J., and Hildebrand, G. (2010). "Continuous bearing capacity profile of 18,000 km Australian road network in five months". In: *ARRB Conference 24th.* Melbourne, Australia.

Bondt, A. H. de (1999). "Anti-reflective cracking design of (reinforced) asphaltic overlays". PhD thesis. Delft University of Technology. URL: http://resolver.tudelft.nl/uuid:130b757f-436d-4ee0-a15a-e07b132f4f1a.

Burmister, D. M. (1943). "The Theory of Stresses and Displacements in Layered Systems and Applications to the Design of Airport Runways". In: *Highway Research Board, Vol. 23,* pp. 126–148. URL: https://onlinepubs.trb.org/Onlinepubs/hrbproceedings/23/23-016.pdf.

Burmister, D. M. (Mar. 1945a). "The General Theory of Stresses and Displacements in Layered Soil Systems. II". *Journal of Applied Physics* 16.3, 126–127. DOI: 10.1063/1.1707562.

Burmister, D. M. (May 1945b). "The General Theory of Stresses and Displacements in Layered Soil Systems. III". *Journal of Applied Physics* 16.5, 296–302. DOI: 10.1063/1.1707590.

Burmister, D. M. (Feb. 1945c). "The General Theory of Stresses and Displacements in Layered Systems. I". *Journal of Applied Physics* 16.2, 89–94. DOI: 10.1063/1.1707558.

Chen, F., Song, M., Ma, X., and Zhu, X. (June 2019). "Assess the impacts of different autonomous trucks' lateral control modes on asphalt pavement performance". *Transportation Research Part C: Emerging Technologies* 103, 17–29. DOI: 10.1016/j.trc.2019.04.001.

Cleveland, G. S., Button, J. W., and Lytton, R. L. (2001). *Geosynthetics in Flexible and Rigid Pavement*. Tech. rep. URL: http://www.scribd.com/doc/136341942/Geosynthetics-in-Flexible-and-Rigid-Pavement#scribd.

Collop, A. C., Thom, N. H., and Sangiorgi, C. (Nov. 2003). "Assessment of bond condition using the Leutner shear test". *Proceedings of the Institution of Civil Engineers - Transport* 156.4, 211–217. DOI: 10.1680/tran.2003.156.4.211.

Correia, N. S. and Zornberg, J. G. (June 2016). "Mechanical response of flexible pavements enhanced with geogrid-reinforced asphalt overlays". *Geosynthetics International* 23.3, 183–193. DOI: 10.1680/jgein.15.00041.

Correia, N. S. and Zornberg, J. G. (Feb. 2018). "Strain distribution along geogrid-reinforced asphalt overlays under traffic loading". *Geotextiles and Geomembranes* 46.1, 111–120. DOI: 10.1016/j.geotexmem.2017.10.002.

EAPA and NAPA (2011). *The Asphalt Paving Industry: A Global Perspective*. Tech. rep. European Asphalt Pavement Association. URL: http://www.asphaltpavement.org/images/stories/GL_101_Edition_3.pdf.

Elfa Distrelec (2014). *HSENS/101/B-P0101438*. URL: https://www.elfadistrelec.no/Web/Downloads/_t/ds/Atexis_UK02_PT100_eng_tds.pdf.

EN 12697-26C (2022). *Bituminous mixtures - Test methods - Part 26: Stiffness*.

Geokon (2023). *Model 3500 Series Earth Pressure Cells*. URL: https://www.geokon.com/content/manuals/3500_Earth_Pressure_Cells.pdf.

GEUS (1986). *DGUnr 201. 3760 Brøndborers boringsnr.: B6 (Danish)*. URL: https://data.geus.dk/JupiterWWW/borerapport.jsp?dgunr=201.3760.

Goodman, J. R. and Popov, E. P. (Nov. 1968). "Layered Beam Systems with Interlayer Slip". *Journal of the Structural Division* 94.11, 2535–2548. DOI: 10.1061/JSDEAG.0002116.

Hansen, L. M. F., Kindler, R. B., and Brøndmark, J. L. (2023). *Investigation of asphalt pavements loaded by heavy off-road vehicles*. URL: https://findit.dtu.dk/en/catalog/63f56b6594ebad91f72e7a03.

Huang, Y. H. (2004). *Pavement Analysis and Design (Second edition)*, p. 775. URL: http://docshare04.docshare.tips/files/14013/140138713.pdf.

Khodaii, A., Fallah, S., and Moghadas Nejad, F. (Feb. 2009a). "Effects of geosynthetics on reduction of reflection cracking in asphalt overlays". *Geotextiles and Geomembranes* 27.1, 1–8. DOI: 10.1016/j.geotexmem.2008.05.007.

Khodaii, A., Fallah, S., and Moghadas Nejad, F. (Feb. 2009b). "Effects of geosynthetics on reduction of reflection cracking in asphalt overlays". *Geotextiles and Geomembranes* 27.1, 1–8. DOI: 10.1016/j.geotexmem.2008.05.007.

Kimura, T. (2014). "Studies on stress distribution in pavements subjected to surface shear forces". *Proceedings of the Japan Academy Series B: Physical and Biological Sciences* 90.2, 47–55. DOI: 10.2183/pjab.90.47.

Kyowa Electronic Instruments (2022). *KM Series Embedded Strain Gages*. URL: https://www.kyowa-ei.com/eng/product/category/strain_gages/km/index.html.

Lee, J. H., Baek, S. B., Lee, K. H., Kim, J. S., and Jeong, J. H. (2019). "Long-term performance of fiber-grid-reinforced asphalt overlay pavements: A case study of Korean national highways". *Journal of Traffic and Transportation Engineering (English Edition)* 6.4, 366–382. DOI: 10.1016/j.jtte.2018.01.008.

Lee, J., Kim, Y. R., and Lee, J. (2015). "Rutting performance evaluation of asphalt mix with different types of geosynthetics using MMLS3". *International Journal of Pavement Engineering* 16.10, 894–905. DOI: 10.1080/10298436.2014.972916.

Leischner, S., Canon Falla, G., Gerowski, B., Rochlani, M., and Wellner, F. (2019). "Mechanical Testing and Modeling of Interlayer Bonding in HMA Pavements". *Transportation Research Record* 2673.11, 879–890. DOI: 10.1177/0361198119843254.

Levenberg, E. (June 2013). "Inverse analysis of viscoelastic pavement properties using data from embedded instrumentation". *International Journal for Numerical and Analytical Methods in Geomechanics* 37.9, 1016–1033. DOI: 10.1002/nag.1132.

Levenberg, E. (2015). "Backcalculation with an Implanted Inertial Sensor". *Transportation Research Record: Journal of the Transportation Research Board* 2525.1, 3–12. DOI: 10.3141/2525-01.

Levenberg, E. (2016). "Viscoelastic Pavement Modeling With a Spreadsheet". In: *Proceedings of the Eighth International Conference on Maintenance and Rehabilitation of Pavements*. Singapore: Research Publishing Services, pp. 746–755. DOI: 10.3850/978-981-11-0449-7-132-cd.

Levenberg, E. (2020). *Pavement Mechanics: Lecture Notes*. 1st ed. DOI: 10.11581/dtu:00000088.

Levenberg, E., Jensen, P. K., and Nielsen, J. (2022). "The dynamic cone penetrometer as a seismic source for geophysical exploration in urban". In: *11th International Symposium on Field Monitoring in Geomechanics*. URL: https://www.issmge.org/uploads/publications/80/112/7._Levenberg_et.al.pdf.

Levenberg, E. and Michaeli, N. (2013). "Viscoelastic characterisation of asphalt-aggregate mixes in diametral compression". *Road Materials and Pavement Design* 14.SUPPL.1, 105–119. DOI: 10.1080/14680629.2013.774749.

Levenberg, E. and Skar, A. (Mar. 2022). "Analytic pavement modelling with a fragmented layer". *International Journal of Pavement Engineering* 23.4, 1108–1120. DOI: 10.1080/10298436.2020.1790559.

Maina, J. W. and Matsui, K. (2004). "Developing software for elastic analysis of pavement structure responses to vertical and horizontal surface loadings". *Transportation Research Record* 1896, 107–118. DOI: 10.3141/1896-11.

Minguela, J. D. and Muñoz, C. B. (2019). "Impact of Electric and Autonomous Conduction on Pavements". In: *26th World Road CongressWorld Road Association (PIARC)*.

Neumann, J. E. et al. (2021). "Climate effects on US infrastructure: the economics of adaptation for rail, roads, and coastal development". *Climatic Change* 167. DOI: 10.1007/s10584-021-03179-w.

Nguyen, M. L., Blanc, J., Kerzrého, J. P., and Hornych, P. (2013). "Review of glass fibre grid use for pavement reinforcement and APT experiments at IFSTTAR". *Road Materials and Pavement Design* 14.SUPPL.1, 287–308. DOI: 10.1080/14680629.2013.774763.

Nielsen, J. (2019). *Inferring pavement layer properties from roadside sensors*. URL: https://findit.dtu.dk/en/catalog/5e089811d9001d578f5d17c7.

Nielsen, J. and Levenberg, E. (2022). "Full-scale validation of a mechanistic model for asphalt grid reinforcement". *Submitted to the International Journal of Pavement Engineering* December.

Nielsen, J., Levenberg, E., and Skar, A. (2020). "Inference of Pavement Properties with Roadside Accelerometers". In: *Proceedings of the 9th International Conference on Maintenance and Rehabilitation of Pavements—Mairepav9*. Vol. 76, pp. 719–728. URL: http://link.springer.com/10.1007/978-3-030-48679-2_67.

Nielsen, J., Levenberg, E., and Skar, A. (2022). "Mechanistic modelling of grid-reinforced milled-and-overlaid asphalt pavements". *International Journal of Pavement Engineering* May. DOI: 10.1080/10298436.2022.2072502.

Nithin, S., Rajagopal, K., and Veeraragavan, A. (Dec. 2015). "State-of-the Art Summary of Geosynthetic Interlayer Systems for Retarding the Reflective Cracking". *Indian Geotechnical Journal* 45.4, 472–487. DOI: 10.1007/s40098-015-0161-7.

Noorvand, H., Karnati, G., and Underwood, B. S. (Jan. 2017). "Autonomous Vehicles". *Transportation Research Record: Journal of the Transportation Research Board* 2640.1, 21–28. DOI: 10.3141/2640-03.

OECD (2023). *Freight transport (indicator)*. DOI: 10.1787/708eda32-en. URL: https://data.oecd.org/transport/freight-transport.htm#indicator-chart.

Omega Engineering Limited (2017). *KFH Series Pre-wired strain gauges*. URL: https://br.omega.com/omegaFiles/pressure/pdf/KFH.pdf.

Ong, G. P., Fwa, T. F., and Tan, S. A. (2004). "Laboratory Evaluation of Rutting Resistance of Geosynthetics Reinforced Asphalt Pavement". *Transportation* 44.2, 29–44.

Osyczka, A. (Sept. 1978). "An approach to multicriterion optimization problems for engineering design". *Computer Methods in Applied Mechanics and Engineering* 15.3, 309–333. DOI: 10.1016/0045-7825(78)90046-4.

Peutz, M. G., Van Kempen, H. P., and Jones, A. (1968). "Layered systems under normal surface loads". *Highway Research Record* 228. URL: http://onlinepubs.trb.org/onlinepubs/hrr/1968/228/228-004.pdf.

Qiao, Y., Guo, Y., Stoner, A. M., and Santos, J. (May 2022). "Impacts of future climate change on flexible road pavement economics: A life cycle costs analysis of 24 case studies across the United States". *Sustainable Cities and Society* 80. DOI: 10.1016/j.scs.2022.103773.

S&P Clever Reinforcement Company AG (2020). *Application Instructions S&P Asphalt Reinforcement*. URL: https://www.sp-reinforcement.eu/sites/default/files/field_product_installation_file/applikationsanleitung_maschinell_eu_en_ver202012.pdf.

S&P Clever Reinforcement Company AG (2023a). *S&P Carbophalt ® G 200/200*. URL: https://p.widencdn.net/rx8gq5/R_CarbophaltG200200_Pub_Tds_Prod___EN_EN.

S&P Clever Reinforcement Company AG (2023b). *S&P Glasphalt ® G*. URL: https://p.widencdn.net/th7sfr/R_GlasphaltG_Pub_Tds_Prod___EN_EN.

Sanders, P. J. (2001). "Reinforced asphalt overlays for pavements". PhD thesis. University of Nottingham. URL: https://eprints.nottingham.ac.uk/12221/1/368938.pdf.

Saride, S. and Kumar, V. (June 2017). "Influence of geosynthetic-interlayers on the performance of asphalt overlays on pre-cracked pavements". *Geotextiles and Geomembranes* 45.3, 184–196. DOI: 10.1016/j.geotexmem.2017.01.010.

Schapery, R. (1962). "Approximate Methods of Transform for Viscoelastic Stress Analysis". In: *Proceedings 4th US National Congress on Applied Mechanics*, pp. 1075–1085.

Shell (1978). *Shell Pavement Design Manual: Asphalt Pavements and Overlays for Road Traffic*. Tech. rep.

Shook, J. F., Finn, F. N., Witczak, M. W., and L., M. C. (1982). "Thickness design of asphalt pavements-the asphalt institute method". In: *Proceedings, 5th International Conference on Structural Design of Asphalt Pavements, Delft University of Technology, The Netherlands, 1982*, Volume 1.

Skar, A. (2021). *ALVA*. DOI: https://doi.org/10.11583/DTU.12387305.v7. URL: https://github.com/asmusskar/ALVA.

Skar, A. and Andersen, S. (2020). "ALVA: An adaptive MATLAB package for layered viscoelastic analysis". *Journal of Open Source Software* 5.55, 2548. DOI: 10.21105/joss.02548.

Skar, A., Andersen, S., and Nielsen, J. (2020a). *Adaptive Layered Viscoelastic Analysis (ALVA)*. DOI: https://doi.org/10.11583/DTU.12387305.v7. URL: https://data.dtu.dk/articles/software/ALVA/12387305.

Skar, A., Levenberg, E., Andersen, S., and Andersen, M. (2020b). "Analysis of a moving measurement platform based on line profile sensors for project-level pavement evaluation". *Road Materials and Pavement Design* 0.0, 1–17. DOI: 10.1080/14680629.2020. 1741429.

Skar, A., Nielsen, J., and Levenberg, E. (2020c). "Pavement instrumentation with near surface LVDTs". In: *Advances in Materials and Pavement Performance Prediction II*, pp. 232–235. DOI: 10.1201/9781003027362-55.

Solatiyan, E., Bueche, N., and Carter, A. (Oct. 2020). "A review on mechanical behavior and design considerations for reinforced-rehabilitated bituminous pavements". *Construction and Building Materials* 257, 119483. DOI: 10.1016/j.conbuildmat.2020.119483.

Steyn, W. J. M., Monismith, C. L., Nokes, W. A., Harvey, J. T., Holland, T. J., and Burmas, N. (2012). "Challenges confronting road freight transport and the use of vehicle-pavement interaction analysis in addressing these challenges". *Journal of the South African Institution of Civil Engineering* 54.1, 14–21.

Sugihara, M. (1987). "Methods of numerical integration of oscillatory functions by the DE-formula with the Richardson extrapolation". *Journal of Computational and Applied Mathematics* 17.1-2, 47–68. DOI: 10.1016/0377-0427(87)90038-0.

Thacker, B. H., Doebling, S. W., Hemez, F. M., Anderson, M. C., Pepin, J. E., and Rodriguez, E. (Oct. 2004). *Concepts of Model Verification and Validation*. Tech. rep. Los Alamos, NM: Los Alamos National Laboratory (LANL). DOI: 10.2172/835920.

Tokyo Measuring Instruments Laboratory (2023). *Mold Strain Gauge*. URL: https://tml. jp/e/product/strain_gauge/mold.html.

Vinay Kumar, V. and Saride, S. (2017). "Use of digital image correlation for the evaluation of flexural fatigue behavior of asphalt beams with geosynthetic interlayers". *Transportation Research Record* 2631.2631, 55–64. DOI: 10.3141/2631-06.

Williams, M. L., Landel, R. F., and Ferry, J. D. (1955). "The Temperature Dependence of Relaxation Mechanisms in Amorphous Polymers and Other Glass-forming Liquids". *Journal of the American Chemical Society* 77.14, 3701–3707. DOI: 10.1021/ja01619a008.

Znidaric, A. (2015). *Heavy-Duty Vehicle Weight Restrictions in the EU*. Tech. rep. Ljubljana, Slovenia: ZAG – Slovenian National Building and Civil Engineering Institute. URL: https://www.acea.auto/files/SAG_23_Heavy-Duty_Vehicle_Weight_Restrictions_in_ the_EU.pdf.

Zofka, A., Maliszewski, M., and Maliszewska, D. (2017). "Glass and carbon geogrid reinforcement of asphalt mixtures". *Road Materials and Pavement Design* 18, 471–490. DOI: 10.1080/14680629.2016.1266775.

Appendices

APPENDIX **A**

Supplementary details about experimental test setups

A.1 DTU Smart Road

The following content is intended to provide supplementary details with respect to the DTU Smart Road and measurement campaigns, for which data is available and can serve future studies related to the problem at hand. This involves some undisclosed details about the experimental setup, as well as details from the FWD campaign, the Raptor campaign, and the campaign with the tank, dumper truck, and VIAFRIK (refer to the appended Paper iii for all relevant information regarding the HYSTER forklift campaign).

A.1.1 Test setup

DTU Smart road was built during the period of 30th of September 2021 to 7th of October 2021. It is located at Henrik Dams Allé on DTU Campus in Kgs. Lyngby (Denmark). Each test section is 25 m long (100 m in total) and 7.9 m wide. It comprises two traffic lanes, one in each direction (where embedded sensors are placed at the lane's intersection).

The entire pavement construction procedure of the four test sections (refer to Figure 3.16 for a cross-sectional view of the final pavement structure) was done as follows. The existing pavement system was milled to a depth of 15 cm, i.e. removing about 100 mm of existing AC and some of the unbound granular material below. The existing UGS was then leveled with excess asphalt, compacted, and protected by a prime coat of bituminous emulsion. Next, AGRs were installed on top of the prime-coated UGS in S-1; this was done using the so-called S&P Asphalt Unroll Equipment (S&P Clever Reinforcement Company AG 2020). Specifically, AGRs were rolled out in 1 m or 2 m wide lanes (25 m long) with a (transverse) overlap of about 150 mm. In this procedure, the grids are preheated prior to deployment to melt the bitumen coating for improving adhesion with the underlying layer. The AGR installation procedure is depicted in Figures A.1(a)-(b). Hereafter ASGs and PT100s were installed on top of the exposed UGS (in S-0, S-2, and S-3) or the AGR in S-1 (see Figures A.1(c)-(d)). They were each placed in warm mastic and fixed until cool down, and the cables were subsequently bundled and led through cable tubes into a manhole located outside the road. Four manholes with cable tubes were constructed (prior to the sensor installation), and placed roadside next to each test section. Cables were then protected with hot mix asphalt (HMA) (manually compacted), and the paver and asphalt delivery trucks were instructed to only pass where the cables had been covered. The sensors themselves were exposed until AC paving. The sensor installation procedure is depicted in Figures A.1(c)-(d). After installing the sensors, a 40 mm layer of AC was paved, compacted, and covered by a thin layer of tack coat. The procedures were repeated, where AGRs were placed in S-2, PT100s were installed (one in each test section), and a 70 mm AC lift paved, compacted, and covered with tack coat. Finally, the procedures were repeated again with AGRs placed in S-3, followed by PT100s installed in each section (as well as a single longitudinal ASG on top of the grid in S-3), before a final 40 mm AC lift was paved and compacted. The road was opened for traffic four days later.

(a)   (b)

(c)   (d)
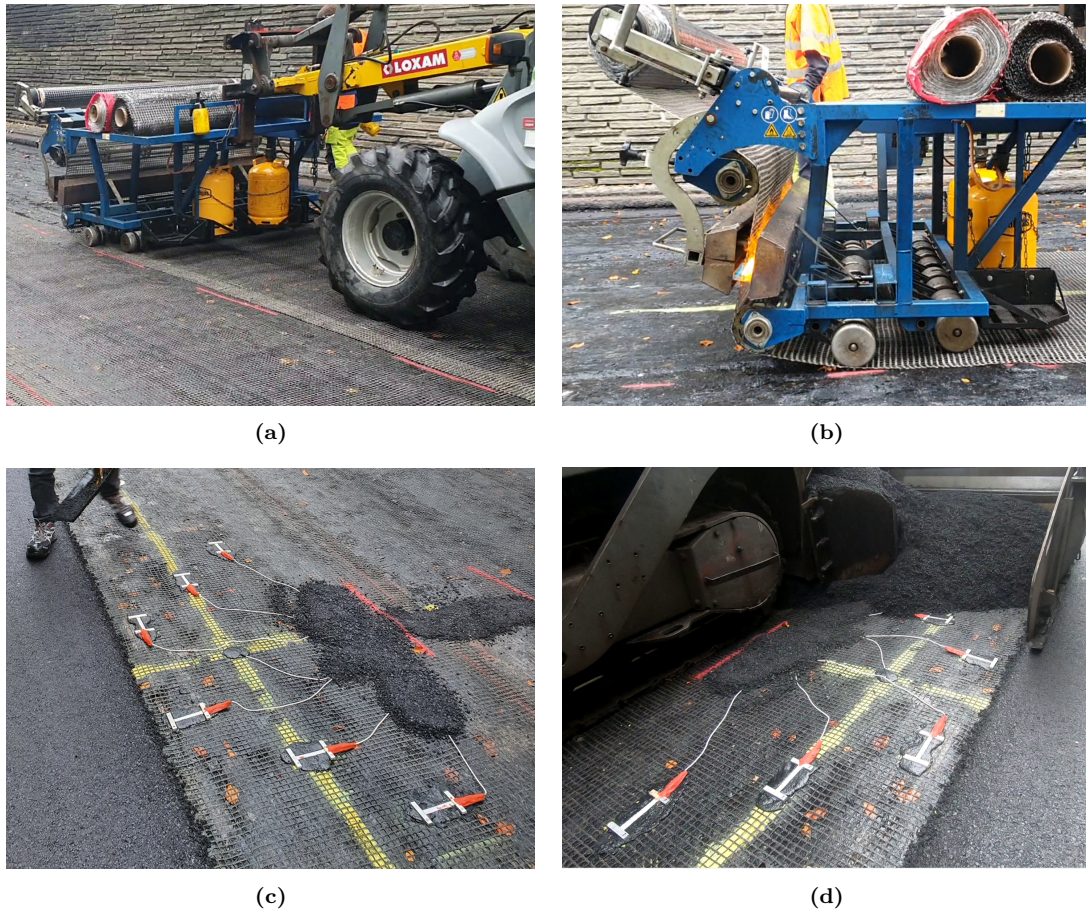
Figure A.1: Pictures from the construction procedure at DTU Smart Road: (a) and (b) shows the installation of AGR using the S&P Asphalt Unroll Equipment, whereas (c) and (d) shows the ASGs installed in S-1 before/during paving.

The three AC lifts were all made of the same asphalt mix with properties given in Table A.1 and a gradation curve depicted in Figure A.2. The utilized prime and tack coat was a SE 50 % Emulsion provided by Sjællands Emulsionsfabrik (in Danish). The prime coat (on top of the UGS) was applied with a rate of 1000 g/m^2, whereas the tack coats (between AC lifts) were applied at a rate of 350 g/m^2.

Table A.1: Asphalt mix properties from DTU Smart Road.

Properties	Value
Bitumen content	5.6%
Air void content	2.2%
Bitumen penetration grade	70/100
NMAS	8 mm
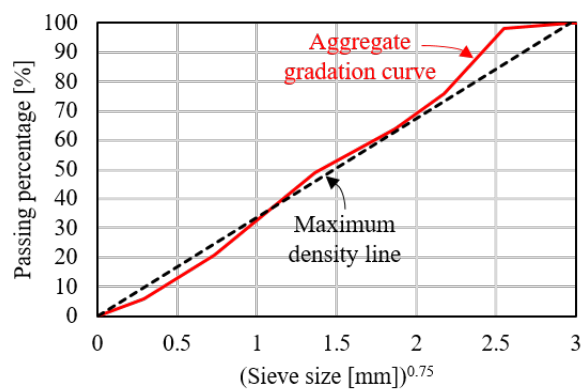
Figure A.2: Asphalt aggregate gradation curve from DTU Smart Road.

The UGS was visually classified as GP (poorly-graded gravel-sand mixture with little to no fines) according to the Unified Soil Classification System (ASTM D2487 2017). The visual inspection indicated a sandy appearance with about 2% cobbles, and the overall NMAS was estimated to be 37.5 mm. The UGS thickness was assessed by using the DCP (also carried out before paving). In each test section, a single DCP test was performed directly in the section center (i.e., 12.5 m from the section intersections and 4 m from the road edge). Figure A.3 presents the measured DCP profiles for the four test sections, down to a depth of about 2 m. Each chart shows the cumulative number of drops along the abscissa and the rod penetration depth along the ordinate; the penetration depth was adjusted to start from the AC surface level (after paving). Moreover, the penetration rates, i.e., penetration depth per drop, are indicated by dashed regression lines. Finally, the formation level, i.e., the interface between the UGS and the subgrade, is visualized. The formation level is revealed by the abrupt change in the penetration rate along the DCP profiles. As can be seen, the formation level was found at a depth of approximately 900 mm in both S-0 and S-1, whereas the formation level in S-2 and S-3 was found at a depth of approximately 650 mm. Accordingly, the UGS thickness is taken as 750 mm in S-0 and S-1 and 500 mm in S-2 and S-3 (see Figure 3.16).
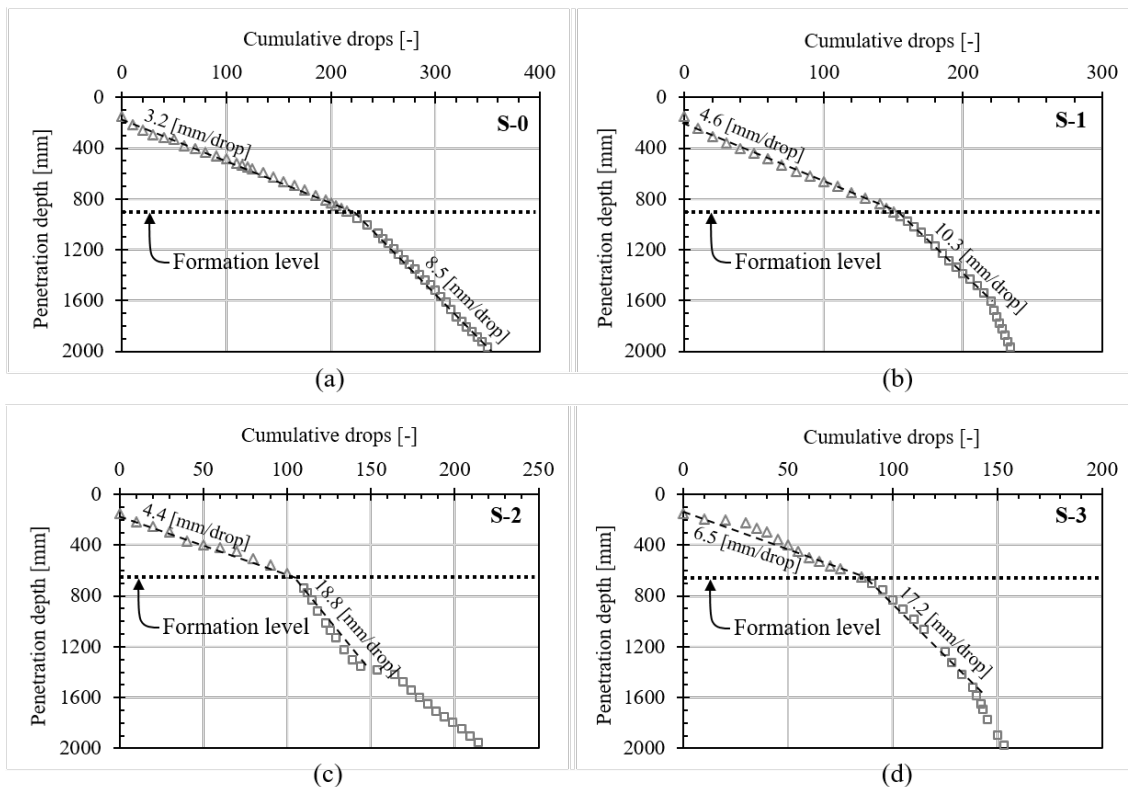
Figure A.3: DTU Smart Road: DCP profile in (a) S-0, (b) S-1, (c) S-2, and (d) S-3.

Lastly, it is anticipated that the UGS was directly supported by the local soil in the region. From a local core report (GEUS 1986), the local soil is estimated to be of fine-grained overconsolidated inorganic silty sand – classified as SM according to the Unified Soil Classification System (ASTM D2487 2017).

The utilized AGR product Carbophalt®G 200/200 (S&P Clever Reinforcement Company AG 2023a) is composed of bitumen-coated strands of carbon fibers arranged in a mesh with an equal amount of fibers in each direction (see Figure A.4). The associated grid specifications are listed in Table A.2.

Figure A.4: Carbophalt®G 200/200.

Table A.2: Carbophalt®G 200/200 properties.

Properties	Value
Bitumen coating (per grid area)	$200\,\text{g/m}^2$
Bitumen penetration grade	30/40
Aperture size	$15\,\text{mm} \times 15\,\text{mm}$
Young's modulus	265,000 MPa
Poisson's Ratio	0.15
Fiber area	$46\,\text{mm}^2/\text{m}$
Elongation	1.5%
Tensile strength	200 kN/m

The type of ASGs utilized herein was a KM-120-120-H2-11 (Kyowa Electronic Instruments 2022), which are designed for being embedded in Portland Cement Concrete (PCC) or AC and can operate at a temperature range of −10℃ to +70℃. The type of PT100s was HSENS/101/B-P0101438 (Elfa Distrelec 2014), which can operate at a temperature range of −50℃ to +260℃. Cables were collected in separate manholes, which was done to limit the cable lengths that otherwise (if too long) could disturb the sensor measurements. This also meant that only one section could be connected to the data acquisition system at a time. Thus, test sections had to be tested one by one. After the construction phase, it was discovered that all ASGs survived the paving activities except for ASG2 in S-1 and ASG1 in S-2. This resulted in a ASG-survivability rate of 92%. With respect to the PT100s, all sensors survived, i.e., resulting in a PT100-survivability rate of 100%.

A.1.2 Measurement campaigns

Several measurement campaigns were carried out at DTU Smart Road. One involved an FWD, while three others involved different moving vehicle types (refer back to Table 3.7).

FWD test

An FWD test campaign was carried out in March 2022 at DTU Smart Road for subsequent assessment of pavement layer properties. In each test section, FWD drops were applied in five location points (see Figure A.5); they were placed along the road center line at 0, ±1, ±3 meters from the section center (in the longitudinal direction). A total of 396 drops were executed across all four sections, distributed between three load levels, i.e., 60 kN, 80 kN, 100 kN, and two load pulse lengths, i.e., 30 ms and 50 ms. Temperatures at the pavement surface and in the air were measured during the campaign, ranging from 5-11℃.
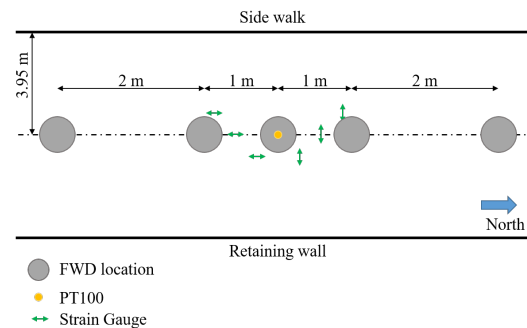
Figure A.5: FWD test campaign: (a) a picture of the FWD test and (b) top view layout of the FWD drop point.

Along with the FWD test, ASG measurements were collected; however, the exact load locations (within a few cm of precision) were not measured. In addition, accelerometer measurements were collected as part of a different research topic dealing with seismic analysis. In-pavement temperature measurements were not recorded as the PT100 acquisition system was not available at this point.

Raptor campaign

A measurement campaign was carried out in September 2022 using Ramboll's Raptor (see Figure A.6(a)). The Raptor is equipped with 12 gocators that provide information about surface displacements below the truck while driving. The Raptor is supported by eight wheels distributed over three axles as shown in Figure A.6(b). The front axle load was (about) 60 kN, the middle axle load was 55 kN and the rear axle load was 96 kN. All six tires were of a similar size/type, characterized by a contact width of 300 mm.

(a)   **(b)**
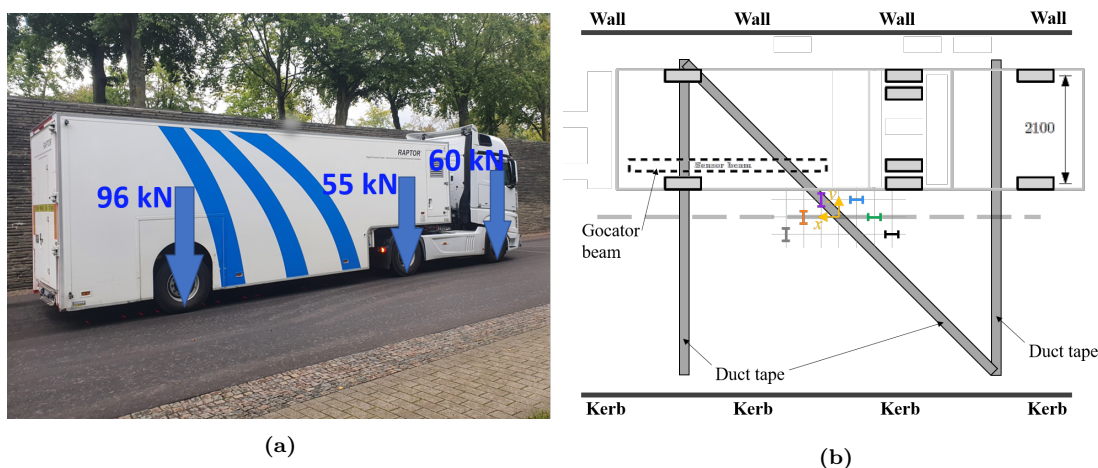
Figure A.6: (a) Ramboll's Raptor, and (b) top view illustration of the campaign setup.

ASG measurements were generated by the Raptor passing the array of sensors several times, first by collecting measurements from S-0 and then from S-1. 12 passes were applied in total, aimed at two different speeds, i.e., 5 km/h and 40 km/h. Table A.3 provides an overview of the different passes with respect to aimed speed and detected section. The driver was instructed to drive with one of the wheel paths as close to the sensor array as possible. Its lateral positions, which varied from pass to pass, were assessed by the Raptor gocators. Duct tape patterns (indicated in Figure) were applied on the surface to generate a different surface texture, which can be detected by the gocators. Based on this method, it is possible to determine the lateral wheel positions relative to the embedded ASG, which has previously been examined in Nielsen 2019s. During each pass, six ASG response traces were recorded in S-0, and five ASG response traces were recorded in S-1 (no response in ASG2). All ASG measurements were recorded with a sampling rate of 1200 Hz. PT100 measurements were also recorded at 1 Hz; they indicated a constant temperature of 14 °C for all passes, uniformly distributed across the AC thickness.

Table A.3: Number of passes for each section and speeds.

Speed	S-0	S-1
5 km/h	2	4
40 km/h	3	3

An example of response measurements from the longitudinal and transverse ASGs is given in Figure A.7. Herein (and forward on), positive values represent compressive strains and negative values represent tensile strains. It can be observed that peaks associated with the three axle loads can be systematically observed in the ASG readings.
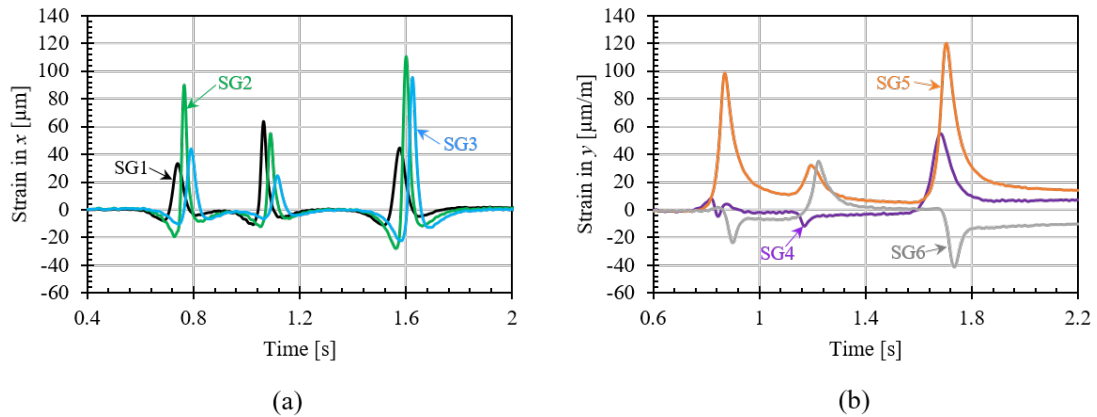
Figure A.7: ASG readings from a pass in S-0 aimed at 40 km/h, where (a) indicates longitudinal strains and (b) indicates transverse strains.

Additionally, gocator measurements from the Raptor were also recorded during each pass. The gocator reading provides some Raptor Deflection Indices (RDI), which can be used to estimate pavement deflections and in backcalculation of pavement layer properties (Athanasiadis and Zoulis 2019).

Campaign with military tank, dumper truck, and VIAFRIK

A measurement campaign was carried out in October 2022 using three different types of vehicle loadings, i.e., a military tank, a dumper truck, and the VIAFRIK. The entire military tank load, 296 kN in total, was supported by seven rollers that rotate on two continuous tracks – depicted in Figure A.8(a)-(b). The dumper truck, shown in Figure A.8(c), was supported by six wheels distributed over three axles; the front axle and middle axle load was about 40 kN each, and the rear axle load was about 85 kN. All six wheels were equipped with ribbed tires as depicted in Figure A.8(d). Lastly, the VIAFRIK, shown in Figure A.8(e), was supported by six wheels – two on the front axle and four on the rear axle. The front axle load was about 70 kN and the rear axle load was about 110 kN. All six (regular) tires were of a similar size/type, shown in Figure A.8(f), with a contact width of about 230 mm.

The measurement campaign involved testing all four test sections. Several passes with the three vehicles were generated in each section, aimed at two different speeds, i.e., 10 km/h and 30 km/h. Table A.4 provides an overview of the different passes with respect to aimed speed and detected section. The driver of each vehicle was instructed to drive with one of the wheel/track paths as close to the sensor array as possible. The lateral vehicle positions were assessed by GoPro footage (mounted on the vehicle), video footage taken from roadside, and modeling clay. With respect to the latter, modeling clay was placed on the pavement surface, and the imprints from the passing vehicles (see Figure A.9) were measured relative to the sensor array. During each pass, ASG response traces were recorded with a sampling rate of 1200 Hz (ASG2 in S-1 and ASG1 in S-2 were defective). PT100 measurements were recorded at 1 Hz; they indicated a uniformly distributed temperature across the AC thickness, varying from 18 °C to 22 °C from the beginning to the end of the measurement campaign.

Figure A.8: Test vehicles: (a) military tank, (b) military tank track, (c) dumper truck, (d) dumper truck tires, (e) VIAFRIK, and (f) VIAFRIK tires.

Table A.4: Number of passes for each vehicle, section, and speed.

Vehicle type	Speed	S-0	S-1	S-2	S-3
Military tank	10 km/h	3	3	3	3
	30 km/h	3	3	3	3
Dumper truck	10 km/h	2	2	2	2
	30 km/h	2	2	2	2
VIAFRIK	10 km/h	2	2	2	2
	30 km/h	2	2	2	2

Figure A.9: Imprint from the military tack rubber pads using modeling clay.

An example of ASG response measurements, triggered by the military tank, is given in Figure A.10(a)-(b). Here, the load from each of the seven rollers can be systematically observed by the peak formations in the ASG readings. In general, the transverse ASG measured larger tensile strains compared to the longitudinal ASGs. An example of ASG response measurements, triggered by the dumper truck, is given in Figure A.10(c)-(d).

Here, the three axle loads can be systematically observed by the three peaks in the ASG readings. Finally, an example of ASG response measurements, triggered by the dumper truck, is given in Figure A.10(e)-(f). Here, the two axle loads are also occurs systematically, indicated the two peak formed in the ASG readings. It should be noted, that it is difficult to directly compare the strain magnitudes across the different vehicle types. This is because the vehicle's speed and lateral positions varied from pass to pass. In order to make such a comparison, a computational model must be involved in the assessment. For more details about the measurement campaign, the reader can refer to the MSc's thesis (Hansen et al. 2023).
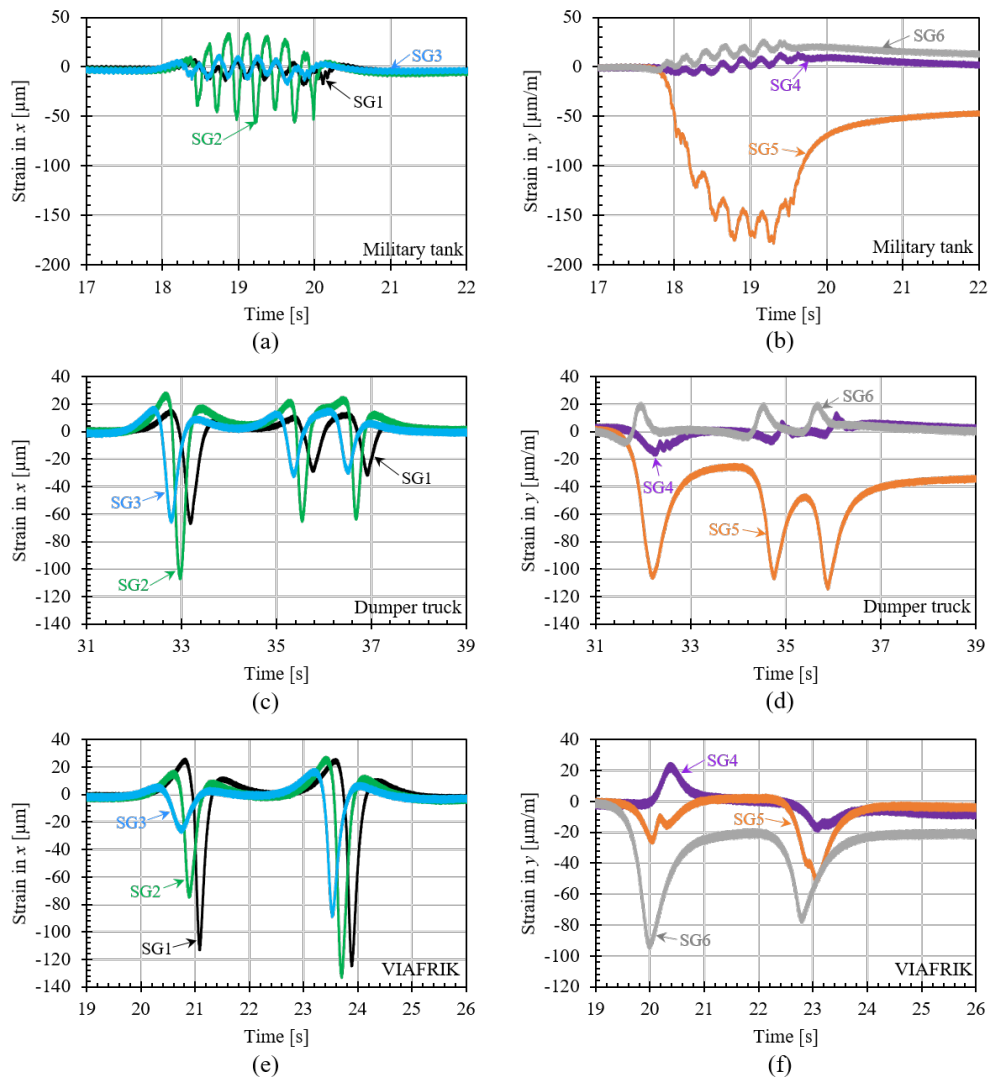

Figure A.10: ASG readings during passes in S-0 aimed at 30 km/h: (a) longitudinal strains from the military tank, (b) transverse strains from the military tank, (c) longitudinal strains from the dumper truck, (d) transverse strains from the dumper truck, (e) longitudinal strains from the VIAFRIK, and (f) transverse strains from the VIAFRIK.

A.2   APT setup in Arlington, Texas

The following content is intended to provide supplementary details about the APT setup in Arlington (Texas). This involves some undisclosed details about the experimental setup, as well as details from the measurement campaign with the PTM.

A.2.1   Test setup

The PhD project team was involved in the construction phase during the installation of the AGR and embedded sensors. The entire pavement construction procedure of the four main test sections S1, S2, S3, and S4 (refer to Figure 3.20 for a cross-sectional view of the final pavement structure), as well as the utilized materials, are described as follows:

  (i)   a existing subgrade surface area was prepared by leveling and compaction;

 (ii)   pressure cells were hereafter installed on the exposed subgrade surface according to Figure A.11(a). The type of pressure cells was a Model 3510 Contact Pressure Cell from Geokon (Geokon 2023), designed for measuring dynamic soil pressures on structures. The pressure cell cables were led to roadside boxes;

(iii)   the UGS was then placed, compacted, and covered by a prime coat of bituminous emulsion;

 (iv)   next, AGRs were installed on top of the prime-coated UGS in S1, S3, and S4. The installation procedure was similar to the description given in Subsection A.1.1, where AGRs were rolled out on a prime-coated UGS in 2 m wide lanes with a (transverse) overlap of about 150 mm. Carbophalt®G 200/200 was utilized in sections S1 and S4 (with similar properties given in Table A.2), whereas Glassphalt®G was utilized in S3. Glassphalt®G is a bitumen-coated grid made of glass fibers and is characterized by the properties given in Table A.5;

  (v)   ASGs were hereafter installed on top of the exposed UGS (in S2) or on top of the AGR (in S1, S3, and S4). They were each placed in fresh HMA (see Figure A.11(b) before being topped by an additional amount of HMA. The HMA covering the ASGs was subsequently compacted manually. The type of asphalt ASGs utilized herein was a PMFLS series Asphalt Mold strain gauge from Tokyo Measuring Instruments Lab. (Tokyo Measuring Instruments Laboratory 2023);

 (vi)   grid gauges were also installed directly onto the AGR ribbons. This was done by locally removing the bitumen coating (around the fibres), and subsequently gluing strain gauges directly onto the fibres (see Figure A.11(c)). The type of grid gauges was a KFH-2-120-C1-11L3M3R from Omega (Omega Engineering Limited 2017);

(vii)   cables from ASGs and grid gauges were bundled and led into roadside boxes (together with cables from pressure cells). The cables were subsequently protected by HMA (similar to DTU Smart Road in Subsection A.1.1). Two roadside boxes were considered, each grouping all sensors from S1+S2 or S3+S4. By means, S1+S2 or S3+S4 can be connected to the data acquisition system at the same time;

(viii) AC was then paved in two lifts with an application of tack coat between the two lifts. It was discovered (after construction) that all pressure cells survived the construction activities. In S1, one set of transverse and longitudinal ASGs survived, whereas in S2, only one transverse ASG survived; all grid gauges survived in S2. In S3 and S4, all ASGs survived; however, only one grid gauge survived in S4. Overall, this resulted in a survivability rate of 100% for pressure cells, 69% for ASGs, and 78% for grid gauges; and

(ix) finally (after construction) the AC surface was exposed to artificial aging. This involved placing a so-called aging box on top of the tested area, which applies radiation to the asphalt surface. A picture from inside the box is given in Figure A.11(d). A total of five weeks of artificial aging were applied to all four sections before subsequent testing.

Table A.5: Glassphalt®G properties.

Properties	Value
Bitumen coating (per grid area)	$200\,\text{g/m}^2$
Bitumen penetration grade	30/40
Aperture size	$15\,\text{mm} \times 15\,\text{mm}$
Young's modulus	73,000 MPa
Poisson's Ratio	0.15
Fiber area	$46\,\text{mm}^2/\text{m}$
Elongation	3.0%
Tensile strength	120 kN/m

(a)

(b)

(c)

(d)

Figure A.11: Pictures from the APT test setup at UTA: (a) pressure cell, (b) ASG, (c) grid gauge, and (d) aging box (inside).

A.2.2   Measurement campaign

In the measurement campaign carried out at S3 and S4, several load cycles were applied with the PTM. With reference to Figure 3.21, the bogie begins from the right side (of the green area), then moves to the left side, after which it reverses back to the right side again during a single load cycle. Table A.6 provides an overview of the number of cycles applied

at the different speed-temperature combinations.

As part of the measurement campaign, LVDTs and dual-axis tiltmeters were installed on the pavement surface (after positioning of the PTM). Figure A.12(a)-(b) provides a picture of the post-installed surface sensors. The LVDTs were installed horizontally inside a 20 mm deep blind-hold with a 50 mm diameter, oriented in the direction of travel. The tiltmeters were installed by gluing them to the AC surface using super glue. Here, a wood block was introduced between the AC and the tiltmeters to avoid the direct application of super glue to the sensor. The technical specifications for the utilized LVDTs and tiltmeters are given in Table A.7 and A.8, respectively.

Table A.6: Number of load cycles for different load speeds and AC temperatures.

Speed	$T = 16\,°C$	$T = 27\,°C$
1 km/h	1.5	1.5
2.4 km/h	3	3
4.8 km/h	4	4

(a)

(b)

Figure A.12: Surface sensors: (a) LVDT in blind-hole, and (b) tiltmeter.

Table A.7: Technical specifications for LVDT sensors.

Name	GT0500XRA
Manufacturer	RDP Electrosense
Type	Spring return
Range	± 0.5 mm
Linearity error	$\pm 0.25\%$
Sensitivity	110 mV/V
Repeatability	$0.15\,\mu$m
Temperature coeff.	$\pm 0.01\%/°C$ (typical)
Signal conditioner	Metrolog SD20
Resolution	$1\,\mu$m
Sampling rate	~ 250 Hz

Table A.8: Technical specifications for tiltmeter sensors.

Name	TILT-57A
Manufacturer	CTi Sensors
Type	MEMS
Range	Pitch: $\pm 90°$, Roll: $\pm 180°$
Zero offset error	$< \pm 0.02°$ (@20 °C)
Static accuracy	$< 0.03°$ (Typical)
Dynamic accuracy	$< 0.5°$ (Typical)
Temperature coeff.	$\pm 0.002°/°C$ (typical)
Noise	$0.001°/\sqrt{\text{Hz}}$
Angular resolution	$< 0.003°$
Sampling rate	2000 Hz

An example of response measurements from all embedded sensors and surface sensors during one load cycle is given in Figure A.13. The responses were recorded during a load speed of $V = 2.4$ km/h, a uniform AC temperature of 16 °C, and zero lateral wander. Figure A.13(a) represents all asphalt ASG measurements in the longitudinal direction (as a function of time), Figure A.13(b) represents all measurements from transverse asphalt ASG and a single grid gauge (only one working), Figure A.13(c) represents readings from

the pressure cells, Figure A.13(d) represents the LVDT readings, and A.13(e)-(f) represents the tiltmeter readings around the x-axis and the y-axis, respectively. As can be seen across all subfigures, the bogie triggers a response twice during a single load cycle as it moves from right to left and then back to right (with respect to Figure 3.21).
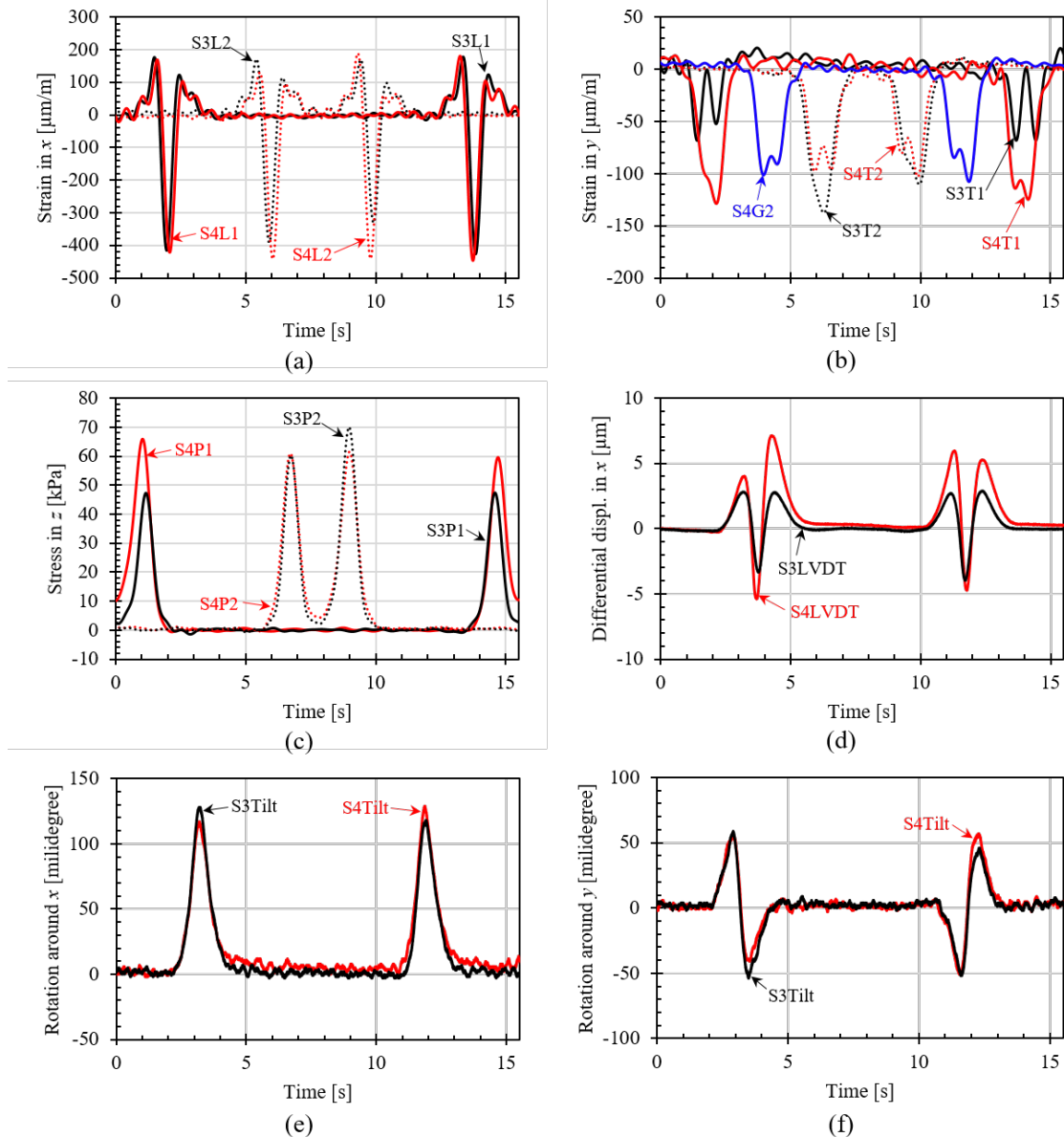
Figure A.13: Sensor measurements from S3 and S4 during one load cycle with a speed of 2.4 km/h and at $T = 15.6\,°C$: (a) longitudinal ASGs (L), (b) transverse ASGs (T) and a singe grid gauge (G2), (c) pressure cells (P), (d) LVDTs, (e) tiltmeter around the longitudinal direction, and (f) tiltmeter around the transverse direction.

A.3   Test areas in Switzerland

The following content is intended to provide supplementary details about the two test areas in Switzerland. This involves some undisclosed details about the experimental setups, as well as details from the measurement campaigns carried in La Ferrière and Neuchâtel. The PhD project team was not involved in the construction phase of the two test sections near La Ferrière and in Neuchâtel. However, they were invited to lead a measurement campaign in each test area in the early stage of the PhD project.

A.3.1   Test setup in La Ferrière

The entire test area near La Ferrière considers the cantonal road RC-18 in the municipalities of La Ferrière. It consists of two lanes of opposite directions, each with a width of 3.65 m. The test area is divided into three sections – section (C) including Carbophalt®G 200/200 grids, section (G) installed with Glasphalt®G grids, and section (R) without AGR. Both AGR products were provided by S&P, with properties given in Tables A.2 and A.5. The two reinforced sections have a length of 50m each and are separated by the reference section of 13m in length.

All sections were built as part of a reconstruction of an existing live road. Specifically, 120 mm of the existing AC was milled and repaved with a new support layer and a new wearing course (see Figure 3.24). The three AC layers were of different mix types described as follows: the existing AC was an AC 0/16, the new support layer was an AC T 22 N, and the wearing course was an AC 11 N, PmB Styrelf C85 with S-type aggregates. A tack coat was applied to the milled surface one day before repaving. In both reinforced sections, the AGRs were only installed in one of the lanes, in the direction toward La Cibourg train station. They were installed on top of the milled surface before overlay (and after tack coat). The grids were rolled out in 2 m wide lanes with an approximate overlap of 100-150 mm, with a similar procedure as in Subsection A.1.1. The entire AC structure was supported by an unbound granular base layer with an approximate thickness of 400 mm (varying ±30 mm). The layer thickness was provided by a single DCP test for each test section. An additional soil layer was identified, sandwiched between the granular base layer and the local bedrock; the additional soil varied in thickness between sections ranging from 400 mm to 700 mm. The materials of the existing sublayers (i.e., the granular base, soil, and bedrock) were not identified.

ASGs and PT100s were installed in all test sections. In each section, they were arranged in a line along the traveling direction with a spacing of 2.5 m. The sensor line is placed 2.95 m from the road edge. In addition, a single PT100 was placed in each section at the same level as the ASGs. In total, 18 ASGs and three PT100s were installed at the test site. The ASG and PT100 types, as well as their respective installation procedures (including protection of cables), were similar to those utilized at DTU Smart Road (see Subsection A.1.1). Sensor cables from all three sections were collected and led into a single roadside manhole. By means, all sections can be connected to the data acquisition system simultaneously; however, sensor cables were more that 25 m long, which can influence the sensor accuracy. After construction, it was discovered that all ASGs and PT100s survived the paving activities, except for two ASGs in section G. This resulted in a survivability rate of 89% for ASGs and 100% for PT100s.

A.3.2   Test setup in Neuchâtel

The test section considers a road of four lanes (two in each direction). In each direction, the road is divided into a bus lane and a normal lane. The bus lane has a width of 4.20m, whereas the normal lane has a width of 3.95m. The bus lane in the direction from west to east constitutes the tested area. It consists of three sections – one section (C) including Carbophalt®G 200/200 grids, one section (G) installed with Glasphalt®G grids, and one section (R) without AGR. Both AGR products were provided by S&P, with properties given in Tables A.2 and A.5. The two reinforced sections have a length of 20m each and are separated by section R of 15 m in length.

All sections were built as part of a full-depth reconstruction of the existing live road. Specifically, it was repaved by two lifts of AC base, two lifts of supporting AC, and a wearing course (see Figure 3.27). The AC layer types were of different mixes, with the

following information provided: the AC base and support layer was an AC-EME C2, and the wearing course was an AC-MR. In both reinforced sections, the AGRs were installed on top of the upper AC base before the bottom AC support lift (after tack coat). The grids were rolled out in 1 m and 2 m wide lanes with an approximate overlap of 150-200 mm, with a similar procedure as in Subsection A.1.1. The lower layer composition was unknown.

ASGs and PT100s were installed in all test sections. In each section, they were arranged in a line along the traveling direction with a spacing of 2.5 m. The sensor line is placed 1.2 m from the road edge. In addition, a single PT100 was placed in each section at the same level as the ASGs. In total, 18 ASGs and three PT100s were installed at the test site. The ASG and PT100 types, as well as their respective installation procedures (including protection of cables), were similar to those utilized at DTU Smart Road (see Subsection A.1.1). Sensor cables from all three sections were collected and led into a single roadside manhole. By means, all sections can be connected to the data acquisition system simultaneously. After construction, it was discovered that all ASGs and PT100s survived the paving activities, except for two ASGs in section G. This resulted in a survivability rate of 89% for ASGs and 100% for PT100s.

A.3.3 Measurement campaign in La Ferrière

A measurement campaign was carried out on the 24th of August 2020 at the test area near La Ferrière. The campaign involved a heavy two-axle truck (see Figure 3.29(a)), equipped with a water tank with an adjustable load level. During testing, the water tank was filled at three different levels, i.e., empty, half-full, and full, and the corresponding axle loads are given in Table A.9. The load configuration of the truck comprised six wheels distributed over two axles as indicated in Figure A.14. Front tire contact widths were about 270 mm, whereas rear tire contact widths were about 240 mm.

Table A.9: Axle load levels of the truck used in La Ferrière.

Level	Axle	Load [kN]	Total [ton]
Full	Front	73	16.5
	Rear	92	
Half	Front	68	15.5
	Rear	87	
Empty	Front	64	13.7
	Rear	73	
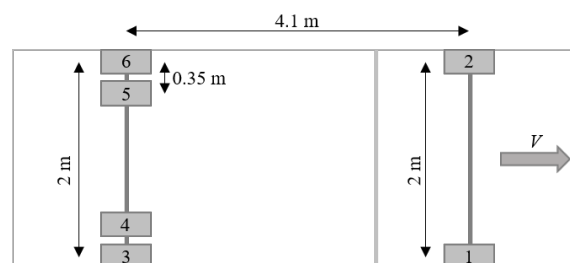
Figure A.14: Top view illustration of the truckload arrangement used in La Ferrière.

ASG measurements were generated by the two-axle truck passing the array of sensors, starting from section C and ending in section G. During each pass, the truck driver was instructed to maintain a certain speed and lateral position relative to the embedded sensor configuration. The truck's position was adjusted to achieve three different targeted offsets: (1) aligning the front-left wheel path with the embedded sensor line (0 mm), (2) shifting the wheel path 250 mm relative to the sensor line, and (3) shifting the wheel path 500 mm relative to the sensor line. Orientation lines were drawn on the asphalt to guide the driver (see Figure A.15(a)). Table A.10 provides an overview of the different passes with respect to aimed speeds, targeted offsets, and load levels. 57 passes were applied in total over all three test sections.

To capture the exact load location relative to the sensors (which varied from pass to pass), a distance laser sensor was utilized. The distance laser was placed on a tripod at the roadside (400 mm from the road edge), pointing transversely toward the other side of
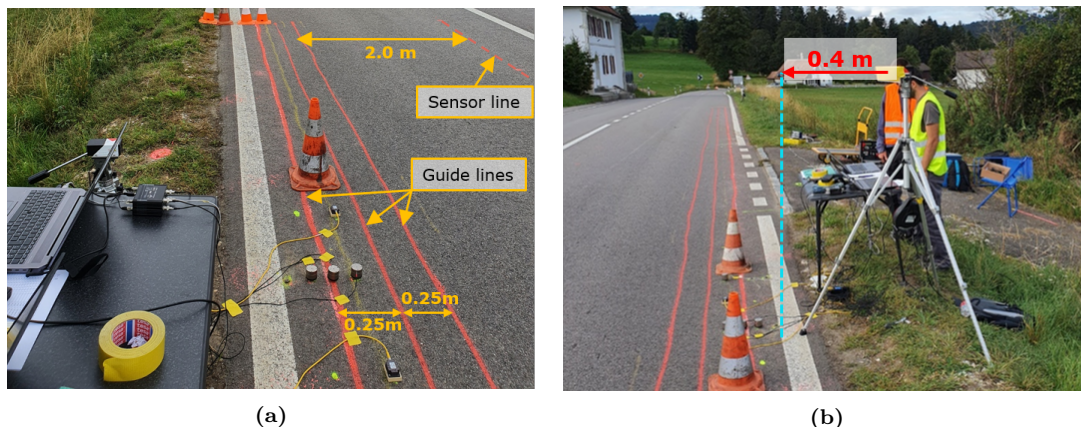
Figure A.15: La Ferrière: (a) orientation lines, and (b) distance laser sensor.

Table A.10: Number of passes at different load speeds and AC temperatures at La Ferrière.

Load level	Position	Speed [km/h]	Repetitions
Full	(1)	10, 20, 30, 40, 50, 60, 70	3
	(2)	40	3
	(3)	40	3
Half	(1)	20, 40, 60	3
	(2)	40	3
	(3)	40	3
Empty	(1)	20, 40, 60	3
	(2)	40	3
	(3)	40	3

the road (see Figure A.15(b)). When the truck passes, the sensor measures the distance to the body of the truck, which can later be used to assess the lateral offset. The distance to the edge of tire number 3 was measured to be approximately 70 mm, which must be added to the laser readings. The distance laser was first located outside Section C, and was later moved to Section R. In addition, a video camera was fixed at the end of section G to capture the lateral offset. Yellow tape with markings for every 100 mm was fixed to the pavement surface at the end of the test section to indicate the lateral position during subsequent video assessment.

As part of the measurement campaign, accelerometers and dual-axis tiltmeters were installed on the pavement surface near the road egde. Figure A.16(a)-(b) provides a picture of the post-installed surface sensors. The accelerometers were fixed to screws that were drilled into the asphalt surface. Tiltmeters were fixed to a wood block that was glued to the surface (similar to Subsection A.2.2). The technical specifications for the utilized accelerometers and tiltmeters are given in Tables A.11 and A.8, respectively. A total of four accelerometers and two tiltmeters were fixed to the pavement; they were first placed in Section C and later replaced in Section R. In each of the two sections, two sensor arrangements were considered to protect the surface sensors from being run over by the truck during certain targeted lateral offsets. The two sensor arrangements are illustrated in Figure A.17. The left-side arrangement was used for lateral offsets targeted at 0 mm relative to the sensor line, whereas the right-side arrangement was used for lateral offsets aimed at 250 mm. For lateral offsets aimed at 500 mm, the entire surface sensor setup was removed. The surface sensor configuration was placed in Section C during full water tank

loadings, and moved to Section R during half-full water tank loadings.

(a)   **(b)**

Figure A.16: Surface sensors in La Ferrière: (a) accelerometer and (b) tiltmeter.

Table A.11: Technical specifications for accelerometer sensors.

Name	KB12VD
Manufacturer	Metra Mess- und Frequenztechnik (MMF)
Type	Piezoelectric
Range	$\pm 0.6\,\mathrm{g}$
Linearity frequency range	0.08 to 260 Hz
Sensitivity	10000 mV/g
Residual noise	$1\,\mu\mathrm{g}$ (0.5 to 300 Hz)
Sampling rate	$\sim$96,000 Hz

(a)   **(b)**
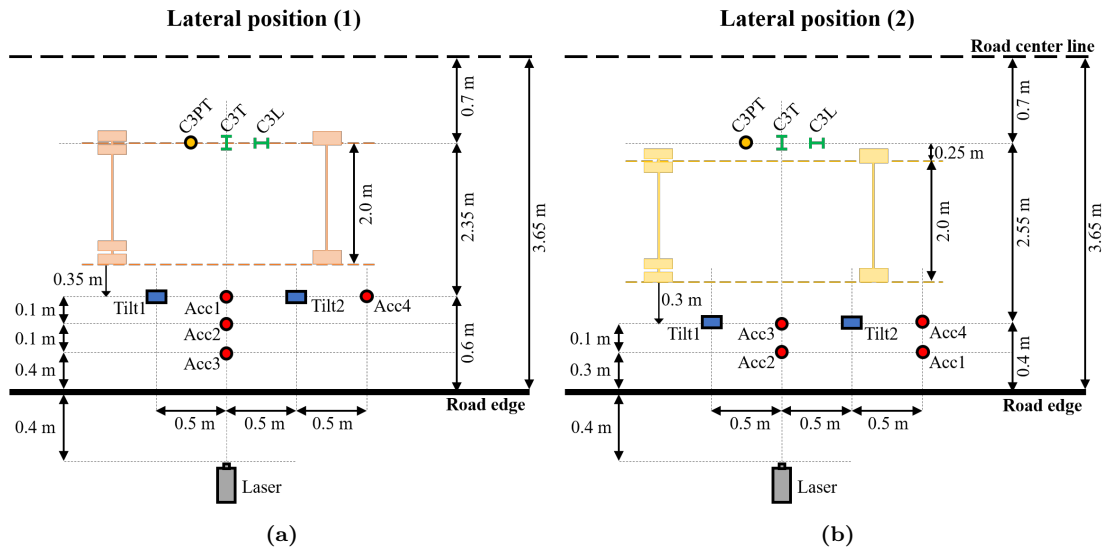
Figure A.17: Surface sensor array at La Ferrière for two lateral positions in section C: (a) position (1), and (b) position (2).

An example of sensor measurements from a single pass in section C for a full load level, a speed aimed at 60 km/h, and a targeted offset of 0 mm is given in Figure A.18. The AC temperature was 19 °C during this truck pass. Figure A.18(a) represents all ASG measurements in the longitudinal direction (as a function of time), Figure A.18(b) represents all measurements from transverse asphalt ASG, Figure A.18(c) represents the accelerometer readings, and Figure A.18(d)-(e) represents the tiltmeter readings around the x-axis and

the y-axis, respectively. As can be seen across all subfigures, the silhouette of the passing truck can be systematically observed by the formed signal peaks, which are associated with its two axle loads.
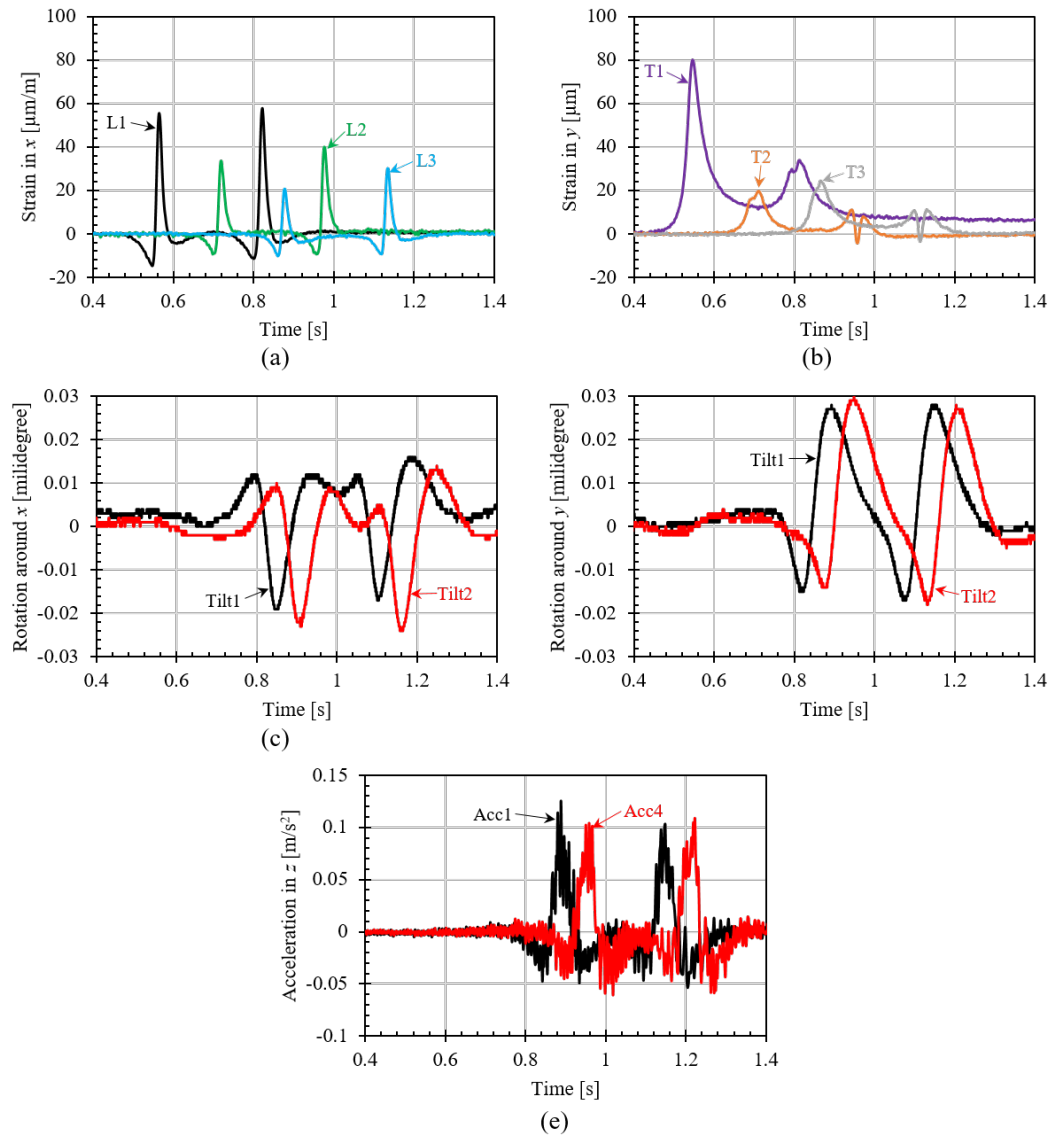
Figure A.18: Sensor measurements from La Ferrière during a fully loaded truck passage with a speed of 60 km/h, and an offset of 0 mm: (a) longitudinal ASG (L), (b) transverse ASG (T), (c) tiltmeter around x, (d) tiltmeter around y, and (e) accelerometer.

A.3.4   Measurement campaign in Neuchâtel

A measurement campaign was carried out on 27th of August 2020 at the test area in Neuchâtel city. The campaign involved a heavy four-axle truck (see Figure 3.29(b)), equipped with a water tank with an adjustable load level. During testing, the water tank was filled at two different levels, i.e., empty and full. The corresponding axle loads are given in Table A.12. The load configuration of the truck comprised ten wheels distributed over four axles as indicated in Figure A.19. All tire contact widths were about 270 mm.

Table A.12: Axle load levels of the truck used in Neuchâtel.

Level	Axle	Load [kN]	Total [ton]
Full	A1	53	
	A2	73	
	A3	145	35.2
	A4	82	
Empty	A1	57	
	A2	69	
	A3	65	23.5
	A4	45	
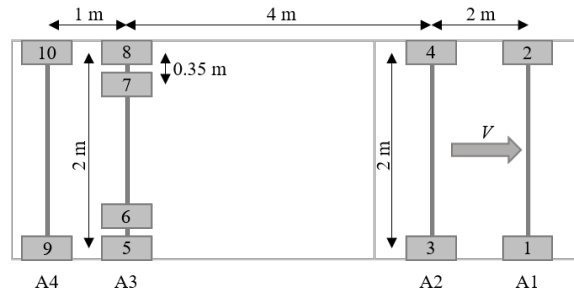
Figure A.19: Top view illustration of the load arrangement of the truck used in Neuchâtel.

ASG measurements were generated by the four-axle truck passing the array of sensors, starting from section C and ending in section G. During each pass, the truck driver was instructed to drive the truck at a certain speed and as close as possible to the sensor line. Since the test sections were affected by construction works, there was no space for changing the lateral position of the truck. Furthermore, to avoid conflicting with traffic in the adjacent road lanes, the target lateral truck position, i.e. the distance from tire 1 to the sensor line was 250 mm. A orientation line were drawn on the asphalt to guide the driver (see Figure A.20(a)). Table A.13 provides an overview of the different passes with respect to aimed speeds and load levels. 24 passes were applied in total over all three test sections.
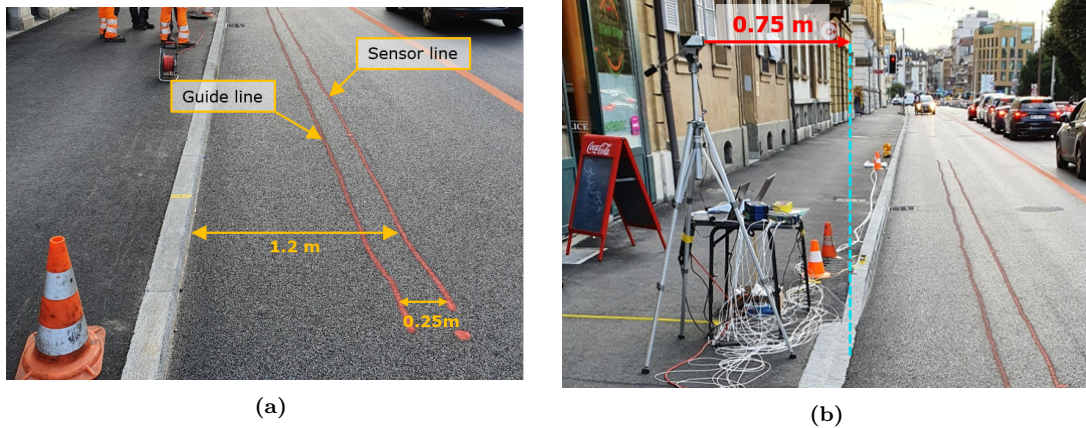
Figure A.20: Neuchâtel: (a) orientation lines, and (b) distance laser sensor.

Table A.13: Number of passes at different load speeds and AC temperatures in Neuchâtel.

Load level	Speed [km/h]	Repetitions
Full	10, 20, 30, 40	3
Empty	10, 20, 30, 40	3

To capture the exact load location relative to the sensors (which varied from pass to pass), a distance laser sensor was utilized (similar to the test in La Ferrière). The distance laser was placed on a tripod at the roadside (750 mm from the road edge) – see Figure A.20(b). The distance laser was located outside Section R during the entire campaign. In addition, a video camera was fixed at the end of section G to capture the lateral offset by video assessment (similar to the test in La Ferrière).

An example of all sensor measurements during a single pass at the "full" load level and a speed aimed at 40 km/h is given in Figure A.21. The AC temperature was 25 °C during this truck pass. Figure A.21(a) represents all asphalt ASG measurements in the longitudinal direction (as a function of time) and Figure A.21(b) represents all measurements from transverse asphalt ASG. As can be seen across all subfigures, the silhouette of the passing truck can be systematically observed by the formed signal peaks, which are associated with its four axle loads.
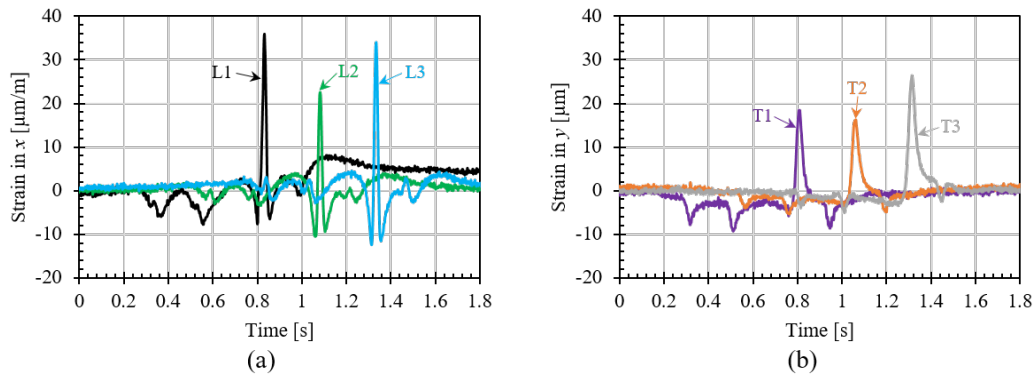

Figure A.21: ASG measurements from Neuchâtel during a fully loaded truck passage with a speed of 40 km/h: (a) longitudinal ASG (L), and (b) transverse ASG (T).

Part II

Appended Papers

Modeling and Analysis of Pavements with Asphalt Reinforcement

Analytic analysis of a grid-reinforced asphalt concrete overlay

Julius Nielsen, Klavs Olsen, Eyal Levenberg, and Asmus Skar

Published in: Eleventh International Conference on the Bearing Capacity of Roads

Analytic analysis of a grid-reinforced asphalt concrete overlay

J. Nielsen & K. Olsen
S&P Reinforcement Nordic ApS, Odder, Denmark

A. Skar & E. Levenberg
Department of Civil Engineering, Technical University of Denmark, Kgs. Lyngby, Denmark

ABSTRACT: This paper presented an analytic investigation of pavement systems subjected to mill-and-overlay treatments - including grid reinforcement in-between the new asphalt concrete (AC) overlay and the underlying (existing) cracked and aged AC. The investigation was based on an updated version of the classic layered elastic theory capable of handling a fragmented layer. Such a layer mechanically replicates a multi-cracked AC offering considerable vertical stiffness alongside low bending rigidity. A thin high-modulus layer represented the reinforcing grid, fully bonded to the abutting AC layers. Three mill-and-overlay cases and an additional reference case were investigated for a pavement system under the loading of a dual-tire configuration. The cases differed by the milling depth (thin, medium, and thick), and by the inclusion or exclusion of a reinforcing grid. Key responses in the structure and subgrade, commonly associated with different pavement distress, were calculated and compared across the different cases. The analysis suggests that a reinforcing grid can potentially reduce bottom-up cracking and permanent deformation within the AC overlay for the medium and thick mill-and-overlay cases. For the thin mill-and-overlay case, the analysis suggests that top-down cracking is the expected distress mechanism. In this context, the inclusion of a reinforcing grid seemed to be ineffective. Finally, it is found that adding reinforcement to any of the mill-and-overlay cases produces only a marginal effect on key responses linked to the development of permanent deformation deeper in the structure and subgrade.

Keywords: Pavement analysis, mill-and-overlay, reinforcement, layered elastic theory, fragmented layer formulation

1 INTRODUCTION

Pavement systems serve as the economic and social foundation of every country, with asphalt pavements being the most common type (EAPA and NAPA 2011). These systems continually deteriorate under traffic loadings in combination with weather effects and therefore require regular maintenance. With the increase in traffic loadings (e.g., heavier trucks, platooning), and with climate change effects (i.e., more extreme weather situations, sea rise, prolonged rain periods, higher moisture contents in the unbound layers), maintenance activities often prioritise the improvement of load-carrying capacity (i.e., the time until major repair work is needed) – and not just damage repair and return to pristine conditions. One common maintenance treatment in asphalt pavements is mill-and-overlay (Correia and Bueno 2011). This treatment applies to the full-width of the pavement or the full-width of a lane, and consists of partial-depth milling of the existing –

aged and damaged – asphalt concrete (AC), and then repaving with new AC. When the paved thickness has (nominally) the same thickness as the milled depth, the original load carrying capacity may be approached; when the paved thickness is larger, the overall structural thickness is increased, and the pavement's load-carrying capacity may be improved. Mill-and-overlay is also often employed to address functional distress, such as poor skid resistance and excessive unevenness.

After a mill-and-overlay, pavement systems consist of new AC that is supported by an aged and damaged AC layer. From a mechanistic standpoint, an aged and damaged AC layer – especially if severely cracked – exhibits little bending rigidity and therefore sub-optimal support to the new overlay. A possible approach to tackle this situation is to introduce grid reinforcement at the interface between the existing (aged) AC and the new overlay. Asphalt grid reinforcements are commonly made of carbon-, glass-, or polymer-fibres which are geometrically arranged in a thin bituminous-coated mesh, and thus offer high in-plane stiffness and tensile strength (Zofka et al. 2017).

The engineering analysis of asphalt pavement systems is currently based on layered elastic theory (LET), wherein each layer is considered a continuum. When it comes to including the effects of densely cracked AC layers in LET, it is a common approach to assign them reduced elastic properties (Mamlouk et al. 1990; Baltzer et al. 2017), even though AC stiffens with age (Bell et al. 1994; Harvey and Tsai 1997; NASEM 2007; Baek et al. 2012). Such approach originates from continuum damage mechanics, where properties are degraded isotropically to represent randomly oriented cracks (Lemaitre and Desmorat 2005). Due to the nature of traffic loadings, in combination with environmental effects, cracking in AC has a preferred vertical orientation – with layers gradually transforming under service into a fragmented state, e.g., alligator cracking and block cracking. Thus, from a mechanistic standpoint, the isotropic modulus reduction approach results in under-estimation of the vertical rigidity and over-estimation of the bending rigidity.

To address this shortcoming, Levenberg and Skar (2020) recently proposed an analytic formulation (validated against finite element solutions) for a fragmented layer (FL) that can be incorporated into LET. The idea is to model the FL as a Winkler spring-bed with Pasternak-type shear layer(s) for introducing some interaction between the Winkler springs. The spring-bed stiffness, characterised by k, represents the vertical rigidity of the FL; the Pasternak layer-(s), characterised by G, produce some bending rigidity for the FL. An additional horizontal spring-bed, characterised by k_h, is included in the FL model to represent the ability to transfer parallel-oriented (horizontal) shear stresses.

As for analysing the effects of grid-reinforcement, there is currently no accepted engineering approach. Models based on the Finite Element Method (e.g., Taherkhani and Jalali, 2017), are computationally expensive and mandate a large number of input parameters. Such an approach is unlikely to gain acceptance among practitioners. Nielsen et al. (2020) proposed to treat a reinforcing grid as a thin layer within the LET framework, characterised by: (i) Young's modulus, (ii) Poisson's Ratio, (iii) an effective thickness, and (iv) conditions of bonding with the adjoining AC layers. From this simple consideration, representing a grid reinforcement could be achieved by relatively few input parameters, without adding extra computational demand to the framework.

The objective of the current work is to analyse and generate initial intuition on the expected effects of installing an interlayer reinforcing grid as part of a mill-and-overlay maintenance treatment. This is pursued synthetically (i.e. utilizing a computational model and not measurements from the field), by considering a layered elastic system representing a traditional asphalt pavement consisting of AC layer, unbound granular base layer, and soil subgrade. A FL is employed to describe an existing (damaged and aged) AC after milling, and a thin high-modulus layer is employed to represent the grid-reinforcement. The paper investigates several cases for a dual-tire assembly loading that differ by the milling depth and by the inclusion or exclusion of an interlayer grid reinforcement. In each case, key responses commonly linked to performance in pavement design are calculated and presented in contour plots; response peaks are subsequently identified and compared. A summary of findings and a short discussion are offered at the end.

2 CASES FOR ANALYSIS

Consider a three-layered pavement system with a 150 mm thick aged and cracked AC layer. This layer rests on an unbound granular base and subbase with a combined thickness of 500 mm. The structure is supported by a subgrade soil extending to a large depth. This pavement is maintained by a mill-and-overlay treatment considering four cases which differ by the milling depth and overlay thickness – see Figure 1. Common to all cases is that the milling depth is equal to the overlay thickness, i.e., returning to the original surface elevation. In Case (a) 30 mm are milled and repaved, in Case (b) 60 mm are milled and repaved, in Case (c) 90 mm are milled and repaved, and in Case (d) the entire aged AC thickness of 150 mm is milled and repaved.
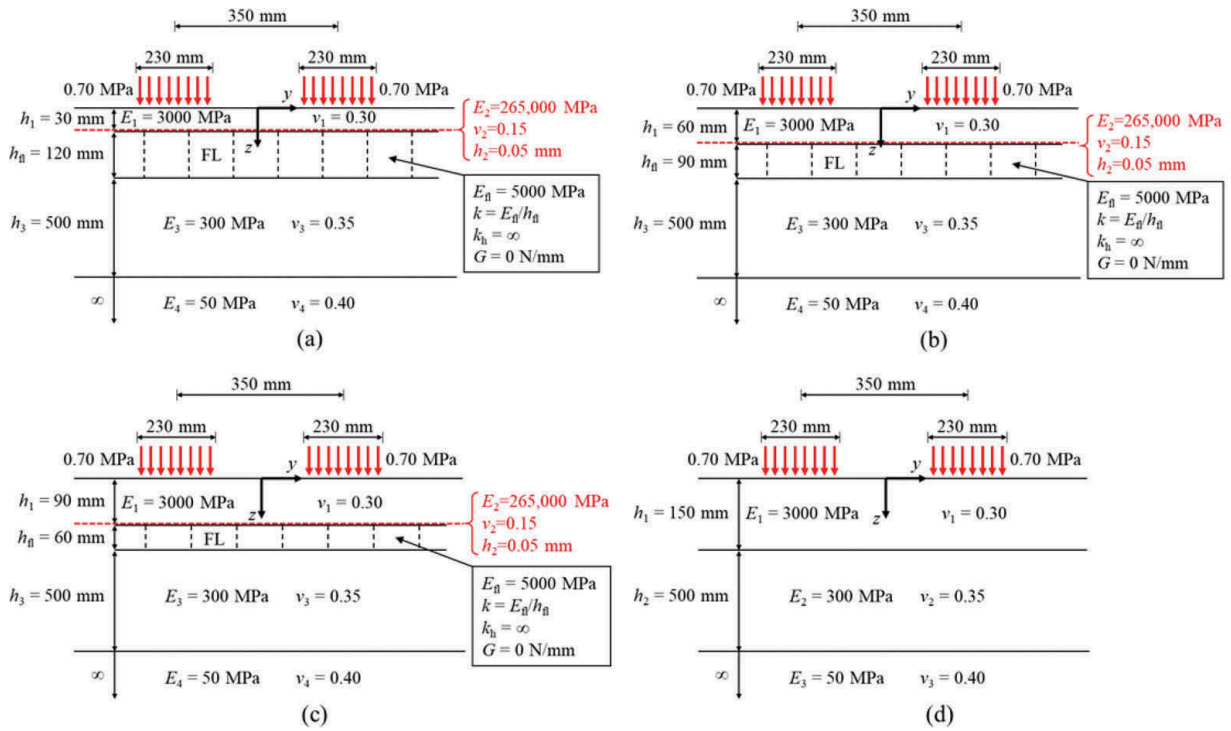
Figure 1.   Cross-sectional view of four pavements for model analysis: (a) 30 mm mill-and-overlay, (b) 60 mm mill-and-overlay, (c) 90 mm mill-and-overlay, and (d) 150 mm mill-and-overlay.

The pavements in Figure 1 are modelled within the LET framework. A Cartesian coordinate system is considered with its origin located at the surface, and the z-axis is oriented towards the subgrade. The model layers are parallel to the x-y plane and extend to infinity. The top layer, representing the AC overlay, has a modulus of $E_1 = 3000$ MPa and Poisson's Ratio $v_1 = 0.30$. Any existing (aged) AC is treated as a FL with a Winkler spring-bed stiffness (k) that is equal to a modulus of $E_{fl} = 5000$ MPa divided by the FL thickness h_{fl}, a horizontal spring-bed stiffness k_h of infinity, and a Pasternak layer providing zero resistance to shear deformation (i.e., $G = 0$). The latter assumption corresponds to a densely cracked AC layer with fragments that do not interact. The choice of 5000 MPa to represent an aged AC modulus (and not 3000 MPa as done for the AC overlay) aims to embody age stiffening. The unbound granular materials are represented by a single layer, with a modulus of $E_3 = 300$ MPa and a Poisson's Ratio $v_3 = 0.35$. The subgrade soil is treated as a semi-infinite medium with $E_4 = 50$ MPa and $v_4 = 0.40$.

As can be seen in Figure 1, a thin layer representing grid-reinforcement is included for the first three mill-and-overlay cases. This layer resides in-between the top layer and the FL and is assumed to be fully bonded to both. The properties of this layer are directly based on an existing grid product – S&P Carbophalt® G 200/200 (S&P 2020). This grid consists of carbon fibres characterised by a modulus of 265 GPa and Poisson's Ratio of 0.15. The carbon fibres are arranged in square openings, 15 mm × 15 mm in size, with an average cross-sectional area per unit width of the grid of about 50 mm^2/m. Thus, the grid characteristics are smeared based on the volume of fibres per unit area to correspond to an layer thickness of $h_2 = 0.05$ mm, modulus of $E_2 = 265,000$ MPa, and Poisson's Ratio $v_2 = 0.15$. In actuality, the grid is almost 1 mm thick because of a bituminous material that coats the fibres. This coating contributes to the bonding with the adjacent AC layers; its contribution to the elastic properties and tensile strength of the grid is considered negligible.

Finally, as shown in Figure 1, all four cases are loaded by two circular areas representing the tire-pavement contact due to a dual-tire assembly. The centres of the circles are located along the y-axis, on each side of the coordinate origin with equal offset. The centre-to-centre spacing is 350 mm, and the diameter is 230 mm. Both areas are uniformly loaded by vertical stress with an intensity of 0.7 MPa. The above-described characteristics are based on the Danish pavement design guidelines for a standard single-axle load of 120 kN (Baltzer et al. 2017).

3 ANALYSIS AND RESULTS

In this section, the first three mill-and-overlay cases in Figures 1a–1c are analysed. The analysis is repeated twice – without and with the inclusion of grid reinforcement. Because Case (d) consists of full removal and repaving of the AC layer, it serves as a reference. Assuming that damage and ageing effects are only confined to the AC layer, Case (d) also represents the pristine mechanical condition of the pavement system. Ultimately, the reinforced cases, unreinforced cases, along with the reference case amount to a total of seven different pavement systems. Calculations were done utilising the LET code ALVA (Skar and Andersen 2020; Skar et al. 2020) that was extended to include the FL formulation from Levenberg and Skar (2020). ALVA is an open-source LET kernel code based on the numerical computing package MATLAB. Soil mechanics sign convention is followed, wherein compressive stresses and strains are positive.

Four key responses are investigated, namely: (i) horizontal strain oriented along the axle direction in the AC overlay ε_y; (ii) von Mises stress in the AC overlay σ_{vm}; (iii) vertical stress in the aggregate base layer σ_z^b; and (iv) vertical stress in the upper 500 mm of the subgrade σ_z^{sg}. The choice to focus on these responses is related to their correlation with cracking and rutting distresses. Specifically, horizontal tensile strains in the AC are closely associated with crack initiation. The von Mises stress in the AC, and the intensity of vertical compressive stresses in the unbound layers and subgrade soil, are all linked to the accumulation of permanent deformation in these materials (Oeser and Möller 2004; Baltzer et al. 2017).

The analysis commenced with a graphical investigation of key response distributions. This was done in the y-z plane for $x = 0$ and for y in the range of ± 600 mm (z is variable). In this context, Figures 2 and 3 present colour-coded contour plots for Case (a) and Case (c) respectively (see Figure 1); these represent a thin overlay situation and a thick overlay situation. Each figure includes four pairs of heat maps, each representing a different key response – one for an unreinforced pavement system (left-hand side) and another for a reinforced pavement system (right-hand side). Peak values of key responses for all four cases are included in Table 1. Note that the colour-coding differs in-between heat map pairs as well as in-between the two figures. To prepare the plots, calculations were performed over a 2 mm × 2 mm grid in the y-z plane.
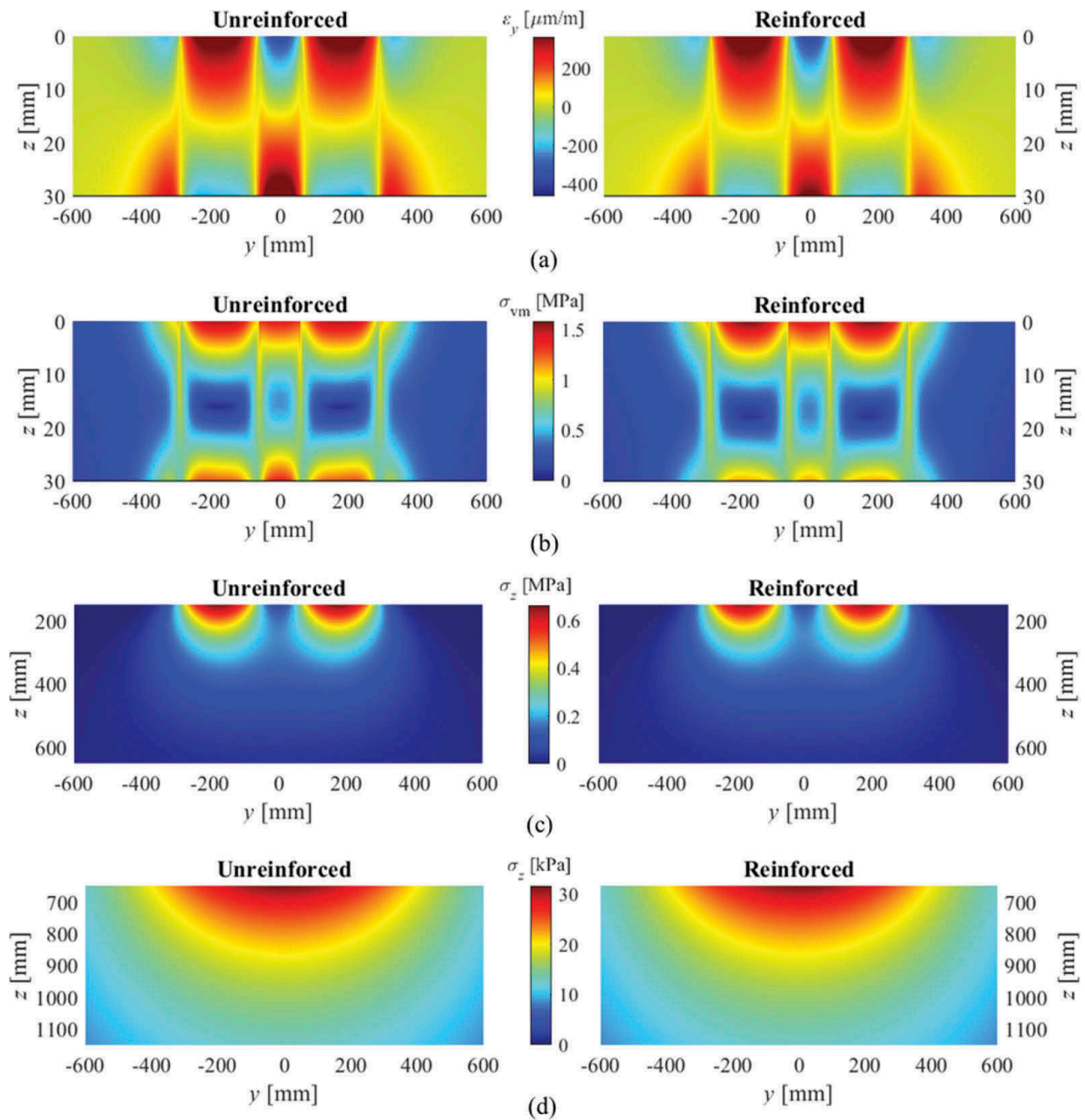
Figure 2. Distributions of the sought key responses in Case (a) of Figure 1: (a) horizontal strain in AC overlay, (b) Von Mises stress in AC overlay, (c) vertical stress in the aggregate base layer, and (d) vertical stress in the subgrade.

Figure 2a presents contour plots of the horizontal strain in y-direction within the thin AC overlay, i.e., for the range of $z = 0$ to $z = 30$ mm. In both plots, it can be observed that under the two loading areas, compressive horizontal strains occur at the AC surface while tensile strains occur at the AC bottom. Outside the loading areas, the strain changes sign from compression to tension at the top, and from tension to compression at the bottom. The peak tensile strain is located in-between the two loading areas. While the two contour plots appear visually similar, the introduction of reinforcement causes a slight reduction in the compressive and tensile strain magnitudes at the bottom of the AC overlay, and a slight increase of strains at the AC surface. Figure 2b presents contour plots of the von Mises stress within the thin AC overlay. In both plots, it can be observed that two peak stress values occur at the top and bottom – directly under and in-between the two loading areas. Visually, the stress peaks are of slightly larger magnitude at the top. The reinforcement appears to generate a reduction in the von Mises stress at the bottom and a slight increase at the top (compared to the unreinforced situation). Figure 2c presents contour plots of the vertical stress in the aggregate base layer

350

within the range of $z = 150$ mm to $z = 650$ mm. In both plots, it can be seen that stresses are only compressive (positive) with two peaks occurring at the surface – directly under the two loading areas. Visually, the stress distributions appear similar for both the unreinforced and reinforced situations. Lastly, Figure 2d presents contour plots of the vertical stress within the subgrade for the depth range $z = 650$ mm (i.e., formation level) to $z = 1150$ mm. In both plots, it can be observed that stresses are only compressive with one peak located at the subgrade surface in-between the two loading areas. Visually, the unreinforced and reinforced situations appear identical.
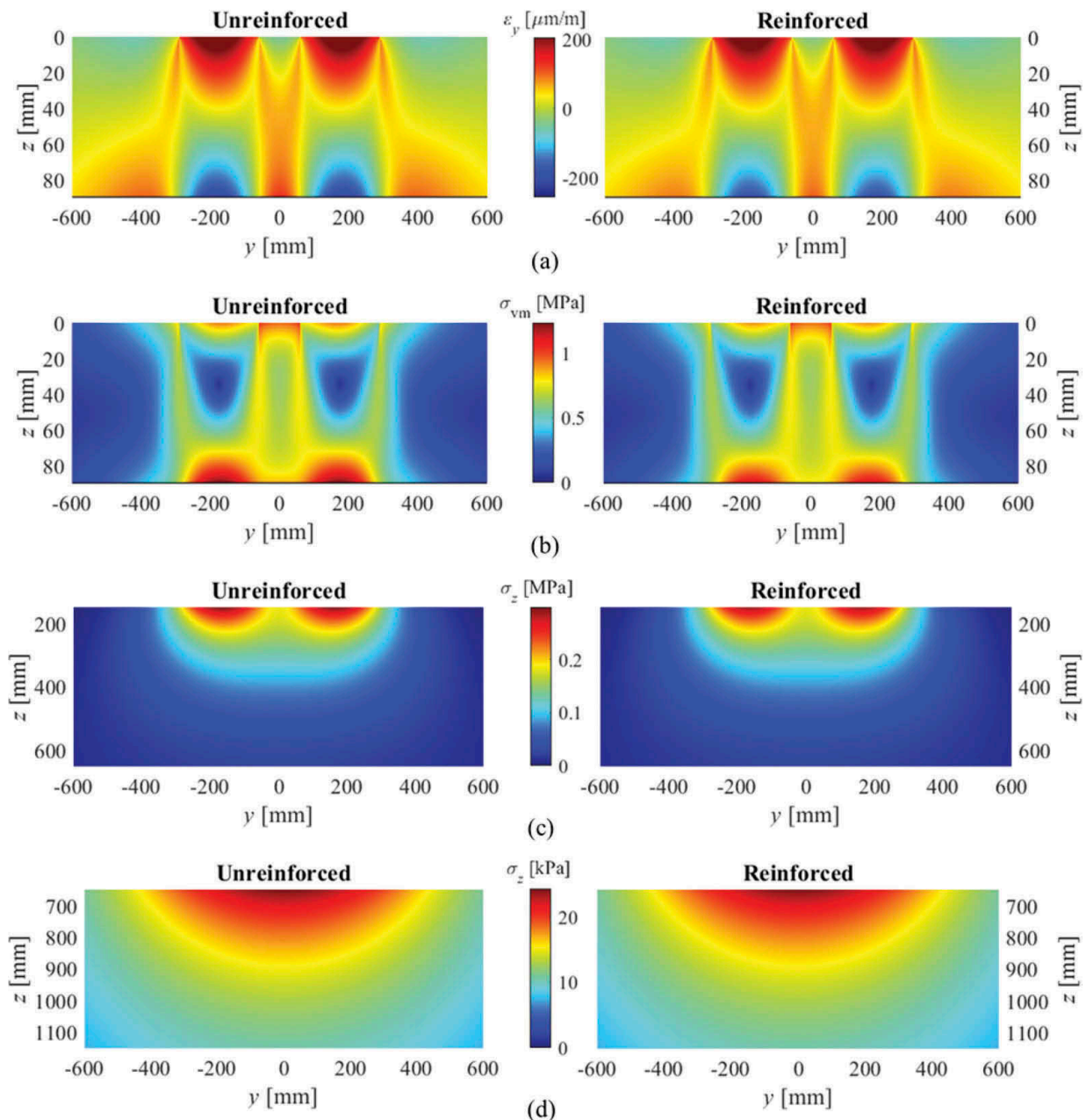
Figure 3. Distributions of the sought key responses in Case (c) of Figure 1: (a) horizontal strain in AC overlay, (b) Von Mises stress in AC overlay, (c) vertical stress in aggregate base layer, and (d) vertical stress in subgrade.

Figure 3a presents contours plots of the horizontal strain in the y-direction within the thick AC overlay, i.e., for the range of $z = 0$ to $z = 90$ mm. In both plots, it can be observed that under the two loading areas, compressive horizontal strains occur at the AC surface while tensile strains occur at the AC bottom. Outside the loading areas, the strain changes sign from compression to tension at the top, and from tension to compression at the bottom. Two peak tensile strains are

identified, each located under one of the two loading areas at the AC bottom. While the two contour plots appear visually similar, the introduction of reinforcement causes a slight reduction in the compressive and tensile strain magnitudes at the bottom of the AC overlay, and a slight increase of strains at the AC surface. Figure 3b presents contour plots of the von Mises stress within the thick AC overlay. In both plots, it can be observed that two peak stress values occur at the bottom – under the two loading areas. The reinforcement appears to generate a reduction in the peak von Mises stress (compared to the unreinforced situation). Figure 3c presents contour plots of the vertical stress in the aggregate base layer within the range of z = 150 mm to z = 650 mm. In both plots, it can be seen that stresses are only compressive (positive) with two peaks occurring at the base's surface – under the two loading areas. Visually, the stress distributions appear similar for both the unreinforced and reinforced situations. Lastly, Figure 3d presents contour plots of the vertical stress within the subgrade for the depth range z = 650 mm (i.e., formation level) to z = 1150 mm. In both plots, it can be observed that stresses are only compressive with one peak located at the subgrade surface in-between the two loading areas. Visually, the unreinforced and reinforced situations appear identical.

Contrasting the contour plots of Figure 2 and Figure 3 (i.e., thin overlay vs. thick overlay), several observations can be made. First, concerning the horizontal tensile strain in the AC layer: in the thin overlay case (Figure 2a) the peak value is located at the surface, in-between the two loading areas (for both situations without and with reinforcement); in the thick overlay case (Figure 3a) there are two peaks, both located at the bottom of the AC, each under a loading area (for both situations without and with reinforcement). Second, concerning the von Mises stresses in the AC layer: in the thin overlay case (Figure 2b) there are two peaks, each located at the surface under a loading area (for both situations without and with reinforcement); in the thick overlay case (Figure 3b), there are also two peaks – however, they are both located at the bottom – each under a loading area (for both situations without and with reinforcement). Third, concerning the vertical stresses in the aggregate base layer: in the thin overlay case (Figure 2c) the stress fields at the base surface are highly concentrated under each of the loading areas (for both situations without and with reinforcement); in the thick overlay case (Figure 3c) the stress fields at the base surface are more smeared in-between the loading areas (for both situations without and with reinforcement). Lastly, concerning the vertical stresses at the top of subgrade; stress fields appear similar when contrasting the thin overlay case (Figure 2d) against the thick overlay case (Figure 3d), regardless of the inclusion or exclusion of reinforcement.

The next analysis step utilised the contour plots in Figures 2 and 3, as well as contour plots for Cases (b) and (d) (which are not presented) to identify response peaks across the different mill-and-overlay cases in Figure 1 (with and without reinforcement). The results are summarised in Table 1 for a total of seven situations. The considered peaks are: (i) horizontal tensile (negative) strain in AC overlay $\varepsilon_{y,min}$, (ii) von Mises stress in AC overlay $\sigma_{vm,max}$, (iii) vertical stress in the aggregate base layer $\sigma^b_{z,max}$, and (iv) vertical stress in the subgrade $\sigma^{sg}_{z,max}$.

Table 1. Peak values of key responses for all four cases in Figure 1 without reinforcement (w/o) and with reinforcement (w).

	Case (a)		Case (b)		Case (c)		Case (d)
	w/o	w	w/o	w	w/o	w	w/o
$\varepsilon_{y,min}$ [μm/m]	-355	-364	-260	-222	-206	-181	-134
$\sigma_{vm,max}$ [MPa]	1.51	1.58	1.49	1.31	1.24	1.11	0.83
$\sigma^b_{z,max}$ [MPa]	0.66	0.65	0.43	0.42	0.30	0.29	0.17
$\sigma^{sg}_{z,max}$ [kPA]	31.7	31.5	27.7	27.7	24.3	24.2	18.6

First, with respect to the peak tensile strain in the AC overlay: in the thin overlay case, i.e., Case (a), including reinforcement leads to a marginal 2% increase compared to the unreinforced situation; in the thicker overlay cases, i.e., Case (b) and Case (c), including reinforcement lead to a 15% and 12% reduction (respectively) compared to the unreinforced situation. Second, with respect to the peak von Mises stress in the AC overlay: in the thin overlay case, i.e., Case (a), including reinforcement leads to a marginal 4% increase compared to the unreinforced situation; in the thicker overlay cases, i.e., Case (b) and Case (c), including reinforcement lead to an 11% and 10% reduction (respectively) compared to the unreinforced situation. Third, with respect to the peak vertical stress in the aggregate base layer, including reinforcement has a marginal reduction in Case (a), Case (b) and Case (c) compared to the unreinforced situation (respective reduction of 2%, 4%, and 3%). Fourth, with respect to the peak vertical stress on top of the subgrade, including reinforcement has a negligible effect in Case (a), Case (b) and Case (c) compared to the unreinforced situation. Lastly, the table shows that all four peak responses are lowest for Case (d).

4 CONCLUSION

The objective of this work was to provide initial intuition on the effects of introducing inter-layer reinforcing grid into a mill-and-overlay maintenance treatment. The analysis was based on a three-layered pavement system subjected to surface loading of a dual-tire assembly, consisting of an AC layer supported by an aggregate base layer resting on a subgrade soil extending to a large depth. The analysis utilised the LET framework to synthetically investigate three mill-and-overlay cases and a reference case. A FL was applied to represent the fully damaged and aged AC layer that was retained in the structure after milling. The reinforcing grid, introduced in-between the FL and the AC overlay, was modelled as a thin high-modulus layer. In each case, horizontal strains and von Mises stresses in the AC overlay, along with vertical stresses in the aggregate base and subgrade were simulated and presented in contour plots for selected cases. Based on these simulations, peaks were identified and contrasted across the different cases.

From this investigation it was found that: (i) for a thick overlay case, the peak tensile strain was located at the bottom – implying bottom-up cracking mode. Adding reinforcement reduced the peak horizontal tensile strain and peak von Mises stress – suggesting potential reduction in cracking and permanent deformation within the overlay; (ii) for a thin overlay case, the peak tensile strain was located at the surface – implying top-down cracking mode. Adding reinforcement marginally increased the peak tensile strain and peak von Mises stress (possibly due to a slight downward shift in the neutral bending axis of the overlay) – suggesting that the reinforcement is ineffective; and (iii) for both thick and thin overlay cases, adding reinforcement has marginal positive effect on the peak vertical stress in the aggregate base layer, and negligible effect on the peak vertical stress in the subgrade.

In studies dealing with grid-reinforced granular base layers, it has been shown that the presence of the grid affects the medium properties in its vicinity – within a so-called transition zone (Luo et al. 2017). This is due to the stress-dependent nonlinear nature of geo-materials, and was not considered in the current analysis. One approach to account for the transition zone within LET framework is to assign an effective (fictitious) modulus to the grid and retain its physical smeared thickness. Such an approach was suggested in the work of Kutay et al. (2020) for grid-reinforced granular base layers, where the modulus within the transition zone was increased. In this context, the grid modulus utilised in this research can be considered as a lower limit value, given that it only represents the actual reinforcement modulus and does not account for the transition zone. In future studies, it is planned to characterise the effective grid modulus based on full-scale experimental investigations. Furthermore, it is anticipated that the effective modulus would appear to be rate- and temperature-sensitive, corresponding to the mechanical nature of AC mixtures.

REFERENCES

Baek, C., Underwood, B. S., Kim, Y. R., 2012. *Effects of Oxidative Aging on Asphalt Mixture Properties.* Transportation Research Record, Vol. 2296(1), pp. 77–85. https://doi.org/10.3141/2296-08

Baltzer, S., Tønnesen, P., Gleerup, S., Holst, M. L., & Thorup, C, 2017. *Design of pavements and reinforcement layers.* Vejregler – Danish Road Directorate, Ministry of Transport, Building and Housing.

Bell, C. A., Wieder, A. J., and Fellin., M.J., 1994. *Laboratory aging of asphalt-aggregate mixtures: field validation.* Washington, DC: Strategic Highway Research Program, National Research Council.

Correia, N. d. S and Bueno, B.d. S., 2011. *Effect of bituminous impregnation on nonwoven geotextiles tensile and permeability properties.* Geotextiles and Geomembranes, vol. 29, no. 2, pp. 92–101. https://doi.org/10.1016/j.geotexmem.2010.10.004

EAPA and NAPA, 2011. *The asphalt paving industry a global perspective.* Third Edition

Harvey, J., and B. W. Tsai., 1997. *Long-Term Oven Aging Effects on Fatigue and Initial Stiffness of Asphalt Concrete.* Transportation Research Record. Vol. 1590(1), pp. 89–98.

Kutay, M. E., Hasnat, M., and Levenberg, E., 2020. *Layered Nonlinear Cross Anisotropic Model for Pavements with Geogrids.* Submitted for proceedings of Advances in Materials and Pavement Performance Prediction, Aug 3–7.

Lemaitre, J. and Desmorat, R., 2005. *Engineering Damage Mechanics.* Springer-Verlag Berlin Heidelberg. https://doi.org/10.1007/b13888210

Levenberg, E. and Skar, A., 2020. *Analytic pavement modeling with a fragmented layer.* International Journal of Pavement Engineering, 1–13. https://doi.org/10.1080/10298436.2020.1790559

Luo, R., Gu, F., Luo, X., Lytton, R. L., Hajj, E. Y., Siddharthan, R. v., Elfass, S., Piratheepan, M., Pournoman, S., 2017. *Quantifying the Influence of Geosynthetics on Pavement Performance.* Transportation Research Board. https://doi.org/10.17226/24841

Mamlouk, M., Zaniewski, J., Houston, W. and Houston, S., 1990. *Overlay design method for flexible pavements in Arizona.* Transportation research record, Vol. 1286, pp. 112–122.

National Academies of Sciences, Engineering, and Medicine (NASEM), 2007. *Environmental Effects in Pavement Mix and Structural Design Systems.* Washington, DC: The National Academies Press. https://doi.org/10.17226/23244

Nielsen, J., Olsen, K., Levenberg, L., and Skar, A., 2020. *Fleksible belægninger med asfaltarmering - Mekanisk beregningsmodel.* Trafik og Veje - April, pp.15–18. (In Danish)

Oeser, M., and Möller, B, 2004. *3D constitutive model for asphalt pavements.* International Journal of Pavement Engineering, 5(3), 153–161. https://doi.org/10.1080/10298430412331314281

S&P (2020), *S&P Carbophalt® G 200/200 Pre-bituminised asphalt reinforcement.* https://www.sp-reinforcement.eu/sites/default/files/field_product_col_doc_file/tds_carbophalt_g_200200_eu_en_0.pdf (date accessed October 7, 2020).

Skar, A. and Andersen, S., 2020. *ALVA: An adaptive MATLAB package for layered viscoelastic analysis.* Journal of Open Source Software, Vol. 5(52), 2548. https://doi.org/10.21105/joss.02548

Skar, A., Andersen, S., and Nielsen, J., 2020. *Adaptive Layered Viscoelastic Analysis (ALVA).* Technical University of Denmark. Software. https://doi.org/10.11583/DTU.12387305

Taherkhani, H. and Jalali, M., 2017. *Investigating the performance of geosynthetic-reinforced asphaltic pavement under various axle loads using finite-element method.* Road Materials and Pavement Design, Vol. 18(S5), pp. 1200–1217. https://doi.org/10.1080/14680629.2016.1201525

Zofka, A., Maliszewski, M., and Maliszewska, D., 2017. *Glass and carbon geogrid reinforcement of asphalt mixtures.* Road Materials and Pavement Design, Vol. 18(S1), pp. 471–490. https://doi.org/10.1080/14680629.2016.1266775

Paper i.   Analytic analysis of a grid-reinforced asphalt concrete overlay

Modeling and Analysis of Pavements with Asphalt Reinforcement

Mechanistic modelling of grid-reinforced milled-and-overlaid asphalt pavements

Julius Nielsen, Eyal Levenberg, and Asmus Skar

Taylor & Francis
Taylor & Francis Group

Check for updates

Mechanistic modelling of grid-reinforced milled-and-overlaid asphalt pavements

Julius Nielsen [a,b], Eyal Levenberg [a] and Asmus Skar [a]

aDepartment of Civil Engineering, Technical University of Denmark, Kgs. Lyngby, Denmark; bS&P Reinforcement Nordic ApS, Odder, Denmark

ABSTRACT

This study was motivated by the need for a mechanistic-empirical (ME) design method applicable to asphalt pavements after mill-and-overlay repairs that include reinforcing grids; the focus was solely on the mechanistic component. A new model, based on layered theory, was developed – coupling in one single framework the following features: elastic layers for representing subgrade and unbound layers, fragmented layers for representing existing aged and densely cracked asphalt concrete (AC), imperfect bonding conditions for representing any differential slippage between adjoining layers, thermo-viscoelastic layer properties for representing new AC, and moving loads for representing traffic conditions. Grid effects were modelled as a combination of three contributions: the presence of an additional thin high-modulus elastic layer within the pavement system, the influence of a grid on interlayer bonding between layer above and below it, and the influence of a grid on the properties of the surrounding AC. These contributions require new grid-related modelling inputs that are physically meaningful and generic – not limited to any specific product. A secondary objective of the work was to generate some initial intuition on the mechanistic effects of interlayer grids. Accordingly, the new model was demonstrated in a parametric investigation covering a synthetic milled-and-overlaid structure with and without reinforcement. Findings from this demonstration provided an initial validation for the new model, given the conformity to findings from experimental studies. Overall, the new model is deemed a candidate computational engine for a ME design applicable to new and rehabilitated asphalt pavement systems. Furthermore, it can serve as an analysis tool to guide manufacturers on improving their products or showcasing existing capabilities in a quantified manner. Lastly, the new model can support the design of experimental setups for assessing grid effects within asphalt pavement systems, and therefore ensure the collection of usable measurements for subsequent mechanistic interpretation.

1. Introduction

Mill-and-overlay is a widely used repair technique for asphalt pavements (Huang 2004; MTO 2013; Caltrans 2020); it refers to partial-depth milling of the existing asphalt concrete (AC) followed by repaving with new AC. The overlay thickness can vary within a wide range, from tens of millimetres (paved in a single lift) up to tens of centimetres (paved in several lifts). This technique eliminates surface cracks, ruts, and local unevenness; it improves skid resistance and reduces roughness. The entire operation is relatively fast, does not require lane closures for extended periods, and causes minimal delays as vehicles are often permitted to travel over the milled surface before overlaying. In milled-and-overlaid pavements, exposed to a given set of loading and environmental conditions, the overlay's longevity depends on its thickness and properties, as well as on the support offered by the underlying pavement system. With respect to the latter, the overlay is commonly paved directly on top of the existing (retained) AC, which is usually in a damaged and cracked state. The presence of cracks and discontinuities in the retained AC is often a contributing factor to the premature failure of the new overlay (Germann and Lytton 1979; Lytton 1989).

One emerging approach for prolonging overlay longevity is installing a reinforcing grid on top of the milled surface prior to paving or alternatively within the overlay itself in-between two new AC lifts (Lytton 1989; Chang et al. 1999; de Bondt 1999; Cleveland et al. 2001; Button and Lytton 2007; Asphalt Academy 2008; Khodaii et al. 2009). Reinforcing grids, also referred to as geogrids or paving grids, are a sub-category of geosynthetics that are composed of high-modulus materials in a mesh-like arrangement (Cleveland et al. 2001; Asphalt Academy 2008; Nithin et al. 2015; Solatiyan et al. 2020). Grid materials commonly include: polyester, glass-fibre, and/or carbon-fibre (Cleveland et al. 2001; Sanders 2001; Zofka et al. 2017; Lee et al. 2019). Limited-scale studies, isolated laboratory experiments, and some full-scale test sections have demonstrated a potential for grids to benefit pavement performance in terms of fatigue cracking (Nguyen et al. 2013; Arsenie et al. 2017; Vinay Kumar and Saride 2017; Correia and Zornberg 2018) and rutting (Ong et al. 2004; Sobhan 2005; Lee et al. 2015; Correia and Zornberg 2016). Despite these potential benefits, there is currently no widely accepted method to quantify grid reinforcement effects in a unified and rational manner.

This study is motivated by the need for a mechanistic-empirical (ME) design method (ARA Inc. 2004) applicable to asphalt pavements after mill-and-overlay repairs that include reinforcing grids. The focus herein is on the mechanistic component, which is concerned with response evaluation

(and not on the empirical component). This component can later be used for quantifying pavement performance. Additionally, it provides a rational framework for evaluating different scenarios with no past experience and can guide the design of experimental setups for calibration and field validation. Accordingly, the development of a mechanistic model is sought, capable of providing traffic-induced stresses, strains, and displacements in such pavement systems. The choice herein is to rely on Layered Elastic Theory (LET) as a modelling kernel (Burmister 1943, 1945a, 1945b, 1945c; Peutz *et al.* 1968) that is further expanded to include time- and-temperature dependent layer properties with moving loads (Levenberg 2016), as well as other effects that are relevant for the problem at hand. The main reason for this choice is that LET, which already serves the majority of current pavement design and analysis codes (e.g. Shell 1978; Shook *et al.* 1982; ARA Inc. 2004; AUSTROADS 2004; Huang 2004), is a computationally efficient and verified engineering-accepted mechanistic engine.

The paper commences with a literature review focussed on current engineering approaches for the mechanistic modelling of milled-and-overlaid asphalt pavements and grid-reinforced AC layers. The review is followed by stating the specific study objectives and outlining the methodology chosen for achieving them. Presented next is a new modelling formulation that is capable of emulating principal mechanisms associated with grid-reinforced milled-and-overlaid asphalt pavements. This is followed by demonstrating the new model, wherein two mill-and-overlay systems are synthetically investigated – one excluding reinforcement and another including reinforcement. The paper ends with a summary of the entire work effort and a discussion of the main findings and their general/future implications.

2. Literature review

2.1. Modelling of milled-and-overlaid pavements

Milled-and-overlaid asphalt pavements typically contain aged and cracked AC purposefully retained to facilitate the repair activities, e.g. avoiding the need to deal with the supporting/ underlying unbound materials. From a mechanical viewpoint, a cracked and aged AC layer can offer high vertical rigidity due to material ageing (Bell *et al.* 1994; Harvey and Tsai 1997; Baek *et al.* 2012), alongside poor bending rigidity due to discontinuities (cracks). The prevailing LET-based approach for modelling such rehabilitated systems is to assign a reduced elastic modulus to the damaged AC (Ullidtz 1987). The overall idea originates from continuum damage mechanics (Lemaitre and Desmorat 2005), which deals with the behaviour of a medium containing many small randomly distributed cracks. In practice, the damaged AC modulus is estimated based on matching surface deflections (Maestas and Mamlouk 1992; Collop and Cebon 1996; Le *et al.* 2017; Skar *et al.* 2020b) or based on visual inspections (ASTM 2020). Numerous design guides follow this approach, e.g. American Association of State Highway and Transportation Officials ME (AASHTO ME) (ARA Inc. 2004), California ME (CalME) (Ullidtz *et al.* 2010), CART Overlay Design for Arizona (CODA) (Mamlouk *et al.* 1990),

Mathematical Model of Pavement Performance (MMOPP) (Vejdirektoratet 2017), and Trafikverkets tekniska krav Väg-konstruktion (TRVK) (Trafikverket 2011).

The reduced modulus approach was experimentally evaluated by Mateos *et al.* (2013). In this study, a full-scale experiment was carried out at the Centro de Estudios y Experimentacion de Obras Publicas (CEDEX) Transport Research Center test track. A 65 kN dual-wheel load, moving at a speed of 40 km/h, was repeatedly applied (until failure) to newly constructed asphalt pavement sections. These sections were instrumented with embedded sensors for measuring stresses, strains, and surface displacements. The measured responses were compared to LET calculations combined with the CalME reduced AC modulus approach. The study demonstrated that the modulus reduction approach worked well for matching surface displacements under tire loads before and after cracks appeared. However, it was unable to correctly capture and reproduce the measured in-pavement responses once the AC was cracked. In particular, unrealistically low-modulus values for the damaged AC were required in order to match measured in-pavement vertical stress levels. The authors concluded by stating that the reduced modulus approach should not be considered appropriate for rehabilitation design.

The modelling challenge of including cracked layers within LET was addressed in Levenberg and Skar (2020) by introducing fragmented layers (FLs). Essentially a FL is composed of Winkler spring-bed(s) (Winkler 1867) coupled to Pasternak-like shear layer(s) (Pasternak 1954). Two FL arrangements were proposed, a P-Type where a Winkler spring-bed is placed in-between two shear layers, and a K-type where a shear layer is placed in-between two spring-beds. Unlike continuous isotropic layers, a FL can reproduce high vertical rigidity and simultaneously low or negligible bending rigidity. This is more in tune with the actual/expected behaviour when an existing aged and cracked AC is retained in the process of mill-and-overlay repairs. The new formulation was applied to the case of block paving (another type of discontinuous layer) and compared against finite element analysis (FEA). It was shown that for small block sizes relative to the radius of the loaded area, the formulation yields results similar to the FEA, while for large block sizes, the results diverge. This means that the FL formulation is applicable for representing densely cracked layers, but not for representing layers with a single or a few cracks.

2.2. Modelling of grid reinforcement in AC layers

Although LET is employed as a response model in the majority of accepted mechanistic-based design codes, attempts to incorporate grid reinforcement within this framework are scarce. Graziani *et al.* (2014) investigated the mechanical responses of full-scale grid-reinforced asphalt pavements instrumented with embedded stress and strain sensors. LET was employed to analyse sensor readings under moving truckloads and falling weight deflectometer (FWD) drops. As the reinforcement was placed in-between two AC layers, two modelling approaches were attempted: (i) the reinforcing grid and its neighbouring AC layers were treated as one single (combined) layer, characterised by an equivalent modulus; and (ii) each AC layer was

assigned an individual modulus, and an imperfect bonding level was introduced between them. As an independent component, the grid was not directly included in either approach; its mechanical effect was assumed to be included as part of the AC properties. This study showed that it is possible to match each sensor reading by manipulating the LET model parameters. A simultaneous matching of all sensor and FWD readings was not demonstrated. The authors noted that a more advanced modelling approach is required for analysing the experimental data.

The work of Sanders (2001) was focussed on the performance of grid-reinforced overlays; it included laboratory and large-scale wheel-tracking tests as well as two-dimensional FEA. As part of this work, the author suggested including the grid within LET as a thin layer, with a thickness corresponding to the grid's thickness and a high elastic modulus to represent the grid's material. The idea was put forward purely based on intuition; it was not experimentally or synthetically explored further. Noted limitations to this approach were: (i) how to correctly account for bonding conditions with the grid; (ii) how to account for grid geometry, which is mesh-like; and (iii) how to deal with cracked layers supporting the grid.

Nielsen *et al.* (2020) followed the suggestion of Sanders (2001), and modelled a reinforcing grid (within LET) as a thin high-modulus layer. To address some of the above limitations, imperfect bonding between the grid and one of the adjacent AC layers was assumed; the other interface was taken as perfectly bonded. This was done by assigning a horizontal spring constant to the partially bonded interface, following the classical approach of Goodman and Popov (1968). To account for the mesh-like grid geometry, the reinforcement was assigned an effective thickness based on smearing the physical grid into a uniform continuous solid. From a synthetic study, it was concluded that the critical horizontal tensile strain at the bottom of an AC layer is highly influenced by choice of the effective thickness and the horizontal spring constant value. With respect to the latter, studies have pointed out that bonding conditions in-between AC layers or between reinforcement and an AC layer are time- and temperature-dependent (Canestrari and Santagata 2005; Leischner *et al.* 2019; Sagnol *et al.* 2019).

In the work of Nielsen *et al.* (2021), LET including a FL was considered in order to analyse grid-reinforced milled-and-overlaid asphalt pavements. A thin high-modulus layer was used to represent the reinforcement, located in-between a continuous layer (representing an AC overlay) and a FL – representing an existing aged and cracked AC. An effective thickness for the reinforcement layer was chosen based on the geometry of an existing grid product, and fully bonded layer interfaces were assumed. From a synthetic investigation that considered a dual-tire loading, it was found that adding reinforcing grids to cases with thick overlays would potentially benefit the AC overlay in terms of permanent deformation and bottom up cracking. For thin overlay cases, the grid reinforcement effect was deemed negligible.

2.3. Summery and research gaps

When attempting to model grid-reinforced asphalt pavement systems, the formulation must consider several concurrent/simultaneous mechanisms that have not yet been included in previous studies. First and foremost, this involves AC's visco-elastic (VE) nature. Nowadays, an increased emphasis is placed on the inclusion of linear VE properties and moving loads to mechanistic response models (Chabot *et al.* 2010; Levenberg 2016; Skar and Andersen 2020). VE characterisation is already an indirect part of several design codes (AASHTO 2011, 2017; CEN 2012). Second, studies dealing with grid reinforcement in unbound granular layers (Konietzky *et al.* 2004; Kwon and Tutumluer 2009; Gu *et al.* 2016; Luo *et al.* 2017; Kutay *et al.* 2020) commonly refer to a mechanism called the Zone of Influence (ZoI) (McDowell *et al.* 2006; Schuettpelz *et al.* 2009). The ZoI mechanism originates from local interlocking between aggregates and grid apertures (or openings). Under certain stress conditions, this interlocking generates added confinement in the granular material, leading to an increase in moduli within zones close to the grid – above and below it. Under load-induced stress conditions, the added confinement diminishes away from the loaded area; hence the ZoI mechanism is fundamentally nonlinear. Like granular materials, studies have shown that stress confinement has a similar effect on AC under high-temperature conditions and slow loading situations (Pellinen and Witczak 2002; Zhao *et al.* 2012). Accordingly, the ZoI mechanism should also apply to grid-reinforced AC layers in some situations.

In summary, a modelling approach that combines all features above is missing. Specifically, a single model that includes the following: (i) FLs to represent damaged and cracked AC; (ii) time- and temperature-dependent bonding conditions between layers; (iii) AC with VE properties; (iv) moving loads; and (v) interlayer grid-reinforcement with ZoI mechanism;.

3. Objective and methodology

The main objective of this work is to outline a mechanistic modelling approach for analysing the situation of an asphalt pavement that has been repaired by mill-and-overlay and includes an interlayer grid reinforcement. The computational engine for the proposed model is based on further extending the semi-analytic LET framework to include the following: (i) FLs for capturing old and damaged AC behaviour according to Levenberg and Skar (2020); (ii) imperfect bonding for capturing relative slippage between layers adopting the horizontal spring approach of Goodman and Popov (1968); (iii) linear VE properties and moving loads under isothermal conditions for capturing realistic AC responses and traffic loads using Schapery's quasi-elastic approximation (Schapery 1962); (iv) grid reinforcement as a thin high-modulus isotropic and homogeneous elastic layer – continuing the approach suggested in Nielsen *et al.* (2021); and (v) the ZoI effect for simulating the potential influence of a grid on nearby material. With respect to the latter, a new formulation is suggested for this purpose, wherein the grid's neighbouring layers are divided into sub-layers, and the material properties of the sub-layers closest to the grid are manipulated.

A secondary objective of this work is to generate some initial intuition on the mechanistic effects interlayer grids have on pavement responses. Accordingly, the new model is

applied/demonstrated in a parametric investigation covering a synthetic milled-and-overlaid structure with and without reinforcement – subjected to a single tire load moving at a constant speed along a straight line. Key responses, commonly associated with pavement performance in ME design, are computed and contrasted for some pre-selected set of model input parameters and for a wide range of AC temperature levels and load travel speeds.

4. Modelling

A new mechanistic modelling approach is outlined hereafter for analysing a mill-and-overlay repair solution with the inclusion of an interlayer grid reinforcement. The approach is split into three components: (i) a time-independent elastic formulation, essentially based on the LET solution with static loading, variable bonding level at the interfaces, and the consideration of FLs; (ii) a linear VE formulation that extends the elastic formulation to accept time and temperature dependence in some of the system properties, as well as moving loads; and (iii) a new interlayer grid reinforcement formulation that accounts for the grid's material properties and geometry. Ultimately, the modelling approach offers elastic and VE layer properties, moving loads, presence of FLs, imperfect interlayer bonding, and grid effects – in one single framework.

4.1. Elastic formulation

The elastic formulation (see Figure 1(a)) considers $I-1$ parallel layers, each of finite thickness h_i (where the subscript i is a layer identifier) resting on top of a semi-infinite medium (Layer I). Undamaged layers are assumed isotropic, homogeneous and weightless, each characterised by two elastic parameters: Young's modulus E_i and Poisson's ratio ν_i. Damaged and cracked layers are treated as P-type FLs (see Levenberg and Skar 2020), each characterised by the following parameter set (replacing E_i and ν_i): vertical stiffness k_i (units of force/length^3), horizontal stiffness $k_{h,i}$ (units of force/length^3), and a shear deformation resistance G_i (units of force/length).

The surface of the top layer (Layer 1) is exposed to a stationary vertical load with uniform stress intensity q operating over a circular area with radius a. With respect to a cylindrical coordinate system having its origin positioned under the load, the responses within the undamaged layers are: stresses $(\sigma_r)_i$, $(\sigma_\theta)_i$, $(\sigma_z)_i$, and $(\tau_{rz})_i$; corresponding strains $(\varepsilon_r)_i$, $(\varepsilon_\theta)_i$, $(\varepsilon_z)_i$, and $(\varepsilon_{rz})_i$; and displacements $(U_r)_i$ and $(U_z)_i$. Since a FL is not a continuum solid, stresses and strains cannot be reported in such a layer – only displacements.

Imperfect bonding conditions are introduced between an undamaged layer i and an undamaged layer $i+1$. The modelling is done according to Goodman's approach by introducing a horizontally-oriented spring-bed $k_{b,i}$ (units of force/ length^3) at the interface. In the extreme case of $k_{b,i} \to \infty$, a fully bonded interface between the two layers is obtained, i.e. forcing the continuity of U_r across the interface $(U_r)_i = (U_r)_{i+1}$. The case of $k_{b,i} = 0$ means zero bonding, i.e. no shear stresses are transferred between the two layers, i.e. $(\tau_{rz})_i = (\tau_{rz})_{i+1} = 0$ is forced on the interface.

4.2. Viscoelastic formulation with moving loads

The elastic formulation (outlined in the previous subsection) is herein extended to a VE formulation that provides the time-temperature dependent pavement responses triggered by a non-stationary load. The formulation is based on Schapery's quasi-elastic approximation considering isothermal conditions. The system configuration in the elastic problem is utilised (see Figure 1(b)), but with time-dependency assigned to the undamaged layer properties, the FL properties, the interface bonding conditions, and the loading intensity. The applied loading moves along the surface with an instantaneous speed $V(t)$ along a defined path.

The starting point for the formulation is the solution to a corresponding elastic system under static loading with unit step stress intensity:

$$R^e(t) = R_H^e(b_1, b_2, \ldots, c_1, c_2, \ldots) \cdot H(t) \qquad (1)$$

where $R^e(t)$ is any elastic response of interest at a specific location (i.e. stress, strain, or displacement) at time t; $R_H^e(\cdot)$ is the kernel function or unit-response function of the elastic problem; $b_1, b_2, \ldots$, denote the following inputs to the elastic problem: layer thicknesses, load radius (if several loads operate simultaneously, then radii and spacings), and coordinates of the response location relative to the load position(s); $c_1, c_2, \ldots$, denote the following inputs to the elastic problem: elastic moduli, Poisson's ratios, interface bonding conditions, and FL properties. The distinction between the b inputs and the c inputs is that the former remain constant for the VE formulation while the latter can accept time-dependence. Lastly, $H(t)$ denotes the Heaviside function – representing a unit step stress.

The next formulation step follows the quasi-elastic approximation, which states that the unit response function of the corresponding VE system $R_H^{ve}(t)$ is basically the elastic kernel $R_H^e(\cdot)$ with some inputs replaced by their corresponding time-dependent inputs. The formal representation of this approximation is:

$$R_H^{ve}(t) \approx R_H^e(b_1, b_2, \ldots, c_1(t), c_2(t), \ldots) \qquad (2)$$

where $c_1(t), c_2(t), \ldots$, are time-dependent properties corresponding to $c_1, c_2, \ldots$,.

The last formulation step is introduced to account for a loading that is non-stationary. This is done by superposing several VE stationary solutions that are closely spaced along a movement path where every location is loaded and later unloaded. Mathematically, unloading is done through re-loading but with a negative sign. When this load-unload procedure is done sequentially, a moving load is simulated. The delay in time between loading and unloading, together with the spacing between adjacent solution locations, reflects the instantaneous moving speed $V(t)$. Ultimately, the formulation takes the following form:

$$R^{ve}(t) = \sum_\alpha \int_{\tau=0}^t R_{H,\alpha}^{ve}(t - \tau) \, dI_\alpha(\tau) \qquad (3)$$

where $R^{ve}(t)$ is the VE response evaluated at time t and at a specific position (triggered by the moving load), τ is a time-
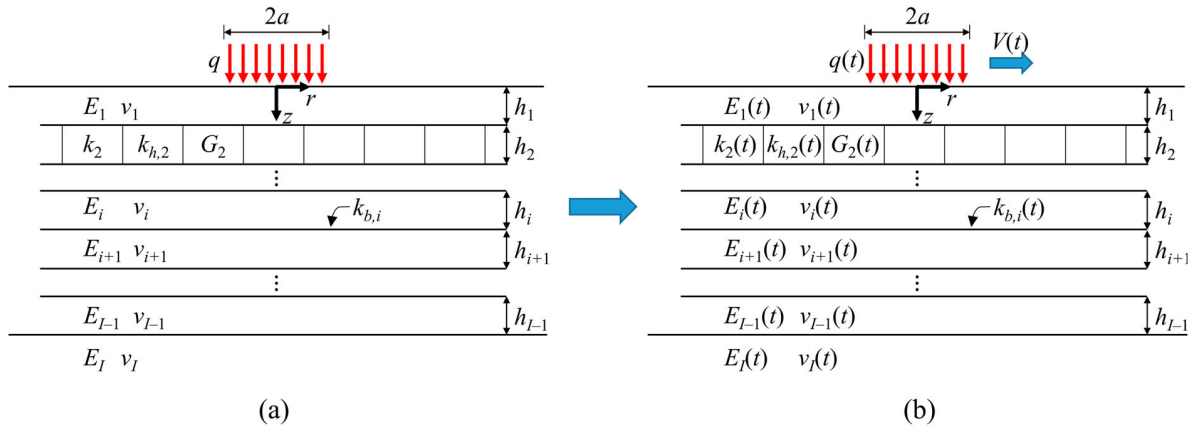
Figure 1. Cross-sectional view of: (a) a stratified pavement model with variable interlayer bonding conditions containing elastic layers and a FL, exposed to a stationary load, and (b) a time-dependent stratified pavement model with variable interlayer bonding conditions containing VE layers and a FL, exposed to a moving load.

like integration variable, and $I_\alpha(t)$ denotes a stationary time-dependent load-unload stress history (applied at the surface). The subscript α (an integer) indicates the location where $I_\alpha(t)$ operates and the terms $R_{H,\alpha}^{ve}(t)$ are individual VE kernel functions each associated with the location α. The integration part is essentially the Boltzmann superposition integral, which allows for evaluating the effect of $I_\alpha(t)$ on the VE response at time t. The summation over all α values ultimately produces the sought (overall) VE response at the point of interest. More details as well as graphical representation of this formulation can be found in Levenberg (2013).

4.3. Formulation of grid reinforcement in AC layers

The effects of introducing an AC reinforcing grid into a pavement system are decomposed into three contributions: (i) the existence of the grid itself as a new material in the system, (ii) the influence the grid has on interlayer bonding, and (iii) the influence the grid has on the properties of the surrounding AC due to the ZoI effect.

4.3.1. Grid as a new material in the pavement system
The first grid contribution is captured by modelling the grid as a thin undamaged elastic layer. In this case, there are three model inputs: an effective thickness and effective elastic properties (Young's modulus and Poisson's ratio). The effective thickness is a model entity that translates the grid's aperture

Figure 2. Conceptual behaviour of bonding parameters above and below the grid as a function of EAS over NMAS.

geometry (i.e. grid opening shape) and any differences in thickness (e.g. due to a different number of fibre strands in different directions) into a uniformly thick homogeneous layer. Herein, the effective thickness is obtained by smearing out the overall grid's volume. The validity of smearing a grid into a layer is viewed herein to depend on the ratio between some effective aperture size (EAS), e.g. the square root of an aperture area, and the AC's nominal maximum aggregate size (NMAS). For a continuum model to apply, this ratio should comply with representative volume element (RVE) considerations and therefore should not exceed about five (Weissman *et al.* 1999; Kim *et al.* 2010). When the EAS-NMAS ratio approaches zero, a membrane situation transpires – for which the reinforcement is, in fact, a thin homogeneous layer.

The effective elastic properties are model entities that reflect the grid's material composition. If the grid ribs are made of one material, the effective elastic properties are taken as the rib properties. Suppose the grid ribs are made of more than one material; in that case, some averaging must be done to assign an effective modulus (given the isotropic assumption in the modelling framework). In general terms, if the effective grid modulus is higher than the instantaneous (short-term) modulus of the surrounding AC, a beneficial reinforcing effect can be potentially realised at all times. If the effective grid modulus is lower than the equilibrium (long-term) modulus of the surrounding AC, then no reinforcing effect can be realised at any time. For intermediate cases, the reinforcing effect is only realised under certain situations, e.g. under slow loads or high-temperature conditions (or both).

4.3.2. Interlayer bonding
The second grid contribution is captured by associating the reinforcement layer with two interfaces – one associated with the layer above and another associated with the layer below. Hence, the model requires two bonding parameters to be specified. Considering the reinforcement layer as layer j, this implies specifying $k_{b,j-1}$ and $k_{b,j}$ (refer to Subsection 4.1). While in reality, the two AC layers adjacent to a grid are in partial contact through the grid apertures, modelling the grid as a thin layer produces a complete separation. In
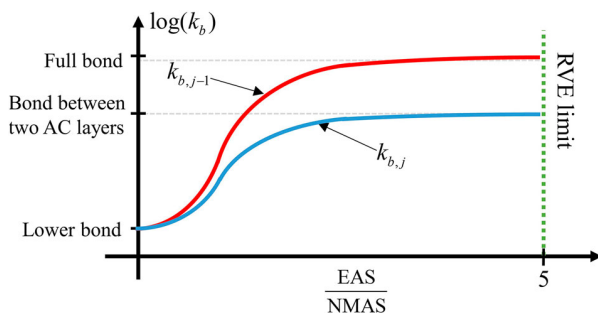
the model, this partial contact is captured by an appropriate choice of values for $k_{b,j-1}$ and $k_{b,j}$.

It is anticipated that these bonding values are (also) related to the EAS-NMAS ratio according to the curves in Figure 2. In this figure, both $k_{b,j-1}$ and $k_{b,j}$ are seen to be equal when EAS/NMAS $\rightarrow$ 0. This situation represents a membrane, for which there is no reason to expect a different bond level between top and bottom. In addition, a low bond level is expected since a membrane prevents aggregate interlocking between the adjacent AC layers. As the EAS-NMAS ratio increases, the $k_{b,j}$ approaches the bond level between two AC lifts, and $k_{b,j-1}$ approaches perfect bonding conditions. Conceptually, the reason for the anticipated difference between $k_{b,j-1}$ and $k_{b,j}$ in this situation is related to the construction sequence. The grid is usually placed over an already-compacted AC lift or a milled surface and then overlayed with fresh hot asphalt mix. Thus, the grid can better interlock with the upper AC lift than the lower AC. Lastly, if the bond level between two AC lifts is considered perfect (i.e. no slippage), then the two curves merge into a single curve, i.e. $k_{b,j-1}$ and $k_{b,j}$ are equal across all EAS-NMAS ratios.

It is further noted that the model proposed herein can naturally accept time-temperature dependent interface bonding behaviour (refer to Subsection 4.2), e.g. as observed in Leischner et al. (2019). In this case, the horizontal spring values should be treated as time functions, i.e. $k_{b,j-1}(t)$ or $k_{b,j}(t)$ that are (each) associated with a certain temperature level.

4.3.3. ZoI effect

The third grid contribution, dealing with the ZoI mechanism, is captured by first assigning a thickness δ^{ZoI} to define the range in which the ZoI takes action; and second, by dividing the neighbouring AC layers into sub-layers and changing the original AC master curve associated with the sub-layers (within the ZoI). That is shown in Figure 3(a) for a situation where the ZoI is taken as two sub-layers – one above and one below the grid. The suggested change to the AC master curve within a sub-layer is schematically presented in Figure 3(b), where it can be seen that the ZoI effect is more pronounced at long times (or high temperatures). In the figure, $E(t)$ denotes the relaxation modulus curve of the original AC (associated with some reference temperature level), and $E^{ZoI}(t)$ denotes the corresponding relaxation modulus curve of the AC within the ZoI. Furthermore, E_0 and E_∞ denote (respectively) the instantaneous modulus and the equilibrium modulus of the original AC, and E_∞^{ZoI} denotes the equilibrium modulus of the AC within the ZoI. As can be seen, $E^{ZoI}(t) \geq E(t)$ at all times with the greatest relative deviation occurring as $t \rightarrow \infty$. The underlying assumption for this chart is that the effective grid modulus is higher than E_0.

The rationale for the above modelling assumptions is associated with additional stress confinement caused by the reinforcing grid that extends δ^{ZoI} into the surrounding AC – on both sides of the grid. Intuitively, the extent of this thickness is somehow linked to the AC's aggregate characteristics, e.g. some multiple of the NMAS. Based on laboratory tests and discrete element models applied to granular soils, this multiple exhibits a range of unity to three (McDowell et al. 2006; Schuettpelz et al. 2009; Chen et al. 2012, 2014).

Considering time-temperature superposition (see e.g. Levenberg 2020), the additional confinement within the ZoI is expected to be more pronounced when AC temperatures are high or when loads move slow (or both). Under these conditions, the bitumen's viscosity is low, and AC exhibits a more granular-like mechanical behaviour with sensitivity to confinement. Inversely, the ZoI effect is expected to be negligible when AC temperatures are low or when loads move fast (or both). In light of the time-temperature-age shifting properties of AC (Ling et al. 2017), reduced sensitivity to confinement is also expected in aged AC. Thus, the ZoI effect is expected to be more pronounced at an early age – and diminish with time as the bitumen progressively oxidises.

A pragmatic way of embodying the increase in E_∞^{ZoI}, see Figure 3(b), is to introduce a unitless κ factor as follows:

$$E_\infty^{ZoI} = \kappa E_\infty, \quad 1 \leq \kappa \leq \frac{E_0}{E_\infty} \tag{4}$$

This expression essentially links the VE properties within δ^{ZoI} to the adjacent AC properties. In doing so, the ZoI effect is emulated by only introducing a single parameter, thereby avoiding the need to introduce a completely new set of material parameters to each sub-layer. The lower limit case of $\kappa = 1$ implies that no ZoI effect takes place, as $E_\infty^{ZoI} = E_\infty$. The upper limit case of $\kappa = E_0/E_\infty$ (i.e. $E_\infty^{ZoI} = E_0$) is introduced to safeguard compliance with VE theory, i.e. fading memory (Malkin and Isayev 2017).

The κ factor is analogous to a geogrid gain factor (Potyondy et al. 2016; Siekmeier and Casanova 2016; Mahmud et al. 2018). The value of κ is expected to (also) depend on the EAS-NMAS ratio, as schematically charted in Figure 4. In the lower limit case, where EAS/NMAS $\rightarrow$ 0 (which refers to a membrane situation), the interaction intensity with the adjacent AC layers is expected to be unsubstantial; hence it is anticipated that κ will be unity or slightly above – as shown in the chart. As the EAS-NMAS ratio increases, κ increases until attaining a peak and then decreases. With further increase of the EAS-NMAS ratio, the ZoI effect is expected to diminish, such that $\kappa \rightarrow 1$. This behaviour coincides with work in granular soils dealing with particle-geogrid aperture interaction (Indraratna et al. 2012; Liu et al. 2021).

5. Model demonstration

5.1. Inputs

The proposed modelling approach is applied hereafter for the situation of a mill-and-overly repair. The original pavement system, prior to repair, consists of 200 mm thick aged and densely cracked AC resting on top of a 500 mm thick unbound granular base layer, underlain by a subgrade soil extending to a large depth. This layering arrangement conforms to standard European design requirements for heavily trafficked primary roads and motorways, e.g. European Commission (1999) and Vejdirektoratet (2017). Two milled-and-overlaid pavement systems are considered – presented in Figure 5. In both systems, 100 mm of the aged AC is milled off and replaced by a new 100 mm AC overlay – returning to the
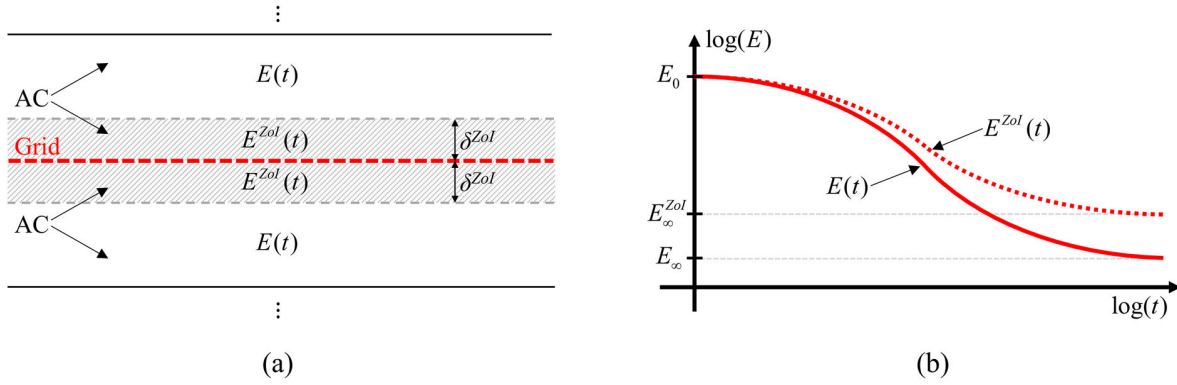
Figure 3. Emulation of the ZoI effect: (a) sub-division of the AC layers adjacent to the grid and (b) contrasting the AC relaxation modulus inside and outside the ZoI.

original surface elevation. The NMAS of the new AC is assumed 10 mm. The systems differ by the inclusion or exclusion of an interlayer grid reinforcement. System I in Figure 5(a) considers a situation without a reinforcing grid, whereas System II in Figure 5(b) considers a reinforcing grid placed on top of the retained (cracked) AC before the overlay. All layers presented in the two systems are assumed perfectly bonded to each other; this assumption also applies to the reinforcement.

Figure 5 includes layer identifiers associated with the model. The top layer ($i = 1$) represents the overlay in both pavement systems; it is modelled as undamaged and VE, characterised by a constant Poisson's ratio $\nu_1 = 0.30$ and a relaxation modulus $E_1(t)$ analytically expressed as follows (Levenberg 2013):

$$E_1(t) = \frac{E_\infty \left(1 + (t/\tau_D)^{n_D}\right)}{(t/\tau_D)^{n_D} + (E_\infty/E_0)} \quad (5)$$

where n_D is a unitless shape parameter, and $\tau_D = \tau_D^0 a_T$. Here, τ_D^0 is a shape parameter (units of time) that is linked to a certain reference temperature level T_0, and a_T is a (unitless) time-temperature shift factor, taken as Williams *et al.* (1955):

$$\log_{10}(a_T) = \frac{-C_1(T - T_0)}{C_2 + (T - T_0)} \quad (6)$$

where T denotes the desired analysis temperature of layer 1
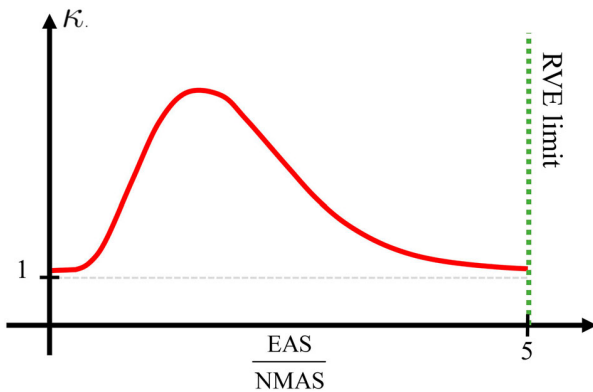
Figure 4. Conceptual sketch of κ as a function of the EAS-NMAS ratio.

(uniformly distributed across the thickness), and C_1 (unitless) and C_2 (units of temperature) are constants. The chosen numerical values associated with Equations (5) and (6) are as follows: $E_0 = 25,000$ MPa, $E_\infty = 100$ MPa, $\tau_D^0 = 2.0 \cdot 10^5$ s, $n_D = 0.35$, $C_1 = 25$, $C_2 = 200°$C, and $T_0 = 15°$C. These values are roughly based on lab-measured properties of Mix 1 in Levenberg *et al.* (2009).

The reinforcement layer, $i = 3$ in System II, is taken as a thin undamaged elastic layer. Its properties are chosen based on the S&P Carbophalt® G 200/200 product (S&P Clever Reinforcement Company AG 2020), which is a pre-bituminised grid made of carbon fibres and designed to be installed in contact with AC. The carbon fibres have a modulus of 265,000 MPa and Poisson's ratio of 0.15. The average cross-sectional area of the grid per unit width is approximately 50 mm²/m – thus, an effective thickness of 0.05 mm is assigned to the reinforcement layer based on smearing the grid's volume. The product itself has fibres bundled into ribss and arranged in a mesh with square-shaped apertures 15 mm × 15 mm in size. Thus, EAS = 15 mm and the EAS-NMAS ratio is 1.5 – well within RVE limits.

In this particular case, the grid generates a ZoI effect only in the overlay above it. The ZoI effect below the grid (within the aged and cracked AC layer) is neglected, assuming that the aged and cracked AC is insensitive to confinement conditions. The ZoI is introduced as a sub-layer of the 100 mm overlay, i.e. layer $i = 2$ in Figure 5(b), with a thickness of $\delta^{ZoI} = 30$ mm corresponding to three times the NMAS. Furthermore, the AC in this zone is characterised by a constant Poisson's ratio $\nu_2 = 0.30$ similar to the overlay and a relaxation modulus $E^{ZoI}(t)$ taken as:

$$E^{ZoI}(t) = \frac{\kappa E_\infty \left(1 + (t/\tau_D)^{n_D}\right)}{(t/\tau_D)^{n_D} + (\kappa E_\infty/E_0)} \quad (7)$$

where the κ factor embodies the modulus increase of the equilibrium modulus using Equation (4). Two κ values are analysed and contrasted hereafter: $\kappa = 1$ representing no ZoI effect, and $\kappa = 3$ representing an active ZoI effect.

The aged and densely cracked AC, i.e. layer $i = 2$ for System I and layer $i = 4$ for System II, is treated as a time-independent FL with: (i) a Winkler spring-bed stiffness of $k_i = 100$ MPa/mm. This value corresponds to a Young's modulus of 10,000 MPa representing an aged AC divided by the FL

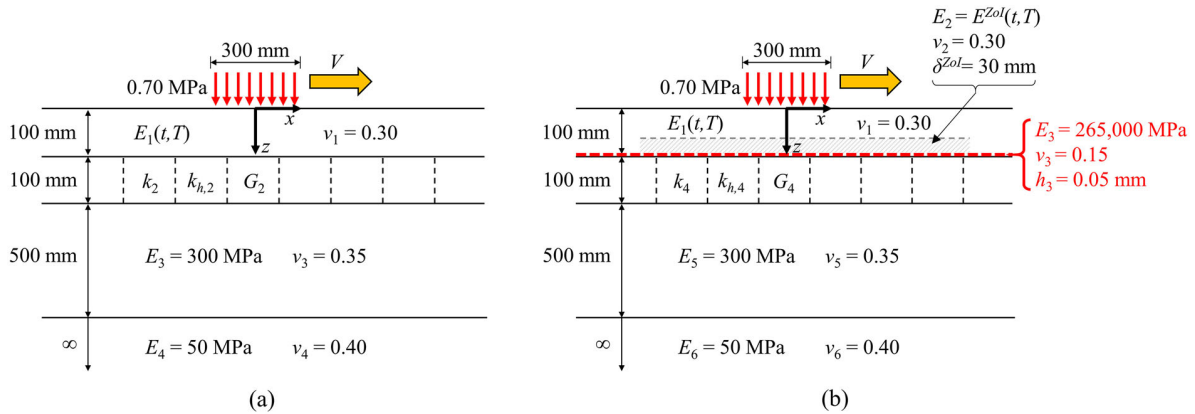**Figure 5.** Cross-sectional view of two milled-and-overlaid pavements: (a) an unreinforced system – System I, and (b) a reinforced system – System II.

thickness of 100 mm; (ii) a very high horizontal spring-bed stiffness for $k_{h,i}$ to prevent differential horizontal displacements between the top and bottom of the FL; and (iii) a Pasternak layer with $G_i = 0$, i.e. no resistance to vertical shear deformation between the fragments.

As for the remaining pavement layers, the unbound granular base, i.e. layer $i = 3$ for System I and $i = 5$ for System II, is represented by an elastic layer with a modulus of $E_i = 300$ MPa and a Poisson's ratio $\nu_i = 0.35$. The subgrade soil, i.e. $i = 4$ for System I and $i = 6$ for System II, is treated as a semi-infinite medium with $E_i = 50$ MPa and $\nu_i = 0.40$.

Both pavement systems are subjected to a single moving load, uniformly distributed over a circular area. A circular load with an intensity of $q = 0.7$ MPa and a diameter of $2a = 300$ mm is considered, corresponding to a 10-ton axle load with one wheel on each side. Cartesian coordinates are introduced in both systems in Figure 5 with the origin fixed to the pavement surface (i.e. not moving with the load), the x-axis pointing along the load travel direction, the y-axis pointing out of the plane (transverse to the travel direction), and the z-axis pointing towards the subgrade. The load moves with a constant speed V along a straight line centred over the y-axis (i.e. $y = 0$).

5.2. Calculation of key responses

Numerical evaluations of the model equations were obtained based on an open-source MATLAB® based code called: Adaptive Layered Viscoelastic Analysis (ALVA) (Skar and Andersen 2020; Skar et al. 2020a). The ALVA code solves the standard LET formulation in a normalised format (Huang 2004; Levenberg 2020). As a preliminary step, it has been verified that ALVA can correctly handle thin high-modulus layers by comparison against solutions derived analytically in Maple™. Next, the ALVA code was extended to include the FL formulation (Levenberg and Skar 2020). Correctness of the extended version was also verified against solutions derived analytically in Maple™. Lastly, the code was extended to handle VE behaviour and moving loads according to the quasi-elastic approach (refer to Subsection 4.2). The VE simulations of a moving load were generated using 2000 steps of equally spaced (stationary) unit step load-unload histories, i.e. 2000 sequential

α-values in Equation (3). The loading was first applied at $x = -10,000$ mm, allowed to travel with constant speed to $x = 10,000$ mm, and then removed from the system.

Traces of key responses were evaluated for coordinates $(0, 0, z)$, i.e. for points residing at several depths below the surface but fixed along the travel direction. The evaluation considered five key response traces of: (i) horizontal strain in the direction of travel at the AC overlay bottom, $\varepsilon_x(0, 0, 100 \text{ mm})$; (ii) horizontal strain in the direction transverse to the load travel path at the AC overlay bottom, $\varepsilon_y(0, 0, 100 \text{ mm})$; (iii) vertical strain at the top of the unbound base layer, $\varepsilon_z(0, 0, 200.1 \text{ mm})$; (iv) vertical strain at the top of the subgrade, $\varepsilon_z(0, 0, 700.1 \text{ mm})$; and (v) vertical displacement at the pavement surface, $U_z(0, 0, 0)$. The choice to focus on these key response traces is based on their association with cracking and rutting in common pavement design codes (Huang 2004). Specifically, horizontal tensile strains at the bottom of AC layers are linked to bottom-up fatigue cracking, and vertical compressive strains are linked to rutting. While pavement performance was neither investigated nor quantified in this work, the peak levels of the chosen key responses can be seen as indicative of expected performance. The reason for including surface displacements in the analysis is their widespread utilisation in non-destructive condition assessment (ASTM 2009; Horak et al. 2015).

5.3. Results

Simulated key response traces, triggered by the moving load, are presented and contrasted in Figure 6. This figure was prepared to assess the effect of grid reinforcement by comparing System I and System II in Figure 5 for two combinations of AC overlay temperature T and loading speed V. The following combinations were chosen: (i) $T = 45°C$ and $V = 5$ km/h (left-hand side charts); and (ii) $T = 5°C$ and $V = 80$ km/h (right-hand side charts). These two combinations essentially engage different ranges of the overlay's relaxation modulus. The figure contains five charts for each combination – corresponding to the five key responses. In the charts, the horizontal axes denote the x-coordinate of the load position as it approaches the evaluation point, passes over it, and then recedes; the vertical axes depict the associated key response values. As is
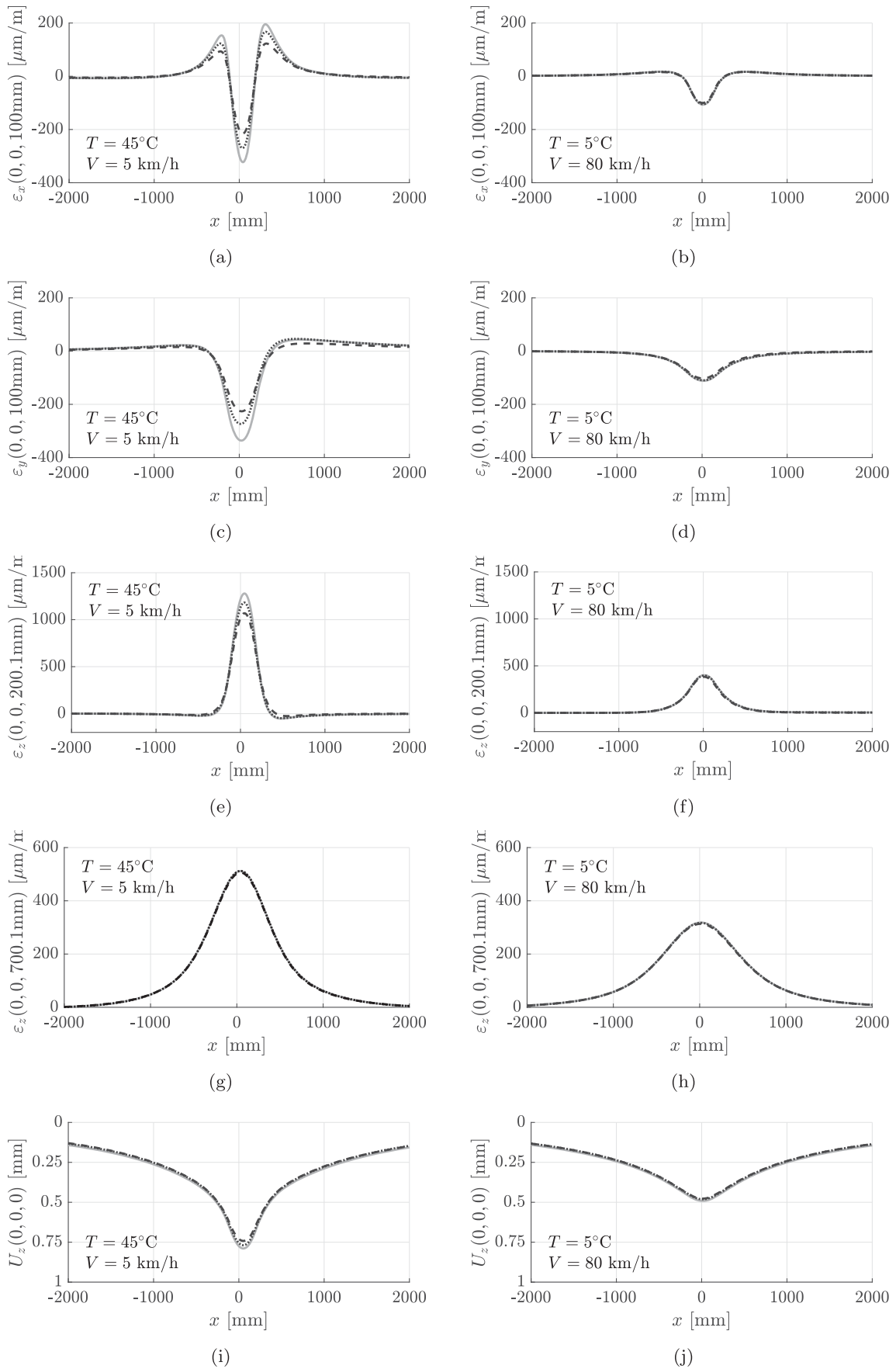
Figure 6. Calculated key response traces as a function of load position in the two pavement systems (see Figure 5) for two temperature-speed conditions: solid line (———) for the unreinforced system; dotted line (······) for the reinforced system with $\kappa = 1$; and dashed line (- - - -) for the reinforced system with $\kappa = 3$.

common in soil mechanics, the sign convention is that compressive stresses and strains are considered positive. Each chart contains three curves: (——) a reference trace for the unreinforced pavement in System I; (······) a trace for the reinforced pavement in System II, without considering the ZoI effect (i.e. $\kappa = 1$); and (----) a trace for the reinforced pavement in System II, considering the ZoI effect (with $\kappa = 3$).

Across all charts in Figure 6, it can be seen that reinforcement does not affect the overall shape of the response traces. However, reinforcement positively influences peak responses for both $\kappa = 1$ and $\kappa = 3$; the impact is more considerable for the latter when the ZoI effect is activated. In general, the reinforcement appears most effective under the high-temperature slow-speed combination. Under the low-temperature high-speed combination, the reinforcement effect seems negligibly small (graphically indistinguishable).

The numerical values of the trace peaks are listed in Table 1; these are provided alongside their relative change in magnitude caused by the reinforcement. As can be seen, the largest reinforcement effects are generally obtained for $\varepsilon_x(0, 0, 100\,\text{mm})$ and $\varepsilon_y(0, 0, 100\,\text{mm})$, where a choice of $\kappa = 3$ provides a reduction of 33% in both peak strains (compared to the corresponding unreinforced system). In contrast, a strain reduction of 16% and 19% is realised, respectively, when disregarding the ZoI effect ($\kappa = 1$). For the low-temperature high-speed combination, the reduction in trace peaks caused by reinforcement does not exceed 3% for any demonstrated systems.

Figure 7 further investigates the influence of different AC temperatures and travel speeds on the reinforcement effect. There are ten charts in this figure such that each row of charts represents one of the five key responses. The charts on the left-hand side are associated with a speed of $V = 5\,\text{km/h}$, while the charts on the right-hand side are associated with $V = 80\,\text{km/h}$. The horizontal axes denote the overlay temperature in the range of 0°C to 70°C; the vertical axes denote the corresponding trace peaks values for a given key response (similar to what is presented in Table 1). Every chart contains three curves, each representing one of the three pavement situations (similar to Figure 6): (——) the unreinforced system, (······) the reinforced system with $\kappa = 1$, and (----) the reinforced system with $\kappa = 3$. The reinforcement effect is manifested by the difference between the unreinforced curve (associated with System I) and one of the two curves associated with the reinforced System II.

As can be observed in all ten charts in Figure 7, the response peaks in the reinforced cases are always smaller than the corresponding responses in the unreinforced case. Across the range of considered AC temperatures, reinforcement is seen to mostly influence the overlay strains, and to a lesser degree influence the vertical strains on top of the base layer. Including reinforcement seems to produce a negligible effect on the vertical strains on top of the subgrade across all considered travel speed and temperature combinations. Only a small effect on the surface displacement is visible for $\kappa = 3$ combined with high temperatures and slow speeds conditions. From Figure 7(a–d), it can be seen that the peak (negative) tensile strain drops after a certain temperature level. The reason for this drop is related to a drop in the 'effective overlay modulus'

(which is essentially time-temperature dependent) compared to the moduli of the lower layers (which are assumed time-temperature independent). In the reinforced case that includes the ZoI effect (with $\kappa = 3$), the reinforcement effect (i.e. the difference between solid and dashed curves) seems to increase with rising AC temperature until the point where the peak strain drops, after which the effect slightly decreases. The same does not seem to apply when the ZoI effect is excluded ($\kappa = 1$), where the reinforcement effect continues to increase with rising AC temperature. The difference between the two dashed curves in Figure 7 quantifies the ZoI contribution to the overall reinforcement effect. From Figure 7(a–f) this contribution can be seen to be a primary part of the reinforcement effect for temperatures levels up to about $T = 40°C$ ($V = 5\,\text{km/h}$) to $T = 50°C$ ($V = 80\,\text{km/h}$). Beyond this temperature range, the overall reinforcement effect is led by the sheer presence of the reinforcement as a thin high-modulus layer in the system. In Figure 7(a,c) (both referring to a speed of $V = 5\,\text{km/h}$), a crossing point appears between the two dashed curves, indicating that the ZoI – even if active – is ineffective.

Lastly, calculations were repeated with $E_2 = 73, 000\,\text{MPa}$ in System II instead of 265,000 MPa. This corresponds to the S&P Glasphalt® G product (S&P Clever Reinforcement Company AG 2021), which is made of glass fibres instead of carbon fibres, but otherwise similar to S&P Carbophalt® G 200/200. The results are not shown here because, graphically, they closely resemble those in Figure 7. Specifically, the response peaks behaved similarly when changing speeds and temperatures. A noticeable dissimilarity was that the peak magnitudes in reinforced cases diminished towards the unreinforced peak values for all considered key responses. Furthermore, the ZoI contribution to the overall reinforcement effect was a primary part for temperatures of about $T = 60°C$ for $V = 5\,\text{km/h}$ or across the entire temperature range for $V = 80\,\text{km/h}$.

6. Summary and discussion

6.1. Modelling effort

This work offered a new mechanistic model for milled-and-overlaid asphalt pavement systems with grid reinforcement (see Section 4). The model formulation covers: elastic layers for representing subgrade and unbound layers, FLs for representing existing aged and densely cracked AC, imperfect bonding conditions for representing any differential slippage between adjoining layers, VE layer properties for representing new AC lifts, and moving loads for representing traffic conditions. Grid effects were modelled as a combination of three contributions (see Subsection 4.3): (i) the existence of an additional thin high-modulus elastic layer within the pavement system – characterised by an effective thickness, Young's modulus, and Poisson's ratio; (ii) the influence of a grid on interlayer bonding between layer above and below it – characterised by two horizontal spring values; and (iii) the influence of a grid on the properties of the surrounding AC – characterised by a ZoI thickness and a κ factor. Overall, seven physically meaningful modelling inputs are required for representing a reinforcing grid in this new formulation. Figure 8 offers a graphical representation of the proposed model inputs and

Table 1. Peak response values across pavement systems and time-temperature conditions.

System	$\varepsilon_x(0, 0, 100\,mm)$ [μm/m]	$\varepsilon_y(0, 0, 100\,mm)$ [μm/m]	$\varepsilon_z(0, 0, 200.1\,mm)$ [μm/m]	$\varepsilon_z(0, 0, 700.1\,mm)$ [μm/m]	$U_z(0, 0, 0)$ [mm]
	Peak response for $T = 45°C$ and $V = 5$ km/h				
Unreinforced	−329.1	−336.1	1288	513.1	0.7893
Reinforced $\kappa = 1$	−277.5 (−16%)	−273.4 (−19%)	1288 (−7%)	513.1 (0%)	0.7706 (−2%)
Reinforced $\kappa = 3$	−219 (−33%)	−226.2 (−33%)	1074 (−17%)	507.0 (−1%)	0.7410 (−6%)
	Peak response for $T = 5°C$ and $V = 80$ km/h				
	$\varepsilon_x(0, 0, 100\,mm)$ [μm/m]	$\varepsilon_y(0, 0, 100\,mm)$ [μm/m]	$\varepsilon_z(0, 0, 200.1\,mm)$ [μm/m]	$\varepsilon_z(0, 0, 700.1\,mm)$ [μm/m]	$U_z(0, 0, 0)$ [mm]
System					
Unreinforced	−107.1	−111.8	402.1	318.4	0.4914
Reinforced $\kappa = 1$	−105.3 (−1%)	−109.7 (−1%)	397.7 (0%)	317.2 (0%)	0.4813 (−1%)
Reinforced $\kappa = 3$	−100.3 (−2%)	−102.5 (−3%)	383.1 (−1%)	313.4 (−1%)	0.4771 (−2%)

main features. It includes three shaded areas, each corresponding to a subsection within Section 4.

Given that the modelling framework is built on a linear layered theory, it is limited to lateral uniformity of the layers. This means that properties are not influenced by, e.g. layer variabilities, loading position or loading intensity. Thus, concerning the ZoI effect, the κ factor applies to an entire ZoI sub-layer in the lateral direction and is insensitive to whether local conditions are tensile or compressive (even though the effect is fundamentally nonlinear and should vary laterally). However, the modelling framework can handle nonuniform behaviour in the vertical direction (e.g. thermal gradients), which can be readily and efficiently addressed by further sub-layering. Thus, by considering multiple sub-layers, each assigned a different κ, vertical nonuniformity can be introduced into the ZoI effect.

6.2. Demonstration effort

The model was demonstrated over three milled-and-overlaid pavement cases (see Section 5): a reference system excluding reinforcement, a grid-reinforced system excluding the ZoI effect, and a reinforced system including the ZoI effect with $\kappa = 3$. Key responses commonly related to pavement performance, triggered by a single moving load, were simulated for different combinations of AC temperatures and load travel speeds. The demonstration was carried out with two grid types, both fully bonded to its adjacent layers.

The main findings from the model demonstration (see Subsection 5.3) were as follows: (a) key responses were positively affected by the presence of reinforcement, especially horizontal strains at the AC overlay bottom (both in the longitudinal and transverse directions) and, although to a lesser degree, vertical strain at the top of the base layer; (b) vertical strain at the subgrade top and vertical surface displacement (i.e. deflection) were both practically unaffected by the reinforcement; (c) under low-temperature/high-speed conditions, the reinforcement effect was negligible across all key responses while under high-temperature/slow-speed conditions the reinforcement effect was notable; (d) with increasing AC temperature (for a given speed), the ZoI effect represented by κ was the primary contributor to the overall reinforcement effect – up to a certain temperature level beyond which the grid's effective modulus and effective thickness became the primary contributors to the overall reinforcement effect; and (e) the overall reinforcement effect was more noticeable when the effective modulus of the grid was higher.

7. Conclusion

The newly proposed model (refer to Section 4) combines, for the first time and in one single mechanistic framework, all relevant effects to the problem at hand. Specifically, it offers a rational approach for capturing and emulating the effects of asphalt grid reinforcement; it does so in a generic manner that is not limited to any specific product and is applicable to a wide range of pavement systems. By building upon linear layered theory, numerical stability and high computational efficiency are assured – increasing the chances of industry acceptance. Thus, the new model is deemed a potential candidate to serve as a computational engine for a ME design method applicable to both new and rehabilitated asphalt pavement systems. In this context, for a given grid type and pavement system, the new model can be used to optimise installation location considering the prevailing loading and temperature conditions. Furthermore, the new model can serve as an analysis tool to guide manufacturers on improving their products or showcasing existing capabilities – all in a quantified manner.

An initial validation for the proposed model is obtained based on findings from the demonstration effort. Specifically, findings (a) and (c) (see Subsection 6.2) imply that adding grid reinforcement on top of an existing cracked AC (before overlay) can potentially prolong the overlay's service life in terms of bottom-up fatigue cracking or rutting (or both). These implications conform to previous findings in studies that have experimentally evaluated the effect of an asphalt grid reinforcement on pavement performance in terms of fatigue cracking (Nguyen *et al.* 2013; Arsenie *et al.* 2017; Vinay Kumar and Saride 2017; Correia and Zornberg 2018) and rutting (Ong *et al.* 2004; Sobhan 2005; Lee *et al.* 2015; Correia and Zornberg 2016). It should be noted, that these performance improvements are anticipated based on existing transfer functions in ME design, that were developed without reinforcement. Given that these functions are empirical in nature, they will require field re-calibration to the case where reinforcing grids are included. Furthermore, finding (b) suggests that adding a grid reinforcement has no notable effect on pavement deflections, especially when considering fast loading and low temperatures (see finding (c)). This statement coincides with
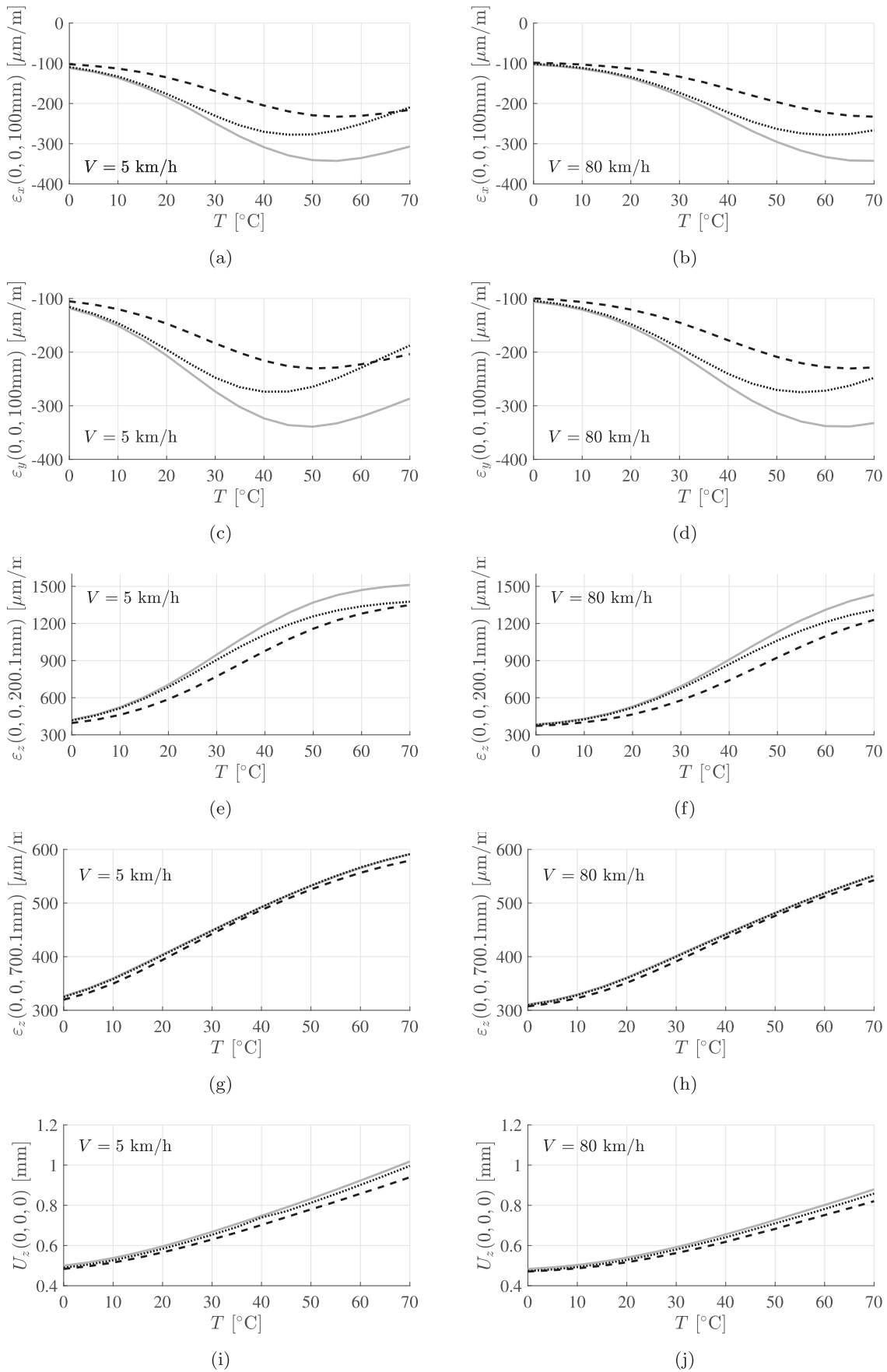
Figure 7. Calculated trace peak values of key responses as a function of temperature in the two pavement systems (see Figure 5) for two load speeds: solid line (———) for the unreinforced system; dotted line (·······) for the reinforced system with $\kappa = 1$; and dashed line (- - - -) for the reinforced system with $\kappa = 3$.
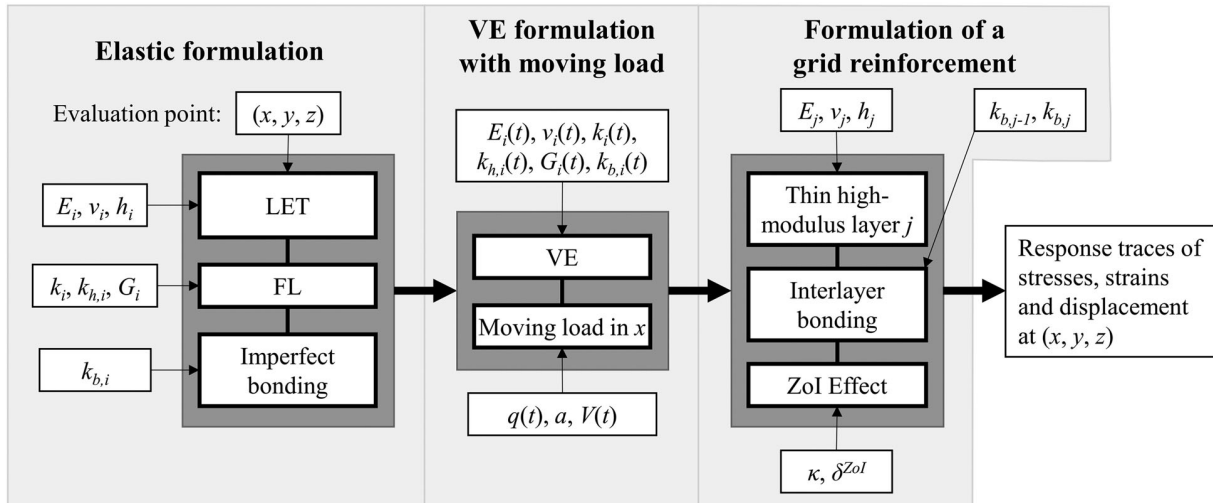
Figure 8. Graphical representation of the proposed model inputs and features.

the observations in Nguyen *et al.* (2013), but negates the reported results in, e.g. Graziani *et al.* (2014) and Correia and Zornberg (2016).

8. Future work

In light of the model's potential usefulness, there is a need for more targeted validation activities. These should preferably involve a combination of field and laboratory tests designed to calibrate the different inputs and subsequently allow forecastability assessments. In this context, some of the findings from the model demonstration effort provide example guidance for testing. Specifically, findings (a) and (e) suggest that either strain sensing at the overlay bottom or pressure cells at the base layer top should, as a minimum, be considered when quantifying grid reinforcement effects. Moreover, finding (b) suggests that it is practically challenging to quantify grid reinforcement effects based on subgrade sensors or deflection testing. Lastly, finding (c) suggests that field investigations should consider the application of moving loads, operating at different speeds and under different temperature levels, with noticeable reinforcement effects expected mainly under high-temperature/slow-speed conditions. In terms of addressing grid properties, the effective grid thickness and modulus can be directly quantified in the laboratory by examining the grid product. As for the interface bond between a grid and its surrounding AC, the most likely technique for estimating the associated horizontal spring stiffnesses (see Figure 2) is laboratory shear testing of cores (Uzan *et al.* 1978; Romanoschi and Metcalf 2001). The ZoI thickness can be obtained from discrete element modelling (Chen *et al.* 2012, 2014); then after, and based on the logic of findings (a) and (d), it should be possible to evaluate κ through inverse analysis of strain measurements in the field tests (Levenberg 2013, 2015). Characterisation of FL inputs could also be achieved from inverse analysis based on field measurements. All other model inputs related to the overlay AC, unbound layers, and subgrade, can be obtained from accepted/standard field or laboratory tests. Overall, the model itself should serve as a guide

for designing experimental setups when assessing grid effects within new or rehabilitated asphalt pavement systems; this is to ensure the collection of usable measurements for subsequent mechanistic interpretation.

ORCID

Julius Nielsen ⅮＩ http://orcid.org/0000-0002-2225-9799
Eyal Levenberg ⅮＩ http://orcid.org/0000-0003-1188-8458
Asmus Skar ⅮＩ http://orcid.org/0000-0003-3176-791X

References

AASHTO, 2011. *Standard method of test for determining dynamic modulus of hot mix asphalt (HMA).* Washington, DC: American Association of State Highway and Transportation Officials, AASHTO T 342.

AASHTO, 2017. *Standard method of test for determining the dynamic modulus and flow number for asphalt mixtures using the asphalt mixture performance tester (AMPT).* Washington, DC: American Association of State Highway and Transportation Officials, AASHTO T 378.

ARA Inc., 2004. *Guide for mechanical-empirical design of new and rehabilitated pavement structures.* NCHRP.

Arsenie, I.M., *et al.*, 2017. Laboratory characterisation of the fatigue behaviour of a glass fibre grid-reinforced asphalt concrete using 4PB

tests. *Road Materials and Pavement Design*, 18 (1), 168–180. Available from: https://doi.org/10.1080/14680629.2016.1163280.

Asphalt Academy, 2008. *TG3 – asphalt reinforcement for road construction*. Asphalt, November.

ASTM, 2009. *Standard test method for deflections with a falling-weight-type impulse load device*.

ASTM, 2020. *D6433-20 Standard practice for roads and parking lots pavement condition index surveys*.

AUSTROADS, 2004. Pavement design: a guide to the structural design of road pavements. *In*: *Deterioration and maintenance of pavements*, 233–243. Available from: www.austroads.com.au.

Baek, C., Underwood, B., and Kim, Y., 2012. Effects of oxidative aging on asphalt mixture properties. *Transportation Research Record*, 2296 (1), 77–85.

Bell, C.A., Wieder, A.J., and Fellin, M.J., 1994. *Laboratory aging of asphalt-aggregate mixtures: field validation*. Strategic Highway Research Program, 254–262.

Burmister, D.M., 1943. The theory of stresses and displacements in layered systems and applications to the design of airport runways. *In*: *Highway Reseach Board: Proceedings of the Twenty-third Annual Meeting*; 27–30 November; Chicago, Illinois.

Burmister, D.M., 1945a. The general theory of stresses and displacements in layered soil systems. II. *Journal of Applied Physics*, 16 (3), 126–127.

Burmister, D.M., 1945b. The general theory of stresses and displacements in layered soil systems. III. *Journal of Applied Physics*, 16 (5), 296–302.

Burmister, D.M., 1945c. The general theory of stresses and displacements in layered systems. I. *Journal of Applied Physics*, 16 (2), 89–94.

Button, J.W., and Lytton, R.L., 2007. Guidelines for using geosynthetics with hot-mix asphalt overlays to reduce reflective cracking. *Transportation Research Record*, 2004 (1), 111–119.

Caltrans, 2020. *Highway design manual*. 7th ed. California Department of Transportation.

Canestrari, F., and Santagata, E., 2005. Temperature effects on the shear behaviour of tack coat emulsions used in flexible pavements. *International Journal of Pavement Engineering*, 6 (1), 39–46.

CEN, 2012. *Bituminous mixtures – test methods – part 26: stiffness*. European Committee for Standardization (CEN), EN 12697-26.

Chabot, A., *et al.*, 2010. ViscoRoute 2.0 A: tool for the simulation of moving load effects on asphalt pavement. *Road Materials and Pavement Design*, 11 (2), 227–250.

Chang, D.T.T., *et al.*, 1999. Laboratory and case study for geogrid-reinforced flexible pavement overlay. *Transportation Research Record*, 1687 (1), 125–130.

Chen, C., McDowell, G.R., and Thom, N.H., 2012. Discrete element modelling of cyclic loads of geogrid-reinforced ballast under confined and unconfined conditions. *Geotextiles and Geomembranes*, 35, 76–86. Available from: http://dx.doi.org/10.1016/j.geotexmem.2012.07.004.

Chen, C., McDowell, G.R., and Thom, N.H., 2014. Investigating geogrid-reinforced ballast: experimental pull-out tests and discrete element modelling. *Soils and Foundations*, 54 (1), 1–11. Available from: http://dx.doi.org/10.1016/j.sandf.2013.12.001.

Cleveland, G.S., Button, J.W., and Lytton, R.L., 2001. *Geosynthetics in flexible and rigid pavement*. Fhwa/Tx-02/1777- 1, 7 (2). Available from: http://www.scribd.com/doc/136341942/Geosynthetics-in-Flexible-and-Rigid-Pavementscribd.

Collop, A.C., and Cebon, D., 1996. Stiffness reductions of flexible pavements due to cumulative fatigue damage. *Journal of Transportation Engineering*, 122 (2), 131–139.

Correia, N.S., and Zornberg, J.G., 2016. Mechanical response of flexible pavements enhanced with geogrid-reinforced asphalt overlays. *Geosynthetics International*, 23 (3), 183–193.

Correia, N.S., and Zornberg, J.G., 2018. Strain distribution along geogrid-reinforced asphalt overlays under traffic loading. *Geotextiles and Geomembranes*, 46 (1), 111–120. Available from: https://doi.org/10.1016/j.geotexmem.2017.10.002.

de Bondt, A.H., 1999. *Anti-reflective cracking design of (reinforced) asphalt overlays*. Thesis (PhD).

European Commission, 1999. *COST 333: development of new bituminous pavement design method: final report of the action*. Vol. 18906. European Communities.

Germann, F., and Lytton, R., 1979. *Methodology for predicting the reflection cracking life of asphalt concrete overlays*. Interim Report.

Goodman, J.R., and Popov, E.P., 1968. Layered beam systems with interlayer slip. *Journal of the Structural Division*, 94 (11), 2535–2548.

Graziani, A., *et al.*, 2014. Structural response of grid-reinforced bituminous pavements. *Materials and Structures/Materiaux et Constructions*, 47 (8), 1391–1408.

Gu, F., *et al.*, 2016. Numerical modeling of geogrid-reinforced flexible pavement and corresponding validation using large-scale tank test. *Construction and Building Materials*, 122, 214–230. Available from: http://dx.doi.org/10.1016/j.conbuildmat.2016.06.081.

Harvey, J., and Tsai, B.W., 1997. Long-term oven-aging effects on fatigue and initial stiffness of asphalt concrete. *Transportation Research Record: Journal of the Transportation Research Board*, 1590 (1), 89–98. Available from: http://journals.sagepub.com/doi/10.3141/1590-11.

Horak, E., *et al.*, 2015. Flexible road pavement structural condition benchmark methodology incorporating structural condition indices derived from falling weight deflectometer deflection bowls. *Journal of Civil Engineering and Construction*, 4 (1), 12.

Huang, Y.H., 2004. *Pavement analysis and design*. 2nd ed. Upper Saddle River, NJ: Pearson Education, Inc. Available from: http://docshare04.docshare.tips/files/14013/140138713.pdf.

Indraratna, B., Hussaini, S.K., and Vinod, J.S., 2012. On the shear behavior of ballast-geosynthetic interfaces. *Geotechnical Testing Journal*, 35 (2), 305–312.

Khodaii, A., Fallah, S., and Moghadas, F., 2009. Effects of geosynthetics on reduction of reflection cracking in asphalt overlays. *Geotextiles and Geomembranes*, 27 (1), 1–8. Available from: http://dx.doi.org/10.1016/j.geotexmem.2008.05.007.

Kim, Y., Lee, J., and Lutif, J.E., 2010. Geometrical evaluation and experimental verification to determine representative volume elements of heterogeneous asphalt mixtures. *Journal of Testing and Evaluation*, 38 (6), 660–666.

Konietzky, H., *et al.*, 2004. Use of DEM to model the interlocking effect of geogrids under static and cyclic loading. *In*: *Numerical Modeling in Micromechanics via Particle Methods – 2004*, 28–29 October, Kyoto, Japan. London: CRC Press Taylor & Francis Group, 3–12.

Kutay, M.E., Hasnat, M., and Levenberg, E., 2020. Layered nonlinear cross anisotropic model for pavements with geogrids. *In*: *Materials and Pavement Performance Prediction II: Contributions to the 2nd International Conference on Advances in Materials and Pavement Performance Prediction (AM3P 2020)*, 27–29 May, 2020, San Antonio, TX. CRC Press.

Kwon, J., and Tutumluer, E., 2009. Geogrid base reinforcement with aggregate interlock and modeling of associated stiffness enhancement in mechanistic pavement analysis. *Transportation Research Record*, 2116 (1), 85–95.

Le, V.P., *et al.*, 2017. Development of a simple asphalt concrete overlay design scheme based on mechanistic–empirical approach. *Road Materials and Pavement Design*, 18 (3), 630–645. Available from: https://doi.org/10.1080/14680629.2016.1182059.

Lee, J.H., *et al.*, 2019. Long-term performance of fiber-grid-reinforced asphalt overlay pavements: a case study of korean national highways. *Journal of Traffic and Transportation Engineering (English Edition)*, 6 (4), 366–382. Available from: https://doi.org/10.1016/j.jtte.2018.01.008.

Lee, J., Kim, Y.R., and Lee, J., 2015. Rutting performance evaluation of asphalt mix with different types of geosynthetics using MMLS3. *International Journal of Pavement Engineering*, 16 (10), 894–905.

Leischner, S., *et al.*, 2019. Mechanical testing and modeling of interlayer bonding in HMA pavements. *Transportation Research Record*, 2673 (11), 879–890. Available from: https://doi.org/10.1177/0361198119843254.

Lemaitre, J., and Desmorat, R., 2005. *Engineering damage mechanics: ductile, creep, fatigue and brittle failures*. Berlin, Heidelberg: Springer Science & Business Media.

Levenberg, E., 2013. Inverse analysis of viscoelastic pavement properties using data from embedded instrumentation. *International Journal for Numerical and Analytical Methods in Geomechanics*, 37 (9), 1016–1033.

Levenberg, E., 2015. Backcalculation with an implanted inertial sensor. *Transportation Research Record: Journal of the Transportation Research Board*, 2525 (1), 3–12.

Levenberg, E., 2016. Viscoelastic pavement modeling with a spreadsheet. *In*: *Eighth International Conference on Maintenance and Rehabilitation of Pavements (MAIREPAV8)*, 27–29 July, Singapore.Singapore: Research Publishing Services, 746–755.

Levenberg, E., 2020. *Pavement Mechanics: Lecture Notes*. 1st ed. Eyal Levenberg.

Levenberg, E., McDaniel, R.S., and Olek, J., 2009. *Validation of NCAT structural test track experiment using INDOT APT facility*. West Lafayette, Indiana: Joint Transportation Research Program, Indiana Department of Transportation and Purdue University, September.

Levenberg, E., and Skar, A., 2020. Analytic pavement modelling with a fragmented layer. *International Journal of Pavement Engineering*, 23 (4), 1108–1108. doi:10.1080/10298436.2020.1790559.

Ling, M., et al., 2017. Time-temperature-aging-depth shift functions for dynamic modulus master curves of asphalt mixtures. *Construction and Building Materials*, 157, 943–951. Available from:https://doi.org/10.1016/j.conbuildmat.2017.09.156.

Liu, C., Indraratna, B., and Rujikiatkamjorn, C., 2021. An analytical model for particle-geogrid aperture interaction. *Geotextiles and Geomembranes*, 49 (1), 41–44.

Luo, R., et al., 2017. *Quantifying the influence of geosynthetics on pavement performance*.

Lytton, R.L., 1989. Use of geotextiles for reinforcement and strain relief in asphalt concrete. *Geotextiles and Geomembranes*, 8 (3), 217–237.

Maestas, J.M., and Mamlouk, M.S., 1992. Comparison of pavement deflection analysis methods using overlay design. *Transportation Research Record*, 1377, 17–25.

Mahmud, S.M., Mishra, D., and Potyondy, D.O., 2018. Effect of Geogrid Inclusion on Ballast Resilient Modulus: The Concept of 'Geogrid Gain Factor'. *In*: ASME/IEE Joint Rail Conference (JRC 2018), 18–20 April, 2018, Pittsburgh, PA. New York: The American Society of Mechanical Engineers.

Malkin, A.Y., and Isayev, A.I., 2017. *Rheology: concepts, methods, and applications*. Elsevier.

Mamlouk, M.S., et al., 1990. Overlay design method for flexible pavements in Arizona. *Transportation Research Record*, 1286, 112–122.

Mateos, A., Ayuso, J.P., and Jáuregui, B.C., 2013. Evaluation of structural response of cracked pavements at CEDEX transport research center test track. *Transportation Research Record*, 2367 (1), 84–94.

McDowell, G.R., et al., 2006. Discrete element modelling of geogrid-reinforced aggregates. *Proceedings of the Institution of Civil Engineers: Geotechnical Engineering*, 159 (1), 35–48.

MTO, 2013. *Pavement design and rehabilitation manual*. 2nd ed. Ontario Ministry of Transportation.

Nguyen, M.L., et al., 2013. Review of glass fibre grid use for pavement reinforcement and APT experiments at IFSTTAR. *Road Materials and Pavement Design*, 14 (SUPPL.1), 287–308.

Nielsen, J., et al., 2020. *Fleksible belægninger med asfaltarmering – Mekanisk beregningsmodel*. Trafik & Veje.

Nielsen, J., 2021. Analytic analysis of a grid-reinforced asphalt concrete overlay. *In*: *Eleventh International Conference on the Bearing Capacity of Roads, Railways and Airfields*, Volume 1, 27–30 June, 2022, Trondheim, Norway. CRC Press Taylor & Francis Group, 346–354.

Nithin, S., Rajagopal, K., and Veeraragavan, A., 2015. State-of-the art summary of geosynthetic interlayer systems for retarding the reflective cracking. *Indian Geotechnical Journal*, 45 (4), 472–487.

Ong, G.P., Fwa, T.F., and Tan, S.A., 2004. Laboratory evaluation of rutting resistance of geosynthetics reinforced asphalt pavement. *Transportation*, 44 (2), 29–44.

Pasternak, P.L., 1954. On a new method of an elastic foundation by means of two foundation constants. *In*: *Gosudarstvennoe Izdatelstvo Literaturi po Stroitelstuve i Arkhitekture*.

Pellinen, T., and Witczak, M.W., 2002. Stress dependent master curve construction for dynamic (complex) modulus. *In*: *Asphalt Paving Technology: Association of Asphalt Paving Technologists-Proceedings of the Technical Sessions*, 18–20 March, 2002, Colorado Springs, CO. Association of Asphalt Paving Technologists (AAPT), 281–309.

Peutz, M.G., Van Kempen, H.P., and Jones, A., 1968. *Layered systems under normal surface loads*. Highway Research Record, 228.

Potyondy, D., Siekmeier, J., and Petersen, L., 2016. *Aggregate-geogrid interaction model incorporating moisture effects*.

Romanoschi, S.A., and Metcalf, J.B., 2001. Characterization of asphalt concrete layer interfaces. *Transportation Research Record*, 1778 (1), 132–139.

Sagnol, L., et al., 2019. Effect of glass fibre grids on the bonding strength between two asphalt layers and its contact dynamics method modelling. *Road Materials and Pavement Design*, 20 (5), 1164–1181. Available from: https://doi.org/10.1080/14680629.2018.1439764.

Sanders, P.J., 2001. *Reinforced asphalt overlays*. University of Nottingham, 381, October.

Schapery, R., 1962. Approximate Methods of Transform Inversion for Viscoelastic Stress Analysis. *In*: *Proceedings 4th US National Congress on Applied Mechanics*, Berkely, CA, 1075–1085.

Schuettpelz, C., Fratta, D., and Edil, T.B., 2009. Evaluation of the zone of influence and stiffness improvement from geogrid reinforcement in granular materials. *Transportation Research Record*, 2116 (1), 76–84.

Shell, 1978. *Shell pavement design manual: asphalt pavements and overlays for road traffic*. London, UK: Shell International Petroleum Co. Ltd.

Shook, J.F., et al., 1982. Thickness design of asphalt pavements-the asphalt institute method. *In*: *Proceedings, 5th international conference on structural design of asphalt pavements*. Vol. 1. The Netherlands: Delft University of Technology.

Siekmeier, J., and Casanova, J., 2016. *Geogrid reinforced aggregate base stiffness for mechanistic pavement design*. Minnesota Department of Transportation, (2016–24), July.

Skar, A., et al., 2020b. Analysis of a moving measurement platform based on line profile sensors for project-level pavement evaluation. *Road Materials and Pavement Design*, 22 (9), 1–17. Available from:https://doi.org/14680629.2020.1741429.

Skar, A., and Andersen, S., 2020. ALVA: an adaptive MATLAB package for layered viscoelastic analysis. *Journal of Open Source Software*, 5 (55), 2548.

Skar, A., Andersen, S., and Nielsen, J., 2020a. *Adaptive layered viscoelastic analysis (ALVA)*. Available from: https://github.com/asmusskar/ALVA.

Sobhan, K., 2005. *Effects of geosynthetic reinforcement on the propagation of reflection cracking and accumulation of permanent deformation in asphalt overlays*. 1–9, June.

Solatiyan, E., Bueche, N., and Carter, A., 2020. A review on mechanical behavior and design considerations for reinforced-rehabilitated bituminous pavements. *Construction and Building Materials*, 257, Article ID 119483. Available from: https://doi.org/10.1016/j.conbuildmat.2020.119483.

S&P Clever Reinforcement Company AG, 2020. S&P Carbophalt® G 200/200. Available from: https://p.widencdn.net/rx8gq5/R_CarbophaltG200200_Pub_Tds_Prod__EN_EN.

S&P Clever Reinforcement Company AG, 2021. S&P Glasphalt® G.

Trafikverket, 2011. *Trafikverkets tekniska krav Vägkonstruktion*.

Ullidtz, P., 1987. *Pavement analysis. Developments in civil engineering, 19*.

Ullidtz, P., et al., 2010. CalME, a mechanistic-empirical program to analyze and design flexible pavement rehabilitation. *Transportation Research Record*, 2153 (1), 143–152.

Uzan, J., Livneh, M., and Eshed, Y., 1978. Investigation of adhesion properties between asphaltic-concrete layers. *Asphalt Paving Technol*, 47, 495–521.

Vejdirektoratet, 2017. *Mmopp – Dimensioneringsprogram for vejbefæstelser*. Vejregler, 68. September.

Vinay Kumar, V., and Saride, S., 2017. Use of digital image correlation for the evaluation of flexural fatigue behavior of asphalt beams with geosynthetic interlayers. *Transportation Research Record*, 2631 (1), 55–64.

Weissman, S.L., et al., 1999. Selection of laboratory test specimen dimension for permanent deformation of asphalt concrete pavements. *Transportation Research Record*, 1681 (1), 113–120.

Williams, M.L., Landel, R.F., and Ferry, J.D., 1955. The temperature dependence of relaxation mechanisms in amorphous polymers and other glass-forming liquids. *Journal of the American Chemical Society*, 77 (14), 3701–3707.

Winkler, E., 1867. *Die Lehre von der Elasticitaet und Festigkeit: mit besonderer Rücksicht auf ihre Anwendung in der Technik, für polytechnische Schulen, Bauakademien, Ingenieure, Maschinenbauer, Architecten, etc.* H. Dominicus.

Zhao, Y., Tang, J., and Liu, H., 2012. Construction of triaxial dynamic modulus master curve for asphalt mixtures. *Construction and Building Materials*, 37, 21–26. Available from:http://dx.doi.org/10.1016/j.conbuildmat.2012.06.067.

Zofka, A., Maliszewski, M., and Maliszewska, D., 2017. Glass and carbon geogrid reinforcement of asphalt mixtures. *Road Materials and Pavement Design*, 18, 471–490. Available from:https://doi.org/10.1080/14680629.2016.1266775.

Full-scale validation of a mechanistic model for asphalt grid reinforcement

Julius Nielsen and Eyal Levenberg

Full-scale validation of a mechanistic model for asphalt grid reinforcement

Julius Nielsen[a,b] and Eyal Levenberg[a]

[a]Department of Environmental and Resource Engineering, Technical University of Denmark, Kgs. Lyngby, Denmark; [b]S&P Reinforcement Nordic ApS, Odder, Denmark

ARTICLE HISTORY
Compiled April 17, 2023

ABSTRACT

The pavement engineering community currently lacks an accepted response model that can practically capture and emulate the effects of asphalt grid reinforcement (AGR) products. A candidate model in this context was recently developed in the work of Nielsen *et al.* (2022), and the main objective of this (current) study was to validate it experimentally. A full-scale test setup was designed and constructed for this purpose; it involved two road sections instrumented with strain gauges and temperature sensors. The sections were nominally identical to each other, except that one included an AGR – installed at the bottom of the asphalt concrete layer. Initially, the as-constructed properties of the two sections were investigated by a combination of field and laboratory tests. Then after, they were loaded by several passes of a heavy vehicle with known weight and dimensions. The experimental campaign targeted slow speeds and relatively high asphalt concrete temperatures for which, according to the model, the AGR effect was expected to be most pronounced. The model was validated by demonstrating its ability to simultaneously reproduce all strain gauge readings; this was achieved in both the unreinforced and reinforced sections for any given vehicle pass. Overall, the investigation provided evidence that: (i) it was possible to observe the AGR effect and quantify the associated model parameters; and (ii) it was necessary to activate the AGR model-component for replicating the sensor measurements in the reinforced section. These findings attest to the potential suitability of the new model as a mechanistic component for asphalt pavement design – especially when including AGR products.

KEYWORDS
Model validation, mechanistic pavement modelling, asphalt grid reinforcement, layered elastic theory, viscoelasticity, full-scale testing, pavement instrumentation.

1. Introduction

1.1. *Background and motivation*

The term asphalt grid reinforcement (AGR) refers to a planar product with a mesh-like geometry composed of high-modulus materials, e.g., steel, polyester, glass fibres, and carbon fibres. AGRs are specifically designed for installation in direct contact with asphalt concrete (AC), either in-between new AC lifts, between a new AC lift and an old/aged (possibly cracked and damaged) AC, or between a new (bottom) AC lift and

---

its supporting granular base layer (Lytton 1989, Chang *et al.* 1999, de Bondt 1999, Cleveland *et al.* 2001, Button and Lytton 2007, Asphalt Academy 2008, Khodaii *et al.* 2009). The technical literature includes several studies focused on AGR effects. These studies are essentially experimental, contrasting the laboratory behaviour of reinforced and unreinforced AC test specimens (Chang *et al.* 1999, Arsenie *et al.* 2017, Saride and Kumar 2017, Zofka *et al.* 2017), or involving the construction and loading of reinforced and unreinforced pavement test sections – followed by comparing responses acquired from buried sensors (Nguyen *et al.* 2013, Graziani *et al.* 2014, Correia and Zornberg 2018). It was demonstrated in these studies that AGR products can potentially benefit pavement performance and prolong service life. Despite these promising advantages, there is currently no mechanistic empirical (ME) design method for asphalt pavements (e.g., ARA Inc. (2004)) that can generically handle AGR products.

One reason for this shortcoming is the lack of an accepted mechanistic response model that can correctly capture and emulate AGR effects. A candidate for such a model was recently developed and presented in the work of Nielsen *et al.* (2022). The development was based on further extending and enriching layered elastic theory (LET), which is the currently-accepted mechanistic component in ME design, to offer the following features: (i) linear thermo-viscoelastic behaviour for reproducing realistic AC layer properties; (ii) moving loads for representing realistic vehicular effects; (iii) fragmented layers for capturing the behaviour of old and severely damaged AC layers (Levenberg and Skar 2020); and (iv) relative sliding between any two adjoining layers for emulating imperfect bonding conditions. In particular, AGR effects were introduced into the new formulation as a combination of three contributions: (i) the existence of an AGR as an additional thin high-modulus elastic layer within the pavement system; (ii) the influence of an AGR on interlayer bonding; and (iii) the influence of an AGR on the properties of the surrounding AC. The work included a parametric investigation of the proposed model, and provided indirect validation that emulated AGR effects are in tune with reported field observations; it also provided guidelines for designing a test campaign that can highlight AGR effects and support direct model validation.

This (current) study is motivated by further evaluating the pavement modelling approach proposed by Nielsen *et al.* (2022), and judging its suitability and eventual acceptance to serve as a mechanistic component in ME design. The focus herein is on model validation, and specifically on the ability to emulate field-measured responses in a full-scale test setup that includes AGR. The paper commences with a literature review focused on full-scale validation approaches of existing asphalt pavement response models. The review is followed by stating the study objectives and outlining the associated methodology. Next, for completeness, the modelling formulation of Nielsen *et al.* (2022) is briefly re-stated; this is followed by a description of a full-scale experimental campaign designed and constructed for model validation. The approach for model validation and the validation results are presented afterwards, followed by a parametric investigation that evaluates and quantifies AGR effects for a specific pavement system. The paper concludes with a short summary of the entire effort, its main findings and implications, and ends with recommendations for future work.

1.2. *Literature review*

To gain acceptance as a mechanistic component in ME design, pavement models must be validated, i.e., shown to adequately reproduce and forecast responses in full-scale constructions. One of the earliest contributions in this context is the work of Burmister

(1943), which commenced with the presentation of a semi-analytic solution for layered elasticity, and continued with providing evidence of reproducibility. Specifically, utilising field-measured data from several test pavements, it was shown that LET is able to emulate load-deflection responses. Burmister concluded that: "...the theory of the two-layer system is in reasonably good agreement with the real phenomena." Over the years since 1943, the validity and limitations of LET for pavement modelling has been demonstrated in numerous investigations, e.g., Gusfeldt and Dempwolff (1967), Terrel and Krukar (1970), Krukar and Cook (1972), Chadbourn *et al.* (1997), Levenberg *et al.* (2009).

Nilsson *et al.* (1996) focused on validating the computer program VEROAD (ViscoElastic ROad Analysis Delft), which is a linear viscoelastic (VE) multilayer pavement response model. VEROAD takes into account horizontal and vertical moving loads with an option to include layer temperature dependency. As means of validation, in-pavement horizontal strains were measured in two full-scale accelerated pavement testing (APT) facilities, namely the LINear TRACKing (LINTRACK) facility at Delft University of Technology and the Road Testing Machine (RTM) at the Technical University of Denmark (DTU). The LINTRACK test section consisted of a 150 mm AC layer placed on top of 5 m compacted sand. The RTM test section comprised of a 60 mm AC layer on top of about 1.5 m of the combined unbound base, subbase, and soil layers. Both sections were instrumented with longitudinal and transverse asphalt strain gauges (ASGs) installed at the bottom of the AC, and temperature sensors installed at several levels within the AC. Falling weight deflectometer (FWD) tests were utilised in both test sections to estimate the elastic properties of the unbound layers. Furthermore, VE properties of the AC were estimated from laboratory testing of cores – taken only from the LINTRACK section. Triggered by a moving super-single tire configuration at LINTRACK and a dual-tire configuration at RTM, ASG responses were measured directly under the single tire and directly under one of the dual tires. Corresponding strain responses were simulated with VEROAD, and contrasted against measured responses. Based on a graphical comparison, it was concluded that the model was able to reproduce the measurements from the LINTRACK test. A less satisfactory match was observed for the RTM test, which was ascribed to utilising estimated VE properties for the AC.

In 1998, the Advanced Models for Analytical Design of EUropean pavement Structures (AMADEUS) (European Commission 2000) research project was set in motion for developing an advanced European pavement design method (European Commission 1999). As part of the project, several existing pavement models were evaluated by comparing simulated responses against responses measured in three APT facilities. Several European pavement research organisations were brought together to perform the analysis. Among the investigated models, the majority were based on LET. In addition, the layered VE model VEROAD, the anisotropic elastic layered model CIRCLY, the finite element codes SYSTUS and CAPA-3D, and the method of equivalent thickness were also evaluated. It was stated that VEROAD was superior to LET in matching horizontal AC strains. In addition, modelling features such as imperfect interface bonding and anisotropy were not found to produce a noticeable effect on the match between measured and simulated responses. Lastly, it was concluded that more advanced modelling efforts are needed to acceptably match measured vertical strains and stresses in unbound layers.

In the work of Mateos and Snyder (2002), the goal was to validate a LET-based pavement response model using field measurements from the instrumented asphalt pavement test area at the Minnesota road research facility (Mn/ROAD). This was

done by comparing simulations of longitudinal and transverse horizontal strains at the bottom of the AC layer to corresponding ASG readings. Two truck types were utilised, passing the ASG array at different speeds. A video camera attached to the trucks helped assess the lateral vehicle position relative to the ASG array. The AC temperature was measured for every truck pass using embedded thermocouples. Pavement layer properties were estimated based on elasto-static backcalculation of FWD measurements. Due to the VE nature of AC, the associated modulus input in the model was re-adjusted using ASG readings in a separate backcalculation procedure. The validation was done by identifying measured and calculated strain peaks from multiple truck passes and then contrasting them graphically. It was concluded that LET is incapable/insufficient – since longitudinal and transverse strains could not be matched simultaneously.

Graziani *et al.* (2014) set out to investigate the responses of a full-scale asphalt pavement near Ancona (Italy). The objective was to evaluate the mechanical effect of including AGR between two AC layers. The test consisted of three pavement sections; one including a glass fibre polymer AGR, a second including a carbon/glass fibre AGR, and a third section without reinforcement serving as a reference. The pavement comprised of a 50 mm surface AC layer paved over a 40 mm base AC layer, both resting on a 200 mm granular base course. In the two reinforced sections, the AGR was positioned between the two AC layers. All three sections were instrumented with embedded pressure cells and ASGs. The pressure cells were placed 50 mm below the top of the granular base course, while the ASGs were placed approximately 10 mm below the interface between the two AC layers. Temperature sensors were located at the same level as the ASGs. Dynamic cone penetrometer (DCP) tests, FWD tests, and complex modulus tests on AC specimens were carried out to obtain layer properties needed as modelling inputs. A three-axle truck with a target speed of 20 km/h was utilised for triggering the embedded instrumentation. A reference line was used to guide the driver for lateral positioning relative to the sensor array; the position was not directly measured. A LET model was employed to analyse the FWD drops and sensor readings under moving loads. Two modelling approaches were attempted: one including partial interlayer bond conditions (due to the presence of an AGR) and another assuming perfect/full interlayer bond conditions. The mechanical influence of the AGR was included as part of the AC properties. Achieving a match between measured and calculated stresses and strains was pursued through a trial-and-error procedure. However, it was impossible to obtain a simultaneous match of all sensor readings. One reason for this is the lack of precise information on the lateral truck position. Hence, AGR effects (and model validation) could not be realised in the study.

The study of Correia *et al.* (2018) included a validation effort of a reinforced asphalt pavement model using a prototype-scale experimental setup. The setup was a large steel box (1.8 m in length, 1.6 m in width, and 1.8 m in height) hosting an asphalt pavement. The pavement comprised two AC lifts: 60 mm (top) and a 50 mm (bottom) supported over a 200 mm unbound granular base, and underlain by a 1.0 m thick soil layer. A geocomposite was placed between the two AC lifts; it consisted of a geogrid attached to a nonwoven geotextile. The pavement system was loaded with a reduce-size single wheel equipped with a rubber tire, moving along a straight line with a peak speed of 3.6 km/h. Deflections were monitored with surface LVDTs (anchored to the box), AC strains were monitored with embedded ASGs, and vertical stresses were monitored with embedded pressure cells. Also, geocomposite strains were measured using extensometers glued to the geogrid ribs. The above-described setup was modelled in PLAXIS 2D assuming axisymmetry. All pavement layers were modelled

as linear elastic. The geocomposite was modelled by the built-in PLAXIS geogrid tool, which assumes a spring-like behaviour. The interaction between the grid and the AC layers was assumed fully bonded. Loading conditions were taken as static. The authors tried to match the measured responses of all embedded setup sensors with the model; the input choices were not fully explained. The best-achieved match was only shown graphically, without quantification, focusing on deflections, vertical stresses, and geocomposite strains (not ASGs). Visually, the fitting obtained was good at matching response peaks but not good at matching overall response shapes. This indicates that the chosen modelling framework is lacking. Also, the study did not include a reference (unreinforced) experimental setup to demonstrate the reinforcement effect and the model's ability to reproduce it.

To summarise, full-scale validation of pavement response models typically involved sections with embedded ASGs, pressure cells, and temperature sensors. Usually, ASGs were placed at the AC bottom, both longitudinally and transversely with respect to the loading direction, pressure cells were positioned in the unbound layers (mainly base and subgrade), and temperature sensors were placed inside the AC layer. Validation studies were often carried out with APT facilities, offering control over the applied loading (both intensity and location) and environmental conditions. Alternatively, they were carried out with vehicle loadings on exposed road sections (i.e., without any environmental control). In these cases, information about AC temperatures and lateral vehicle position are identified as critical for subsequent interpretation. In general terms, validation efforts were based on matching measured responses with simulated pavement responses. Unsurprisingly, modelling efforts accounting for the VE behaviour of AC layers were superior to models based solely on LET. Reproducibility was commonly demonstrated through a graphical comparison of response traces (peaks and shapes). For generating such comparisons, modelling inputs were obtained from separate sets of field and laboratory tests. Commonly applied tests for this purpose were FWD (mainly for estimating the moduli of unbound layers, DCP (for evaluating layer thicknesses), and laboratory complex-modulus (obtaining AC thermo-VE properties). In terms of full-scale validation of pavement response models including AGR, studies were very limited. Specifically, only two studies were identified; however, successful validation of pavement response models including AGR was not demonstrated. Accordingly, there is a need for a more targeted full-scale validation approach for validating the proposed model by Nielsen *et al.* (2022).

1.3. *Objective and methodology*

The main objective of this work is to provide experimental validation for the mechanistic pavement response model proposed by Nielsen *et al.* (2022). In general terms, the validation is assessed through the model's ability to capture and reproduce field-measured strain responses under vehicular loading. Particular attention is placed on validating the AGR model-component.

To achieve this, a test setup is designed and constructed, involving two road sections instrumented with ASGs and temperature sensors. The two sections are nominally identical except that an AGR is included in one, while the other serves as an unreinforced reference. Pavement layering and properties are assessed from field and laboratory tests; these are utilised as independent inputs for subsequent modelling. The two sections are loaded by a slow-moving vehicle of known weight, dimensions, and lateral position. Model validation is assessed through the ability to simultaneously

match all the ASG readings – in both the unreinforced and reinforced sections. In particular, the AGR model-component is validated by proving that it must be activated to correctly/reliably reproduce the field measurements in the reinforced section.

A secondary objective of this work is to evaluate the AGR effects in a synthetic investigation, i.e., purely computational. Here, the reinforced and unreinforced test sections are re-considered; a loading simulation is performed with a super-single tire travelling at two speeds (slow and fast) for two AC temperature levels (high and low). Key responses, commonly utilised for ME design are calculated; this is followed by quantifying and comparing the effects of including or excluding an AGR in the pavement system.

2. Theoretical Background

This section briefly re-states the modelling framework of Nielsen *et al.* (2022) for mechanistically capturing and emulating AGR effects. The reader should consult Nielsen *et al.* (2022) for more details and a deeper explanation of the concepts presented hereafter. In general terms, the modelling is split into two parts: (i) a linear formulation of a layered VE system subjected to moving loads that can accommodate imperfect bonding conditions and fragmented layers; and (ii) an AGR formulation that considers the material properties and geometry of the reinforcement product. The first part is based on extending the time-independent LET to include thermo-VE behaviour and moving loads – which has also been demonstrated in several studies (Levenberg 2013, Ahmed and Erlingsson 2016). The second part constitutes the main research contribution in Nielsen *et al.* (2022).

2.1. *Formulation of a layered VE system with moving loads*

Formulating a layered VE system with moving loads was based on LET originating from the work of Burmister (1943, 1945c,a,b). LET allows for calculating an elastic response R^e, i.e., stress, strain, or displacement, at any location in the system under a stationary vertical surface load uniformly distributed over a circular area (see Figure 1(a)). The system comprises $I-1$ layers of finite thickness placed on top of a half-space (layer I). Every layer, identified by a subscript i, is assumed homogeneous, isotropic, characterised by a Young's modulus (E_i), a Poisson's ratio (ν_i), and a thickness h_i ($h_I = \infty$).

Imperfect bonding conditions between layer i and $i+1$ were introduced according to Goodman and Popov (1968) – characterised by a horizontally oriented spring-bed with stiffness $k_{b,i}$. Fragmented layers were introduced to the layered elastic system following the formulation in Levenberg and Skar (2020). Accordingly, each fragmented layer is characterised by a vertical stiffness k_i, a horizontal stiffness $k_{h,i}$, and a shear deformation resistance (G_i) (replacing E_i, ν_i, and h_i).

The VE response R^{ve} (corresponding to R^e) of a layered system with time-dependent properties exposed to a stationary load (see Figure 1(b)) was obtained following Schapery's quasi-elastic approximation for isothermal conditions (Schapery 1962). In particular, the Young's modulus of the AC was 'replaced' with a time-dependent (and temperature-dependent) relaxation modulus $E(t)$. Finally, moving loads were emulated by superposing numerous VE stationary solutions after applying several loading-unloading sequences – see Levenberg (2016).
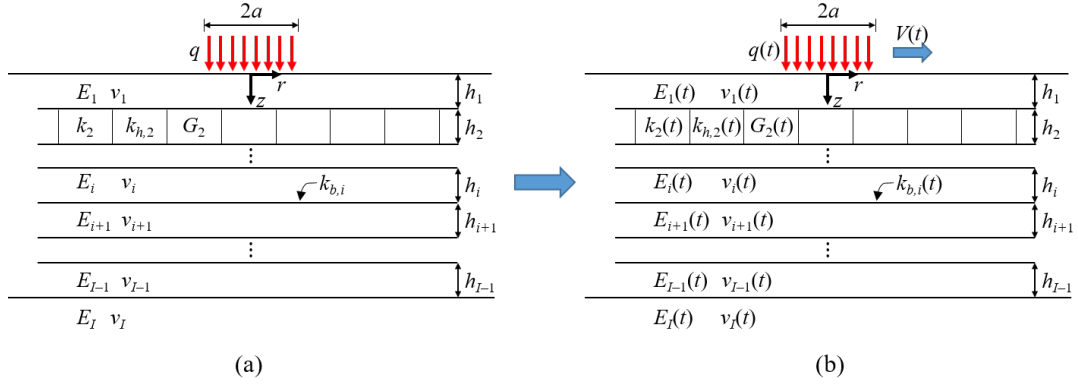
Figure 1. Cross-sectional view of: (a) a layered elastic system with variable interlayer bonding conditions and a fragmented layer, subjected to a stationary load; and (b) a corresponding system with time-dependent VE layer properties subjected to a moving load (Nielsen *et al.* 2022).

2.2. *Formulation of AGR effects*

Within the VE system (under moving loads), AGR effects were modelled as a combination of three contributions: (i) the presence of the AGR as an additional thin layer inside the pavement system; (ii) the AGR influence on the bonding conditions between the layer above it and the layer below it; and (iii) the AGR influence on the VE properties of the surrounding AC. The latter two contributions are deemed applicable only when the ratio between the grid's effective aperture size (EAS) and the AC's nominal maximum aggregate size (NMAS), i.e., EAS/NMAS, is smaller than (about) five. This requirement is linked to complying with representative volume element considerations, i.e., to the statistical justification for working with a continuum mechanics framework (see e.g., Kim *et al.* (2010)).

The first contribution was captured by adding a thin elastic layer to the stratified system. For this purpose, the AGR is described by a set of 'effective' properties, namely: Young's modulus, Poisson's ratio, and a certain thickness. The effective elastic properties reflect the product's material composition; if the AGR ribs are made of different materials, then some averaging must be done to arrive at an effective modulus and an effective Poisson's ratio. In this context, the theory assumes that the effective AGR modulus is larger than the instantaneous AC modulus (E_0). If this assumption is not met the effective grid modulus may (in some instances) be lower than the surrounding AC modulus, and a reinforcing effect is not active at all times. In addition, the effective thickness is attained from 'smearing' the AGR's material volume into a homogeneous layer with uniform thickness.

The second contribution is captured by assigning two horizontal springs to the thin layer j representing the AGR – one with the layer above it ($k_{b,j-1}$), and another with the layer below it ($k_{b,j}$). The two horizontal spring values are related to the EAS-NMAS ratio, as schematically presented in Figure 2(a).

The third contribution deals with the so-called zone of influence (ZoI) effect that originates from local interlocking between AC aggregates and AGR apertures. Under loading, this interlocking is assumed to partially restrain aggregates from moving, creating additional confinement within an influence zone near the grid – leading to a modulus increase (Schuettpelz *et al.* 2009). This effect is emulated (see Figure 3(a)) by sub-dividing the AC layers neighbouring the AGR, and assigning the adjacent sub-layers a thickness δ^{ZoI} and a relaxation modulus $E^{ZoI}(t)$ (that differs from $E(t)$). δ^{ZoI}
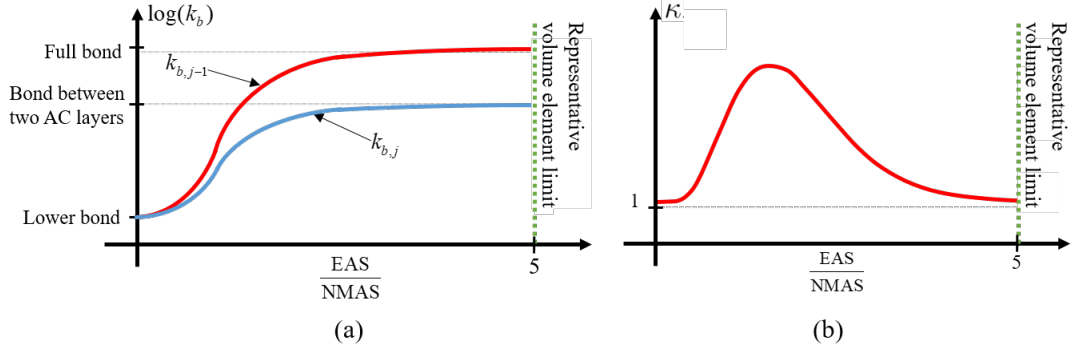
Figure 2. Conceptual sketches describing the influence of the EAS-NMAS ratio: (a) on the bonding conditions above and below the AGR, and (b) on the κ factor (Nielsen *et al.* 2022).

is expected to be somewhere within the range of one to three times the NMAS of the adjacent material; this range is based on studies dealing with grid-reinforced granular materials (McDowell *et al.* 2006, Schuettpelz *et al.* 2009, Chen *et al.* 2012, 2014). The added confinement within the defined ZoI is captured by increasing the AC equilibrium modulus from E_∞ to E_∞^{ZoI} (see Figure 3(b)). This increase is mathematically expressed by a unitless and time-independent κ factor, defined as:

$$E_\infty^{ZoI} = \kappa E_\infty \quad , \quad 1 \leq \kappa \leq \frac{E_0}{E_\infty} \tag{1}$$

The lower limit imposed on κ prevents the model from producing a decrease in E_∞; the upper limit ensures that E_∞^{ZoI} cannot exceed E_0 (which will violate the concept of fading memory). Moreover, the value of κ is expected to depend on the EAS-NMAS ratio according to the schematic representation in Figure 2(b).
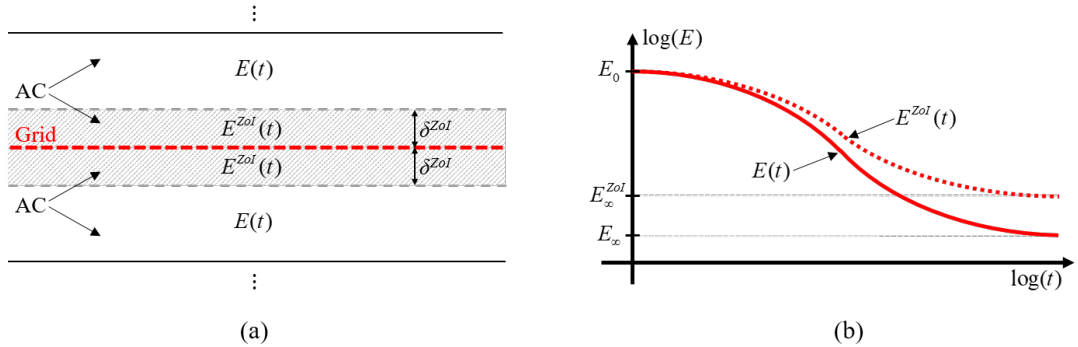
Figure 3. Emulation of the ZoI effect, where: (a) sub-division of the AC layer adjacent to an AGR and (b) Relaxation modulus of the AC inside and outside the ZoI (Nielsen *et al.* 2022).

2.3. *Model implications on validation efforts*

The above formulation was implemented in a computational model tentatively named GRIDPAVE-MM. The implementation involved utilising the open-source MATLAB code ALVA (Skar *et al.* 2020b, Skar and Andersen 2020), and extending its elastic component to handle fragmented layers, VE layers, moving loads, and AGR effects.

8

GRIDPAVE was verified by comparison against existing closed-form solutions and other mechanistic tools. A parametric investigation of GRIDPAVE yielded some recommendations for designing an experimental setup that supports validation and ensures the collection of usable measurements for quantifying AGR effects. Specifically, it was proposed to utilise instrumented pavement sections with ASGs or pressure cells at the AC bottom, and avoid placing sensors in the subgrade or focusing on deflection testing. These recommendations were based on observations that showed a pronounced and measurable AGR effect on the strain levels at the bottom of the AC and at the top of a supporting granular base layer. AGR effects were not pronounced for surface deflections and subgrade strains. Moreover, it was observed that reinforcement effects are greater when loads move slowly in combination with high AC temperature conditions. Lastly, it was suggested to maximise laboratory characterisation for a priori determination of several modelling inputs, specifically: effective AGR thickness and modulus, interface bond conditions between an AGR and adjacent pavement layers, and VE properties of the AC. The evaluation of κ was recommended through inverse analysis of strain measurements in a full-scale test setup.

3. Experimental investigation

The experimental investigation involved the construction of an instrumented asphalt road (DTU Smart Road), consisting of four adjoining sections, each 25 m long. Three sections contained an AGR at different depths while the fourth was unreinforced – serving as a reference section. The DTU Smart Road was built in October 2021, as a reconstruction of an existing pavement located in Kongens Lyngby (Denmark) within DTU's campus. It is a two-lane, 7.9 m wide road, serving live campus traffic. For the experimental investigation presented herein, the road was closed to the public, and subsequently loaded by several passes of a slow-moving heavy forklift. This was done in June 2022, while the AC temperatures were relatively high, on two of the Smart Road sections: Section S-0 (reference) and Section S-1 where the AGR was placed at the AC bottom.

3.1. *Full-scale test design*

The S-0 and S-1 sections in the DTU Smart Road were constructed with a 150 mm thick AC layer, paved in three lifts: 40 mm (bottom), 70 mm (middle), and 40 mm (top). All lifts were made from the same asphalt mix-type complying with EN 13108-1 (2016) requirements, having a flat S-shaped aggregate gradation curve about the maximum density line with a NMAS of 8 mm. A neat bitumen with a penetration grade of 70/100 was utilised; the bitumen content was 5.6%. Constructing the AC layer from one single mix-type was purposefully done in order to simplify subsequent modelling and validation efforts.

The AC was paved on top of an existing unbound granular structure (UGS), 750 mm in thickness, that was recompacted and prime-coated before the paving operations. Visually, and following ASTM D2487 (2017) terminology, the UGS was classified as GP, i.e., poorly-graded gravel-sand mixture with little to no fines. It had a sandy appearance, included about 2% cobbles, and was characterised by a NMAS of 37.5 mm. Section S-0 was unreinforced, while Section S-1 had an AGR installed on top of the prime-coated granular structure (before paving); a picture taken during the AGR installation process is presented in Figure 4(a). The specific AGR utilised was a Car-

bophalt®G 200/200 (S&P Clever Reinforcement Company AG 2020) consisting of bituminous-coated carbon fibres with square openings 15 mm × 15 mm in size, corresponding to an EAS = 15 mm. This grid has (approximately) a similar amount of fibres in each direction – characterised by a Young's modulus of 265 GPa, a Poisson's ratio of 0.15, and an average (smeared) cross-sectional area of about 50 mm^2/m. Lastly, the UGS was founded on the local soil in the region, extending to a large depth. It is a fine-grained overconsolidated inorganic silty sand, classified as SM according to ASTM D2487 (2017). A cross-sectional view of the two above-described pavement systems is presented in Figure 4(b).

(a)   (b)
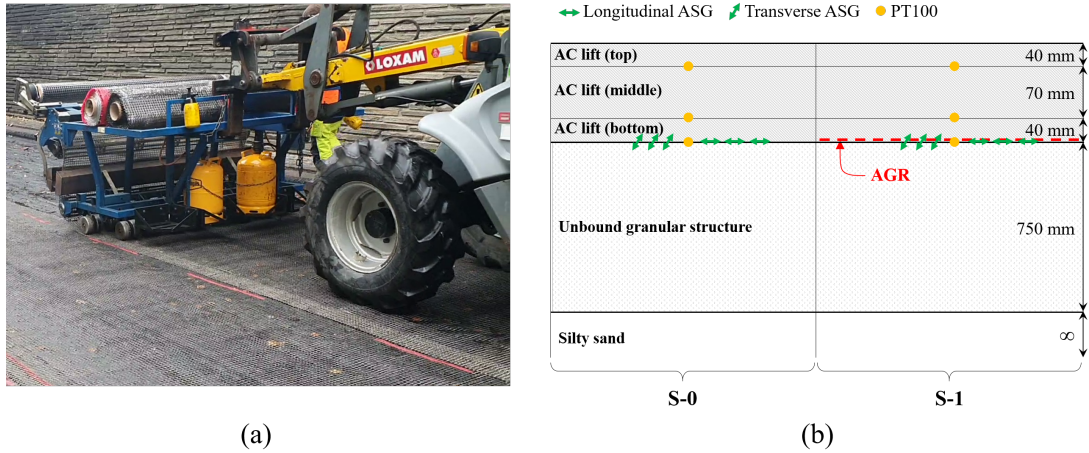
Figure 4. The DTU Smart Road: (a) installation picture of an AGR, and (b) a cross-sectional view (not in scale) of the layering and instrumentation in sections S-0 and S-1.

Six ASGs were embedded in each section before AC paving operations. These were installed to capture horizontal strains at the AC bottom in two perpendicular directions. The utilised ASGs were all of type KM-120-120-H2-11 (Kyowa Electronic Instruments 2022), specifically designed for AC embedment with an operational temperature range of −10°C to +70°C. The ASGs were centrally positioned in each test section to lessen any edge effects or interference with neighbouring test sections. With respect to the direction of travel, they were oriented to measure longitudinal strains and transverse strains. In terms of spacing, they were placed 300 mm from each other in both the longitudinal and transverse direction; this was to measure strain responses in different locations within the AC. The instrumentation arrangement is depicted in Figure 5(a) alongside ASG naming. As can be seen, ASG1, ASG2, and ASG3 measured longitudinal strains, while ASG4, ASG5, and ASG6 measured transverse strains. In section S-0 the ASGs were installed directly on top of the prime-coated UGS, while in section S-1 the ASGs were installed directly on top of the AGR (see Figure 5(b)).

To ensure the ASGs remained in place during the paving process, they were fixed to the UGS/AGR surface with heated mastic asphalt. The mastic was applied first, and then the ASGs were (each) placed into it and manually held until cool-down. Afterwards, the cables were bundled and led into a roadside manhole – separately for each individual section. The bundles were manually covered with hot mix asphalt to protect from paving operations. Figure 5(b) offers a visual representation of this preparation stage. Finally, to prevent any damage to the ASGs, the asphalt paver and asphalt delivery trucks were strictly guided to only cross over areas where the cables had been protected. The ASGs were left exposed until coverage with hot mix asphalt

by the paver. After construction, it was discovered that all ASGs survived the paving activities except for ASG2 in S-1, i.e., achieving a post-construction survivability of 92%.

Lastly, three PT100 temperature sensors were installed per test section to capture the thermal conditions across the AC thickness. These were placed at the bottom of each AC lift above one another at the depths: 150 mm, 110 mm, and 40 mm (see Figure 4(b)). A similar installation process to the ASGs was followed for the PT100s, achieving a post-construction survivability of 100%.

(a)   (b)
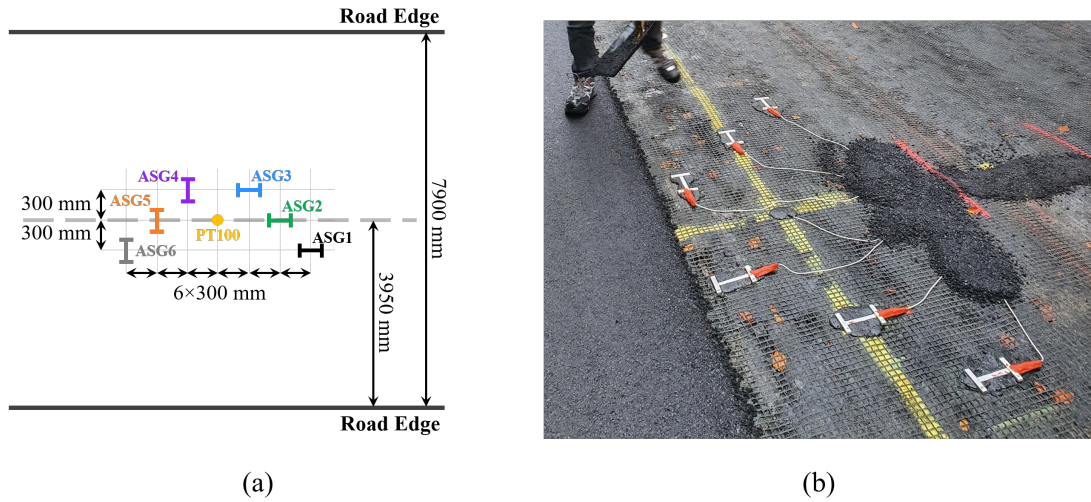
Figure 5. The DTU Smart Road: (a) top view layout of the ASGs, and (b) a picture of the ASGs before being covered with AC.

3.2. *Direct estimation of pavement properties*

3.2.1. *DCP test*

Before paving, while the UGS was exposed, a DCP test according to ASTM D6951/D6951M (2018) was carried out in each section down to a depth of about 2 m; this was done to estimate the thickness of the UGS and assess the similarity level between sections S-0 and S-1. Figure 6 presents the measured DCP profiles for S-0 (left) and S-1 (right); both charts utilise markers to depict measured penetration depth versus the cumulative number of drops. In these charts, the penetration depth was adjusted to start from the AC surface level. Moreover, regression lines (dashed) are included to help visualise the penetration rates, i.e., penetration depth per drop. As can be seen, at a depth of approximately 900 mm an abrupt change in penetration rate is observed for both DCP profiles. This change, indicated with a horizontal dotted line, represents the formation level, i.e., the interface between the UGS and the local silty sand; evidently, both sections share a UGS thickness of 750 mm. Especially in granular materials, the DCP test is known to exhibit high variability in penetration rates (Konrad and Lachance 2001). This can explain the differences in penetration rates (of about 30%) between the granular structures of the two sections. For the top part of the local silty sand, the penetration rates are within 17% of one another. This difference does not necessarily imply a large gap in moduli, given that the DCP is only weakly correlated with modulus (Newcomb *et al.* 1995).
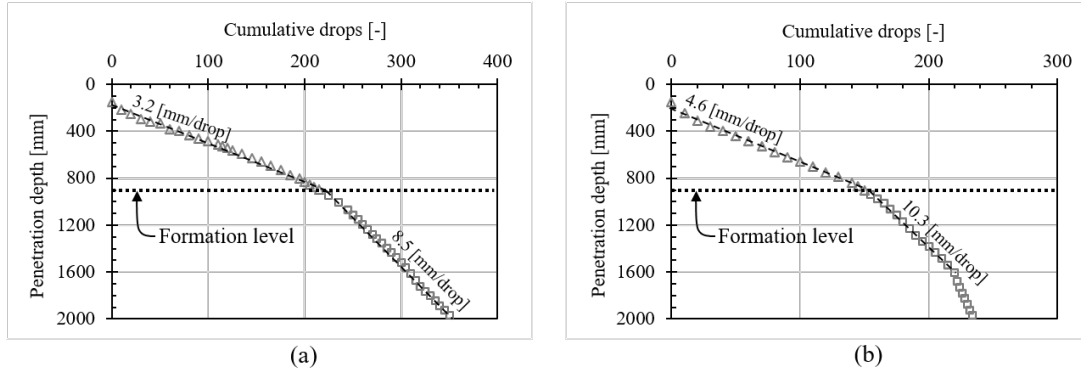
Figure 6. DCP profile in (a) S-0 and (b) S-1.

3.2.2. FWD test

An FWD campaign according to ASTM D4694 (2009) was carried out in March 2022; a total of 18 drops were executed in each of the two test sections S-0 and S-1. The drops were applied along the road centre line in the vicinity of the ASG arrays, in three locations spaced 1 m apart. Surface AC temperatures of 5 °C to 7 °C were recorded during the testing. The FWD had a 300 mm load-plate diameter and 14 geophones at radial distances ranging from zero (load-plate centre) up to 2400 mm. At every test location, drops were applied from three heights, aiming for three peak stress levels: 0.8 MPa, 1.1 MPa, and 1.4 MPa. Elastostatic backcalculation was carried out with the FWD measurements. This was done separately for each FWD drop, providing a total of 36 sets of estimated layer moduli. The aim of this effort was to estimate layer moduli, assess the nonlinear behaviour (or stress-level sensitivity) of the UGS, and assess the structural similarity across the two pavement sections.

Listed in Table 1 is the layering arrangement of the two sections based on the DCP results and construction records; also listed are the assumed Poisson's ratios. The backcalculation algorithm minimised the average absolute relative difference between measured and computed deflections, achieving best-match errors in the range of 1.27% to 1.55%. Forward deflection calculations were done with ALVA (Skar *et al.* 2020b, Skar and Andersen 2020). The means of all derived Young's moduli sets are listed in Table 1, with results separated according to the different FWD peak stress levels. As can be seen, relatively high AC moduli, of about 20 GPa, and relatively low UGS moduli, of about 100 MPa, were obtained. The reliability of these results is somewhat limited given that the AC layer thickness of 150 mm is smaller than the spacing between the FWD geophones that are closest to the loading plate (200 mm), and smaller than the loading plate's diameter (300 mm). Nonetheless, when comparing the moduli results across peak stress levels, there is a general tendency of modulus to increase with FWD peak stress. The effect is relatively small for the AC and silty sand, and is more pronounced for the UGS – indicating nonlinear behaviour. Lastly, it is noted that the silty sand moduli in sections S-0 and S-1 were within ±11 MPa of the average shown in the table. This validates a mechanical similarity of the subgrade and deeper soil layers across the two pavement sections.

12

Table 1. Pavement sections S-0 and S-1: layer thicknesses, Poisson's ratios, and backcalculated moduli from FWD testing.

		Peak FWD stress level:	0.8 MPa	1.1 MPa	1.4 MPa
Layer	Thickness [mm]	Poisson's ratio [-]		Young's modulus [MPa]	
AC	150	0.30	19730	21486	22199
Granular	750	0.35	95	105	112
Silty sand	∞	0.40	162	171	174

3.2.3. VE characterisation of AC

After construction, the AC layer in the DTU Smart Road was cored for subsequent VE characterisation in the laboratory. Two AC specimens were tested under cyclic loading in an indirect tensile configuration (EN 12697-26C 2018), each 100 mm in diameter and 50 mm in thickness. Load-displacement histories were recorded at eight temperature levels ranging from 0 °C to 35 °C at 5 °C increments. The choice for the low end was due to equipment limitation of maintaining a constant temperature level below 0 °C. The choice for the high end was due to concerns about nonlinearity and excessive viscoplasticity above 35 °C. Ultimately, VE properties were estimated through inverse analysis following the approach outlined in Levenberg and Michaeli (2013) with the relaxation modulus $E(t)$ mathematically expressed as follows (Levenberg 2013):

$$E(t) = \frac{E_\infty(1 + (t/\tau_D)^{n_D})}{(t/\tau_D)^{n_D} + (E_\infty/E_0)} \tag{2}$$

where t denotes time, E_0 and E_∞ are the instantaneous and equilibrium moduli (respectively), n_D is a unitless shape parameter, and $\tau_D = \tau_D^0 a_T$ is a shape paremeter with time units. τ_D^0 (units of time) is related to a reference temperature T_0, and the time-temperature shift factor a_T (unitless) was taken as (Williams *et al.* 1955):

$$\log_{10}(a_T) = \frac{-C_1(T - T_0)}{C_2 + (T - T_0)} \tag{3}$$

where C_1 (unitless) and C_2 (units of temperature) are constants.

The final VE material properties are listed in Table 2; they represent an average over the properties of the two specimens. In the analysis, E_0 and E_∞ were pre-chosen and fixed because it is impossible to test specimens in an indirect tensile configuration under the two extreme conditions. Thus, the inverse analysis was done with the following four unknowns: n_D, τ_D^0, C_1, and C_2. The typical range for E_0 is 20 GPa to 40 GPa and the typical range for E_∞ is 80 MPa to 200 MPa (Witczak and Fonseca 1996, Andrei *et al.* 1999, Cho *et al.* 2010). Accordingly, 30 GPa and 100 MPa were selected for the instantaneous and long-term relaxation moduli (respectively). The specific numerical values chosen for E_0 and E_∞, as long as they reside within the typical ranges, have practically no effect on calculated pavement responses under moving traffic loads. This is because they represent speed-temperature combinations that are extreme/unrealistic.

Table 2. VE properties of the AC associated with a reference temperature of $T_0 = 20°C$.

E_0 [MPa]	E_∞ [MPa]	n_D [-]	τ_D^0 [s]	T_0 [°C]	C_1 [-]	C_2 [°C]
30000	100	0.47	47	20	23	197

3.3. *Measurement campaign*

In June 2022, a measurement campaign was carried out to capture load-induced pavement responses from the embedded ASGs. The campaign utilised a heavy two-axle forklift with a load configuration as shown in Figure 7(a). The front axle load was 110 kN and the rear axle load was 120 kN – see Figure 7(b). The front axle accommodated two sets of dual tires, whereas the rear axle hosted two single tires. All six tires were of a similar size/type, characterised by a contact width of 270 mm. Strain measurements were triggered by the forklift passing the ASG array at a speed of about 2 km/h. This choice was driven by the expectation of a more pronounced AGR effect under slow-moving loads (refer to Subsection 2.3). Six passes were applied in total; three passes over the S-1 section, followed by three passes over the S-0 section. The lateral forklift positions, which varied from pass to pass, were assessed by a GoPro camera attached to the vehicle. This camera captured the edge of the leftmost front tire (Tire 1) crossing two transversely-oriented measuring tapes that were glued to the road surface – see Figure 7(a). Based on the GoPro footage, it was possible to establish the offset Y_0, defined as the lateral distance from the centre of Tire 1 to the road centre line. The GoPro footage showed that lateral positions could vary within ± 50 mm between the two measuring tapes, indicating that the vehicle was not travelling perfectly parallel to the road's centre line. For analysis purposes, the Y_0 of a given pass was taken as the average of the two readings.
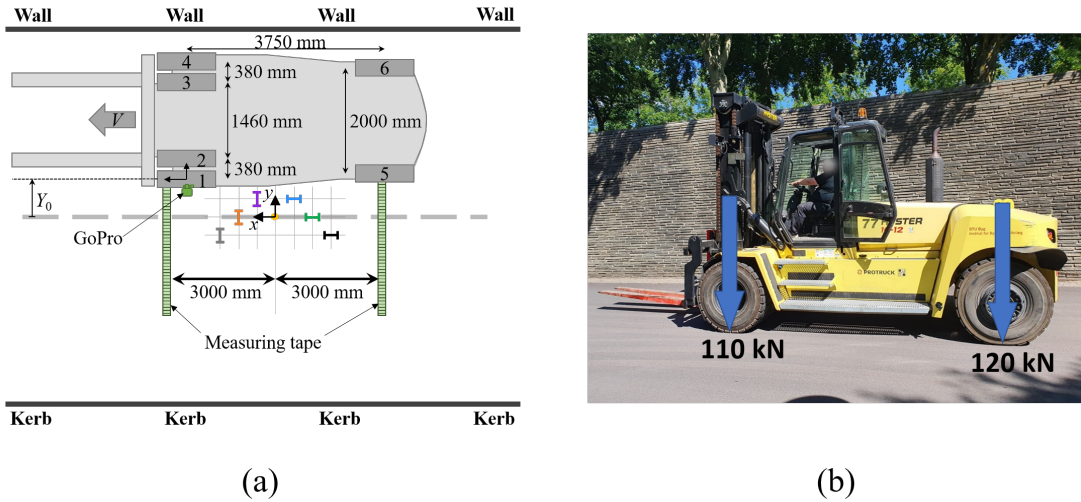
Figure 7. Loading of the DTU Smart Road: (a) top view illustration of the test setup, and (b) picture of the heavy two-axle forklift utilised to generate ASG readings.

During passes over the S-1 section, five ASG response traces were recorded (no response in ASG2); during passes over the S-0 section, six ASG response traces were recorded. All ASG measurements were recorded with a sampling rate of 50 Hz. An example of response measurements from the longitudinal and transverse ASGs is given in Figure 8; these correspond to Pass #5 in the S-0 section. The soil mechanics sign

convention is utilised in the figure (and hereafter), wherein a positive sign represents compressive conditions, and a negative sign represents tensile conditions. It can be observed that different lateral distances between each ASG and the vehicle tires result in different strain responses in terms of intensity and shape. Furthermore, peaks associated with the two-axle loads can be clearly observed in the ASG readings; the first occurring peaks are associated with the front axle, while the second peaks are associated with the rear axle. The actual vehicle speed V for each pass was estimated based on the distance between the two axles and the time delay between measured strain peaks. It is further noticed that, within the plotted range, the strain level in the longitudinal ASGs returns back to its starting point in-between the two axles. A similar return to zero does not occur in some transverse ASG readings; these exhibit signal recovery that is unrealistically slow, as well as irrecoverable readings that are unrealistically large. All six recorded passes exhibited this type of 'drift' behaviour. In the case presented in Figure 8, the measurements do not return to their starting point for ASG4 and – more significantly – for ASG5. While part of this behaviour can be due to time-dependent viscoplastic effects, it seems more plausible that the behaviour is mainly due to artificial drift – mechanical or electrical (or both).
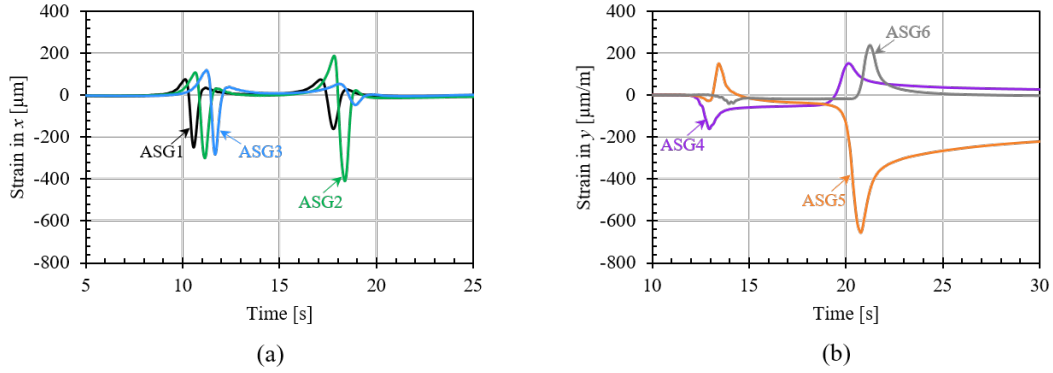
Figure 8. ASG readings during Pass #5 (S-0), where (a) indicates longitudinal strains and (b) indicates transverse strains.

Temperature measurements were recorded with the PT100 sensors during each pass (at three depths). Based on these readings, a continuous temperature profile across the entire AC thickness was reconstructed by fitting a second-degree polynomial. Examples of measured PT100 results and estimated temperature profiles in the S-0 and S-1 sections are illustrated in Figure 9. It is noteworthy that temperatures in the AC varied by about $25\,°C$ across the $150\,mm$ thickness (top to bottom). For each of the six passes in the experimental campaign, Table 3 provides a summary of the lateral vehicle offset (Y_0), speed (V), and AC temperatures.

Table 3. Summary of lateral offsets (Y_0), travel speeds (V), and AC temperatures during the forklift passes.

Section	Pass #	Offset, Y_0 [mm]	Speed, V [km/h]	T at $z = 40\,mm$ [°C]	T at $z = 110\,mm$ [°C]	T at $z = 150\,mm$ [°C]
S-1	1	+215	1.9	34.7	24.7	21.0
S-1	2	+330	1.9	34.9	24.9	21.2
S-1	3	+290	1.9	35.2	25.3	21.5
S-0	4	+360	1.9	38.4	26.6	22.7
S-0	5	-145	1.9	38.4	26.7	22.8
S-0	6	-90	1.9	38.9	27.4	23.4

15

Figure 9. Temperature conditions in the AC during Pass #1 (S-1) and Pass #4 (S-0): PT100 sensor measurements (circular markers) and estimated continuous temperature profiles (solid lines).

4. Model validation

4.1. *Preliminary considerations*

GRIDPAVE was validated based on providing evidence of reproducibility, i.e., the ability to fit field ASG measurements with model-predicted strain responses. This ability was demonstrated for both the unreinforced and reinforced sections, with specific attention to the contribution of the AGR model-component (see Subsection 2.2). Prior to presenting the analysis details, three preliminary aspects are hereafter addressed.

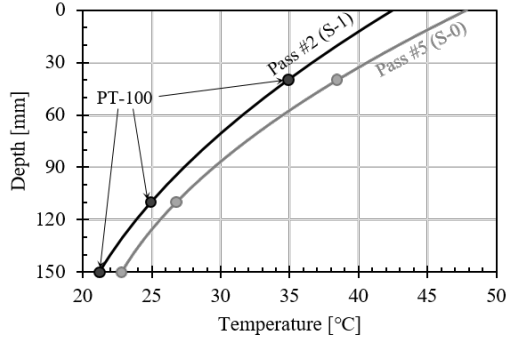The first aspect concerns the non-linear behaviour of the UGS, which was observed in the FWD results as the increase in UGS modulus with an increase in FWD peak stress level (see Table 1). It is recognised that the stress-strain behaviour of unbound granular materials is governed by a resilient modulus, which is a function of the stress state. Given that GRIDPAVE imposes a linear theory, the effective (or representative) modulus of the UGS becomes dependent on a given loading scenario and (indirectly) on the overlying AC relaxation modulus. Accordingly, a representative UGS modulus must be chosen in relation to the applied loading configuration, intensity, speed, and AC temperature conditions during the measurement campaign. This is especially important/influential when considering the big differences in the prevailing temperature and loading conditions between the FWD test campaign (AC at 6 °C, short loading pulses) and the measurement campaign (AC up to 40 °C, slow-moving tire loads). The UGS modulus was re-calibrated to address this issue, based on fitting the ASG readings from S-0. Furthermore, each forklift pass was split into two separate axle loading events, and an individual UGS modulus was estimated for each event. Such splitting was deemed valid, given that the distance between the axles was large enough. As can be seen in Figure 8, the strain responses at the AC bottom drop to nearly zero between the two axles. The re-calibrated UGS moduli obtained from the unreinforced section were subsequently utilised for analysing S-1.

The second aspect deals with the sensitivity of measured strain responses to the lateral (offset) position of the forklift (Y_0). It is recognised that knowledge of the load position relative to each of the embedded ASGs must be precise, of the order of a centimetre, for the model to reproduce measured responses correctly. However, from a practical perspective, it is challenging to directly measure lateral vehicle-to-ASG distances at the needed precision. In particular, for the given test setup which involved a GoPro camera and surface measuring tapes, there were two practical issues. First, a human-driven vehicle does not move perfectly straight in a line parallel to the

16

ASG array, and second, individual ASGs could have slightly changed their position during paving – which is difficult to assess post-construction. To accommodate these aspects, the measured Y_0 values listed in Table 3 were allowed to slightly change within $\pm 50\,\text{mm}$ during subsequent analyses.

The third aspect relates to artificial signal drift as well as delayed/irrecoverable responses that were observed in the readings of the transverse-oriented ASGs – see Figure 8(b). Signal drift will falsely portray strain relaxation after loading, hence, any drift gained after one axle load will eventually distort the strain peaks associated with the following axle load. As the model cannot (and should not) replicate such a drift, directly contrasting the model with ASG measurements would be misleading. An effort was made to address this aspect by, first, annulling the ASG drift in-between axle loading events. This was achieved (after load splitting) by choosing a starting point for the measured strain responses guided by the model; and second, by matching both the strain responses and their corresponding strain rates. The strain rates represent an additional set of reference signals for model validation. By definition, these additional 'sensors' exhibit diminished signal delays, and no irrecoverable responses.

4.2. Overall approach

A validation approach was established to provide evidence of model reproducibility while incorporating all three above-listed aspects. A graphical representation of the approach is shown in Figure 10, which depicts a three-block flowchart. Block (1) refers to the physical reality, i.e., the experimental activities covered in Section 3. The experimental activities provide the needed modelling inputs along with field-measured ASG readings for the model analysis and validation. Block (2) refers to the modelling and analysis efforts of the reference (unreinfroced) section S-0. In general, ASG measurements from S-0 (i.e., forklift Passes #4–6) were utilised to re-calibrate the Young's modulus of the UGS (E_{ugs}) under each forklift axle. To achieve this, GRIDPAVE without AGR was executed, and E_{ugs} was inferred in an inverse analysis scheme serving as the main unknown parameter. The Y_0's were also allowed to vary, but within a limited range of $\pm 50\,\text{mm}$. Two optimal E_{ugs} values were found from this procedure: one for each of the forklift axles. The optimal E_{ugs} values were then carried over to Block (3), and utilised as fixed/known inputs for modelling and analysis of the reinforced section S-1. Here, ASG measurements from S-1 were utilised to estimate a κ-value for each axle loading event of Passes #1–3. To achieve this, GRIDPAVE with an active AGR-component was utilised, and κ was inferred in an inverse analysis procedure (where Y_0's were also allowed to vary slightly within the limited range of $\pm 50\,\text{mm}$). Ultimately, GRIDPAVE was validated by demonstrating that a superior match to the ASG readings in the reinforced section is only possible if the AGR model-component is active. In the following two subsections, a more detailed explanation is provided for the analyses and results associated with Block (2) and Block (3).

4.3. Analysis of the unreinforced S-0 section

The unreinforced S-0 section was modelled as a fully-bonded eight-layered VE system – see Figure 11(a). The top six layers were VE, representing the $150\,\text{mm}$ AC layer, each with a thickness of $25\,\text{mm}$, a Poisson's ratio of $\nu = 0.30$, and a relaxation modulus $E(t)$ expressed by Equation (2) with the input parameters listed in Table 2. The other two pavement layers were elastic, representing the UGS and the silty sand. Sub-layering of

17
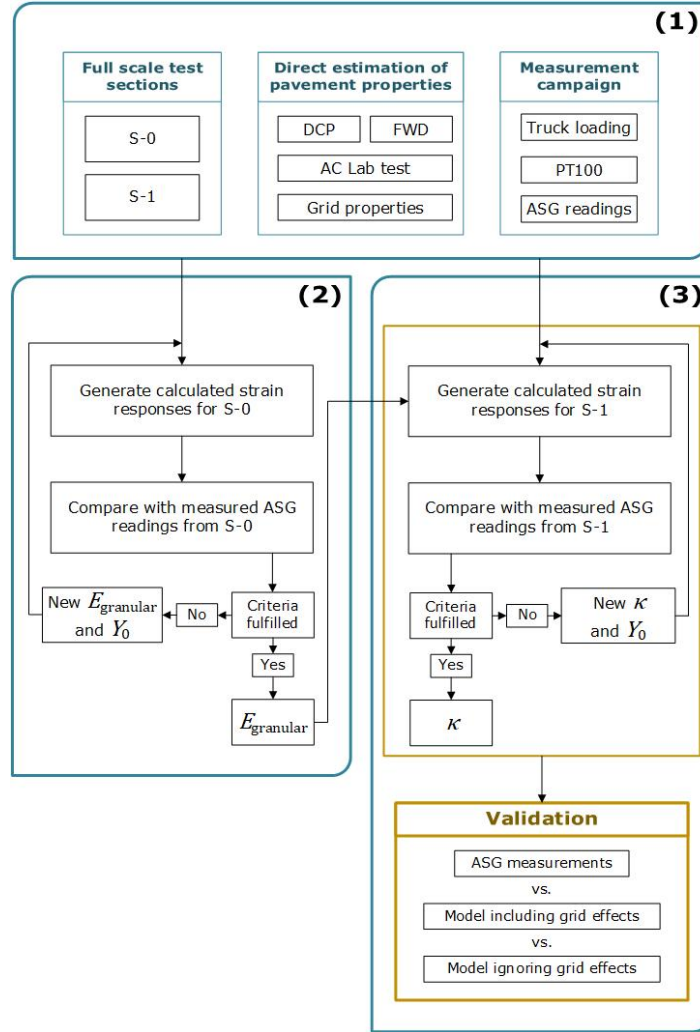
Figure 10. Flowchart showing the model validation approach: (1) physical reality, (2) modelling and analysis of the unreinforced (reference) S-0 section, and (3) modelling and analysis of reinforced S-1 section.

the AC was done to emulate the temperature effects across the AC thickness. In this context, the temperatures from the PT100 sensors were utilised to estimate a single representative temperature level for each AC sub-layer. Then, a time-temperature shift factor (see Equation (3)) was evaluated for each sub-layer using the parameters listed in Table 2. The relaxation modulus of each sub-layer was then shifted accordingly. A silty sand modulus of $E_8 = 169\,\mathrm{MPa}$ was selected as the average Young's modulus across the three peak stress levels listed in Table 1. The UGS modulus, i.e., E_7, was treated as an unknown for subsequent determination from an inverse analysis. The obtained moduli values, one for each axle type, were then carried over to the analysis of the S-1 section.

The pavement surface was subjected to multiple moving loads representing either the front axle or the rear axle of the forklift – see configuration in Figure 7. Each axle load was assumed to move with a constant speed V, along a straight path parallel to the road centreline in the x-axis direction. All loads were modelled as vertically and uniformly applied over circular areas with a radius of $a = 135\,\mathrm{mm}$, corresponding to half the tire width. On the front axle, tires exerted a stress intensity of $q = 0.47\,\mathrm{MPa}$,

18

Figure 11. Pavement modelling as a layered VE system: (a) unreinforced S-0 section, and (b) reinforced S-1 section.

whereas tires on the rear axle exerted a stress intensity of $q = 1.04\,\text{MPa}$. The relative lateral distances between all loads and embedded ASGs were governed by Y_0 (different for the different passes), defined as the lateral distance between the road centreline and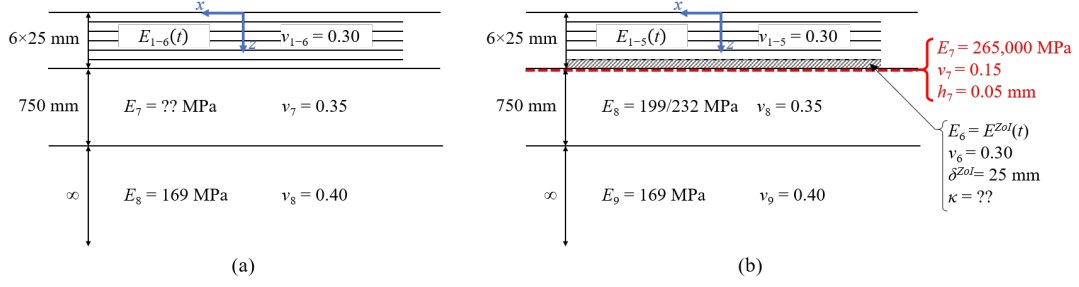 the centre of Tire 1 – see Figure 7. Calculated ASG responses were produced in six evaluation points at the bottom of the AC (i.e., $z = 150\,\text{mm}$), with (x, y)-coordinates corresponding to the six ASG positions in Figure 7. Accordingly, longitudinal strains (in the x-axis direction) were simulated in the following three (x, y)-coordinates (in mm): $(-900, -300)$, $(-600, 0)$, and $(-300, 300)$, corresponding to ASG1, ASG2, and ASG3. Transverse strains (in the y-axis direction) were simulated in the following three (x, y)-coordinates (in mm): $(300, 300)$, $(600, 0)$, and $(900, -300)$, corresponding to ASG4, ASG5, and ASG6.

Next, the model's capability to reproduce reality was assessed by formulating and subsequently solving six optimisation problems – one for each axle load event in S-0. In each problem, all six ASG signals and their corresponding derivatives were simultaneously considered, attempting to fit calculations from a single model to all signals captured during one axle loading event. This was achieved by solving a multi-criterion optimization problem following the so-called min-max approach Osyczka (1978). Doing so means implementing two matching steps, for which two corresponding objective functions are defined for subsequent minimisation: an individual objective function and a global objective function. The individual objective function quantifies the match between the measured and calculated strain (or strain rate) response of a single ASG, which is formulated as:

$$\phi_j = \frac{1}{N} \sum_{n=1}^{N} |\mathcal{M}_j(n) - R_j^{ve}(t_n)| \tag{4}$$

where $\mathcal{M}_j(n)$ is the measured ASG response (or corresponding strain rate) for a given data point n in ASGj, $R_j^{ve}(t_n)$ is the corresponding calculated VE strain (or strain rate) response at the ASGj location for the given data point with timestamp t_n, and N is the total number of data points considered for the match within a single axle load event. The minimal values of all individual objective functions ϕ_j^0 (one for each ASG and its derivatives) are then utilised in the formulation of a global objective function Φ:

$$\Phi = \sum_{j=1}^{J} w_j \left(\frac{\phi_j}{\phi_j^0} - 1 \right) \quad , \quad w_j = \begin{cases} \frac{\overline{\mathcal{M}}_j}{\lambda} & \text{if } \overline{\mathcal{M}}_j < \lambda \\ 1 & \text{if } \overline{\mathcal{M}}_j \geq \lambda \end{cases} \tag{5}$$

where $J = 12$ is the total number of considered signals (six strains and six strain rates), and w_j is a weighting parameter. The latter was introduced to lessen the influence of very weak signals that are close to the accuracy limit of the ASGs. Here, w_j was expressed by two terms: $\overline{\mathcal{M}}_j = \mathcal{M}_j^{\max} - \mathcal{M}_j^{\min}$, which is the difference between the maximum and minimum strain measured in ASGj, and λ, which is an accuracy limit taken as $20\,\mu\text{m/m}$. Consequently, ASG signals that experienced a peak-to-peak strain difference smaller than $20\,\mu\text{m/m}$ were given a weight smaller than unity in the global objective function. The strain rate 'sensors' were weighted according to their corresponding original ASG signals.

The solutions to each optimisation problem (one for each axle load event) were obtained with the MATLAB tool `fminseach`, which is suited for finding the minimum of unconstrained multi-variable functions based on a derivative-free method. A population of $N = 400$ data points per ASG signal was chosen, encapsulating all relevant strain responses triggered by one forklift axle. As a trial/initial set of values, a UGS modulus of $E_7 = 104\,\text{MPa}$ was chosen, taken as the average Young's Modulus across the three peak FWD stress levels listed in Table 1, while GoPro-assessed offsets (listed in Table 3) were used for Y_0 (constrained to change within $\pm 50\,\text{mm}$). In each iteration step, and before estimating the objective function values, cross-correlation was utilised to horizontally shift (along the time axis) calculated signal points such that they best align with the corresponding measured data points. The measured signal values were offset by aligning the first data point from measured signals with the first calculation point from modelled signals. Eventually, by fulfilling one of the several stopping criteria build-in the `fminseach` tool, a minimal/optimal solution for Φ is reached – denoted with a zero superscript, i.e., Φ^0. As a result, six optimal UGS modulus values were obtained and listed in Table 4. As can be seen, moduli values associated with the rear axle load are larger than those associated with the front axle load; this further affirms the non-linear UGS behaviour. On average, a UGS modulus of 199 MPa is associated with the front axle load event, while a modulus of 232 MPa is associated with the rear axle load event.

Table 4. Estimated UGS modulus for each axle load passage in S-0.

Pass	Axle	E_{ugs} [MPa]
4	Front	208
5	Front	199
6	Front	189
4	Rear	225
5	Rear	226
6	Rear	245
Avg.	Front	199 (± 10)
	Rear	232 (± 13)

For visualisation, an example of the optimum fit between measured and model-predicted ASG responses for the rear axle load during Pass#5 is presented in Figure 12. Here, charts on the left-hand side represent the match between measured ASG responses and the corresponding calculated responses, whereas charts on the right-hand side represent the match of the strain rate 'sensors,' i.e., between the ASG time derivatives and their corresponding calculated time derivatives. As can be seen, an acceptable solution that simultaneously matches all field measurements has been reached. It is noted that the strain traces for all ASGs are unique given the different lateral offsets relative to the passing load arrangement. This behaviour is captured

very well by the GRIDPAVE code. Furthermore, it can be observed that modelled responses are well aligned (horizontally) with the ASG measurements. Finally, as seen in the left-hand side charts, most mismatches occur after the response peaks; this further highlights the artificial nature of the signal drift. In the charts on the right-hand side, depicting strain rates, a corresponding mismatch due to drift is nearly eliminated.

4.4. *Analysis of the reinforced S-1 section*

The S-1 section layering was modelled to be similar to the layering of the S-0 section except for an added thin layer (Layer 7) representing the AGR. As shown in Figure 11(b), this thin layer was positioned between the AC layer's bottom and the top of the UGS. The thin layer properties were assumed elastic, with a Young's modulus of 265 GPa and a Poisson's ratio of 0.15 (see Subsection 3.1); based on smearing the grid's cross-sectional area, the effective thickness was 0.05 mm. A full (perfect) bond was assumed between the reinforcement and adjacent layers. The ZoI effect was emulated by modifying the relaxation modulus of the AC sub-layer above the reinforcement (Layer 6). A ZoI thickness of $\delta^{ZoI} = 25$ mm was chosen, which is approximately three times the NMAS of the AC. The modification was governed by the κ-factor (see Subsection 2.2); it meant replacing $E(t)$ with $E^{ZoI}(t)$ (for Layer 6 only). Given that the EAS-NMAS ratio equals 1.9 a notable increase of κ is expected – see Figure 2(b). The ZoI effect below the grid, within the UGS, was presumed negligible considering that the ratio between the grid opening size (15 mm) and the UGS NMAS (37.5 mm) equals 0.4. Such EAS-NMAS ratio is deemed too small to generate any notable increase in the κ-value. For both the AC and UGS the EAS-NMAS ratios are within representative volume element limits. The UGS was assigned a Youngs's modulus based on the re-calibrated values from Subsection 4.3, i.e., 199 MPa for simulating front axle loading events, and 232 MPa for simulating rear axle loading events.

Analyses were done by calculating strain responses at (x, y)-coordinates corresponding to ASG1, ASG3, ASG4, ASG5, ASG6 in Figure 7 (ASG2 did not survive the construction process); all located at $z = 150$ mm. GRIDPAVE, including AGR effects, was applied for this purpose; the analysis involved solving six separate optimisation problems – one for each axle loading event, i.e., Passes #1-3, each with two different axle types. A similar approach to the one covered in Subsection 4.3 was utilised – but this time with κ serving as the main unknown. The offset Y_0 in each case was treated as a secondary unknown, as it was only allowed to vary within a narrow range of ± 50 mm. The initial guess-values were: $\kappa = 1$ (i.e., no ZoI effect) and the GoPro-measured off-sets listed in Table 3. To ensure consistency with the model, κ was constrained to not fall below unity (no upper-bound limit was enforced). The final/optimal κ-values are listed in Table 5; also included in this table are the associated (final/optimal) global objective function values Φ^0. As can be observed, all κ-values were found to be larger than unity with an average of about 2.0. These calculation results provide evidence that treating the AGR as a thin high-modulus layer was necessary for matching the ASG readings, and that including a ZoI-effect was required to further improve GRIDPAVE's reproducibility.

As a final validation step, the AGR-component of GRIDPAVE was deactivated to observe and quantify the degradation in reproducibility. For this purpose, the global objective function values were re-calculated for the S-1 section while completely ignoring the AGR existence – i.e., setting κ to unity and removing the thin high-modulus
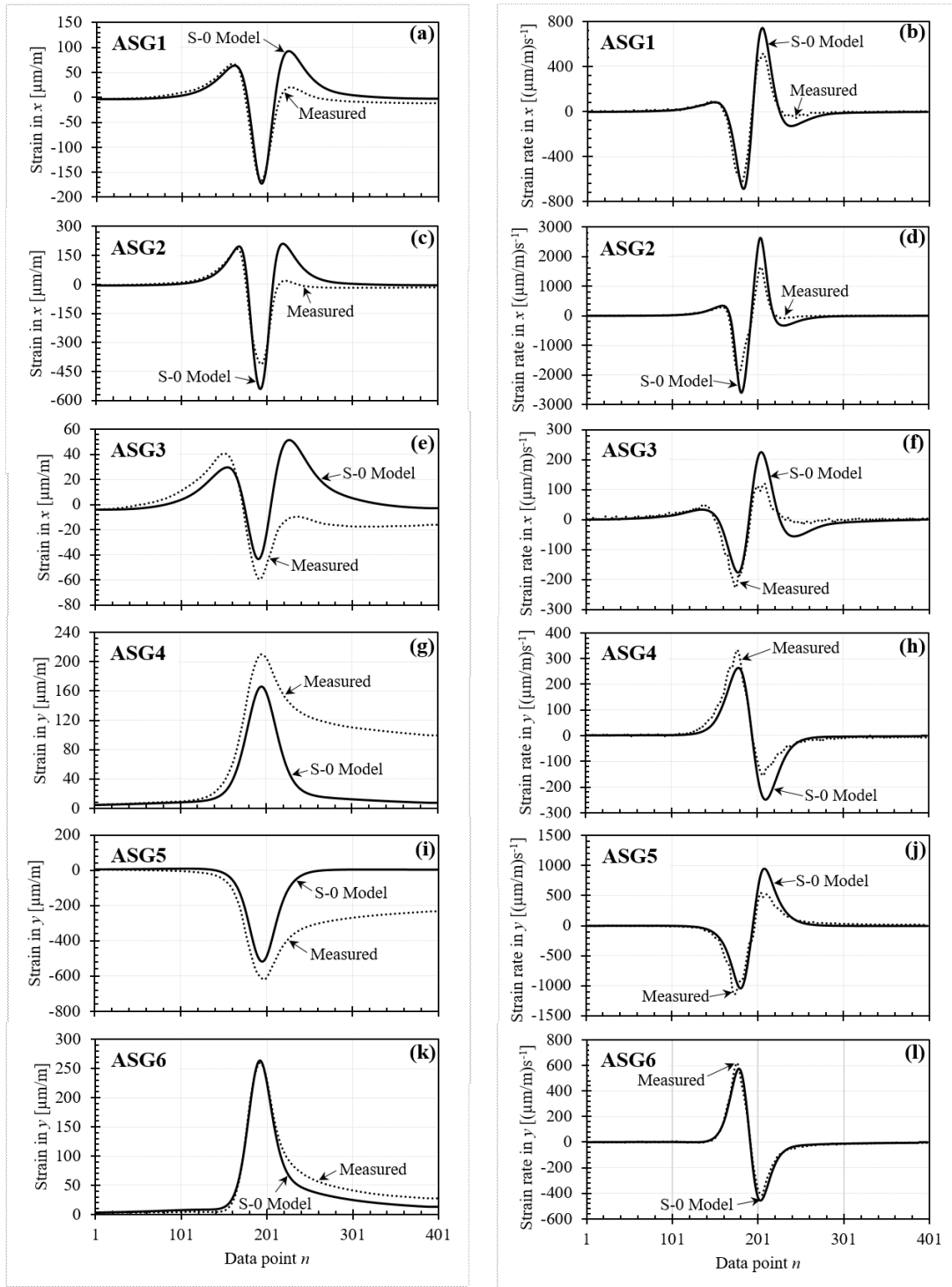
Figure 12. Optimum fit between measured (······) and modelled (———) rear axle responses from Pass #5 in S-0.

22

Table 5. Estimated κ-values for each axle loading event alongside the global objective function values Φ^0 (with AGR effects) and Ψ^0 (ignoring AGR effects), and their relative percentage difference.

Pass	Axle	κ [-]	Φ^0 [-]	Ψ^0 [-]	$\frac{\Phi^0}{\Psi^0} - 1$
1	Front	1.6	1.022	1.156	-12%
2	Front	2.5	0.759	4.806	-84%
3	Front	1.8	1.770	3.604	-51%
1	Rear	1.7	1.608	4.197	-62%
2	Rear	2.6	2.005	6.111	-67%
3	Rear	1.9	2.494	5.525	-55%
	Avg.	2.0			

layer. The resulting values, denoted as Ψ^0 are listed in Table 5 alongside the relative percentage difference to Φ^0. As can be seen, a negative relative difference was obtained across all analysed axle loading events – clearly indicating that the AGR model-component was needed in order to provide a superior match to field measurements. To graphically illustrate these implications, Figure 13 provides an example of simulated GRIDPAVE strain responses with AGR, without AGR, alongside measured ASG responses associated with the rear axle loading during Pass#2. This case corresponds to a situation where GRIDPAVE with AGR provides a global match (to the ASG readings) that is 67% better than GRIDPAVE without an AGR. The figure consists of ten charts, where charts on the left-hand side represent the match between the measured ASG responses and the corresponding calculated responses, whereas charts on the right-hand side represent the match between time derivatives of the measured strain and their corresponding calculated time derivatives. As can be seen, an acceptable solution that simultaneously matches all field measurements has been reached for the model with AGR. Furthermore, across most charts, simulated responses utilising GRIDPAVE with AGR are visually superior to responses generated by GRIDPAVE, but without an active AGR model-component.

5. Synthetic investigation

A synthetic case study was established to demonstrate and quantify the effects of adding an AGR to a pavement system. The studied case was based on the DTU Smart Road test sections subjected to the rear axle loading of the forklift (see Figure 7). The two calibrated models from the S-0 and S-1 sections were utilised – one with an AGR and another without reinforcement. Specifically, both the unreinforced and reinforced models correspond to the two systems shown in Figure 11(a and b) with a UGS modulus of $E_{ugs} = 232\,\text{MPa}$ and a common silty-sand modulus of $169\,\text{MPa}$. The obtained average $\kappa = 2.0$ from Subsection 4.4 was utilised to emulate the AGR effect in the reinforced model.

Four critical key responses located along the wheel path of Tire 5 (see Figure 7) were investigated: (i) ε_x – horizontal strain in the x-axis direction (i.e., travel direction) at the bottom of the AC where $z = 150\,\text{mm}$; (ii) ε_y – horizontal strain in the y-axis direction at the bottom of the AC where $z = 150\,\text{mm}$; (iii) ε_z – vertical strain at the UGS top where $z = 150.1\,\text{mm}$; and (iv) U_z – vertical displacement at the pavement surface where $z = 0$. The first three key responses were chosen based on their relation to pavement performance in ME design. In particular, key responses (i) and (ii) are commonly associated with bottom-up fatigue cracking, while (iii) is usually linked to
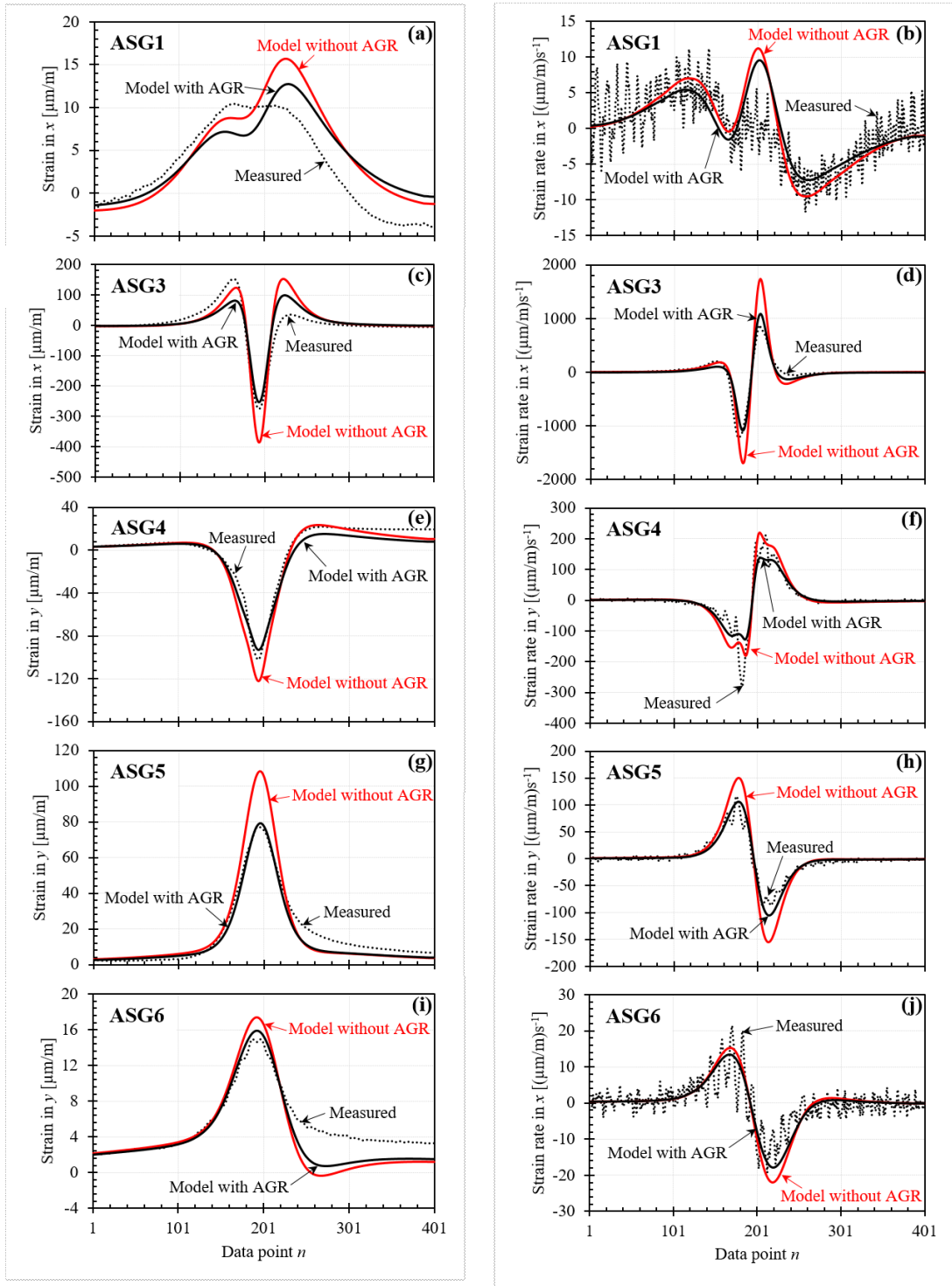
Figure 13. Measured and modelled rear axle responses from Pass #2 in S-1, where: dotted line (······) for measured responses; solid black line (——) for calculations using the optimum model with AGR; and solid red line (——) for the calculations using the nominal identical model without AGR.

24

rutting in the aggregate base course layer (Huang 2004). Key response (iv) was chosen given the focus on deflection testing in pavement evaluation (ASTM D4694 2009).

Figure 14 presents the resulting/calculated key responses. There are eight charts in this figure arranged in two rows. Each row represents one of the four key responses in two combinations of AC temperature T (assumed uniform across the depth) and loading speed V. The combinations are: $T = 45\,°C$ and $V = 5\,km/h$ on the left-hand side, and $T = 5\,°C$ and $V = 80\,km/h$ on the right-hand side. Each chart depicts two response traces: one associated with a model including AGR (solid black line) and another associated with a reference model excluding AGR (solid red line). In the charts, vertical axes depict (each) a key response value, while the horizontal axes represent the x-coordinate of the load position relative to the evaluation point $(x, y) = (0, -110\,mm)$ according to the Cartesian coordinate system given in Figure 7(a). To best visualise the differences between reinforced and unreinforced cases, the vertical axis varies across the chart pairs. Overall, it can be observed that including AGR reduced peak strain levels. The reduction was considerably larger under the high-temperature/low-speed combination compared to the low-temperature/high-speed combination. Furthermore, it can be seen that AGR inclusion had a negligible effect on surface vertical displacements.

Table 6 lists the numerical values of the trace peaks of the four considered key responses. These peaks are listed alongside their relative change in magnitude when compared to peaks from a corresponding unreinforced system. As can be seen, the AGR produced its largest effect on horizontal strains, with a reduction of up to 36% in peak intensity for $T = 45\,°C$ and $V = 5\,km/h$. In contrast, a peak reduction of up to 12% was obtained for the same key response under $T = 5\,°C$ and $V = 80\,km/h$. Furthermore, a decrease in surface displacement peaks caused by the AGR did not exceed 5% in any of the given temperature-speed combinations.

Table 6. Peak response values across pavement systems and time-temperature conditions.

System	Peak responses at $T = 45°C$ and $V = 5$ km/h			
	$\varepsilon_x(z = 150\,mm)$ [μm/m]	$\varepsilon_y(z = 150\,mm)$ [μm/m]	$\varepsilon_z(z = 150.1\,mm)$ [μm/m]	$U_z(z = 0\,mm)$ [mm]
Without AGR	-694	-701	2388	1.271
With AGR $\kappa = 2.0$	-459 (-34%)	-448 (-36%)	2035 (-15%)	1.211 (-5%)
System	Peak responses at $T = 5°C$ and $V = 80$ km/h			
	$\varepsilon_x(z = 150\,mm)$ [μm/m]	$\varepsilon_y(z = 150\,mm)$ [μm/m]	$\varepsilon_z(z = 150.1\,mm)$ [μm/m]	$U_z(z = 0\,mm)$ [mm]
Without AGR	-87	-101	346	0.363
With AGR $\kappa = 2.0$	-80 (-8%)	-89 (-12%)	324 (-6%)	0.357 (-2%)

6. Conclusion

This work dealt with a full-scale validation of the mechanistic response model suggested in Nielsen *et al.* (2022) for pavements that include AGR. Specifically, an instrumented asphalt pavement was designed and constructed, comprising two nominally identical layering arrangements – one including AGR and the other excluding AGR (serving as a reference). ASGs and temperature sensors were buried in the AC layer during construction. Also, DCP, FWD, and laboratory tests were done to characterise
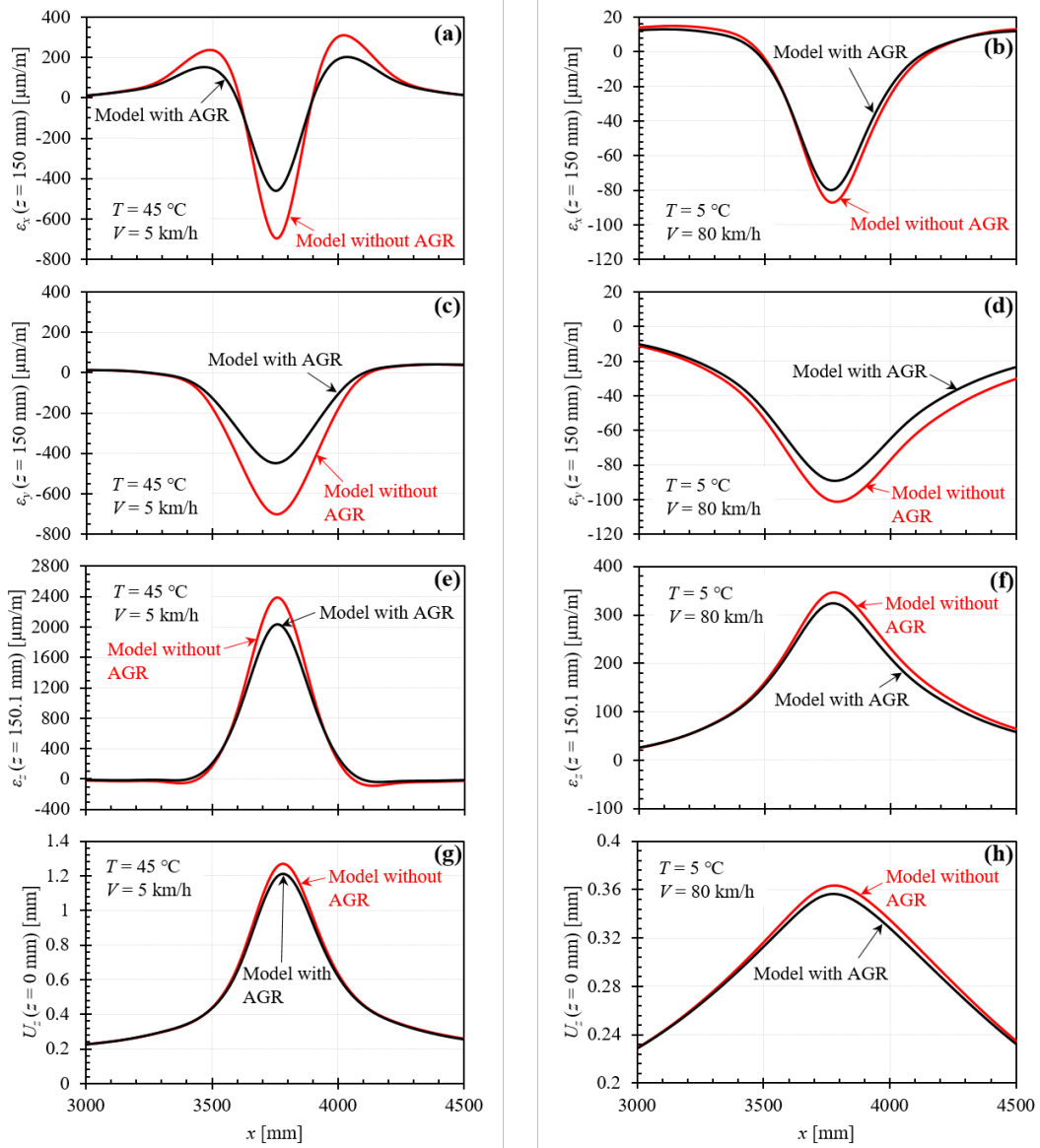
Figure 14. Calculated key responses of a reinforced (——) and unreinforced (——) model vs. the load position in the *x*-direction for two temperature-speed conditions.

26

the as-built pavement system. Triggered by a heavy, slow-moving forklift of known weight, dimensions and position, SG responses were measured for subsequent analysis. Validation was demonstrated by providing evidence that a model with the AGR is superior in its ability to reproduce reality compared to a nominally identical model that ignores the AGR contribution. A synthetic investigation based on the validated model was provided to further quantify the reinforcement effect. This was done for two combinations of AC temperature and loading speed while focusing on key responses commonly employed in ME design and non-destructive pavement evaluation.

The main findings from the overall effort were as follows: (i) it was possible to obtain an acceptable fit between all measured and model-predicted strain responses, suggesting that the model presented in Nielsen *et al.* (2022) is capable of reproducing in-pavement responses – with and without AGR; (ii) a κ-factor larger than unity was obtained for all analysed passes, indicating that a ZoI model component is active and valid; (iii) when AGR was included/activated in GRIDPAVE, calculated strain responses coincided better with field measurements as compared to ignoring AGR effects. This suggests that the proposed framework with AGR formulation is a useful mechanistic component for ME design; and (iv) based on the synthetic investigation, it was observed that adding AGR significantly reduces the AC bottom horizontal strains and, to a lesser degree, the vertical strain on top of the UGS. This finding applies to slow loading speeds combined with high AC temperatures. The reinforcement effect was considerably smaller for cases involving fast loading speeds and low AC temperatures. Lastly, the model predicts that AGR effects hardly influence peak surface deflections within the considered range of speed and temperatures.

Some limitations/shortcoming have emerged during the work. First, some mechanistic behaviours could not be captured, specifically: non-linear stress-strain response of unbound materials, and permanent deformation of the AC and other pavement layers (either time independent or time-dependent). Second, the lateral vehicle position, which is critical for reproducing in-pavement responses, was practically difficult to measure in the field with high precision. Lastly, the presence of artificial signal drift in some of the SG readings distorted GRIDPAVE's ability to match the measurements. While these limitations could not be fully eliminated, they were addressed as part of the effort to validate the proposed model (see Subsection 4.1).

Findings (i), (ii), and (iii) suggest that the mechanistic modelling approach offered by Nielsen *et al.* (2022) is successfully validated in a full-scale pavement system. In particular, it is possible to identify and quantify the reinforcement effect, and subsequently evaluate the associated model parameters. Furthermore, finding (iv) implies that adding an AGR at the AC bottom can potentially prolong the pavement service life in terms of bottom-up fatigue cracking and rutting. This is because the AGR presence lessens key response peaks commonly associated with these distress types. The reinforcement effect is expected to be largest under static loadings that are common to parking lots and storage yards. Finally, the study results imply that reinforcement effects are difficult to quantify in field experiments based on FWD (Horak *et al.* 2015) or moving measurement platforms (Skar *et al.* 2021, Baltzer *et al.* 2010). Conversely, static/long-duration load tests might be able to identify AGR effects such as in Kumar *et al.* (2021). Overall, the model of Nielsen *et al.* (2022) provides a promising tool for reproducing in-pavement strain responses.

While this study focused on conditions of high AC temperatures and slow loading speed, further tests should also target conditions of low AC temperatures and fast loading speeds. Moreover, pavement surface responses could be further examined, either by using moving measurement platforms that target displacements or by installing

surface sensors, e.g., accelerometers, LVDTs, or tiltmeters (Nielsen *et al.* 2020, Skar *et al.* 2020a). If these attempts demonstrate that AGR effects are marginal, they will provide further field evidence for model validation. Moreover, while it was possible to estimate a κ value for an assumed δ^{ZoI} value in this work, future studies should focus on characterising these ZoI properties in the laboratory; this is because it is impractical to estimate these properties in full-scale. Additional aspects for future investigation should deal with the evaluation of other grid types, optimal positioning within the AC layer under different loading scenarios, and bonding conditions between grids and adjacent layers. Concerning the latter point, interface bonding properties, with or without a grid, could be potentially estimated in laboratory shear tests over AC cores (Leischner *et al.* 2019).

References

Ahmed, A. and Erlingsson, S., 2016. Viscoelastic Response Modelling of a Pavement under Moving Load. *Transportation Research Procedia*, 14, 748–757.

Andrei, D., Mirza, W., and Witczak, M., 1999. Development of a Revised Predictive Model for the Dynamic (Complex) Modulus of Asphalt Mixtures. *NCHRP Report 1-37A*.

ARA Inc., 2004. Guide for Mechanical-Empirical Design of New and Rehabilitated Pavement Structures. *Transportation Research Board*, NCHRP 1-37 (Final Report).

Arsenie, I.M., *et al.*, 2017. Laboratory characterisation of the fatigue behaviour of a glass fibre grid-reinforced asphalt concrete using 4PB tests. *Road Materials and Pavement Design*, 18 (1), 168–180. Available from: https://doi.org/10.1080/14680629.2016.1163280.

Asphalt Academy, 2008. TG3 - Asphalt Reinforcement for Road Construction. *Asphalt*, (November).

ASTM D2487, 2017. Standard Practice for Classification of Soils for Engineering Purposes (Unified Soil Classification System).

ASTM D4694, 2009. Standard test method for deflections with a falling-weight-type impulse load device.

ASTM D6951/D6951M, 2018. Standard Test Method for Use of the Dynamic Cone Penetrometer in Shallow Pavement Applications.

Baltzer, S., *et al.*, 2010. Continuous bearing capacity profile of 18,000 km Australian road network in five months.

Burmister, D.M., 1943. The Theory of Stresses and Displacements in Layered Systems and Applications to the Design of Airport Runways. *In*: *Highway Research Board, Vol. 23*. 126–148.

Burmister, D.M., 1945a. The general theory of stresses and displacements in layered soil systems. II. *Journal of Applied Physics*, 16 (3), 126–127.

Burmister, D.M., 1945b. The general theory of stresses and displacements in layered soil systems. III. *Journal of Applied Physics*, 16 (5), 296–302.

Burmister, D.M., 1945c. The general theory of stresses and displacements in layered systems. I. *Journal of applied physics*, 16 (2), 89–94.

Button, J.W. and Lytton, R.L., 2007. Guidelines for using geosynthetics with hot-mix asphalt overlays to reduce reflective cracking. *Transportation Research Record*, (2004), 111–119.

Chadbourn, B.A., D.E., N., and Timm, D., 1997. Measured and Theoretical Comparisons of Traffic Loads and Pavement Response Distributions. *In*: *the Eighth International Conference on Asphalt Pavements*, Seattle, Washington. 229–238. Available from: https://trid.trb.org/view/501630.

Chang, D.T.T., *et al.*, 1999. Laboratory and case study for geogrid-reinforced flexible pavement overlay. *Transportation Research Record*, (1687), 125–130.

Chen, C., McDowell, G.R., and Thom, N.H., 2012. Discrete element modelling of cyclic loads of geogrid-reinforced ballast under confined and unconfined conditions. *Geotextiles and Geomembranes*, 35, 76–86. Available from: http://dx.doi.org/10.1016/j.geotexmem.2012.07.004.

Chen, C., McDowell, G.R., and Thom, N.H., 2014. Investigating geogrid-reinforced ballast: Experimental pull-out tests and discrete element modelling. *Soils and Foundations*, 54 (1), 1–11. Available from: http://dx.doi.org/10.1016/j.sandf.2013.12.001.

Cho, Y.H., Park, D.W., and Hwang, S.D., 2010. A predictive equation for dynamic modulus of asphalt mixtures used in Korea. *Construction and Building Materials*, 24 (4), 513–519.

Cleveland, G.S., Button, Joe W., and Lytton, R.L., 2001. Geosynthetics in Flexible and Rigid Pavement. *Fhwa/Tx-02/1777- 1*, 7 (2). Available from: http://www.scribd.com/doc/136341942/Geosynthetics-in-Flexible-and-Rigid-Pavementscribd.

Correia, N.S., Esquivel, E.R., and Zornberg, J.G., 2018. Finite-Element Evaluations of Geogrid-Reinforced Asphalt Overlays over Flexible Pavements. *Journal of Transportation Engineering, Part B: Pavements*, 144 (2), 04018020.

Correia, N.S. and Zornberg, J.G., 2018. Strain distribution along geogrid-reinforced asphalt overlays under traffic loading. *Geotextiles and Geomembranes*, 46 (1), 111–120. Available from: https://doi.org/10.1016/j.geotexmem.2017.10.002.

de Bondt, A.H., 1999. Anti-reflective cracking design of (reinforced) asphalt overlays. PhD thesis.

EN 12697-26C, 2018. Bituminous mixtures - Test methods - Part 26: Stiffness. *European Standard*.

EN 13108-1, 2016. Bituminous mixtures – Material specifications – Part 1: Asphalt Concrete.

European Commission, 1999. *COST 333: Development of New Bituminous Pavement Design Method: Final report of the Action*.

European Commission, 2000. AMADEUS Advanced Models for Analytical Design of European Pavement Structures. 1–178.

Goodman, J.R. and Popov, E.P., 1968. Layered Beam Systems with Interlayer Slip. *Journal of the Structural Division*, 94 (11), 2535–2548.

Graziani, A., *et al.*, 2014. Structural response of grid-reinforced bituminous pavements. *Materials and Structures/Materiaux et Constructions*, 47 (8), 1391–1408.

Gusfeldt, K. and Dempwolff, K., 1967. Stress and Strain Measurements in Experimental Road Sections Under Controlled Loading Conditions. *In*: *the Second International Conference on the Structural Design of Asphalt Pavements*. 663–669. Available from:

https://trid.trb.org/view/104825.

Horak, E., *et al.*, 2015. Flexible road pavement structural condition benchmark methodology incorporating structural condition indices derived from Falling Weight Deflectometer deflection bowls. *Journal of Civil engineering and Construction*, 4 (1), 12.

Huang, Y.H., 2004. *Pavement Analysis and Design (Second edition)*. Available from: http://docshare04.docshare.tips/files/14013/140138713.pdf.

Khodaii, A., Fallah, S., and Moghadas, F., 2009. Effects of geosynthetics on reduction of reflection cracking in asphalt overlays. *Geotextiles and Geomembranes*, 27 (1), 1–8. Available from: http://dx.doi.org/10.1016/j.geotexmem.2008.05.007.

Kim, Y., Lee, J., and Lutif, J.E., 2010. Geometrical evaluation and experimental verification to determine representative volume elements of heterogeneous asphalt mixtures. *Journal of Testing and Evaluation*, 38 (6).

Konrad, J.M. and Lachance, D., 2001. Use of in situ penetration tests in pavement evaluation. *Canadian geotechnical journal*, 38 (5), 924–935.

Krukar, M. and Cook, J., 1972. Practical Design Applications on Washington State University Test Track Results. *In*: *the Third International Conference on the Structural Design of Asphalt Pavements*, London, UK. 866–875.

Kumar, V.V., Roodi, G.H., and Zornberg, J.G., 2021. Asphalt Strain Response of Geosynthetic-Reinforced Asphalt Overlays under Static Plate Loads. *In*: *Proceedings of Geosynthetics Conference 2021*. 350–361.

Kyowa Electronic Instruments, 2022. KM Series Embedded Strain Gages. Available from: https://www.kyowa-ei.com/eng/product/category/strain$_g$ages/km/index.html.

Leischner, S., *et al.*, 2019. Mechanical Testing and Modeling of Interlayer Bonding in HMA Pavements. *Transportation Research Record*, 2673 (11), 879–890. Available from: https://doi.org/10.1177/0361198119843254.

Levenberg, E., 2013. Inverse analysis of viscoelastic pavement properties using data from embedded instrumentation. *International Journal for Numerical and Analytical Methods in Geomechanics*, 37 (9), 1016–1033.

Levenberg, E., 2016. Viscoelastic pavement modeling with a spreadsheet. *8th International Conference on Maintenance and Rehabilitation of Pavements, MAIREPAV 2016*, 746–755.

Levenberg, E., McDaniel, R.S., and Olek, J., 2009. *Validation of NCAT structural test track experiment using INDOT APT facility*. West Lafayette, Indiana: Joint Transportation Research Program, Indiana Department of Transportation and Purdue University, September.

Levenberg, E. and Michaeli, N., 2013. Viscoelastic characterisation of asphalt-aggregate mixes in diametral compression. *Road Materials and Pavement Design*, 14 (SUPPL.1), 105–119.

Levenberg, E. and Skar, A., 2020. Analytic pavement modelling with a fragmented layer. *International Journal of Pavement Engineering*, 0 (0), 1–13. Available from: https://doi.org/10.1080/10298436.2020.1790559.

Lytton, R.L., 1989. Use of geotextiles for reinforcement and strain relief in asphalt concrete. *Geotextiles and Geomembranes*, 8 (3), 217–237.

Mateos, A. and Snyder, M.B., 2002. Validation of flexible pavement structural response models with data from the Minnesota road research project. *Transportation Research Record*, (1806), 19–29.

McDowell, G.R., *et al.*, 2006. Discrete element modelling of geogrid-reinforced aggregates. *Proceedings of the Institution of Civil Engineers: Geotechnical Engineering*, 159 (1), 35–48.

Newcomb, D.E., *et al.*, 1995. *Initial characterization of subgrade soils and granular base materials at the Minnesota road research project*. Minnesota Department of Transportation.

Nguyen, M.L., *et al.*, 2013. Review of glass fibre grid use for pavement reinforcement and APT experiments at IFSTTAR. *Road Materials and Pavement Design*, 14 (SUPPL.1), 287–308.

Nielsen, J., Levenberg, E., and Skar, A., 2020. Inference of Pavement Properties with Roadside Accelerometers. *In*: *Proceedings of the 9th international conference on maintenance and rehabilitation of pavements—mairepav9*. vol. 76. 719–728. Available from: http://link.springer.com/10.1007/978-3-030-48679-2$_6$7.

Nielsen, J., Levenberg, E., and Skar, A., 2022. Mechanistic modelling of grid-reinforced milled-

and-overlaid asphalt pavements. *International Journal of Pavement Engineering*, (May), 1–16. Available from: https://doi.org/10.1080/10298436.2022.2072502.

Nilsson, R.N., Oost, I., and Hopman, P.C., 1996. Viscoelastic analysis of full-scale pavements: Validation of VEROAD. *Transportation Research Record*, (1539), 81–87.

Osyczka, A., 1978. An approach to multicriterion optimization problems for engineering design. *Computer Methods in Applied Mechanics and Engineering*, 15 (3), 309–333. Available from: https://linkinghub.elsevier.com/retrieve/pii/0045782578900464.

Saride, S. and Kumar, V.V., 2017. Influence of geosynthetic-interlayers on the performance of asphalt overlays on pre-cracked pavements. *Geotextiles and Geomembranes*, 45 (3), 184–196. Available from: http://dx.doi.org/10.1016/j.geotexmem.2017.01.010.

Schapery, R., 1962. Approximate Methods of Transform for Viscoelastic Stress Analysis. *In*: *Fourth USNat Congr Appl Mech.* 1075–1084.

Schuettpelz, C., Fratta, D., and Edil, T.B., 2009. Evaluation of the zone of influence and stiffness improvement from geogrid reinforcement in granular materials. *Transportation Research Record*, (2116), 76–84.

Skar, A., Nielsen, J., and Levenberg, E., 2020a. Pavement instrumentation with near surface LVDTs. *In*: *Advances in materials and pavement performance prediction ii.* CRC Press, 232–235. Available from: https://www.taylorfrancis.com/books/9781000343489/chapters/10.1201/9781003027362-55.

Skar, A. and Andersen, S., 2020. ALVA: An adaptive MATLAB package for layered viscoelastic analysis. *Journal of Open Source Software*, 5 (55), 2548.

Skar, A., Andersen, S., and Nielsen, J., 2020b. Adaptive Layered Viscoelastic Analysis (ALVA). Available from: https://github.com/asmusskar/ALVA.

Skar, A., *et al.*, 2021. Analysis of a moving measurement platform based on line profile sensors for project-level pavement evaluation. *Road Materials and Pavement Design*, 22 (9), 2069–2085. Available from: https://www.tandfonline.com/doi/full/10.1080/14680629.2020.1741429.

S&P Clever Reinforcement Company AG, 2020. S&P Carbophalt ® G 200/200. Available from: https://p.widencdn.net/rx8gq5/R$_C$arbophaltG200200$_Pub_T$ds$_Prod_{ENEN}$.

Terrel, R. and Krukar, M., 1970. Evaluation of Test Tracking Pavements. *In*: *Association of Asphalt Paving Technologists.* 273–296. Available from: https://trid.trb.org/view/101324.

Williams, M.L., Landel, R.F., and Ferry, J.D., 1955. The Temperature Dependence of Relaxation Mechanisms in Amorphous Polymers and Other Glass-forming Liquids. *Journal of the American Chemical Society*, 77 (14), 3701–3707.

Witczak, M.W. and Fonseca, O.A., 1996. Revised predictive model for dynamic (complex) modulus of asphalt mixtures. *Transportation Research Record*, (1540), 15–23.

Zofka, A., Maliszewski, M., and Maliszewska, D., 2017. Glass and carbon geogrid reinforcement of asphalt mixtures. *Road Materials and Pavement Design*, 18, 471–490. Available from: https://doi.org/10.1080/14680629.2016.1266775.

Mechanistic investigation of grid-reinforced asphalt pavements with measured interface properties

Julius Nielsen, Eyal Levenberg, Sabine Leischner, and Gustavo Canon Falla

Submitted to: Road Materials and Pavement Design

The following content is the Author's Original Manuscript, i.e., a preprint version before submission to the journal Road Materials and Pavement Design for peer review. The work is currently under the first round of review.

ARTICLE TEMPLATE

Mechanistic investigation of grid-reinforced asphalt pavements with measured interface properties

Julius Nielsen[a,b], Eyal Levenberg[a], Sabine Leischner[c], and Gustavo Canon Falla[c]

[a]Department of Environmental and Resource Engineering, Technical University of Denmark, Kgs. Lyngby, Denmark; [b]S&P Reinforcement Nordic ApS, Odder, Denmark; [c]Institute of Urban and Pavement Engineering, Technische Universität Dresden, Germany

ABSTRACT

When simulating asphalt pavement responses, layer interface properties must be specified. For design and analysis purposes, perfect interface bonding conditions are commonly assumed when calculating key responses. One emerging approach for prolonging the service life of asphalt pavements, either new or rehabilitated, is installing asphalt grid reinforcement (AGR) products between paving lifts. In these cases, the perfect bond assumption may not hold – undermining the reinforcement potential. Accordingly, the objective of this study was to investigate the effects of interface properties on key responses in pavements with AGR. The investigation was carried out by combining results from a full-scale construction, laboratory tests on asphalt concrete (AC) cores, and synthetic simulations. The latter were performed with a recently developed semi-analytic mechanistic code that can accept AGR products. This code can handle time- and temperature-dependent layer and interface properties, as well as moving loads. It was found that the bond between AC lifts, with and without AGR, is time- and temperature-dependent – best characterized by a relaxation interface stiffness function. This relaxation function was measured to be consistently larger without AGR than with AGR. Nonetheless, simulations showed that including an AGR: (i) has no pronounced effect on strain magnitudes under high-speed/low-temperature conditions; (ii) can, depending on the installation depth, lessen horizontal strain magnitudes at the reinforced interface and at the AC bottom. This beneficial effect transpires under slow-speed/high-temperature conditions; and (iii) has no pronounced effect on deflections regardless of the loading speed and temperature level. It is concluded that even if laboratory measurements display a reduced interface stiffness when including an AGR, the reduction may not have any practical implication on responses, and reinforcement effects are not necessarily undermined. The modeling approach outlined and utilized in this study offers a mechanistic tool for analyzing this matter/question on a case-by-case basis.

layered elastic theory, viscoelasticity, Dresden Dynamic Shear Tester.

1.   Introduction

1.1.   *Background*

Prolonging the service life of new or rehabilitated asphalt pavements can be sought via the inclusion of asphalt grid reinforcement (AGR) products. In general terms, AGRs are a sub-category of geosynthetics composed of high-modulus strands joined in a mesh-like configuration. These products are designed for installation within asphalt concrete (AC), either between two new AC lifts, between an existing (aged/damaged) AC and a new AC overlay, or on top of an unbound granular base, at the AC bottom. Laboratory investigations and full-scale experiments have demonstrated that AGRs can be beneficial in combating several distress types such as fatigue cracking (Nguyen *et al.* 2013, Arsenie *et al.* 2017, Vinay Kumar and Saride 2017, Correia and Zornberg 2018), rutting (Ong *et al.* 2004, Sobhan 2005, Lee *et al.* 2015, Correia and Zornberg 2016), and reflective cracking (Austin and Gilchrist 1996, de Bondt 1999, Khodaii *et al.* 2009, Saride and Kumar 2017).

A rational attempt to capture AGR effects in asphalt pavements was recently proposed by Nielsen *et al.* (2022). The work outlined a mechanistic model that further extends the layered elastic theory (LET) to include: (i) linear viscoelastic (VE) layer properties, (ii) moving loads, and (iii) fragmented layers (Levenberg and Skar 2020). More specifically, AGR was modeled as a thin high-modulus elastic layer alongside a zone-of-influence (ZoI) effect for capturing changes in the mechanical properties of adjoining AC. A full-scale validation effort of the new theory is included in Nielsen and Levenberg (2022).

Similar to LET, the modeling scheme in Nielsen *et al.* (2022) requires as input the prevailing conditions at layer interfaces, and particularly between the top and bottom of the AGR and the adjoining AC. In a typical design of unreinforced asphalt pavements, a perfect bond between all layers is commonly assumed (AASHTO 2008, Sutanto 2009, White 2017). This assumption may not hold when AGR is included, as the presence of a grid influences the bond quality (Le *et al.* 2022). This work is motivated by the desire to further investigate and quantify this issue – both experimentally and theoretically.

The paper commences with a literature review, covering how interface bond conditions are represented within LET, and how the bond level is quantified in laboratory and field experiments. The study's objective and methodology are stated next, followed by the description of an experimental campaign aimed at characterizing the interface properties between AC lifts with and without AGR. Described next is a synthetic investigation of bonding effects on key responses commonly linked to pavement performance in engineering design. The paper ends with a summary of the main findings, conclusions, and recommendations for future research.

1.2.   *Literature review*

1.2.1.   *Interface bonding in LET*

The vast majority of pavement design and analysis procedures/codes are LET-based (Shell 1978, Shook *et al.* 1982, AASHTO 2008, AUSTROADS 2004, Huang 2004). In

this theory, each of the pavement layers is assumed weightless, linear elastic, homogeneous, and isotropic. The interfaces between adjoining layers are assumed to remain in contact at all times; mathematically, this translates into continuity of vertical stresses and displacements. The continuity of horizontal displacements across interfaces depends on the bonding conditions. For a perfect/fully-interlocked bond, the horizontal displacements are continuous, while for a smooth/slippery bond, the interface shear stress vanishes and horizontal displacements are discontinuous. The entire spectrum of bond levels is commonly modeled with a horizontal Winkler-like spring-bed characterized by a spring constant k (units of force per cubic length). This approach is essentially an extension of Goodman's constitutive law for laminated beams (Goodman and Popov 1968).
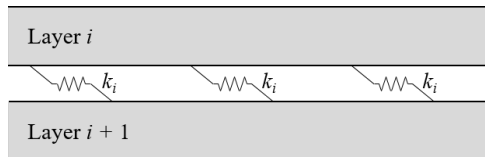

Figure 1. Schematic representation of interface spring constant.

Referring to the standard axisymmetric LET formulation (Burmister 1943, 1945c,a,b, Peutz *et al.* 1968), the interface spring constant k_i, connecting the bottom of layer i with the top of layer $i + 1$ (see Figure 1), is incorporated as follows (Levenberg 2020):

$$(\tau_{rz})_i = k_i \left((u_r)_i - (u_r)_{i+1} \right) \tag{1}$$

or alternatively

$$(u_r)_i = (u_r)_{i+1} - \frac{(\tau_{rz})_i}{k_i} \tag{2}$$

where $(\tau_{rz})_i$ is the $r - z$ shear stress at the interface, $(u_r)_i$ is the radial displacement just above the interface (within layer i), and $(u_r)_{i+1}$ is the radial displacement just below the interface (within layer $i + 1$). Referring to Equation (1), it can be seen that when $k_i \to 0$, a smooth/slippery bond transpires – given that the shear stress at the interface vanishes, i.e., $(\tau_{rz})_i = 0$. Conversely, it can be seen from Equation (2) that when $k_i \to \infty$ a perfect/fully-interlocked bond transpires – given that the radial displacements above and below the interface are forced to be identical, i.e., $(u_r)_i = (u_r)_{i+1}$. For simulating an intermediate bond level, the value of k_i resides within the range $0 < k_i < \infty$.

1.2.2. Monotonic shear testing

The work of Uzan *et al.* (1978) contains one of the earliest attempts to experimentally measure the prevailing spring constant value between two AC lifts. Using a double shear-box apparatus the interface between two lab-prepared AC layers was monotonically sheared under different vertical stress levels (from zero to 0.5 MPa), and tack coat applications (from none to 2 kg/m^2). The tests were carried out at two temperatures (25 °C and 55 °C), and one shear rate of 0.04 mm/s. The smallest level of applied shear displacement was 130 µm and the corresponding/resulting interface spring constant was within the range of 0.5 MPa/mm to 2.0 MPa/mm. A similar testing approach

for evaluating the interface spring constant was employed by Romanoschi and Met-calf (2001). Testing included the application of a monotonous shear rate of 0.2 mm/s until failure under three temperature levels (from 15 °C to 35 °C) and four vertical stress levels (from about 0.14 MPa to 0.52 MPa). The obtained k values, derived from displacements at peak shear stress, were about half those reported by Uzan *et al.* (1978).

Canestrari *et al.* (2005) applied monotonous shear to AC interfaces at a rate of 0.04 mm/s under two temperatures (20 °C and 40 °C) and three normal stresses (from none to 0.43 MPa). Interface spring constants were calculated from a linear regression between measured shear stress versus differential displacement at the interface (up until the peak). Values obtained were in the range of 0.1 MPa/mm to 0.6 MPa/mm. The same test was repeated in Canestrari and Santagata (2005) for lower temperature levels (from -10 °C to 20 °C), yielding to k values in the range of 5 MPa/mm to 0.3 MPa/mm. In the work of Sutanto (2009) a range of interface spring constant values between 0.5 MPa/mm and 1.9 MPa/mm were identified utilizing the so-called modified Leutner test (i.e., applying direct shear without normal stress application), for which the applied shear rate was 0.83 mm/s at a temperature of 20 °C; k values were estimated from displacement levels ranging between 1 mm to 2.4 mm.

Based on a synthetic LET analysis, Al Hakim *et al.* (1999) have concluded that interface spring constant values below 0.01 MPa/mm essentially mean complete de-bonding, while values above 100 MPa/mm indicate perfect bonding. Thus, a verbal categorization for interface bond was proposed: (i) poor $k \leq 0.01$ MPa/mm, (ii) partial 0.01 MPa/mm$< k < 100$ MPa/mm, and (iii) good $k \geq 100$ MPa/mm. A similar verbal categorization was suggested in a recent study by Le *et al.* (2020), but with the 'poor' bond level ascribed to $k \leq 0.1$ MPa/mm. Al Hakim *et al.* (1999) also tried to backcalculate interface stiffnesses between two AC layers (along with the layer moduli) from Falling Weight Deflectometer (FWD) measurements. FWD tests were carried out on several pavements immediately after construction and after six months. A variety of interface spring constants were found in the range of 0.01 MPa/mm to 100 MPa/mm, i.e., from poor to good. The backcalculation results indicated a trend of increasing interface stiffness with time.

1.2.3. Cyclic shear testing

The interface conditions in-between two AC layers have also been evaluated under sinusoidal shear-loading conditions. The first identified work in this context is that of Crispino *et al.* (1997), which involved the design, construction, and application of a new/suitable test apparatus. Under steady-state conditions, a complex interface stiffness K^* was introduced to represent the bond behavior:

$$K^* = \frac{\tau_0}{\Delta U_0} \cos\varphi + i\frac{\tau_0}{\Delta U_0} \sin\varphi = K_1 + iK_2 \tag{3}$$

where $K_1 = \frac{\tau_0}{\Delta U_0} \cos\varphi$ and $K_2 = \frac{\tau_0}{\Delta U_0} \sin\varphi$ denote (respectively) the real and imaginary parts of K^*, τ_0 is the sinusoidal shear stress amplitude, ΔU_0 is the differential displacement amplitude between the two specimen layers, and φ is the phase angle between shear stress and displacement. Thus, the norm of the complex interface stiffness

$|K^*|$ is given by:

$$|K^*| = \sqrt{K_1 + K_2} = \sqrt{\left(\frac{\tau_0}{\Delta U_0}\cos\varphi\right)^2 + \left(\frac{\tau_0}{\Delta U_0}\sin\varphi\right)^2} = \frac{\tau_0}{\Delta U_0} \qquad (4)$$

while the the phase angle is obtained from:

$$\tan(\varphi) = \frac{K_2}{K_1} \qquad (5)$$

Crispino *et al.* (1997) tested 19 different two-layered AC cores (with a tack coat application rate of $0.5\,\text{kg/m}^2$). All tests were done in load-controlled mode at a single frequency of 10 Hz, under two temperature levels (15°C and 35°C), and with zero normal stress application. It was found that, on average, $|K^*| = 3.9\,\text{MPa/mm}$ for 15°C and $|K^*| = 0.8\,\text{MPa/mm}$ for 35°C. Values of ΔU_0 associated with these complex norms were not reported. Overall, the $|K^*|$ values are about three times higher than the k values obtained under monotonous tests (same temperature).

In the work of Kruntcheva *et al.* (2006) a cyclic shear load was applied to AC interfaces in a shear box apparatus. The applied peak-to-peak horizontal displacement ranged between $1\,\mu\text{m}$ and $350\,\mu\text{m}$. Based on their plotted results, the interface spring constant values were of the order of $20\,\text{MPa/mm}$, i.e., ten times higher than those reported in the monotonous tests. The paper mentions a test frequency of 2 Hz but does not provide the temperature level.

In the work of Isailović *et al.* (2017), cyclic shear and static normal (compressive) loadings were applied to investigate the interface bonding properties between two AC layers. Several AC cores were tested for a fixed frequency of 10 Hz, under five temperature levels (from -10 °C to 50 °C) and three normal stresses (from zero to 0.5 MPa). An interface spring constant was estimated for each cycle until failure. During the early loading cycles, interface spring constant values ranged between $4\,\text{MPa/mm}$ to $40\,\text{MPa/mm}$, depending on the temperature and normal stress level. It was also observed that the interface spring constant dropped with an increase in the applied displacement amplitude signifying a non-linear behavior.

A study by Leischner *et al.* (2019) focused on characterizing the time-temperature dependency of the interface spring constant between two AC lifts. The authors developed a testing device called the Dresden Dynamic Shear Tester (DDST), which applies cyclic shear and static normal stress to the interface of two coherent AC elements – placed inside a temperature-controlled direct shear box. Testing was carried out on four lab-constructed AC specimens at five frequency levels (0.1 Hz to 10 Hz), four temperature levels (-10 °C to 50 °C), and four normal stress levels (none to 0.9 MPa). Shear displacement amplitudes were applied at small (albeit varying) levels. Post-processing of the test data resulted in four master curves of the interface stiffness, one for each normal stress level. Each master curve was represented in the frequency domain by a five-parameter sigmoid function, taking into account time-temperature shifting; values of $|K^*|$ were found to be in the range of $1.5\,\text{MPa/mm}$ to $44\,\text{MPa/mm}$, depending on the loading frequency, temperature level, and normal stress.

In a recent work by Roussel *et al.* (2022), the influence of time-temperature-dependent interface behavior on FWD test results was investigated. Interface bond constants were measured in the laboratory on hollow cylinder AC specimens. Two loading conditions were applied, namely cycling torsion and cycling axial loading. The

tests involved the application of small displacements; they were carried out at four frequencies (0.01 Hz to 0.3 Hz) under four temperature levels (10 °C to 40 °C). Two independent complex interface stiffnesses were determined, one associated with axial displacements and another associated with horizontal displacements. Regarding horizontal displacements, complex interface stiffnesses were in the range of 4 MPa/mm to 300 MPa/mm. The work also included a synthetic case study, simulating FWD deflections (at 20 °C), while utilizing the measured complex interface stiffnesses to represent the interaction between two AC lifts. The simulations were based on extending the Spectral Element Method to include VE layer and interface behavior. It was found that the lab-obtained interface properties provided similar deflections to a fully bonded situation.

1.2.4. Tests on AC interfaces with AGR

When it comes to characterizing interface bond conditions including AGR, the existing literature is rather limited, and mainly focused on failure testing under monotonic direct shear conditions (Plug *et al.* 2010, Lee *et al.* 2019, Correia and Mugayar 2021, Solatiyan *et al.* 2021). The general consensus, based on these studies, is that interface shear strengths decrease when AGR products are present. Values of k have been reported in some of the studies, spanning the range of 0.1 MPa/mm to 0.8 MPa/mm (depending on the test conditions). None of the shear failure tests provide any consistent evidence that k values decrease when an AGR is present.

Based on field measurements, Le *et al.* (2022) analyzed the influence of AGR on interface bonding conditions between asphalt lifts. Focus was placed on the pavement's behavior in non-damaged conditions. Glass fiber grids were installed between two AC lifts, and strain gauges were embedded at the interface and at the bottom of the AC. Measured strains, triggered by a moving load, were compared to calculated pavement responses. Calculations were obtained using LET considering two model cases – one with full bonding ($k \to \infty$) and one with zero bonding ($k = 0$ MPa/mm). In the modeling, the AGR was considered indirectly, by manipulating the AC layer modulus. Calculations indicated a reduced bond level in the reinforced pavement section compared to a nominally identical reference section without an AGR. Similar results were found from additional FWD measurements (taken at 15 °C), where backcalculation resulted in an interface spring constant of 4 MPa/mm for the reinforced section and 63 MPa/mm for the unreinforced section.

1.2.5. Summary and research gaps

To summarize, the common approach for considering interface bonding conditions in LET-based pavement models is to introduce a horizontal spring-bed connecting two adjoining layers, characterized by a constant stiffness k. A large body of work exists on characterizing k via laboratory testing, mostly by application of monotonic shear conditions. These tests often proceeded to induce large displacements and ultimate failure of the interface. Some studies attempted to characterize interface bonding by the application of cyclic loading under relatively small displacements. These tests illustrated that the bond between two AC lifts is both time- and temperature-dependent, and can be characterized by a complex interface stiffness K^*.

The existing literature provides a very wide range of values for k or $|K^*|$. The reason for the range is due to differences in test conditions, i.e., rate of loading, temperature, normal stress, displacement level, aging, and the amount of tack coat applied between

the two AC layers. Nonetheless, there is almost an order-of-magnitude difference in shear stiffness values when contrasting tests with monotonic loading against tests with cyclic loading. This difference seems related to the level of applied displacement, which is usually less than a micrometer in cycling testing and in the order of millimeters in monotonous tests. Given that k is influenced by the level of differential shear displacement and the level of normal stress, it is essentially a non-linear entity.

With respect to the presence of AGR at interfaces, only a few studies exist – mostly focused on interface strength under monotonic shear. There seems to be a general consensus that interface shear strengths decrease when AGR products are present. However, there is no consistent evidence that interface k or $|K^*|$ values decrease when AGRs are present. Lastly, no pavement modeling effort was identified in the technical literature that simultaneously considers time- and temperature-dependent interface bonding, time- and temperature-dependent layer properties, AGR effects, and moving loads.

1.3. *Objective and methodology*

The objective of this study is to investigate the effects of interface properties on key responses in pavements with AGR. The key responses are those commonly utilized in the design and analysis of asphalt pavements, and the interface properties are those that govern the bond conditions between neighboring AC lifts or between a grid and its adjoining AC. The investigation is carried out by combining results from a full-scale construction, laboratory tests on AC cores, and synthetic (in silico) simulations. The latter analysis is based on the mechanistic code developed in Nielsen *et al.* (2022). More specifically, two nominally identical asphalt pavement systems are modeled, one unreinforced serving as a reference and a second that includes an AGR. The loading considered is that of a single wheel moving in a straight line at a constant speed. The AC interfaces are characterized as both time- and temperature-dependent, with properties measured at TU Dresden by the DDST. Key responses are quantified for the two pavement systems under two combinations of wheel speed and AC temperature.

2. Experimental Campaign

This section describes an experimental campaign involving laboratory testing of field-produced cores in two separate efforts: (i) characterization of AC properties, and (ii) characterization of interface properties with and without AGR. Both efforts included the application of repeated loadings under controlled isothermal conditions, aiming for time- and temperature-dependent properties.

2.1. *Pavement construction*

An instrumented asphalt road was established within the Technical University of Denmark (DTU) campus. This road, called DTU Smart Road, was built as part of a reconstruction project of an existing 100 m long road serving live campus traffic. It comprises four test sections, each 25 m long, three of which contain an AGR and a fourth unreinforced, serving as a reference. For the experimental investigation considered herein, only two of the four sections are evaluated: a reinforced section where the AGR was installed in-between two AC lifts, and the reference section.
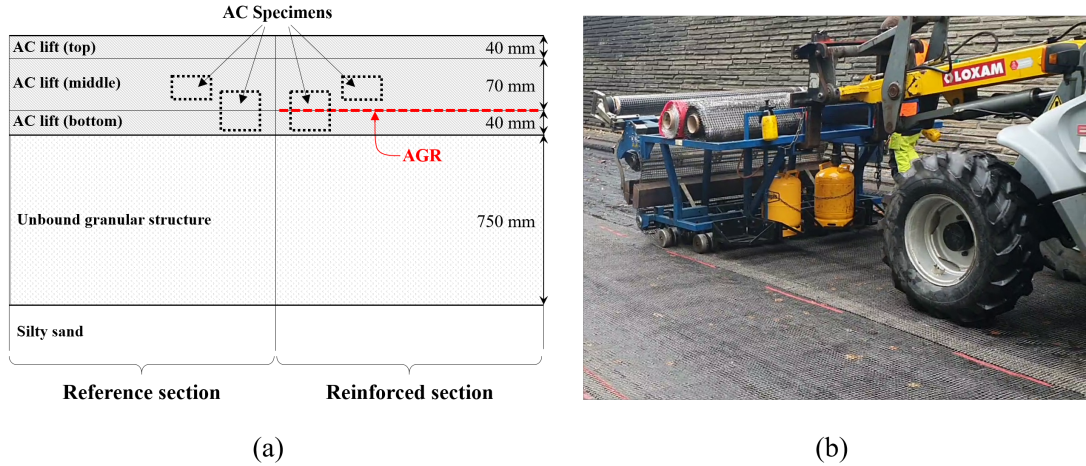
Figure 2. The DTU Smart Road: (a) a cross-sectional view of the two considered pavement sections indicating core locations, and (b) photo of AGR installation.

Figure 2(a) presents a cross-sectional view of the two pavement systems. Both consist of a 150 mm thick AC layer, paved in three lifts with thicknesses of 40 mm (bottom), 70 mm (middle), and 40 mm (top). All lifts were made from the exact same asphalt mix, characterized by a flat S-shaped aggregate gradation curve with a nominal maximum aggregate size (NMAS) of 8 mm, a bitumen content of 5.6%, and a bitumen penetration grade of 70/100. As can be seen in the figure, the reinforced section had an AGR located in-between the bottom and middle AC lifts, i.e., 110 mm below the pavement surface. In both sections, the bottom AC lift was supported by an existing recompacted 750 mm thick unbound granular structure resting on a layer of overconsolidated silty sand extending to a large depth.

The AGR utilized was a Carbophalt®G 200/200 (by S&P Clever Reinforcement), which is made of bitumen-coated strands of carbon fibers arranged in a mesh with an equal amount of fibers in each direction. The amount of bitumen coating corresponds to $200\,\text{g/m}^2$ (bitumen/overall grid area) and has a penetration grade of 30/40. The grid openings are $15\,\text{mm} \times 15\,\text{mm}$ in size, and non-fixed knots (fiber overlaps); it is characterized by a Young's modulus of 265 GPa, a Poisson's ratio of 0.15, and a cross-sectional fiber area of $50\,\text{mm}^2/\text{m}$. Before installation of the AGR, the surface of the bottom AC lift was sprayed with a 350 g/m^2 tack coat. The AGR was then installed using the so-called S&P Asphalt Unroll Equipment (see Figure 2(b)). In this procedure, the grid is preheated just before deployment in order to melt the bitumen coating and promote improved adhesion with the underlying AC lift.

2.2. *Laboratory tests*

About six months after the DTU Smart Road was constructed, four AC cores, $100\,\text{mm}$ in diameter, were taken for subsequent laboratory testing; two cores were taken from the reinforced section and two from a reference section (see Figure 2(a)). One core from each test section was utilized for characterizing the AC properties while the other two were utilized for characterizing the interface bond with and without reinforcement.

2.2.1. AC characterization

An indirect tensile test was conducted to characterize the VE properties of the AC. For this purpose, the middle AC lift (without AGR) was utilized – trimming the core to a length of 50 mm. Two separate tests were carried out (one for each specimen), in which two opposing diametral sectors were loaded, and the resulting transversal diameter changes monitored with linear variable displacement transducers (LVDTs). Load-displacement histories were recorded at eight temperature levels: 0 °C, 5 °C, 10 °C, 15 °C, 20 °C, 25 °C, 30 °C, and 35 °C. In each temperature level, ten displacement-controlled pulse-rest cycles were applied, with a repetition period of 3 s and a pulse duration of 0.25 s.

VE properties were estimated through inverse analysis following the approach of Levenberg and Michaeli (2013). In this context, the AC relaxation modulus $E^{\mathrm{AC}}(t)$ was presumed sigmoidal in shape (in a log-log plot), having the following formulation:

$$E^{\mathrm{AC}}(t) = \frac{E_\infty(1 + (t/\tau_D)^{n_D})}{(t/\tau_D)^{n_D} + (E_\infty/E_0)} \tag{6}$$

where E_0 is the instantaneous modulus (units of force/length^2), E_∞ is the equilibrium modulus (units of force/length^2), and τ_D (units of time) and n_D (unitless) are shape parameters. As part of the analysis, E_0 and E_∞ were pre-chosen: $E_0 = 30,000$ MPa and $E_\infty = 100$ MPa. This was needed because it was technically impossible to test the specimens under the two extreme conditions of zero and infinite time.

The associated time-temperature shifting is included in $\tau_D = a_T \tau_D^0$, where τ_D^0 is a material constant (units of time) associated with some preselected reference temperature T_0, and a_T is the time-temperature shift factor (unitless), assumed to obey the WLF equation (Williams *et al.* 1955):

$$\log_{10}(a_T) = \frac{-C_1(T - T_0)}{C_2 + (T - T_0)} \tag{7}$$

where C_1 (unitless) and C_2 (units of temperature) are constants.

The average VE properties and time-temperature shift constants for a reference temperature of $T_0 = 20°C$ are listed in Table 1. Figure 3(a) shows the resulting relaxation modulus as a function of time for a 20°C reference temperature (Equation (6)), while Figure 3(b) shows the time-temperature shift factor as a function of temperature (Equation (7)).

Table 1. VE AC properties associated with a reference temperature of $T_0 = 20°C$.

E_0 [MPa]	E_∞ [MPa]	n_D [-]	τ_D^0 [s]	T_0 [°C]	C_1 [-]	C_2 [°C]
30,000	100	0.47	47	20	23	197

2.2.2. Interface characterization

For the purpose of characterizing the interface, two AC cores were tested (separately) in the DDST. The cores were cut to a length of 80 mm, such that the interface between the bottom and middle lifts was located in the center. One core had an AGR at the interface while the other was unreinforced (see Figure 2(a)). In the testing, each core
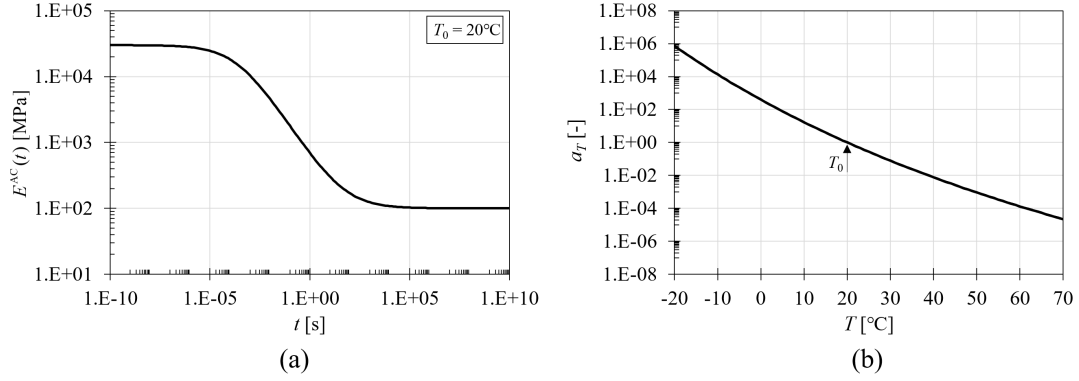
9

Figure 3. Measured AC properties: (a) relaxation modulus $E^{\mathrm{AC}}(t)$ as a function of time for a reference temperature of $T_0 = 20°\mathrm{C}$, and (b) time-temperature shift factor a_T as a function of temperature.

was fixed using a two-component epoxy adhesive inside two steel molds that were separated by a 1 mm gap aligned with the interface. After 24 hours of curing time for the epoxy, the molds were installed inside a direct shear box. A schematic representation of the DDST is provided in Figure 4; the setup applies a cyclic sinusoidal load $F^{\mathrm{m}}(t)$ to one side of the shear box while the other side is fixed – thus shearing the interface. Simultaneously, constant normal stress, denoted as σ_N, is applied perpendicular to the interface. Differential displacements between the two shear box sides, denoted as $\Delta U^m(t)$, were monitored by the average readings of two LVDTs. The entire setup was placed inside a temperature-controlled chamber to induce isothermal conditions. Refer to Leischner *et al.* (2019) for more detailed information about the DDST setup and testing procedure.
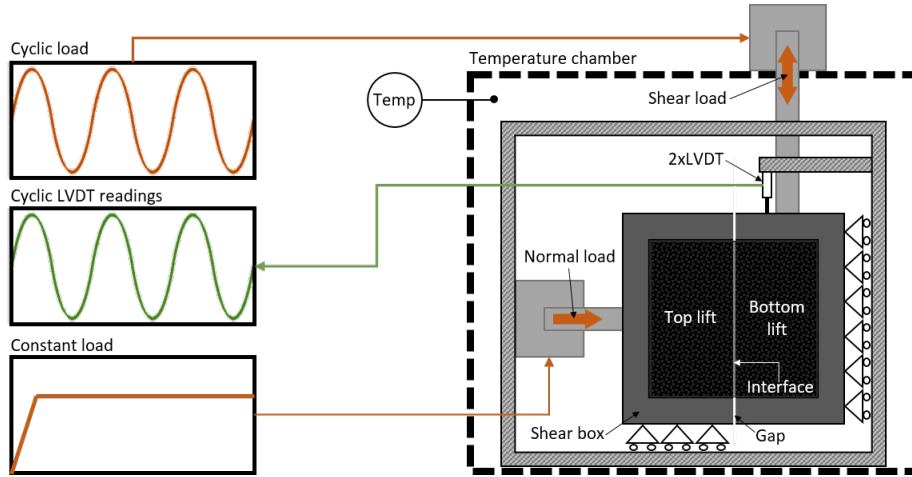
Figure 4. Schematic representation of the DDST.

The shear test was performed in displacement-controlled mode targeting small levels of displacement oscillations. Testing was done at a combination of: (i) four temperature levels (T), i.e., -10 °C, 10 °C, 30 °C, and 50 °C; (ii) five frequencies (f), i.e., 0.1 Hz, 0.3 Hz, 1 Hz, 3 Hz, and 10 Hz; (iii) four σ_N levels, i.e., 900 kPa, 600 kPa, 300 kPa, and 0 kPa, and (iv) three target displacement amplitude levels (ΔU_0^m), i.e., low ($\approx 10\,\mu\mathrm{m}$), medium ($\approx 30\,\mu\mathrm{m}$), and high ($\approx 50\,\mu\mathrm{m}$). The actual displacement amplitudes slightly varied depending on the temperature, normal stress, and frequency level. In effect, each

displacement amplitude level refers to a mean (and standard deviation) of low: 13.1 μm (± 1.8 μm), medium: 33.3 μm (± 1.4 μm), and high: 53.3 μm (± 2.1 μm). A period of two hours was given for temperature regulation between every change in temperature level.

The DDST measurements were utilized to estimate a relaxation interface stiffness for both test specimens. This was done in three steps: (i) fitting analytic sinusoidal functions to the measured load and displacement histories, (ii) using the obtained sinusoidal function parameters to estimate complex norm values of the interface stiffness $|K^*|$ and associated phase angles φ, and (iii) applying interconversion and inverse analysis to produce a relaxation interface stiffness $K(t)$.

Initially, analytic sinusoidal functions were fitted to the measured load and displacement histories for all available combinations of T, f, σ_N, and $\Delta U^m(t)$ (240 combinations in total). For each combination, a five-parameter analytic harmonic time function was matched to the last five cycles. Specifically, the measured differential displacement history $\Delta U^m(t)$ was fitted with an analytic function $\Delta U(t)$:

$$\Delta U(t) = \Delta U_0 \sin(2\pi f_1 t + \varphi_1) + \lambda_1 t + \theta_1 \tag{8}$$

where t is the time, ΔU_0, f_1, and φ_1 denote the amplitude, oscillation frequency, and phase (respectively) of the sinusoidal part, and λ_1 and θ_1 are shape parameters that compensate for drift (trend) and initial offset in the LVDT readings. Similarly, the the applied load in the test $F^m(t)$ was fitted with an analytic function $F_s(t)$:

$$F_s(t) = F_0 \sin(2\pi f_2 + \varphi_2) + \lambda_2 t + \theta_2 \tag{9}$$

where F_0, f_2, and φ_2 denote the amplitude, oscillation frequency, and phase (respectively) of the sinusoidal part, and λ_2 and θ_2 are shape parameters that compensate for trend and initial offset in the load cell readings.

All above-described fittings were done with a nonlinear minimization algorithm; a MATLAB tool `fminsearch`. To achieve this, all five parameters in Equation (8), i.e., ΔU_0, f_1, φ_1, λ_1 and θ_1, or in Equation (9), i.e., F_0, f_2, φ_2, λ_2 and θ_2, were treated as unknowns. The mean absolute error between measured and calculated response histories (either displacements or loads) was utilized as an objective function.

Next, the optimal values of ΔU_0, F_0, φ_1, and φ_2 were employed to estimate the norm of the complex interface stiffness $|K^*|$. This was done according to Equation (4) with $\tau_0 = F_0/A_s$, where A_s is the area of the tested interface (i.e., 7854 mm^2 for 100 mm diameter cores). The phase angle φ was found according to: $\varphi = \varphi_2 - \varphi_1$. Subsequently, the obtained $|K^*|$ and φ values were employed to construct 12 master curves (with reference temperature of 20°C), one for each combination of σ_N and ΔU_0. For this purpose, and based on a side-study, the time-temperature shifting constants of the AC were found adequate – namely C_1 and C_2; see Equation (7) and Table 1.

Figure 5 presents the obtained $|K^*|$ values for a combination of zero normal stress ($\sigma_N = 0$) and low displacement amplitude levels (ΔU_0^m) as a function of reduced frequency ($f_r = a_T f$) associated with $T_0 = 20$°C. Each cluster of data points on the chart represents $|K^*|$ associated with one of the test temperature levels and one of the test specimens (with AGR or without). As can be seen, after temperature shifting the $|K^*|$ values form a sigmoid shape on a log-log scale. In general, the $|K^*|$ values obtained from the specimen with AGR are lower than the ones associated with the reference specimen. It is noted that measured $|K^*|$ values associated with a temperature level of $T = 50$°C were deemed erroneous/invalid; they did not conform to a sigmoid shape and therefore excluded from the chart and from the ongoing analysis.
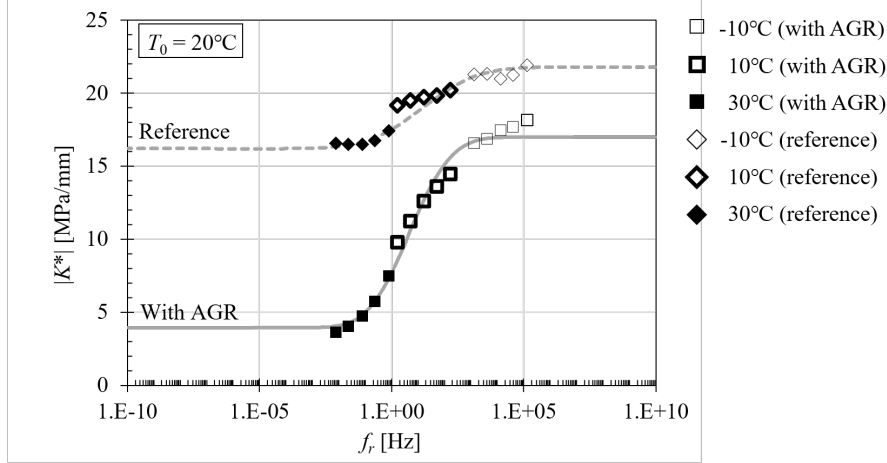
Figure 5. Estimated $|K^*|$ values from the DDST as a function of reduced frequency for $\Delta U_0^m =$ low, $\sigma_N = 0$ kPa, and a reference temperature of $T_0 = 20°$C.

Moreover, when plotted against reduced frequency (f_r), the estimated phase angles (φ) appeared erratic/random and therefore deemed unreliable. As a consequence, the φ values were not considered in the ongoing interpretation.

Hereafter, the $|K^*|$ values were utilized to calculate a relaxation interface stiffness function for each combination of σ_N and ΔU_0^m. These were constructed by fitting a sigmoid function to each of the aforementioned $|K^*|$ master curves in a new inverse analysis step. For this purpose, it was presumed that the relaxation interface stiffness $K(t)$ between two AC lifts is a sigmoid-shaped time function. Accordingly, a four-parameter expression similar to Equation (6) was utilized:

$$K(t) = \frac{K_\infty(1 + (t/\tau_K)^{n_K})}{(t/\tau_K)^{n_K} + (K_\infty/K_0)} \tag{10}$$

where K_0 is the instantaneous (short-term) stiffness (units of force/length^3), K_∞ is the equilibrium (long-term) stiffness (units of force/length^3), while τ_K (units of time) and n_K (unitless) are shape parameters governing the transition between K_0 and K_∞. Also, $\tau_K = \tau_K^0 a_T$ in which τ_K^0 (units of time) is a constant linked to the reference temperature T_0, and a_T is provided by Equation (7).

As Equation (10) provides $K(t)$ in the time domain, interconversion was applied to match the complex norm values in the frequency domain. Interconversion was done according to Park and Schapery (1999) and applied in each iteration step of the inverse analysis. Specifically, $K(t)$ was written as a Prony series with 50 relaxation strengths and 50 relaxation times. Then after, the real and imaginary components of the complex interface stiffness K_1 and K_2 were expressed by the relaxation strength and times. From Equation (4) and (5) it then is possible to estimate both $|K^*|$ and φ. With the established relationship between the measured $|K^*|$-values and Equation (10), the relaxation stiffness parameters K_0, K_∞, τ_0, and n_K, were optimized by minimizing the mean relative error. Best-match results with respect to $\sigma_N = 0$ and $\Delta U_0^m =$low are shown in Figure 5, where interconverted $|K^*|$ values are indicated by gray curves (either dashed or solid).

At the end, 12 sets of interlayer relaxation stiffness parameters were obtained for each AC specimen. Table 2 presents all estimated parameters across the 12 combinations of ΔU_0^m and σ_N. Here, $K^{\text{Ref}}(t)$ refers to the relaxation interface stiffnesses

12

Table 2. Estimated parameters for K^{Ref} and K^{AGR} under a reference temperature of 20°C.

ΔU_0^m	σ_N	K^{Ref} (reference)				K^{AGR} (with AGR)			
		K_0	K_∞	τ_K^0	n_K	K_0	K_∞	τ_K^0	n_K
	[kPa]	$\left[\frac{\mathrm{MPa}}{\mathrm{mm}}\right]$	$\left[\frac{\mathrm{MPa}}{\mathrm{mm}}\right]$	[s]	[-]	$\left[\frac{\mathrm{MPa}}{\mathrm{mm}}\right]$	$\left[\frac{\mathrm{MPa}}{\mathrm{mm}}\right]$	[s]	[-]
Low	0	21.8	16.2	9.0×10^{-3}	0.30	17.0	3.9	1.8×10^{-1}	0.60
	300	23.0	16.4	9.6×10^{-3}	0.29	18.1	3.9	3.8×10^{-1}	0.46
	600	23.3	16.7	9.8×10^{-3}	0.29	17.6	4.6	2.5×10^{-1}	0.51
	900	22.4	16.7	9.2×10^{-3}	0.29	17.1	5.6	1.4×10^{-1}	0.59
Medium	0	16.0	10.7	1.1×10^{-2}	0.28	14.1	2.5	4.1×10^{-1}	0.53
	300	16.0	11.3	1.0×10^{-2}	0.28	14.6	3.3	2.5×10^{-1}	0.53
	600	16.3	11.1	1.1×10^{-2}	0.29	14.8	3.9	2.1×10^{-1}	0.52
	900	16.1	11.5	9.0×10^{-3}	0.29	14.9	4.6	1.8×10^{-1}	0.49
High	0	13.4	8.8	1.7×10^{-2}	0.32	12.1	2.3	2.4×10^{-1}	0.75
	300	14.2	9.1	1.7×10^{-2}	0.26	12.5	3.2	1.7×10^{-1}	0.64
	600	15.9	9.2	1.2×10^{-2}	0.28	12.8	3.6	2.0×10^{-1}	0.55
	900	12.9	9.9	1.0×10^{-2}	0.29	13.3	4.2	1.6×10^{-1}	0.48

obtained for the reference AC specimen, whereas $K^{\mathrm{AGR}}(t)$ refers to the relaxation interface stiffnesses obtained for the reinforced AC specimen. As can be seen in the table, K_0 and K_∞ associated with K^{Ref} are generally larger than K_0 and K_∞ related to K^{AGR}. This observation indicates that adding AGR reduces the interface bond in terms of $K(t)$ at all times. Furthermore, the shape parameters τ_K^0 and n_K associated with K^{AGR} are systematically larger than τ_K^0 and n_K associated with K^{Ref}. This means that the presence of AGR also has an impact on the time-related transition between the instantaneous and equilibrium interface stiffness. The difference between K_0 and K_∞ is generally small for K^{Ref}, indicating that the reference interface (without AGR) is less sensitive to time and temperature, compared to the interface with AGR.

The presented results also indicate non-linear behavior for both K^{Ref} and K^{AGR} as values of K_0 and K_∞ generally decrease with increasing ΔU_0^m. This behavior is similar to what was observed in the literature review for monotonous and cyclic shear tests. In addition, there is a general trend of K_∞ increasing with the normal stress σ_N. The same trend is also expected for K_0, but remains unclear from the given test results. It should be noted that all these implications are based on test results from a single test sample (one for each interface type), and should be checked for statistical significance by testing several AC specimens.

The resulting relaxation interface stiffness for the combination of $\sigma_N = 0$ kPa and ΔU_0^m = low are plotted (in the time domain) for both AC specimens in Figure 6. These two cases are visually presented as they were utilized further on for the synthetic investigation. The figure shows the time along the horizontal axis (log scale) and the corresponding interface stiffness along the vertical axis (linear scale); all associated with $T_0 = 20$°C. The solid curve in the figure represents $K(t)$ for an interface with AGR (i.e., K^{AGR}) while the dashed curve represents $K(t)$ for a reference interface (without AGR, i.e., K^{Ref}). The gray-shaded areas represent the variation of $K(t)$ with respect to
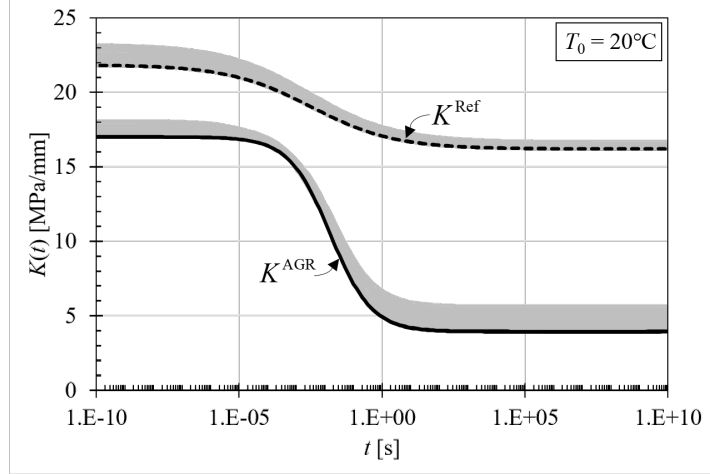
Figure 6. Relaxation interface stiffnesses K^{Ref} and K^{AGR} as a function of time for $\Delta U_0^m = $ low, $\sigma_N = 0$ kPa, and a reference temperature of $T_0 = 20°$C.

the four tested stress levels of σ_N (for $\Delta U_0^m = $low). As can be seen, the two presented relaxation interface stiffnesses associated with $\sigma_N = 0$ kPa constitute the lowest values of $K(t)$ within the grey-shaded area. Furthermore, K^{Ref} is associated with larger interface stiffness compared to K^{AGR} at all times. Finally, the test results indicate that the reference interface (without AGR) is less sensitive to time and temperature, compared to the interface with AGR. These observations repeat the implications of Table 2, indicating a lower level of interface bonding stiffness due to the presence of AGR, and a non-linear interface bonding behavior.

3. Mechanistic investigation of interface bonding effects

This section contains a synthetic investigation focused on quantifying the effects of interface bonding on key responses in asphalt pavements. The section commences with a brief exposition of the overall modeling approach and explains how time- and temperature-dependent interface stiffness is incorporated. Then after, the modeling is applied to the two pavement systems in Figure 2(a). Utilized as inputs (in both cases) are the VE properties of the AC and the relaxation interface stiffnesses obtained from Subsection 2.2. Ultimately, under moving load conditions, several traces of key responses are calculated, presented, and discussed.

3.1. *Modeling Approach*

The pavement modeling approach herein was founded on Schapery's quasi-elastic approximation for isothermal conditions (Schapery 1962). This approximation was chosen because it allows relatively quick, sufficiently accurate, and numerically stable conversion of linear elastic solutions to linear viscoelastic solutions. Specifically, it was applied to a stratified elastic half-space exposed to a stationary load to produce a solution for an equivalent medium but with time-dependent layer and interface properties. In this context, the AC layers were modeled as linear VE, characterized by a relaxation modulus $E^{\text{AC}}(t)$. Similarly, the horizontal spring stiffness k_i from Equation (1) (or (2)) was represented with a time-dependent relaxation interface stiffness. To

14

capture the response under a moving load, the VE solution for a stationary load was extended by decomposing the movement into a sequence of stationary load-unload applications, and then superposing the resulting sequence of VE solutions according to Levenberg (2016c). This modeling approach was coded in a MATLAB environment with ALVA as its LET engine (Skar and Andersen 2020, Skar $et\ al.$ 2020a); numerical considerations are elaborated in Nielsen $et\ al.$ (2022). The code was verified against other codes such as ELLEA1 (Levenberg 2016a), ELLVA1 (Levenberg 2016b,c), and against other known solutions (Burmister 1943, Ike 2018).

AGR effects were included in the modeling according to Nielsen $et\ al.$ (2022), by: (i) adding a thin high-modulus elastic layer to represent the presence of the reinforcement material itself. This layer is characterized by a thickness, Young's modulus, and Poisson's ratio; (ii) specifying the bonding properties between the thin elastic layer and the layers above and below it. These properties are characterized by two distinct relaxation interface stiffnesses, namely $K_{Top}^{AGR}(t)$ and $K_{Bottom}^{AGR}(t)$; and (iii) modifying the VE properties of the layers in contact with the thin high-modulus layer to represent how AGR affects the surrounding AC properties. This ZoI-effect operates over a small part of the adjoining VE layers, within some thickness δ^{ZoI}. The change in the VE properties within the ZoI is captured by κ, a positive unitless scalar parameter residing in the range $1 \leq \kappa \leq \frac{E_0}{E_\infty}$. In effect, κ is utilized to replace E_∞ in $E^{AC}(t)$ (see Equation 6) with κE_∞, producing a slightly modified relaxation function denoted as $E^{ZoI}(t)$.

3.2. General model inputs

A cross-section of the two pavement models considered herein is shown in Figure 7. The models were made to represent the reinforced and unreinforced DTU Smart Road sections shown in Figure 2(a). As can be seen, both pavement models consist of three VE layers of 150 mm in total thickness (representing the AC), separated by two interfaces at $z = 40$ mm and $z = 110$ mm (from the surface). The VE layers not affected by the AGR were characterized by a relaxation modulus $E^{AC}(t)$ and a constant Poisson's ratio of 0.30. $E^{AC}(t)$ was expressed by Equation (6) and (7), utilizing the parameter values listed in Table 1. The temperature (T) of the three VE layers was assumed to be uniformly distributed across the entire 150 mm thickness. In both models, the VE layers were supported on a 750 mm thick elastic layer representing the unbound granular structure, with a Young's modulus of 200 MPa and a Poisson's ratio of 0.35. The lowest semi-infinite model layer, representing the natural subgrade soil, was assigned a Young's modulus of 80 MPa and a Poisson's ratio of 0.40. Perfect interface bonding was assumed between the two elastic layers and at the interface with the bottom of the VE layer.

Pavement responses were calculated by considering a single-wheel load configuration traveling on the surface. Figure 8 shows a schematic illustration of the moving load; it has a circular contact radius of 150 mm and a vertical load intensity of 0.7 MPa. A Cartesian coordinate system is introduced, such that the response evaluation point is located under the coordinate system's origin. The load travels along the x-axis direction with a constant speed V on a line that passes above the evaluation point (i.e., $y = 0$); it first appears at $x = -10,000$ mm and is removed from the system at $x = 10,000$ mm. Investigated in the following are two combinations of load speeds and AC temperatures (uniform across depth), namely a low-speed/high-temperature condition and a high-speed/low-temperature condition.
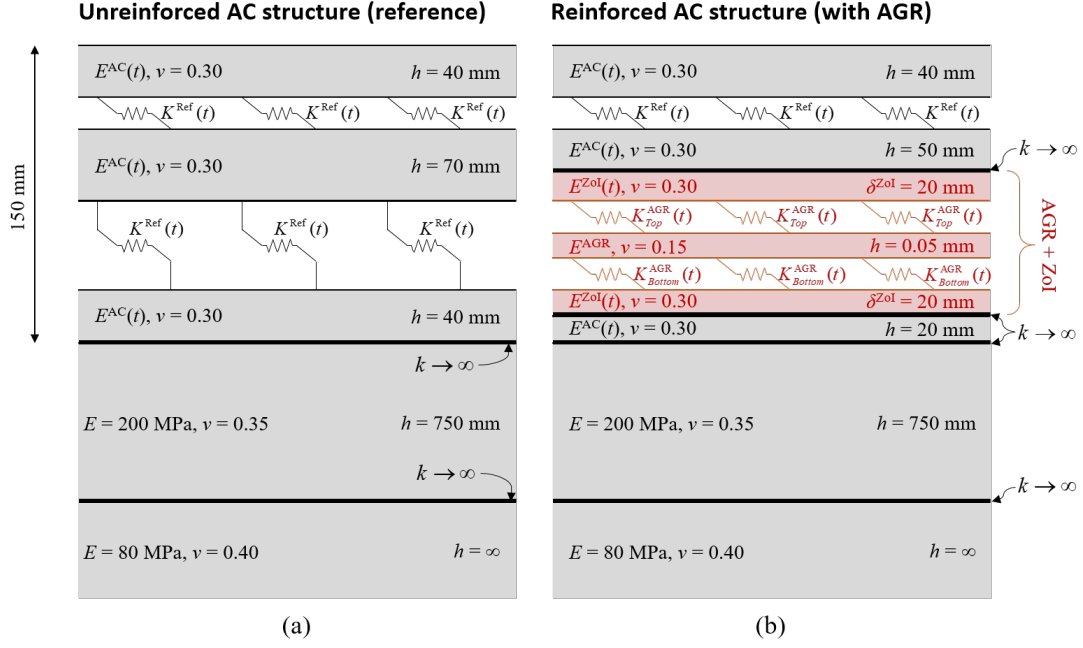
Figure 7. Cross-sectional view of two layered VE systems: (a) a unreinforced pavement system (reference), and (b) a reinforced pavement system (with AGR).
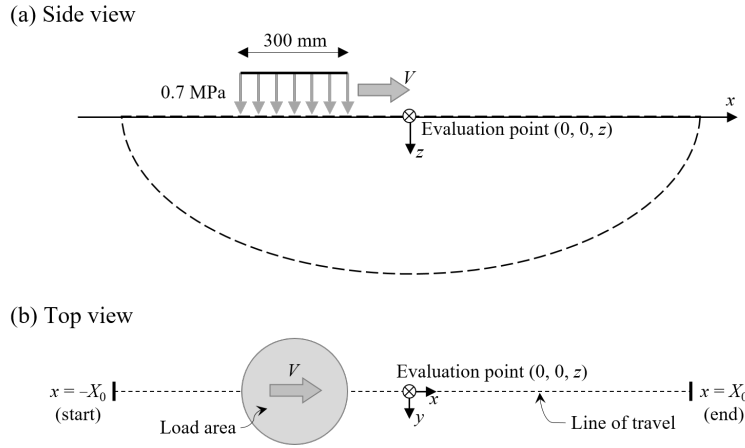

Figure 8. Schematic representation of moving load and evaluation point: (a) side view, and (b) top view.

3.3. *AC interface bonding and AGR inputs*

The relaxation interface stiffnesses $K(t)$ obtained from the DDST were utilized to emulate the bonding at AC layer interfaces with and without AGR. In the unreinforced model, bonding conditions at both AC interfaces, i.e., at $z = 40 \, \text{mm}$ and at $z = 110 \, \text{mm}$ were characterized by the relaxation interface stiffness $K^{\text{Ref}}(t)$, see Figure 6 and Table 2. The specific relaxation interface stiffness properties utilized were those associated with $\sigma_N = 0$ kPa and a low ΔU_0^m. The justification for these choices is discussed in the following subsection. In the reinforced model, the interface at $z = 40 \, \text{mm}$ was also characterized by $K^{\text{Ref}}(t)$. The interface at $z = 110 \, \text{mm}$ includes an AGR, modeled according to Nielsen *et al.* (2022) with: (i) a Young's modulus of 265 GPa, a Poisson's

16

ratio of 0.15, and a thickness of 0.05 mm; (ii) a ZoI effect acting above and below the grid, each with a ZoI-thickness of $\delta^{ZoI} = 20$ mm (corresponding to 2.5 times the NMAS of the AC) and a $\kappa = 2.0$ taken from Nielsen and Levenberg (2022); and (iii) two relaxation interface stiffnesses $K_{Top}^{AGR}(t)$ and $K_{Bottom}^{AGR}(t)$, governing the interaction at the top and bottom of the AGR (respectively).

The DDST test with AGR captured $K^{AGR}(t)$, i.e., the total/entire bonding behavior between the two AC layers. However, because the AGR is modeled as a thin layer, the properties of two separate bonding interfaces are needed. Thus, $K^{AGR}(t)$ was separated into two components while exploring optional bonding models (BMs), named BM1 and BM2, defined as follows:

$$\text{BM1}: \quad K_{Top}^{AGR}(t) \to \infty \quad , \quad K_{Bottom}^{AGR}(t) = K^{AGR}(t) \tag{11}$$

$$\text{BM2}: \quad K_{Top}^{AGR}(t) = 2K^{AGR}(t) \quad , \quad K_{Bottom}^{AGR}(t) = 2K^{AGR}(t) \tag{12}$$

The BMs represent the two extreme relations between the upper and lower bond while complying with the constraint from Nielsen *et al.* (2022), stating that $K_{Top}^{AGR}(t) \geq K_{Bottom}^{AGR}(t)$. This constraint is linked to the construction procedure, where AGR is placed on top of an already-compacted AC lift before overlaying. This sequence should then always allow for a better grid-interlock with the upper AC lift than the lower AC. Accordingly, BM1 corresponds to the case where the DDST-derived properties are ascribed only to the bottom AGR interface, while the top AGR interface is assumed perfectly bonded. In contrast, BM2 corresponds to the case where the DDST-derived properties are equally split between the top and bottom AGR interfaces. The multiplication factor of two comes from the series-type link between $K_{Top}^{AGR}(t)$ and $K_{Bottom}^{AGR}(t)$.

3.4.   *Simulation of interface conditions*

As a preliminary step, the interface conditions of both pavement models were investigated. Specifically, the horizontal differential displacements ΔU_x and the vertical stresses σ_z at each interface, triggered by the moving single-wheel load, were simulated. The associated responses were simulated directly under the wheel path ($y = 0$) at the two interface depths: $z = 40$ mm and $z = 110$ mm. For unreinforced interfaces, ΔU_x denotes the difference in displacements (in the x direction) between two points, one just above and another just below an interface. For the reinforced interface, ΔU_x denotes the difference in displacements between two points, one just above and another just below the thin layer representing AGR (inside the adjoining layers). Stresses and differential displacements were investigated for two combinations of load speeds and AC temperatures, specifically: under low-speed/high-temperature conditions with $V = 5$ km/h and $T = 35\,°C$, and under high-speed/low-temperature conditions with $V = 80$ km/h and $T = 5\,°C$.

Figure 9 presents the results from the above-described simulations for an evaluation point located at $x = y = 0$. Figures 9(a) and (b) refer to the upper interface at $z = 40$ mm, while Figures 9(c) and (d) refer to the lower interface at $z = 110$ mm. Figures 9(a) and (c) are associated with low-speed/high-temperature conditions, whereas Figures 9(b) and (d) are associated with high-speed/low-temperature conditions. Each chart contains two ordinates, one (left) representing the horizontal differential displacements ΔU_x, and another (right) representing the vertical stresses σ_z. The horizontal
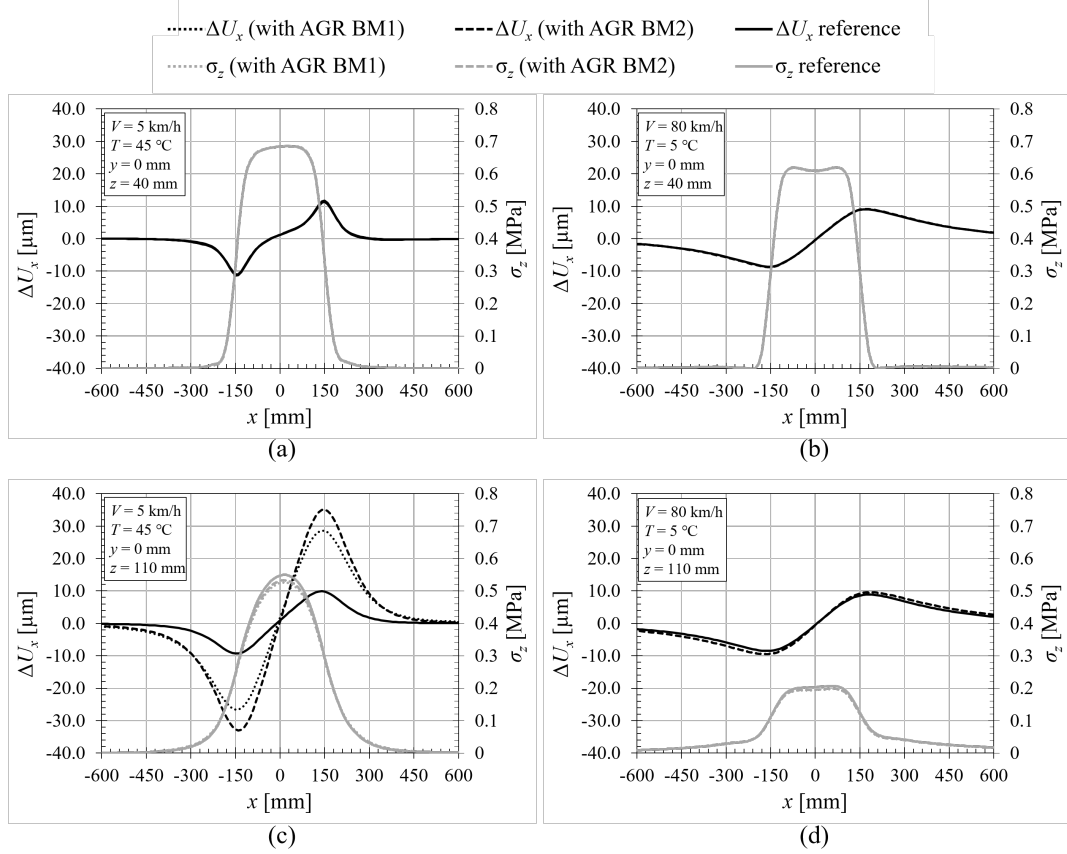
Figure 9. Simulated differential displacements ΔU_x and vertical stresses σ_z at two interface depths $z = 40\,\text{mm}$ and $z = 110\,\text{mm}$, and for two load-speed/temperature conditions.

axis represents the load location in the x direction. Each chart contains six curves; three black curves denote ΔU_x for the reinforced model with BM1, the reinforced model with BM2, and the reference (unreinforced) model. Three gray curves denote σ_z for the reinforced model with BM1, the reinforced model with BM2, and the reference (unreinforced) model. The stress/strain sign convention in the figure (and hereafter) follows a soil mechanics convention, where a positive sign represents compressive conditions and a negative sign represents tensile conditions.

As can be seen in Figures 9(a) and (b), ΔU_x and σ_z seem to be indistinguishable across the three considered models, suggesting that the presence of AGR (regardless of BM) does not influence ΔU_x and σ_z at the upper ($z = 40\,\text{mm}$) interface. Peak differential displacements of about $\Delta U_x = 10\,\mu\text{m}$ and maximum vertical stresses of about $\sigma_z = 0.65\,\text{MPa}$ were obtained across all considered models and do not seem to be highly affected by the load speed and temperature conditions. From Figure 9(c), it can be seen that ΔU_x at $z = 110\,\text{mm}$ is highly influenced by the presence of AGR for the low-speed/high-temperature condition. Peak differential displacements of about $\Delta U_x = 30\,\mu\text{m}$ (BM1) and $\Delta U_x = 35\,\mu\text{m}$ (BM2) are observed for the reinforced interfaces. In contrast, the unreinforced interface is exposed to a peak differential displacement of about $\Delta U_x = 10\,\mu\text{m}$. This indicates that the reinforced interface experiences a larger relative slip between the upper and lower AC lifts in comparison to the unreinforced interface. The three curves representing σ_z seem close to identical, indicating that an increased slip due to AGR has a marginal influence on the vertical

18

stress applied on the interface. From Figure 9(d), it can be seen that ΔU_x and σ_z (at $z = 110$ mm) seem to be indistinguishable across the three considered models. This suggests that the presence of AGR has a marginal influence on the bonding condition related to the high-speed/low-temperature condition. In these conditions, peak differential displacements of about $\Delta U_x = 10$ µm and maximum vertical stresses of about $\sigma_z = 0.2$ MPa were obtained across all considered models.

Lastly, it can be observed across all charts that the differential displacements ΔU_x are mostly below the smallest displacement amplitudes measured in the laboratory test ($\Delta U_0^m \approx 13.1$ µm). In general, ΔU_x exhibits a peak when the load edges are directly above the evaluation point (i.e., $x = \pm 150$ mm). While the reinforced cases reveal a relative slip exceeding 30 µm at the load edges, the value approaches zero when the load center is directly above the point of evaluation. At this point, where key responses generally peak, the interface stiffness is deemed sufficiently higher than what was previously chosen. While the model cannot handle such nonlinear behavior, it is assumed that the relaxation interface stiffness properties associated with $\sigma_N = 0$ kPa and a low $\Delta U_0^m \approx 13.1$ µm are a reasonable choice for representing the bonding conditions.

3.5. *Simulations of key responses*

Several key response traces were simulated for points residing under the path of the moving load ($x = y = 0$), at different depths. This simulation included eight responses, numbered (1), (2),..,(8). Responses (1)...(6) address points residing just above interfaces, chosen given their link to fatigue cracking in the design of asphalt pavements (Shook *et al.* 1982, Huang 2004). Responses (1), (2), and (3) are associated with longitudinal horizontal strains ε_x in the travel direction, while Responses (4), (5), and (6) are associated with transverse horizontal strains ε_y. The evaluation points were located at three different depths, such that Responses (1) and (4) refer to $z = 40$ mm, Responses (2) and (5) refer to $z = 110$ mm, and Responses (3) and (6) refer to $z = 150$ mm. Response (7) denotes the vertical strain ε_z at $z = 150.1$ mm, i.e., at the AC bottom or top of the unbound granular structure. Response (8) refers to the vertical displacements U_z at $z = 0$ mm, i.e., at the pavement's surface (i.e., deflection). Key response (7) was chosen based on its relation to rutting in the unbound granular structure (Huang 2004), while (8) was chosen given its relation to non-destructive deflection testing (ASTM 2009, Horak *et al.* 2015). All response calculations were obtained for two combinations of load speeds and AC temperatures (uniform across depth), namely: a low-speed/high-temperature condition with $V = 5$ km/h and $T = 45\,°\text{C}$, and at a high-speed/low-temperature condition with $V = 80$ km/h and $T = 5\,°\text{C}$.

Figure 10 presents Responses (1), (2), and (3). There are six charts in this figure, arranged in two columns. Each row of charts represents one of the considered depths $z = 40$ mm, $z = 110$ mm, and $z = 150$ mm (from top to bottom). Charts on the left-hand side are associated with $V = 5$ km/h and $T = 45\,°\text{C}$ and charts on the right-hand side are associated with $V = 80$ km/h and $T = 5\,°\text{C}$. In each chart, the horizontal axis denotes the x-coordinate of the wheel (the evaluation point is at $x = 0$), and the vertical axes represent the strain value in the travel (x) direction. Moreover, each chart contains three response traces associated with: (i) the reinforced model with BM1, (ii) the reinforced model with BM2, and (iii) the reference (unreinforced) model. As can be seen across the three key responses, strains are generally larger for the low-speed/high-temperature conditions. Under these conditions, the AGR has
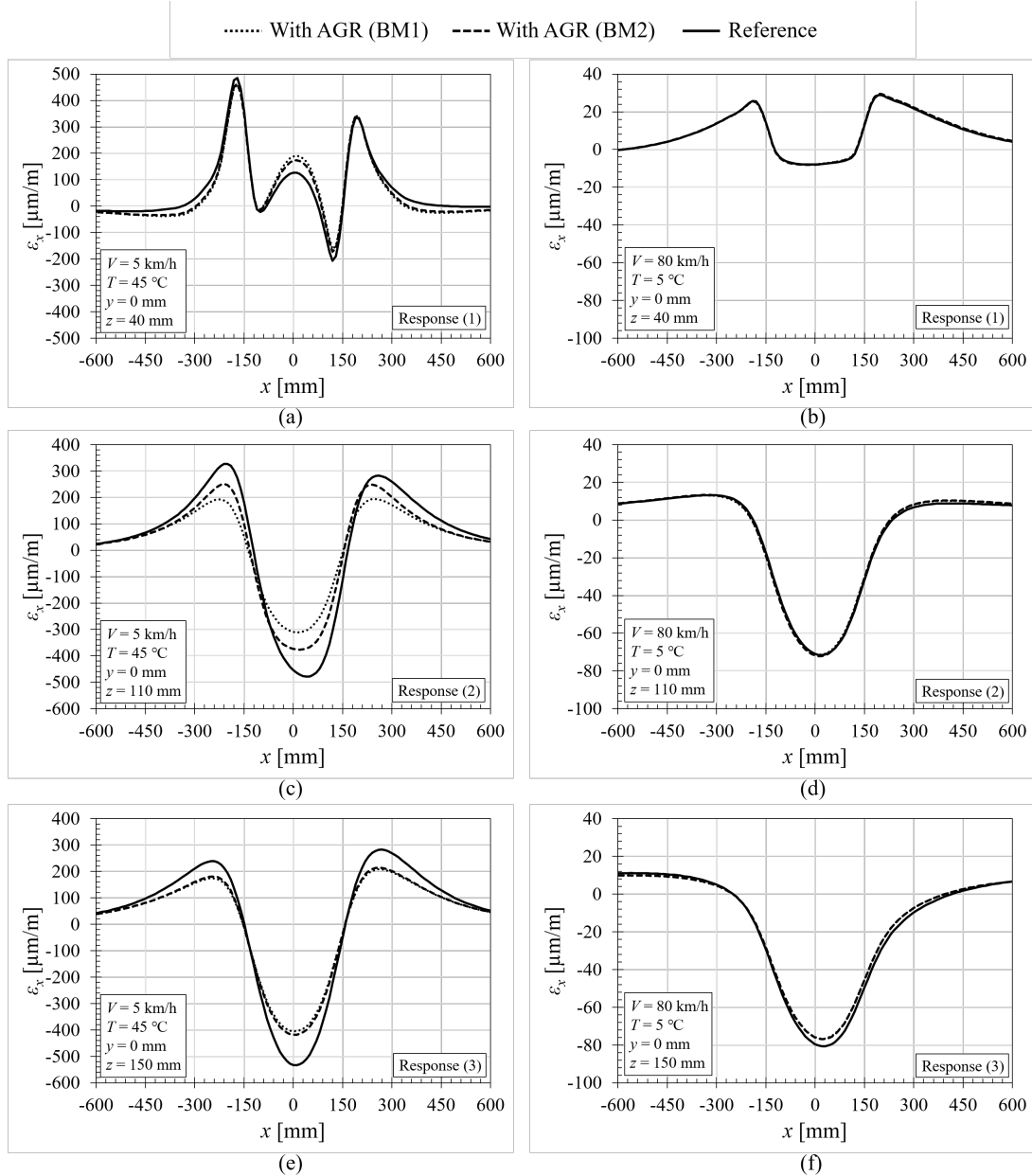
Figure 10. Simulated horizontal strains in the traveling direction ε_x at three depths $z = 40\,\text{mm}$, $z = 110\,\text{mm}$, and $z = 150\,\text{mm}$, and for two load-speed/temperature conditions.

a noticeable effect on reducing longitudinal strains; the effect is mainly realized at $z = 110\,\text{mm}$ and $z = 150\,\text{mm}$. The choice of BM only seems to have a notable influence on the strain level at the grid location (i.e., at $z = 110\,\text{mm}$). Here, BM1 is associated with the largest strain reduction. At $z = 40\,\text{mm}$ and $z = 150\,\text{mm}$ the choice of BM is trivial. For the high-speed/low-temperature conditions, the reinforcement effect is generally small and graphically unnoticeable. Figure 11 presents Responses (4), (5), and (6). There are six charts in this figure with a similar arrangement as Figure 10, representing the simulated strain values in the transverse (y) direction. As can be seen across the six charts, similar AGR effects appear for transverse strains as compared to longitudinal strains.
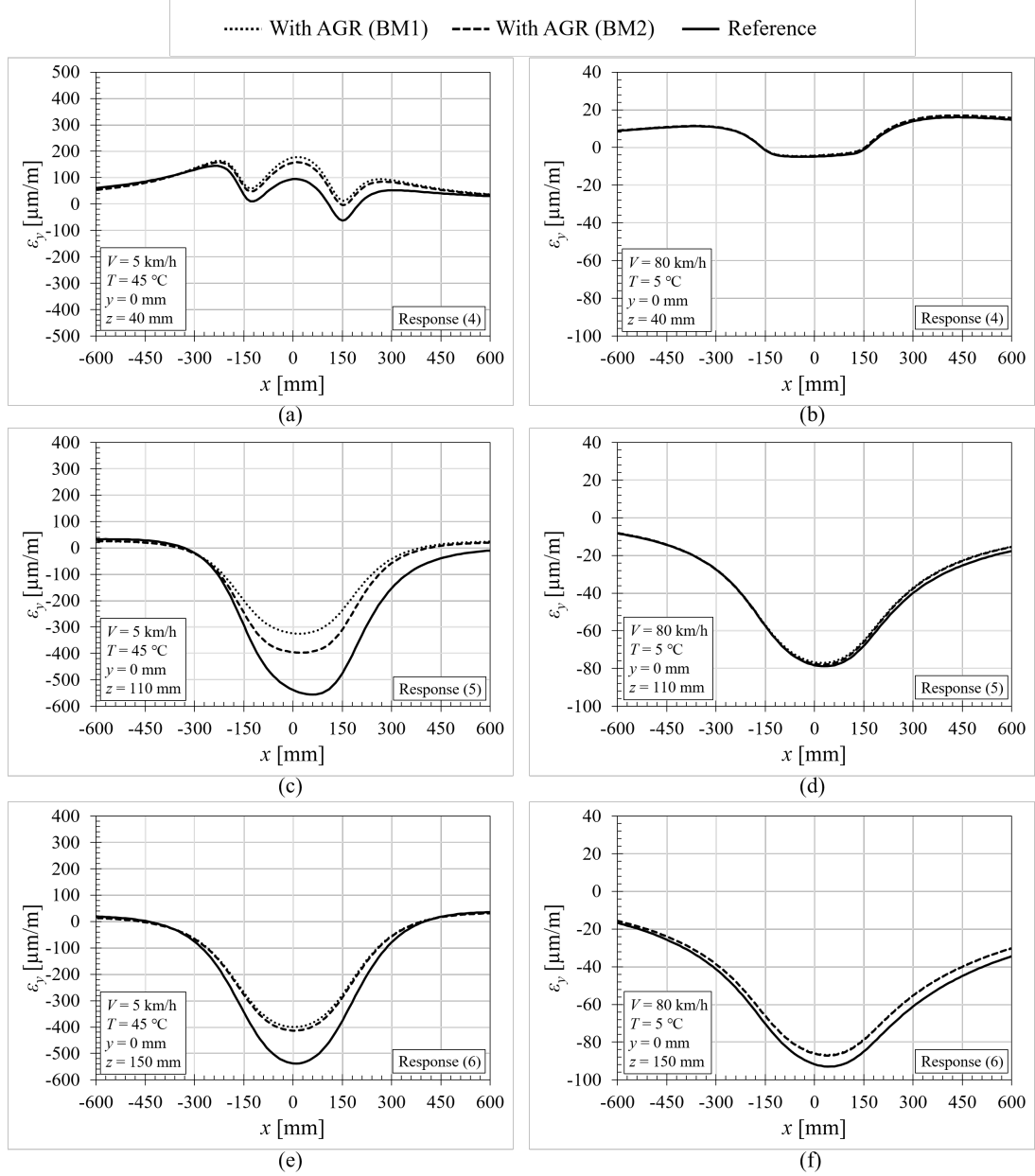
20

Figure 11. Simulated horizontal strains in the transverse direction ε_y at three depths $z = 40\,\text{mm}$, $z = 110\,\text{mm}$, and $z = 150\,\text{mm}$, and for two load-speed/temperature conditions.

Figure 12 presents Responses (7) and (8) in four charts. Figures 12(a) and (b) present vertical strains on top of the unbound granular structure, while Figures 12(c) and (d) present deflections. Charts on the left-hand side are associated with $V = 5$ km/h and $T = 45\,^\circ\text{C}$ and charts on the right-hand side are associated with $V = 80$ km/h and $T = 5\,^\circ\text{C}$; they each include three response traces similar to Figure 10 and 11. As can be seen, for both Responses (7) and (8), only a small AGR effect is realized under the low-speed/high-temperature condition. Specifically, the presence of AGR slightly reduces the strain on top of the unbound granular structure and the deflection. It can also be seen that the chosen BM has a negligible influence on both key responses. No AGR effect is noticeable for the high-speed/low-temperature condition.
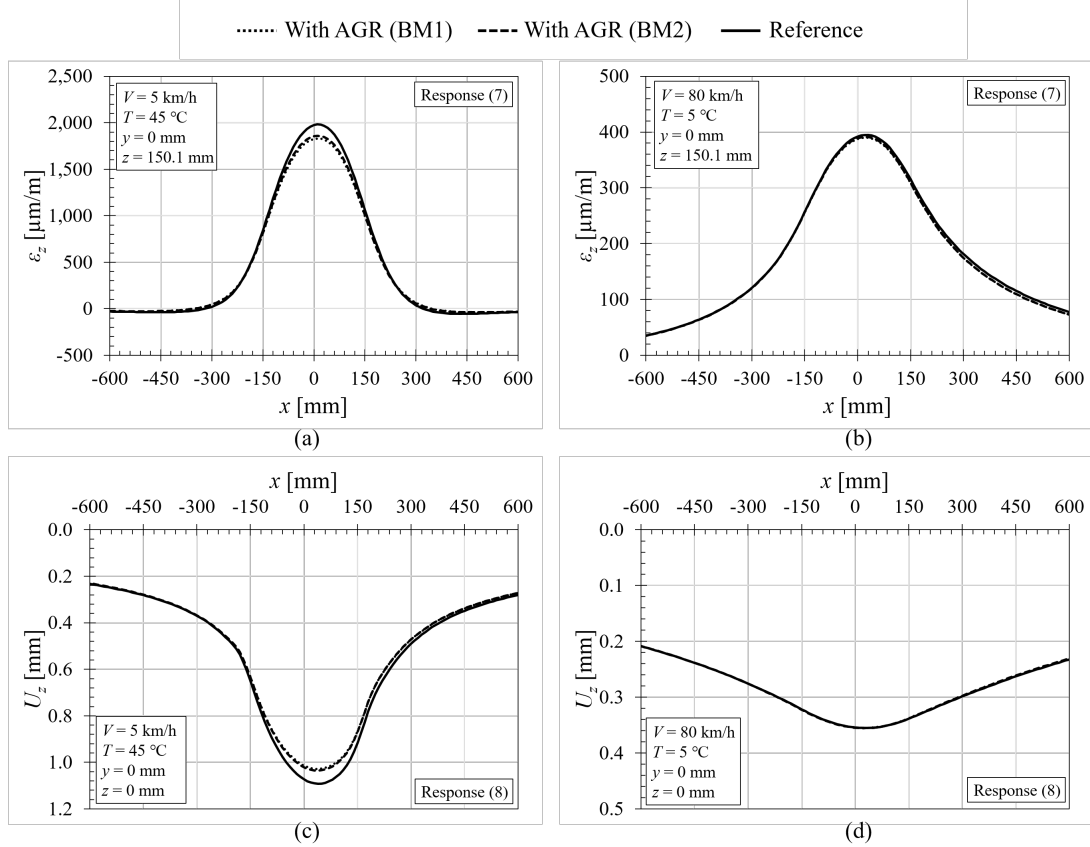
Figure 12. Simulated vertical strains ε_z at $z = 150.1\,\text{mm}$ and vertical displacement U_z at $z = 0\,\text{mm}$, for two load-speed/temperature conditions.

Table 3. Ultimate peak response values across pavement systems and load-speed/temperature conditions.

Model	$\varepsilon_x(z)$ [μm/m]	$\varepsilon_y(z)$ [μm/m]	$\varepsilon_z(z = 150.1\,\text{mm})$ [μm/m]	$U_z(z = 0\,\text{mm})$ [mm]
Peak responses at $T = 45°\text{C}$ and $V = 5$ km/h				
Reference	-534*	-556†	1981	1.092
With AGR (BM1)	-405* (-24%)	-400* (-28%)	1830 (-8%)	1.028 (-6%)
With AGR (BM2)	-418* (-22%)	-414* (-26%)	1859 (-6%)	1.036 (-5%)
Peak responses at $T = 5°\text{C}$ and $V = 80$ km/h				
Reference	-81*	-93*	395	0.355
With AGR (BM1)	-77* (-5%)	-87* (-7%)	390 (-1%)	0.355 (0%)
With AGR (BM2)	-77* (-5%)	-87* (-6%)	391 (-1%)	0.355 (0%)

†at $z = 110\,\text{mm}$
*at $z = 150\,\text{mm}$

Table 3 lists the ultimate peak values of the critical key responses. The ultimate peak values refer to the largest value associated with ε_x, ε_y, ε_z, and U_z. Specifically, the largest value of key responses (1), (2), and (3) refers to the ultimate peak value of ε_x, the largest value of key responses (4), (5), and (6) refers to the ultimate peak

22

value of ε_y, while the largest value of key response (7) and (8) refers to the ultimate peak values of ε_z (at $z = 150.1\,\text{mm}$) and U_z (at $z = 0\,\text{mm}$), respectively. All ultimate peak values associated with the two reinforced pavement models are provided alongside their relative change in magnitude (in %) compared to the reference model. In addition, ultimate peak values associated with ε_x and ε_y are provided alongside their location within the AC. Overall, it can be seen that installing AGR between two AC layers at $z = 110\,\text{mm}$ reduces the ultimate peak values across all key responses for the low-speed/high-temperature condition. The AGR effect is largest for the horizontal strains (i.e., ε_x and ε_y) with a reduction of up to 28% in peak strain intensity. In contrast, a peak reduction of up to 7% is obtained for horizontal strains in the high-speed/low-temperature situation. The remaining key responses, i.e., $\varepsilon_z(z = 150.1\,\text{mm})$ and $U_z(z = 0\,\text{mm})$ are marginally affected by the AGR at $V = 5\,\text{km/h}$ and $T = 45\,°\text{C}$ (between 5% to 8% in peak reduction), and no pragmatic AGR effects are realized at $V = 80\,\text{km/h}$ and $T = 5\,°\text{C}$. Finally, it is observed that the ultimate peak values associated with ε_x and ε_y generally transpire at the bottom of the AC. However, an exception is observed for ε_y at $V = 5\,\text{km/h}$ and $T = 45\,°\text{C}$ in the reference pavement model (without AGR), where the ultimate peak strain occurs at the interface at $z = 110\,\text{mm}$. This exception implies that critical horizontal strains do not always transpire at the AC bottom when accounting for imperfect bonding conditions between AC layers.

4.   Conclusion

4.1.   *Summary and main findings*

This work investigated the effects of interface properties on key responses in asphalt pavements with grid reinforcement placed in-between two AC lifts. Initially, the interface bonding properties of two AC cores were characterized in the laboratory; the cores were taken from two nominally identical full-scale pavement test sections at DTU Smart Road – one including AGR and another without (see Figure 2). Both cores were tested using the DDST (see Figure 4), applying sinusoidal shear loading under small levels of displacement. This was done for several combinations of temperatures, frequencies, normal stress levels, and displacement amplitudes. Analysis of the measurements produced several relaxation interface stiffness functions $K(t)$, each associated with a normal stress and a displacement amplitude (see Equation (10), Figure 6, and Table 2). Additionally, the VE properties of the AC were characterized in a separate laboratory effort (see Equation (6), Figure 3, and Table 1). Next, a synthetic investigation according to the modeling approach of Nielsen *et al.* (2022) was carried out based on the two DTU Smart Road test sections. The AC VE properties and the interface stiffness properties obtained from the laboratory tests were utilized as inputs. Several key responses, commonly linked with pavement performance, were simulated for two different AC temperature levels under a moving wheel traveling at two different speeds.

The main findings from the overall effort are addressed in the following. First, based on the measurements from the DDST, it was found that: (i) it was possible to obtain a time- and temperature-dependent relaxation interface stiffness, which can be directly utilized as a pavement modeling input; (ii) for both the reinforced and unreinforced cases, the relaxation interface stiffness was sensitive to the differential displacement amplitude and to the normal stress level; and (iii) at all times, the relaxation interface

stiffness without AGR was larger than the relaxation interface stiffness with AGR.

Next, based on the synthetic investigation, it was found that: (i) differential displacements across AC interfaces, with or without AGR, were of the order of micrometers. These displacements were larger with an AGR; (ii) adding an AGR between the two lower AC lifts lessened the horizontal strains at the reinforced interface and at the AC bottom. This effect was pronounced for low-speed/high-temperature conditions, and considerably smaller for high-speed/low-temperature conditions; (iii) the presence of AGR between the two lower AC lifts had a marginal influence on deflections and vertical strains on top of the unbound granular structure; and (iv) the choice of BM had a notable influence on horizontal strains and differential interface displacements near the AGR.

4.2. *Implications and limitations*

The main findings of this work imply that adding an AGR between two AC lifts in the bottom half of the AC structure can potentially prolong the pavement service life in terms of bottom-up fatigue cracking. This is because the presence of AGR produces a reduction in horizontal strains – commonly associated with this distress type – despite the lower interface stiffness compared to an unreinforced case. Furthermore, the findings imply that the AGRs can only marginally impact base and subgrade rutting. This is because the presence of AGR between two AC lifts produces an insignificant change in vertical stresses commonly associated with this distress type. This finding is slightly different from what was found in Nielsen and Levenberg (2022), where a similar pavement was analyzed with AGR placed at the bottom of the AC, directly on top of the unbound granular structure. Moreover, the study findings suggest that it is practically challenging, if not impossible, to measure an AGR effect with FWDs (ASTM 2009, Horak *et al.* 2015) or moving measurement platforms (Skar *et al.* 2020b, Baltzer *et al.* 2010). This is because the presence of AGR between two AC lifts produces an insignificant change in vertical surface displacements. Finally, it is concluded that even if laboratory measurements display a reduced interface stiffness when installing an AGR in-between two AC lifts, the reduction may not have any practical implication on key response traces – both in terms of shape and peak magnitudes. Also, the reduction may not necessarily annul beneficial reinforcement effects.

Some limitations emerged during the work. One limitation relates to shear testing and the (known) difficulty of applying pure shear to an interface without introducing moments/rotations. These moments/rotations were amplified with increasing levels of applied shear load and normal stress, and also influenced by temperature level and loading frequency. This caused some of the measurements to deviate from pure sinusoidal shape. Another limitation concerns the selected temperature levels, which did not provide a basis for estimating a set of time-temperature shift parameters associated with each interface; this was because the estimated $|K^*|$ values did not overlap across the considered temperature levels. Furthermore, the study involved a limited number of test specimens, which do not provide a statistical basis for interface properties measured in the laboratory. While some of these limitations can be addressed by modification of the test procedure, the main focus was to investigate the effect of interface bonding on key responses in asphalt pavements including AGR. A final limitation addressed in this study was related to the non-linear nature of the interface stiffness, which cannot be handled in the modeling framework proposed by Nielsen *et al.* (2022). A linear approximation of the interface properties was therefore needed.

4.3. Recommendations for future work

This study focused on laboratory testing and synthetic forecasting of responses with a mechanistic model. Future investigations should target full-scale validation of the model simulations under a wide range of pavement systems, loading configurations, loading speeds, and temperature conditions. Doing so will increase the confidence in the model assumptions and expedite its engineering acceptance. One suggestion in this context is to install LVDTs inside core-drilled holes and monitor diameter changes just above and just below interfaces – with or without AGR. This type of sensing arrangement requires development as it does not currently exist. Additionally, a more extensive laboratory investigation should be carried out, involving more cores, to form a statistical basis for the time- and temperature-dependent interface stiffness function. This effort should include a more closely spaced set of temperature levels to facilitate a reliable time-temperature shifting analysis. Additional aspects for future investigation should deal with the evaluation of more AGR products, different AC types, AGRs deployed on top of milled surfaces, and AGRs placed on top of compacted unbound aggregate bases. In this context, the modeling approach outlined and utilized in this study offers a mechanistic tool for analyzing AGR effects in asphalt pavements on a case-by-case basis.

Disclosure statement

No potential conflict of interest was reported by the authors.

References

AASHTO, 2008. *Pavement Design Guide A Manual of Practice*. No. Interim edition.

Al Hakim, B., Cheung, L.W., and Armitage, R.J., 1999. Use of FWD Data for Prediction of Bonding Between Pavement Layers. *International Journal of Pavement Engineering*, 1 (1), 49–59.

Arsenie, I.M., *et al.*, 2017. Laboratory characterisation of the fatigue behaviour of a glass fibre grid-reinforced asphalt concrete using 4PB tests. *Road Materials and Pavement Design*, 18 (1), 168–180. Available from: https://doi.org/10.1080/14680629.2016.1163280.

ASTM, 2009. Standard test method for deflections with a falling-weight-type impulse load device.

Austin, R.A. and Gilchrist, A.J., 1996. Enhanced Performance of Asphalt Pavements Using Geocomposites. *Geotextiles and Geomembranes*, 14 (3-4 SPEC. ISS.), 175–186.

AUSTROADS, 2004. Pavement Design : A Guide to the Structural Design of Road Pavements. *Deterioration and Maintenance of Pavements*, 233–243. Available from: www.austroads.com.au.

Baltzer, S., *et al.*, 2010. Continuous bearing capacity profile of 18,000 km Australian road network in five months.

Burmister, D.M., 1943. The Theory of Stresses and Displacements in Layered Systems and Applications to the Design of Airport Runways. *In*: *Highway Research Board, Vol. 23*. 126–148.

Burmister, D.M., 1945a. The general theory of stresses and displacements in layered soil systems. II. *Journal of Applied Physics*, 16 (3), 126–127.

Burmister, D.M., 1945b. The general theory of stresses and displacements in layered soil systems. III. *Journal of Applied Physics*, 16 (5), 296–302.

Burmister, D.M., 1945c. The general theory of stresses and displacements in layered systems. I. *Journal of applied physics*, 16 (2), 89–94.

Canestrari, F. and Santagata, E., 2005. Temperature effects on the shear behaviour of tack coat emulsions used in flexible pavements. *International Journal of Pavement Engineering*, 6 (1), 39–46.

Canestrari, F., *et al.*, 2005. Advanced testing and characterization of interlayer shear resistance. *Transportation Research Record*, (1929), 69–78.

Correia, N.S. and Mugayar, A.N., 2021. Effect of binder rates and geogrid characteristics on the shear bond strength of reinforced asphalt interfaces. *Construction and Building Materials*, 269, 121292. Available from: https://doi.org/10.1016/j.conbuildmat.2020.121292.

Correia, N.S. and Zornberg, J.G., 2016. Mechanical response of flexible pavements enhanced with Geogrid-reinforced asphalt overlays. *Geosynthetics International*, 23 (3), 183–193.

Correia, N.S. and Zornberg, J.G., 2018. Strain distribution along geogrid-reinforced asphalt overlays under traffic loading. *Geotextiles and Geomembranes*, 46 (1), 111–120. Available from: https://doi.org/10.1016/j.geotexmem.2017.10.002.

Crispino, M., *et al.*, 1997. Evaluation of the interaction between the asphalt concrete layers by a new dynamic test. *Proceeding of the 8th International Conference on Asphalt Pavements, Seattle, USA*, 741–754.

de Bondt, A.H., 1999. Anti-reflective cracking design of (reinforced) asphalt overlays. PhD thesis.

Goodman, J.R. and Popov, E.P., 1968. Layered Beam Systems with Interlayer Slip. *Journal of the Structural Division*, 94 (11), 2535–2548.

Horak, E., *et al.*, 2015. Flexible road pavement structural condition benchmark methodology incorporating structural condition indices derived from Falling Weight Deflectometer deflection bowls. *Journal of Civil engineering and Construction*, 4 (1), 12.

Huang, Y.H., 2004. *Pavement Analysis and Design (Second edition)*. Available from: http://docshare04.docshare.tips/files/14013/140138713.pdf.

Ike, C.C., 2018. General Solutions for Axisymmetric Elasticity Problems of Elastic Half Space using Hankel Transform Method. *International Journal of Engineering and Technology*, 10 (2), 565–580.

Isailović, I., Falchetto, A.C., and Wistuba, M., 2017. Fatigue investigation on asphalt mixture layers' interface. *Road Materials and Pavement Design*, 18, 514–534.

Khodaii, A., Fallah, S., and Moghadas, F., 2009. Effects of geosynthetics on reduction of reflection cracking in asphalt overlays. *Geotextiles and Geomembranes*, 27 (1), 1–8. Available from: http://dx.doi.org/10.1016/j.geotexmem.2008.05.007.

Kruntcheva, M.R., Collop, A.C., and Thom, N.H., 2006. Properties of Asphalt Concrete Layer Interfaces. *Journal of Materials in Civil Engineering*, 18 (3), 467–471.

Le, M.T., Nguyen, Q.H., and Nguyen, M.L., 2020. Numerical and experimental investigations

of asphalt pavement behaviour, taking into account interface bonding conditions. *Infrastructures*, 5 (2).

Le, X.Q., *et al.*, 2022. Evaluation of interface bonding condition on mechanical responses of full-scale asphalt pavements with and without grid reinforcement. *Eleventh International Conference on the Bearing Capacity of Roads, Railways and Airfields, Volume 2*, 2, 261–270.

Lee, J.H., *et al.*, 2019. Long-term performance of fiber-grid-reinforced asphalt overlay pavements: A case study of Korean national highways. *Journal of Traffic and Transportation Engineering (English Edition)*, 6 (4), 366–382. Available from: https://doi.org/10.1016/j.jtte.2018.01.008.

Lee, J., Kim, Y.R., and Lee, J., 2015. Rutting performance evaluation of asphalt mix with different types of geosynthetics using MMLS3. *International Journal of Pavement Engineering*, 16 (10), 894–905.

Leischner, S., *et al.*, 2019. Mechanical Testing and Modeling of Interlayer Bonding in HMA Pavements. *Transportation Research Record*, 2673 (11), 879–890. Available from: https://doi.org/10.1177/0361198119843254.

Levenberg, E., 2016a. ELLEA1: Isotropic Layered Elasticity in Excel: Pavement analysis tool for students and engineers. Available from: https://orbit.dtu.dk/en/publications/ellea1-isotropic-layered-elasticity-in-excel-pavement-analysis-to.

Levenberg, E., 2016b. ELLVA1: Isotropic Layered Viscoelasticity in Excel (moving load): Advanced pavement analysis tool for students and engineers. Available from: https://orbit.dtu.dk/en/publications/ellva1-isotropic-layered-viscoelasticity-in-excel-moving-load-adv.

Levenberg, E., 2016c. Viscoelastic pavement modeling with a spreadsheet. *8th International Conference on Maintenance and Rehabilitation of Pavements, MAIREPAV 2016*, 746–755.

Levenberg, E., 2020. *Pavement Mechanics: Lecture Notes*. 1st ed.

Levenberg, E. and Michaeli, N., 2013. Viscoelastic characterisation of asphalt-aggregate mixes in diametral compression. *Road Materials and Pavement Design*, 14 (SUPPL.1), 105–119.

Levenberg, E. and Skar, A., 2020. Analytic pavement modelling with a fragmented layer. *International Journal of Pavement Engineering*, 0 (0), 1–13. Available from: https://doi.org/10.1080/10298436.2020.1790559.

Nguyen, M.L., *et al.*, 2013. Review of glass fibre grid use for pavement reinforcement and APT experiments at IFSTTAR. *Road Materials and Pavement Design*, 14 (SUPPL.1), 287–308.

Nielsen, J. and Levenberg, E., 2022. Full-scale validation of a mechanistic model for asphalt grid reinforcement.

Nielsen, J., Levenberg, E., and Skar, A., 2022. Mechanistic modelling of grid-reinforced milled-and-overlaid asphalt pavements. *International Journal of Pavement Engineering*, (May), 1–16. Available from: https://doi.org/10.1080/10298436.2022.2072502.

Ong, G.P., Fwa, T.F., and Tan, S.A., 2004. Laboratory Evaluation of Rutting Resistance of Geosynthetics Reinforced Asphalt Pavement. *Transportation*, 44 (2), 29–44.

Park, S. and Schapery, R., 1999. Methods of interconversion between linear viscoelastic material functions. Part I–a numerical method based on Prony series. *International Journal of Solids and Structures*, 36 (11), 1653–1675. Available from: http://www.sciencedirect.com/science/article/pii/S0020768398000559.

Peutz, M.G., Van Kempen, H.P., and Jones, A., 1968. Layered systems under normal surface loads. *Highway Research Record*, (228).

Plug, C.P., Bondt, A.H.D., and Hydra, R., 2010. Research & Development – Conference Papers 5th World congress on emulsions Lyon , France October 2010. (October).

Romanoschi, S.A. and Metcalf, J.B., 2001. Characterization of asphalt concrete layer interfaces. *Transportation Research Record*, (1778), 132–139.

Roussel, J.M., *et al.*, 2022. Influence of interface properties on heavy weight deflectometer test results. *Road Materials and Pavement Design*, 23 (S1), 162–177. Available from: https://doi.org/10.1080/14680629.2022.2029759.

Saride, S. and Kumar, V.V., 2017. Influence of geosynthetic-interlayers on the performance of

asphalt overlays on pre-cracked pavements. *Geotextiles and Geomembranes*, 45 (3), 184–196. Available from: http://dx.doi.org/10.1016/j.geotexmem.2017.01.010.

Schapery, R., 1962. Approximate Methods of Transform for Viscoelastic Stress Analysis. *In*: *Fourth USNat Congr Appl Mech.* 1075–1084.

Shell, 1978. Shell Pavement Design Manual: Asphalt Pavements and Overlays for Road Traffic. *Shell International Petroleum Co. Ltd., London, UK.*

Shook, J.F., *et al.*, 1982. Thickness design of asphalt pavements-the asphalt institute method. *In*: *Proceedings, 5th International Conference on Structural Design of Asphalt Pavements, Delft University of Technology, The Netherlands, 1982.* Volume 1.

Skar, A. and Andersen, S., 2020. ALVA: An adaptive MATLAB package for layered viscoelastic analysis. *Journal of Open Source Software*, 5 (55), 2548.

Skar, A., Andersen, S., and Nielsen, J., 2020a. Adaptive Layered Viscoelastic Analysis (ALVA). Available from: https://doi.org/10.11583/DTU.12387305.v7.

Skar, A., *et al.*, 2020b. Analysis of a moving measurement platform based on line profile sensors for project-level pavement evaluation. *Road Materials and Pavement Design*, 0 (0), 1–17. Available from: https://doi.org/14680629.2020.1741429.

Sobhan, K., 2005. Effects of Geosynthetic Reinforcement on the Propagation of Reflection Cracking and Accumulation of Permanent Deformation in Asphalt Overlays. (June), 1–9.

Solatiyan, E., Bueche, N., and Carter, A., 2021. Laboratory evaluation of interfacial mechanical properties in geogrid-reinforced bituminous layers. *Geotextiles and Geomembranes*, 49 (4), 895–909. Available from: https://doi.org/10.1016/j.geotexmem.2020.12.014.

Sutanto, M.H., 2009. Assessment of bond between asphalt layers. *University of Nottingham*, 66 (17 2), 292.

Uzan, J., Livneh, M., and Eshed, Y., 1978. Investigation of adhesion propenies between asphalt concrete layers. *In*: *Proceedings of Asphalt Paving Technology.* vol. 47, 495–521.

Vinay Kumar, V. and Saride, S., 2017. Use of digital image correlation for the evaluation of flexural fatigue behavior of asphalt beams with geosynthetic interlayers. *Transportation Research Record*, 2631 (2631), 55–64.

White, G., 2017. State of the art: interface shear resistance of asphalt surface layers. *International Journal of Pavement Engineering*, 18 (10), 887–901. Available from: http://dx.doi.org/10.1080/10298436.2015.1126270.

Williams, M.L., Landel, R.F., and Ferry, J.D., 1955. The Temperature Dependence of Relaxation Mechanisms in Amorphous Polymers and Other Glass-forming Liquids. *Journal of the American Chemical Society*, 77 (14), 3701–3707.

Pavement systems are important for ensuring social and economic equality, but they constantly deteriorate under traffic loads and weather effects. With the marked growth in global shipping, the evolution of new types of vehicles, and rapid climate change effects, it is important to improve traditional pavement systems and rehabilitation methods to maintain an acceptable level of service. This PhD study looked at using asphalt grid reinforcement products to improve road durability. The goal was to create a model that engineers can use to choose a reinforcement alternative for road design. The study included building a test road on DTU campus (in Kgs. Lyngby), called DTU Smart Road. The road was equipped with asphalt grid reinforcement and embedded sensors. Sensor data were used to demonstrate the model's ability to reproduce reality. The main study findings showed that the developed model was able to capture the effects of installing asphalt grid reinforcement inside the DTU Smart Road. Furthermore, model simulations adding reinforcement could potentially delay the development of cracks and ruts in road systems, thus increasing their lifespan. Ultimately, this PhD study has created a valuable tool for engineers, consultants, and contractors to improve the durability of future road networks.